8-2017

Friction Stir Back Extrusion of Aluminium Alloys for Automotive Applications

Zeren Xu
Clemson University, erbantou@hotmail.com

FRICTION STIR BACK EXTRUSION OF ALUMINIUM ALLOYS FOR AUTOMOTIVE APPLICATIONS

A Dissertation
Presented to
the Graduate School of
Clemson University

In Partial Fulfillment
of the Requirements for the Degree
Doctor of Philosophy
Automotive Engineering

---

by
Zeren Xu
August 2017

Accepted by:
Fadi Abu-Farha, Committee Chair
Srikanth Pilla
Hongseok Choi
Mark Hoffman

ABSTRACT

Since the invention of Friction Stir Welding in 1991 as a solid state joining technique, extensive scientific investigations have been carried out to understand fundamental aspects of material behaviors when processed by this technique, in order to optimize processing conditions as well as mechanical properties of the welds. Based on the basic principles of Friction Stir Welding, several derivatives have also been developed such as Friction Stir Processing, Friction Extrusion and Friction Stir Back Extrusion. Friction Stir Back Extrusion is a novel technique that is proposed recently and designed for fabricating tubes from lightweight alloys. Some preliminary results have been reported regarding microstructure and mechanical properties of Friction Stir Back Extrusion processed AZ31 magnesium alloy, however, systematic study and in-depth investigations are still needed to understand the materials behaviors and underlying mechanisms when subjected to Friction Stir Back Extrusion, especially for age-hardenable Al alloys.

In the present study, Friction Stir Back Extrusion processed AA6063-T5 and AA7075-T6 alloys are analyzed with respect to grain structure evolution, micro-texture change, recrystallization mechanisms, precipitation sequence as well as mechanical properties. Optical Microscopy, Electron Backscatter Diffraction, Transmission Electron Microscopy, Vickers Hardness measurements and uniaxial tensile tests are carried out to characterize the microstructural change as well as micro and macro mechanical properties

of the processed tubes. Special attention is paid to the micro-texture evolution across the entire tube and dynamic recrystallization mechanisms that are responsible for grain refinement.

Significant grain refinement has been observed near the processing zone while the tube wall is characterized by inhomogeneous grain structure across the thickness for both alloys. Dissolution of existing precipitates is noticed under the thermal hysterias imposed by Friction Stir Back Extrusion process, resulting in decreased strength but improved elongation of the processed tubes; a post-process aging step can effectively restore the mechanical properties of the processed tubes by allowing for the reprecipitation of solute elements in the form of fine, dispersed precipitates. Texture analysis performed for AA6063 alloy suggests the dominance of simple shear type textures with clear transition from initial texture to stable B/$\bar{B}$ components via intermediate types that are stable under moderate strain levels. In order to identify the texture components properly, rigid body rotations are applied to the existing coordinate system to align it to local shear reference frame. Surprisingly, for AA7075 tubes, <111> and <100> fibers are observed to be the dominant texture components in the transition region as well as thermomechanically affected zone while the processing zone is characterized by random texture. The underlying mechanisms responsible for the formation of random texture are discussed in Chapter 5 based on Electron Backscatter Diffraction analysis. Comparative discussions are also carried out for the recrystallization mechanisms that are responsible for grain structure evolution of both alloys. Continuous grain subdivision and reorientation is cited as the dominant mechanism for the recrystallization of AA6063 alloys, while dynamic

recrystallization occurs mainly in the form of Geometric Dynamic Recrystallization and progressive subgrain rotations near grain boundaries in AA7075 alloys.

ACKNOWLEDGMENTS

First and foremost, I need to thank my academic advisor Dr. Fadi Abu-Farha for his support and help during my study at Clemson, especially for building up the research environment and connections that help me conduct my research smoothly. Also, I learn from his hard working and academic spirits. This thesis can't be finished without his guidance and support.

I need to thank all my committee members for providing informative suggestions on my research directions and scientific details, and also finding time to help me out in extremely tight time schedules.

I need to thank my family members, especially my parents, for all the support and love they give me from the first day I came to this world!

Special thank need to be grant to my girlfriend Xiaoyan Yu for her accompany and support during my study at Clemson and at University of Kentucky since 2012, without her encouragement and support, my study would not be finished at all.

I need to thank George, Dr. Saraf for their help in sample preparation and data analysis of electron microscopy testing at Advance Materials Research Lab of Clemson.

I need to thank my friends Hongbing Yu at Oxford University and Qingshan Dong at Queens University for helping me running TEM for my samples.

I need to thank my previous co-works Bingshu wang and Jianwei cheng for providing informative discussions about my research and EBSD analysis.

I need to thank my friends Jie Pan, Yan Jin and my previous academic advisor Dr. Tongguang Zhai for all the help they provided during my first year study in the U.S.

I need to thank Dr. Robert Sanders for his encouragement and help when I applied for graduate school in the U.S.

I need to thank everyone that come into my life, help me, encourage me, makes me happy, excited, frustrated, and depressed. I appreciated all the help and all the troubles, that all makes me a better person.

TABLE OF CONTENTS

Page

LIST OF TABLES

LIST OF FIGURES

List of Figures (Continued)

Figure Page

List of Figures (Continued)

Figure Page

List of Figures (Continued)

Figure Page

List of Figures (Continued)

Figure Page

List of Figures (Continued)

Figure Page

List of Figures (Continued)

Figure Page

List of Figures (Continued)

Figure Page

List of Figures (Continued)

Figure Page

ABBREVIATIONS

FSW-friction stir welding
FSP-friction stir processing
FSBE-friction stir back extrusion
EBSD-electron backscatter diffraction
DRX-dynamic recrystallization
GDX-Geometric Dynamic recrystallization
PFZ-precipitation free zone
HAZ-heat affect zone
FCC-face-centered cubic
SPN-shear plane normal
SD-shear direction
PF-pole figure
ND-normal direction
TD-transverse direction
RD-rolling direction
SRX-static recrystallization
DDRX-discontinuous dynamic recrystallization
SIBM-strain induced boundary migration
SFE-stacking fault energy
DRV-dynamic recovery
GB-grain boundaries
LAGB-low angle grain boundary
HAGB-high angle grain boundary
PSN-particle stimulated nucleation
OM-optical microscopy
EM-electron microscopy
SEM-scanning electron microscopy
TEM-Transmission Electron Microscopy
EDM-electrical discharge machine
FE-SEM-Field Emission Scanning Electron Microscopy
DIC-Digital Image Correlation
PZ-processing zone
TMAZ-thermomechanically affected zone
ODF-orientation distribution function

CHAPTER ONE

INTRODUCTION

Introduction to FSW and its Derivatives

Fiction stir welding (FSW) was invented by 'The welding Institute' (TWI) at UK in 1991 as a novel solid-state joining technique, which is initially designed for aluminum alloys. The basic concept of the process can be described as: a non-consumable rotating tool with a pin and shoulder is plunged into the faying surface of sheets or plates that are going to be joined, then the tool start moving along the joining line, the heat and materials flow generated by the rotating tool result in the joining in solid states [1-4].

Over the past two decades, significant amount of work have been done on multiple aspects of FSW including tooling [5, 6], materials flow [4, 7-9], processing parameters, grain structure evolution [10-14], precipitation behaviors [12-17], mechanical properties [18-24] and many more.

Recently, several derivatives have been proposed based on the basic principles of FSW. Mishra proposed the concept of friction stir processing (FSP) designed mainly for microstructure modification and grain refinement [1], which is fundamentally similar to the FSW process. A recent investigation performed by Reynolds et al developed an extrusion technique to recycle aluminum chips based on the principle of FSW called friction extrusion [25]. Friction stir back extrusion (FSBE) was developed by Abu-Farha [26] as a method of fabricating lightweight tubes with refined microstructure, based on the principle of FSW. The potential of FSBE for grain refinement and its capacity of

fabricating lightweight tubes have been preliminarily demonstrated. I. Dinaharan et al [27] applied this technique to fabricating pure copper tubes, microstructure analysis performed at multiple locations of the processed tube indicates grain coarsening rather than refinement due to excessive friction heat. Khorrami et al. [28] reported significant grain refinement but inhomogeneous microstructure across the tube wall in a FSBE processed aluminum alloy; however, decreased microhardness value as well as tensile strength were also noticed, which were attributed to annihilation of dislocations. A comprehensive study of microstructure and mechanical properties of FSBE processed AZ31 alloys were conducted by Milner et al. [29, 30]. However, systematic investigations and discussions of microstructure evolution, micro-texture change as well as micro and macro mechanical properties of FSBE processed aluminum alloy, especially age-hardenable series, are still lacking.

Mechanical Properties and Precipitation of Aluminum Alloys under FSW/FSP

A lot of attentions have been paid to the mechanical properties of friction stir welds, especially age-hardenable alloys since they are typically of higher strength and regarded as hard-to-weld by traditional fusion welding due to the presence of large amount of second phase particles. Existing results regarding FSW/FSP of age-hardenable alloys predominantly suggest a decrease in mechanical properties because of dissolution and coarsening of hardening precipitates. Sato et al. [14, 15, 19, 31] performed a series of studies focusing on the precipitation sequence and relevant mechanical property change across the friction stir weld of AA6063-T5 alloy. It is suggested that mechanical

properties of age-hardenable aluminum alloy are mainly controlled by the behaviors of precipitates. The decrease mechanical properties of as-welded materials can be restored by a post-process aging. Whereas in the cases of 7000 series alloys [17, 32], deterioration of mechanical properties have always been noticed under both as-welded condition and after post-weld heat treating due to precipitates coarsening and formation of precipitation free zone (PFZ) near the heat affected zone (HAZ).

Texture Evolution of Aluminum Alloys under FSW/FSP

As a highly investigated topic, micro-texture evolution of the FSW/FSP processed aluminum alloy has been mainly interpreted by simple shear texture since it is believed that the dominant mode deformation during FSW/FSP, especially in the region close to the processing tool, is simple shear. Ideal shear textures that are generated in face-centered cubic (FCC) metals generally favor the alignment of (111) slip plane with the shear plane normal (SPN) and <110>slip direction to the shear direction (SD), forming the so called A and B fiber textures [33-37]. The ideal locations for multiple ideal shear texture components on a standard (111) pole figure are represented in SD-SPN system, as shown in figure 1.1a. This figure is extremely important since it will be used to identify the texture components throughout the entire texture analysis across this dissertation. The corresponding Miller indices are shown in figure 1.1b.

Investigations on texture formation during FSW of aluminum alloys have being reported by a couple of researchers pioneered by Field et al. [38], a strong crystallographic texture gradient across the weld was reported. In his work, the alignment

of (111) plane to SPN was emphasized while the behaviors <110> direction has not been mentioned. A later work done by Sato et al. [39] indicated the alignment of both (111) planes and <110> directions to pin surface and transverse direction of the welded, respectively. However, other components of (110) <001> and (114) <221> have also been observed. Later on, Fonda et al. [40] identified the strengthening of <111>//ND components during their study of microstructure evolution of friction stir welded Al-Li 2195 alloy, and it is preliminarily identified as B and $\bar{B}$ shear components. Jean et al. [41] reported the formation of A/A- and C type texture near the upper surface of the weld and B/$\bar{B}$ texture in the center part of the welds. Afterwards, prevalent opinions regarding the texture formation within the stir zone of aluminum alloys lies in B/$\bar{B}$ texture, which are believed to be stable under high shear strains. The B components are located on B fiber with a close-packed <110> direction aligned with the SD and a close-packed (111) plane aligned with the shear rotation direction, which is normal to both SD and SPN [42]. As shown in figure 1.1a, the B/$\bar{B}$ components exhibit a (112)//SPN and <110>//SD, when viewed from the surface of the welded plate, it can be recognized by <111>//plate surface normal, the direction that is perpendicular to the SPN-SD plane will be called 'z' direction in future discussions. Fonda et al. [43] also observed a periodic variation of crystallographic texture in 2195 Al weld. C and B/$\bar{B}$ components can be strengthened and weakened on a periodic basis, and this periodicity corresponds to the tool advance per revolution as well the onion rings within the welds. At the same time A/A- type textures are also identified while A1* and A2* are absent from that analysis. Several other reports regarding micro-texture evolution of Al alloys mainly points to the

dominance of B/$\bar{B}$ shear texture, especially near the regions where deformation is mainly induced by the rotating pin [42-50]. It has also been pointed out by several researchers that it is necessary to apply systematic rigid body rotations on the measured PFs that are plotted in the macroscopic coordinate systems to project them to local shear reference frameworks, in order to identify the texture components correctly [46, 49, 51, 52]. The fundamental reasons for such deviations from ideal shear reference are believed to be steep strain gradient and constant materials transportations introduced during the process.

Investigations of texture formation during FSW/FSP have been extensively performed due to both scientific and practical merits; however, little information regarding the texture evolution of FSBE processed aluminum alloy have been reported. Even if the fundamental principles of FSBE might be similar to FSW/FSP in the sense that significant amount of shear strain is introduced, materials flow in FSBE is essentially different from FSW/FSP as an extrusion process. Additionally, existing research has been focused mainly on the texture types formed within the SZ while little work has been done to unveil the micro-texture behaviors within the TMAZ and transition regions[53]. In the case of FSBE, the tube wall mainly consists of TMAZ and transition region that are characterized by partially recrystallized grain structures. Thus it is believed that a systematic investigation on the micro-texture evolution across the tube wall will be informative and meaningful. Additionally, the micro-texture of FSW/FSP processed AA7075 alloys have barely been addressed, it is only mentioned briefly by Su et al. [54] as close to random while no additional information is provided. It can be very interesting

to analyze and discuss the micro-texture evolution of FSBE processed AA7075 alloys and correlate the results with dynamic recrystallization mechanisms.

(a)

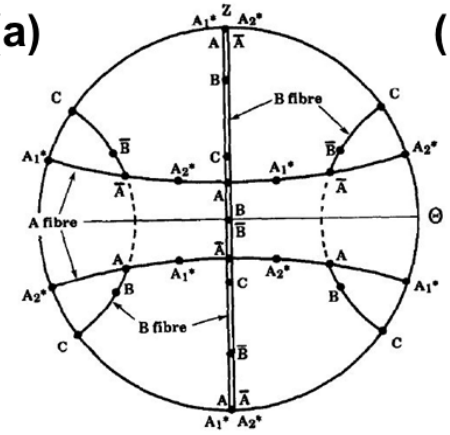

(b)

A	$\{1\bar{1}1\}\langle 110\rangle$	C	$\{001\}\langle 110\rangle$
$\bar{A}$	$\{\bar{1}1\bar{1}\}\langle\bar{1}\bar{1}0\rangle$	D_1	$\{1\bar{2}1\}\langle 111\rangle$
A_1^*	$\{\bar{1}\bar{1}1\}\langle 112\rangle$	D_2	$\{\bar{1}\bar{1}2\}\langle 111\rangle$
A_2^*	$\{11\bar{1}\}\langle 112\rangle$	E	$\{0\bar{1}1\}\langle 111\rangle$
B	$\{1\bar{1}2\}\langle 110\rangle$	$\bar{E}$	$\{01\bar{1}\}\langle\bar{1}\bar{1}\bar{1}\rangle$
$\bar{B}$	$\{\bar{1}1\bar{2}\}\langle\bar{1}\bar{1}0\rangle$	F^*	$\{110\}\langle 001\rangle$

Figure 1.1 (a) (111) pole figure representation of shear texture and (b) notation and Miller indices for common ideal orientations [35, 37]

Recrystallization Mechanisms of Aluminum Alloys

Dynamic recrystallization (DRX) has been a heated topic over the past several decades due to its significance to both scientific understanding and practical applications. Thousands of scientific publications have been made trying to understand the underlying mechanism of recrystallization and its behaviors under different deformation conditions in various alloy systems. Major reasons for the long-lasting research activities on this topic can be summarized into two aspects. First, it is closely related to or even dominates the final grain size and microstructure of hot-formed metallic materials. Additionally, crystallographic texture is also affect by recrystallization and related phenomenon, to a relatively large extent. This can be extremely important for materials used in applications that require certain type of texture formed during its fabrication, for example strong Goss

texture is desirable to enable excellent magnetic properties, otherwise the materials performance would be compromised. Also, the formation of cube texture has been investigated extensively just to understand the root mechanism responsible for its formation, as a side note.

Typically, recrystallization can be categorized into static recrystallization (SRX) and DRX. With the SRX involves the formation of new strain-free grains during subsequent heat treating process, following the deformation stage that is performed in an earlier step; while the DRX typically refer to the process that recrystallization and deformation undergoes simultaneously. The current understanding of SDX is more mature compared to that of DRX since it is relatively simple and less variables are involved. Additionally, since the post heat treatment is applied after deformation as a separate step, the trigger, pause and end of the recrystallization process can be properly controlled to assist experimentation and investigations. On another hand, due to the concurrent nature of DRX with deformation, straining as well as restoration mechanisms are applied to materials and impact the microstructure at the same time. That means, DRX is inherently hard to control and difficult to analyze because of its complexity and concurrent nature. Typically, several recrystallization mechanisms are proposed for metals and they will be reviewed briefly.

Discontinuous Dynamic Recrystallization

In a broad sense, it refers to the dynamic recrystallization process that has clear nucleation and growth stages [55]. The classical nucleation of discontinuous recrystallization involves the formation of new grains via strain induced boundary migration (SIBM) or nucleation at microstructural inhomogeneity such as grain boundaries, second phase particles or shear bands [56]. It should be noted that SIBM involves the bulging of part of a pre-existing grain boundary and the new grains have similar orientations to the initial grains [57]. Additionally, this mechanism is predominant during the static annealing of aluminum alloys after low levels of straining. As for the nucleation at microstructural inhomogeneity, grain boundaries are the most common sites and the newly formed grains are randomly orientated, exhibiting orientations that are not close to their parent grains. The Driving force for the DDRX is regarded as strain induced build-up of store energy in the form of dislocations. The nucleation of DDRX is believed to be closely related to strain-induced grain boundary migrations as well as bulging of grain boundaries. A classical model has been proposed by Sandstrom et al. and Roberts el al. [58, 59] based on the assumption that the growth of dynamically recrystallized grains rely on the distribution and density of mobile locations, regardless of the exact nucleation mechanisms. Their result is briefly summarized as:

$$\frac{\rho_{\mathrm{m}}^{3}}{\&} > \frac{2\gamma_{b}}{\mathrm{KMLGB}^{5}} \quad (1.1)\ [55, 58, 59]$$

with M refers to grain boundary mobility, K as constant, G as the shear modulus, b as burgers vector, L as the mean slip distance of locations and r_b as surface energy. It should be noted that at a particular deformation temperature, the right hand side of the

equation is relatively constant. Thus, in order to trigger dynamic recrystallization, a critical value of the term in the left hand side must be satisfied. For low stacking fault energy (SFE) materials such as pure iron and aluminum alloys, the rate of dynamic recovery is so fast that the parameters on the left side can never reach the critical value to start DDRX. While in materials with low SFE, dislocations can be accumulated to the density level that triggers dynamic recrystallization. However some investigations have also suggested that the origin of dynamic recrystallization in copper might be related to lattice rotations at grain boundary serrations because of boundary sliding [55]. It should be noted that this mechanism is of great similarity to the grain su B division and rotation mechanism that is responsible for the continuous dynamic recrystallization (CDRX) of aluminum as well as magnesium alloys, whose details and corresponding models will be discussed in the following paragraph. As mentioned by McNelley et al. [11], lattice rotations might develop in a progressive fashion at grain boundaries when dislocation movements are inhibited either by lack of slip systems or solute dragging. This lattice rotation leads to the formation of new grains at prior boundaries and form a necklace structure, which is similar to that observed in DDRX. This mechanism is categorized into DDRX in his work, suggesting that the progressive lattice rotation because of inhibited slipping due to lack of slip system or solute dragging might be related to DDRX more than CDRX. Additionally, this mechanism is proven to be responsible for the nucleation of discontinuous dynamic recrystallization in copper by Wusatowska et al. [60]. Also, the bulge and serration described in this mechanism would also fall into the scope of bulge and SIBM that is typically a prelude of DDRX. However, based on the classic textbook

drafted by Humphreys[61], this type of progressive subgrain rotation together with dynamic recovery comprises the standard procedures for CDRX, especially for aluminum alloys.

Based on the author's understanding, this type of recrystallization mechanism should be categorized into CDRX based on classic recrystallization theories and the fact that no rapid grain boundary migration is observed. However, this mechanism can also contribute to the formation of necklace microstructure that is normally identified during the process of DDRX, and in some cases, be interpreted as the controlling mechanism for the nucleation of DDRX [62]. Thus the functionality (either discontinuous or continuous) of this mechanism is vague and needed to be applied to materials base on other information like the SFE or strain level.

Continuous Dynamic Recrystallization

Before addressing the CDRX, another phenomenon that is closely correlated to CDRX is dynamic recovery (DRV). Its corresponding theories will be reviewed briefly to help the understanding and discussions to be carried out for the mechanisms of CDRX. Fundamental mechanisms involved during dynamic recovery process are dislocation climb, cross-slip and dislocation glide that typically result in the formation of low angle grain boundaries (LAGBs). In metals have high SFE, dislocation climb and cross-slip can be easily operated during high temperature deformation, thus dynamic recovery controls the corresponding microstructural evolution and recrystallization process. In a lot of cases, DRV is believed to be the only form of dynamic restoration that occurs at high temperature deformation of high SFC metals [55, 57, 61].

Based on classic theories of thermally activated process, Zener-Hollomon parameter (Z) is constructed by incorporating deformation temperature (T) and strain rate into the following formula:

$$Z = \dot{\varepsilon}\exp\left(\frac{Q}{RT}\right)$$ (1.2) [55], where Q refers to the activation energy

It should be noted that in future discussions, this parameter will be used extensively because of its convenience and efficiency in explaining microstructural change and being able to be correlated to subgrain size and dislocation densities. It has been reported in literature that, during deformation under low level of Z value, grain boundaries can migrate locally because of the boundary tension of the substructure as well local dislocation density change, resulting in serrated grain boundaries with a wavelength closely matches the subgrain size, as can be seen in figure 2a [55]. It should be emphasized that this is a rather extreme case of highly serrated grain boundaries with subgrain size matches serrations frequency very well. In a more realistic situation, the grain boundaries would exhibit bulging and slight serrations without such regularity, as shown in figure 2b. This phenomenon is typically observed during DRV process and serves as an early stage of CDRX process that is going to be addressed in the follow part.

Furu et al. [63] have analyzed subgrain sizes in aluminum alloys under a wide range of deformation conditions and built up a relationship between the Z parameter and subgrain size. An empirical formulation is obtained:

$D = K_1 - K_2 \log Z$ where K1 and K2 are constant (1.3) [55]

However, it should be noticed that the subgrain size (D) refers to the subgrain that are formed across the interior of grains rather than those formed near grain boundareis, whose behavior is controlled by the location deformation conditions.

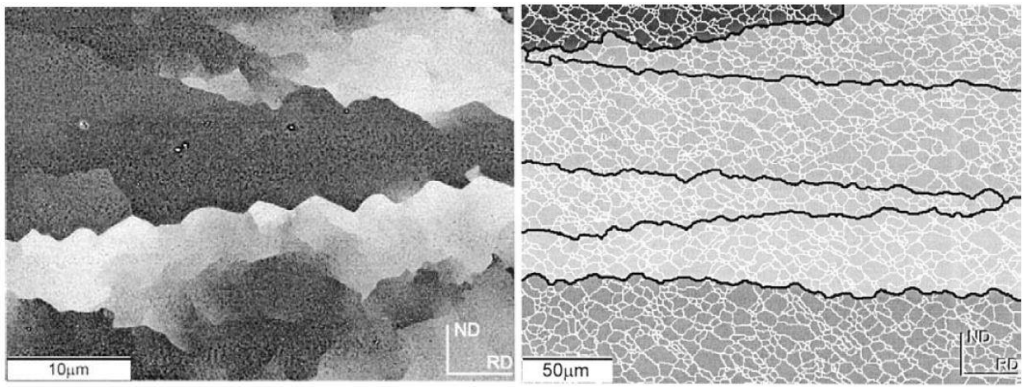

Figure 1.2 Illustration showing the formation of subgrains near grain boundaries as well as in the grain interiors[55]

With the basic knowledge of dynamic recovery, continuous dynamic recrystallization is generally defined as a recrystallization process that nucleation and growth of grains at pre-existing boundaries are not involved. As described by Humphreys [55] at least two separate processes can be classified into the scope of CDRX. The first one is called geometric dynamic recrystallization (GDX), while another process that is present both in metals and minerals involving a gradual rotation of the materials near the grain boundaries (subgrain) is named as rotation recrystallization in Geological. The circumstance of rotation recrystallization will be addressed for the time being, leaving the GDX to be detailed later. In the present dissertation, the recrystallization mechanism that involves gradual subgrain rotation, either near grain boundaries or in grain interiors, will

be considered as CDRX; whereas for GDX, despite of its continuous characteristic in a broad sense, it will be simply termed as geometrical dynamic recrystallization separately.

In a typical scenario, as the materials is strained, misorientations tend to build up at the grain boundaries and form LAGBs while either little evidence of subgrain formation in the grain interiors is noticed or the LAGBs formed near the center of grains are of lower misorientations, especially under relatively low levels of macroscopic strain [55]. Those subgrains formed adjacent to the pre-existing grain boundaries continue to rotate progressively under further straining, meanwhile the corresponding misorientations with respect to their mother grains increases gradually. Historically, the mechanism of progressive lattice/subgrain rotation near grain boundaries is believed to be related to inhibited dislocation movement due to either a lack of slip systems (like in HCP metals) or solute dragging [55]. However, it is definitely true that the deformation conditions near the grain boundaries are more complicated than that of the grain interiors since the grain boundary is always of higher energy and complex deformation conditions. Thus even with minimal solute drag, it is also highly possible that dislocation and LAGBs would evolve in a progressive fashion assisted by the grain boundary plasticity. As noticed by Drury and Humphreys [55], significant lattice rotations tend to develop at grain boundaries under high temperature deformation while subgrain formation within the grains is almost non-existing, as shown in figure 1.3a. Later investigations assisted by EBSD show that serrations are developed near the original grain boundaries and significant orientation gradient is measured near grain boundaries, especially within the

serrations [55]. This work involves deforming a Al-5% Mg alloy at 350 °C in a strain plane compression mode and the EBSD map is shown in figure 1.3b.

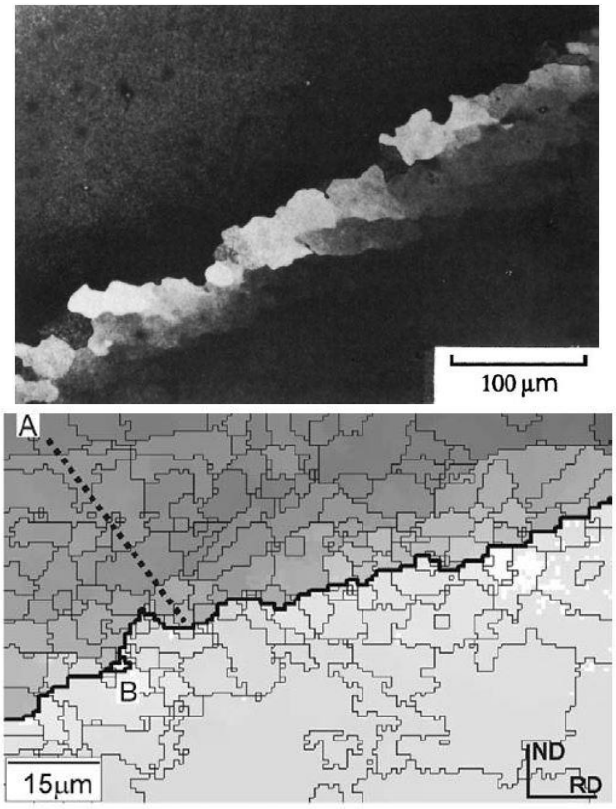

Figure 1.3 Formation of serration near grain boundaries

Two models have been proposed to explain the formation of recrystallized grains near grain boundaries via the combined effects of progressive subgrain rotations and dynamic recovery. The first mechanism proposed by Ion [64] is illustrated in figure 1.4, it is initially designed to understand the formation of new grains near the grain boundaries of magnesium alloys. Even if this model is built for magnesium and based on the assumption of lack of 5 independent slip systems that are necessary for homogeneous plasticity, its philosophy and scientific background has been learned and applied to

understanding the recrystallization mechanisms of other alloys. Another model that is specifically designed for aluminum alloys proposed that the recrystallization mechanism involves the development of serrations near grain boundaries due to interaction with deformation substructure, as illustrated in figure 1.5[55]. Grain boundaries can slide solely on parts of the boundary as indicated by 'A', leaving other regions represented by B have to accommodate macroscopic strain by plastic deformation. Finally, local lattice rotation is achieved by such plastic deformation, as shown in figure 1.5c.

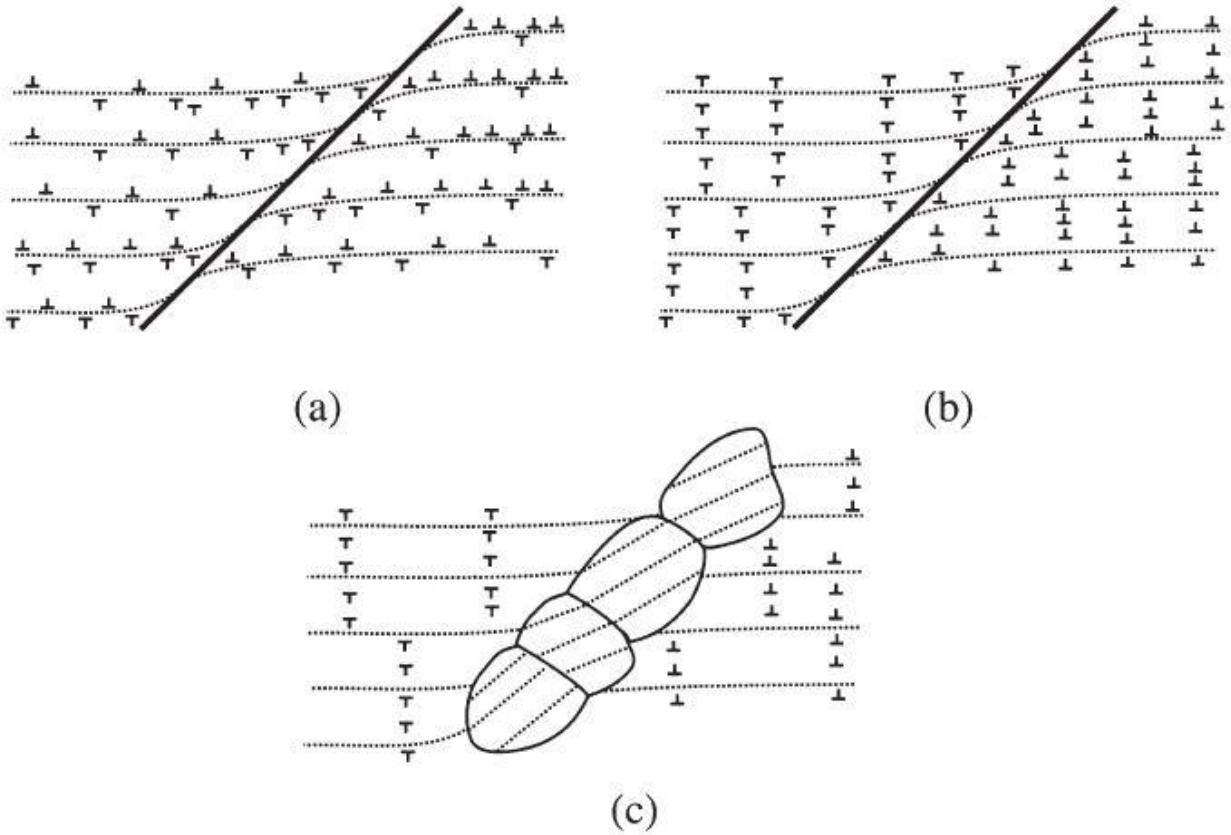

Figure1.4 Schematic illustration showing the mechanism of dynamic recrystallization of magnesium via progressive lattice rotation and dynamic recovery near grain boundaries [64]

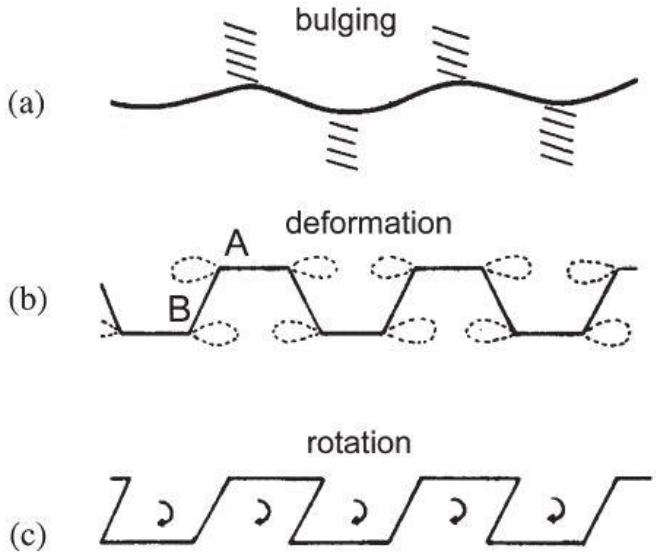

Figure 1.5 Mechanism of dynamic recrystallization by progressive lattice rotation for Al-Mg alloys proposed by Drury and Humphreys (a) serrations forms, (b) grain boundary sliding and slipping near bulged part and (c) lattice rotations associated with the bulges [55].

Geometric Dynamic Recrystallization

As demonstrated in several research papers regarding recrystallization mechanisms, when the materials is subjected to a large deformation, the separation of the initial grain boundaries tend to decrease to such a size that it approach to the subgrain size, the interpenetration of the scalloped boundaries will occur and result in refined equiaxed grains with a grain size comparable with the subgrain size [55, 65, 66]. Similar to the case of CDRX, initial grain boundaries tend to be serrated and develop waviness with a characteristic size close to the subgrain size. An equiaxed microstructure consist mainly of HAGBs is evolved without the operation of nucleation and grain growth.

Typically, this type of microstructure is formed in aluminum alloys under high strain level. One distinct feature of GDX is the newly formed microstructure typically remains the texture component of the starting materials, as pointed out by Gholinia et al. [67].

Recrystallization Mechanism in FSW/FSP Processed Al Alloys

It should be noted that classic models and theories mentioned above are developed based on the roughly uniform and isothermal deformation conditions. Even if hot torsion can be used to simulate the strain level that is imposed to the materials subject to FSW/FSP, the local strain gradient, strain rate and localized plastic flow can't be taken into account. Thus, to interpret the microstructure evolution and understand the relevant recrystallization mechanisms that are involved in the friction stir related process, a combined knowledge of classic theories and new understandings based on experimental results should be adopted. Based on the existing scientific reports about the dynamic recrystallization mechanism of FSW/FSP processed aluminum alloys, the mechanism of DDRX, CDRX, GDX and even particle stimulated nucleation (PSN) are cited as important factors that contribute to the grain refinement and microstructure evolution during FSW/FSP.

Various dynamic recrystallization mechanisms for aluminum alloy under traditional processing conditions such as rolling and plane strain compression have been summarized in a previous part and the classic theory have been addressed. However, FSW/FSP is regarded as a severe plastic deformation route that can introduce heterogeneous plastic strain and steep strain gradient to the processed materials because of the complicated plastic flow. Thus, some fundamental mechanisms related to

dislocation movement, solute dragging and diffusion might be altered. The current understanding and scientific observations that have already been made about the recrystallization mechanism in FSW/FSP will be briefly summarized based on the literature. Additionally, some reports about shear deformation will also be mentioned due to its close relationship to friction stir phenomenon. Also, as a FCC alloy have high SFE, it is believed that dislocation climb and cross-slip occur readily in aluminum alloys, especially at elevated temperatures. The pioneering work performed by Jata et al. [68] indicated the dominance of CDRX during the FSW of a Al-Li-Cu alloy, no observable recrystallization nuclei and grain boundary migration were identified in both EBSD and Transmission Electron Microscopy (TEM) analysis. This philosophy became the most prevalent and well-accepted idea [69].

Traditionally, it is reported that DDRX will not be an operating mechanism for aluminum alloys due to its fast recovery rate, since it is extreme hard to accumulate such a high density of dislocations locally to trigger DDRX, as presented in equation 5.1. However, recent work [10, 70] identified the formation of nano-scale defect-free nuclei in a AA7050 alloy under FSW by a stop-action technique, which is considered as the result of DDRX. These grains are located extremely close to the processing tool where strain gradient thus residual dislocation density is extreme high that EBSD can't be applied to reveal the grain structure due to the deterioration of Kikuchi patterns. Static annealing for very short period of time resulted in the formation of equiaxed grains with 2-5um in size [10, 17], which is typically observed in a standard FSW microstructure. Another investigation performed by Suhuddin et al. [62] on the FSW of 6016 also support the

mechanism of DDRX due to the observation of local grain boundary migration and the instantaneous transition of grain boundary distribution from LABGs to high angle grain boundaries (HAGBs) with high misorientations of around 50 degrees, which can only be achieved by DDRX. However, in another research performed by Fonda et al. [40] also adopted the stop-action techniques, it is found that fine subgrains that are formed because of the imposed shear strain gradually develop greater misorientations and finally become refined grains separated by HAGBs, which is regarded as a continuous process that matches the definition of CDRX. It is believed that the primary mechanism of grain refinement is grain subdivision and dynamic recovery and no DDRX is triggered. The author also related the formation of stable B/B̄ fiber texture to the identified recrystallization mechanism. Also, GDX is cited as the controlling mechanism for the dynamic recrystallization of a 2092 Al alloy during FSW, as discussed by Prangnell et al. [71]. It is pointed out that the grain refinement is a combined result of grain subdivision of the deformation zone and the geometric effects of strain, resulting in the reduced overall high angle boundary spacing with increasing amount of strain. It is noted that the thermally activated local boundary migration is noticed and believed to be important while no evidence was found to support the continuous dynamic recrystallization by subgrain rotations. Interestingly, the texture is characterized by strong B/B̄ textures, which seem to be contradictory to the proposed GDX mechanism. As reviewed by McNelley et al. [11], an ultrafined microstructure fabricated via multi-pass FSP of 5083 alloys is found to exhibit a random texture, the author attribute this randomization to the activation of PSN which is typically believed to contribute to the random texture

formation. However, it seems plausible since the function of the nucleating particles can't be justified based on existing theoretical models.

From the existing literature, it can be seen that almost every possible recrystallization mechanism that is involved in traditional hot deformation method has been cited as the dominant mechanism that contribute to the grain refinement of FSW/FSP processed aluminum alloys. It is also noted that the processing condition, alloy systems and the techniques used to characterize the processed materials are different. Thus it is unclear what types of recrystallization mechanisms are controlling the microstructure of FSBE processed aluminum alloy and how it is related to the texture evolution. Additionally, a comparative study between the recrystallization mechanisms as well as resulting texture formation of AA6063 and AA7075 alloys under similar processing condition is necessary. Finally, despite of the extensive discussion on this topic, some fundamental issues are still under debate and remain to be clarified. All these aspects will justify our investigation on the recrystallization behaviors for both AA6063 and AA7075 alloys processed by FSBE.

CHAPTER TWO

EXPERIMENTAL SETUP AND MATERIALS CHARACTERIZATION

As illustrated in figure 2.1a, the FBSE process involves plunging a non-consumable tool that is rotating at a certain RPM into a solid cylindrical specimen fixed in the die. The friction heat generated at tool-materials interface soften the materials being processed, while axial feed of the tool back extruded the aluminum rod into a tube. High temperature and intense shear deformation is generated during the process, thus refined and recrystallized microstructure is also expected. The FSBE experiments were conducted on an Okuma M B 45VAE vertical 3-axis CNC machines. As shown in figure 2.1b, the entire setup was secured on the CNC machine. An extrusion die with a center hole of 12.7mm was calibrated and clamped on the device. The processing tool employed in the current experiments was made of H13 tool steel, it was tapered and rounded near the corners, as indicated in the inserted picture of figure 2.2b, to facilitate materials flow and reduce extrusion force.

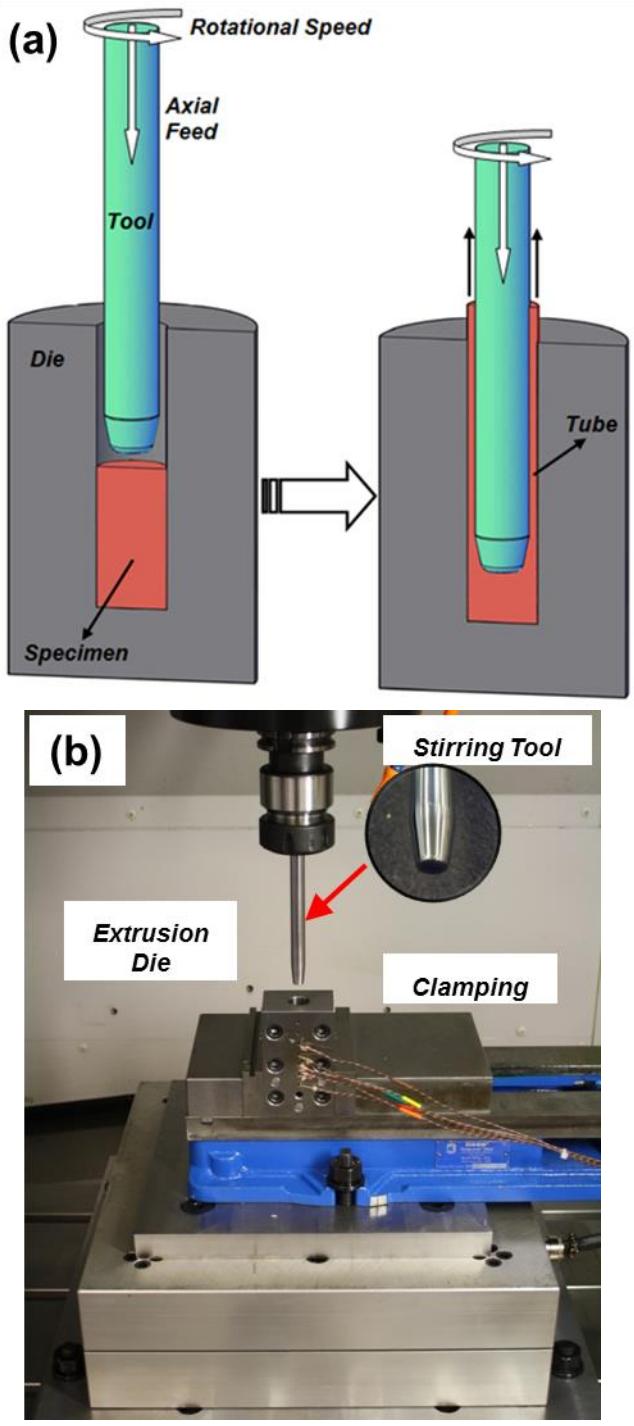

Fig 2.1 Illustration and experiment setup for the FSBE process

The alloys selected in the present study are commercially available AA6063-T53 and AA7075-T651 aluminum rods with a diameter of 12.7mm. FSBE process was performed on these alloys with optimized processing parameters. The optimized parameters for AA7075-T6 alloys were found to be 2000rpm with 1mm/s feed rate, while for AA6063-T53 alloy, it was determined to be 2000rpm and 2mm/s feed rate. The optimized processing parameters depended mainly on the flow stress of materials at the processing temperature and the capacities of the CNC machine. At the initial plunging stage of the process, a much lower feed rate of 0.3mm-0.5mm/s was used for the first 1.5mm penetration, aimed at generating enough heat to start and facilitate the materials flow at the initial stage. Once the extrusion was finished, the tool was extracted from the die while coolant was spayed immediately to minimize the adverse effect of slow cooling on the microstructure and the mechanical properties of the processed specimens. The as-processed tubes were either stored at room temperature for natural aging until being tested or artificially aged. For AA6063 alloy the artificial aging was performed at 177 ℃ for 9 hours while for AA7075 alloy the post aging was performed at 120 ℃ for 24 hours. The post-process aging is similar to the aging step applied to produce T6 tempers in either AA7075 or AA6063 aluminum alloys.

Standard metallographic techniques were applied to prepare samples for optical microscopy (OM) and electron microscopy (EM). Samples of interest were machined by electrical discharge machine (EDM) and mounted in resin based epoxy. Then the mounted specimens were grinded on 240, 600 and 1200 grits sand papers sequentially, followed by polishing using 9um, 3um and 1um diamond suspension. The final polishing

for samples to be analyzed via OM was performed using water based 0.05um colloidal silicon manufactured by Beuhler. For AA6063 alloys, electric-assisted etching was performed at 15V for 60s using Barker's reagent (10 ml HBF4 and 200ml distilled water) to enable grain structure observations under cross polarized conditions. Standard Keller's etchant with a composition of 150 ml water, 3 ml nitric acid, 6 ml hydrochloric acid and 6 ml hydrofluoric acid was applied on the polished surface of AA7075 alloys to reveal grain boundaries. The optical microscope used in the present study was a Zeiss optical microscope, OM images were taken at magnifications ranging from 50X to 1000X. For grain structure exhibiting equiaxed characteristics, average grain size was measured using mean linear intercept method; while for elongated grain structure, the average grain size was estimated based on the surface area of each grains.

Specimens for EBSD analysis were electrolytically polished in a 10% vol. perchloric acid and ethonal solution at -258K (-15℃) for 10-15s with a voltage of 15V. EBSD scans were performed on a Hitachi SU6600 Field Emission Scanning Electron Microscopy (FE-SEM) equipped with high-speed EBSD detector manufactured by Oxford Instruments. For EBSD investigations, the sample was positioned with its surface oriented 70 degrees from the incident beam to maximize the signal strength and the quality of Kikuchi patterns. The SEM was operated at an accelerating voltage of 15 kV and a working distance of 10-12mm, EBSD scans were performed with a step size of 0.3um to 1.5um depending on the critical features to be identified and also the size of the map. Post-acquisition data processing was performed using HKL Channel 5 software.

For TEM investigations, specimen with a thickness of 300um were machined from the locations of interest by wire EDM and then grounded to 50um mechanically. Finally, a twin-jet electropolisher was used to produce electron-transparent regions in the thinned specimens, using 20% vol. nitric acid and 80% vol. methonal solution as electrolyte. Characterization of the microstructure was carried on a Hitachi H-7000 TEM operated at 200 kV. The major focus of the current study was the size, distribution, volume fraction and morphologies of strengthening precipitate since these factors are directly related to the hardness profile as well as the mechanical properties of the entire processed tubes. The incident beam was controlled to a <100> zone axis of the matrix for AA6063 alloys while in the case of AA7075 alloys, either <110> or <112> zone axis was used to enable better identification of the precipitates. Additionally, energy dispersive spectroscopy (EDS) system embedded in the TEM with a spatial resolution of 5nm was also used to perform elemental analysis to capture the size and distribution of the hardening precipitates.

Vickers hardness profiles were measured on the cross section of the processed tube that is parallel to the extrusion direction, using a Vickers indenter with either 500 gf or 1000 gf, depending on the hardness value of the specific materials, for 15 second. Typically, higher load is desirable in the sense that systematic error can be minimized if a larger indent is produced. Micro-hardness measurements were performed at multiple locations across the tube wall with a step size of 0.3mm. At the same time, three measurements were averaged to generate one data point on the hardness profile.

OM, EBSD as well as micro-hardness analysis were carried out at multiple locations across the tube wall as illustrated in figure 2.2b, on the cross section parallel to the extrusion direction. It is noted that 15mm, 30mm and 65mm regions were analyzed for the case of AA6063 tubes while other locations are chosen for AA7075 tubes. These analyzed locations are determined based on the principles of providing a clear understanding of the microstructure evolution and micro-hardness change along the tube. Typical distribution of Vickers indentations across the tube wall is shown in figure 2.2a Additionally, TEM analysis was only carried out on the samples machined from the tube bottom to clarify the evolution of hardening precipitates during the typical thermal cycle of FSBE process.

In order to evaluate the tensile properties of the fabricated tubes, full-tube specimens with a gauge length of 25mm were machined from the tube, as illustrated in figure 2.3. The gripping region of the specimens were threaded and fit into the testing grips. Three tubes were tested for each materials and heat treating conditions. The uniaxial tension tests were performed on a 5985 INSTRON universal testing machine at a constant strain rate of 0.001s-1. Digital Image Correlation (DIC) system was applied to measure the surface strain of the sample during deformation. The entire INSTRON-DIC-grips setup is shown in figure 2.3.

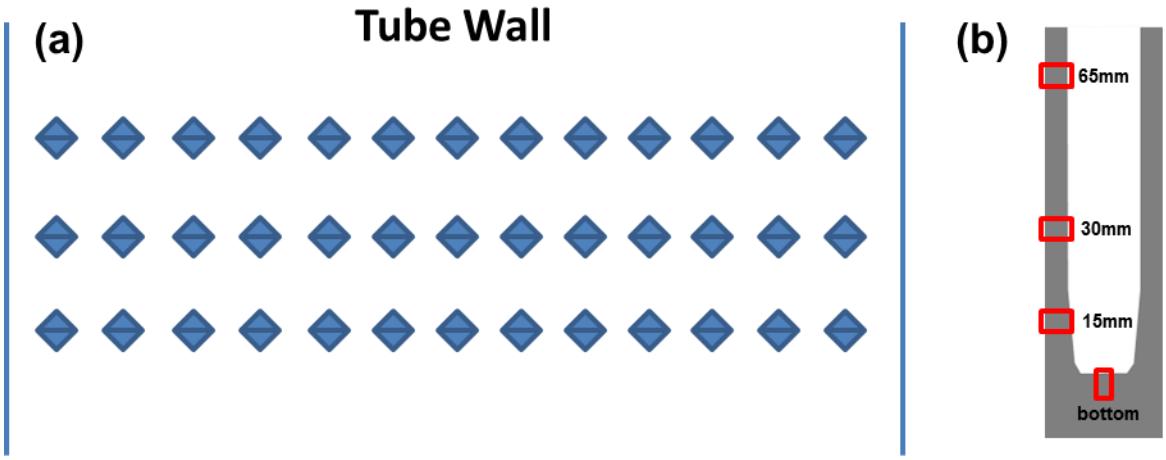

Fig 2.2 (a) distribution of micro-hardness indents and (b) locations to be analyzed

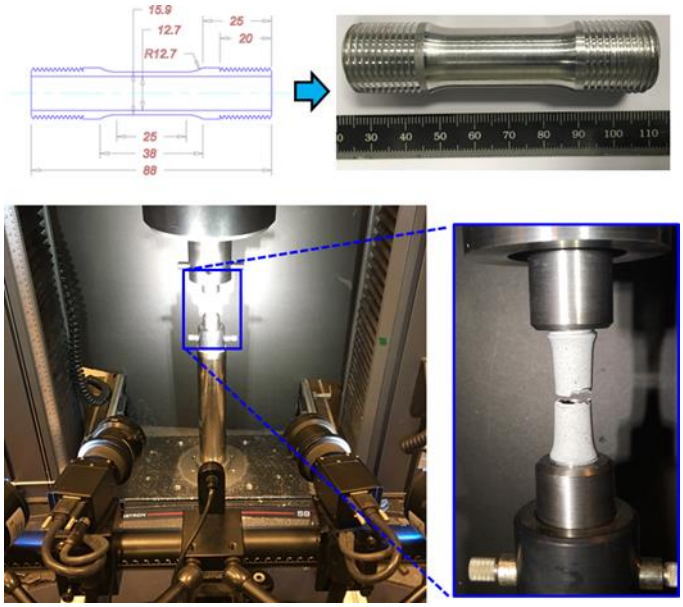

Figure 2.3 Experimental set-ups for uniaxial tension tests aided by DIC

CHAPTER THREE

FRICTION STIR BACK EXTRUSION OF AA6063-T5 ALLOY

Tube Quality and Initial Microstructure

Based on our explorations of the processing conditions, it is found that tube quality is closely related to the processing parameters that are chosen. Unfortunately, with our experiment setups and available equipment, the processing window is relatively narrow. Several sets of optimized parameters are basically determined and used across the entire dissertation. It is founded that, from solely a processing perspective rather than a point view of microstructure or mechanical properties, the crucial part to have a tube processed successfully is properly controlling the thermal input. When heat input is not sufficient, either because of low RPM or high feed rate, CNC machine will be stopped due to excessive extrusion force and the entire process is stuck. In this case, the processing tool is typically stuck with the material being processed due to its shrinking, as illustrated in figure 3.1. On another hand, if the heat input is too high, there will be a chance to locally melt the alloy to be processed or result in material sticking to the processing tool, especially for AA6063 alloy that is sensitive to heat and prone to stick to steels at high temperatures. An extreme case of extra heat input is shown in figure 3.1 where the sample is melted due to excessive heat. It should be noticed that this figure is taken from another type of alloy just trying to show the adverse impact of high heat input. Thus, with optimized parameters of 2000rpm and 2mm/s feed rate with an initial dwelling stage, defect free AA6063 tube can be successfully fabricated, as presented in

figure 3.1c. However, it is noticed that the inner surface is generally very smooth while the part close to the top of the tube shows some shallow marks, which is believed to be related to the interaction between processed materials and the tool at later stage of the FSBE process when the temperature is decreased and aluminum start to shrink significantly. These marks turned out to be very shallow and won't affect the general mechanical properties of the tubes.

The initial microstructure and texture measured for the as-received AA6063-T5 alloy is shown in figure 3.2. The microstructure is characterized by equiaxed grain structure with relatively coarse grain size, confirmed from cross sections both parallel and perpendicular to the extrusion direction. The texture data measured from EBSD shows a strong <100>//ED fiber texture, which is typical for an extruded 6000 series alloy. The initial microstructure and micro-texture shown in figure 3.2 serve as a baseline for the following discussions to be performed on the grain refinement as well as the texture analysis in chapter 4.

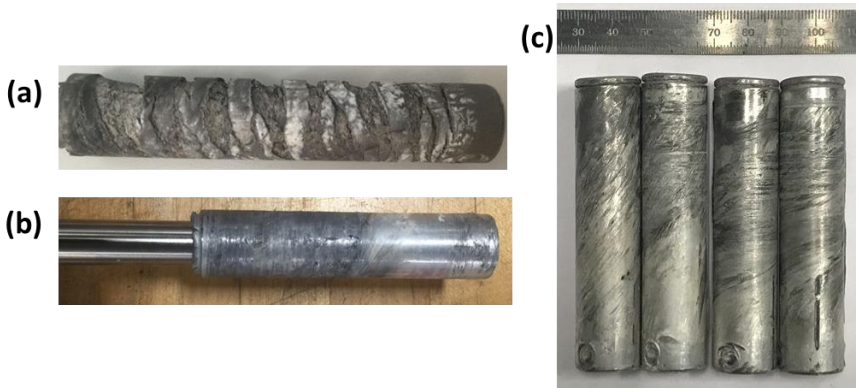

Figure 3.1(a) Demonstration of melted tube due to excessive heat (b) tool stuck with tube because of low heat input and (c) AA6063 tubes

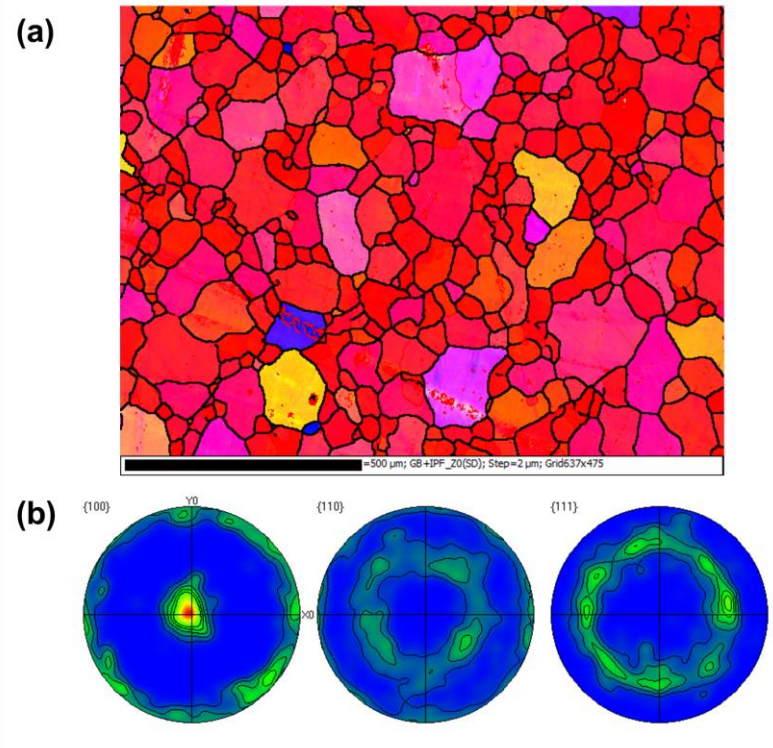

Figure 3.2(a) Microstructure of as-received materials (b) pole figures showing <100> fiber texture

Optical Microstructure of Processed Tube at Multiple Locations

Figure 3.3a is a stitched optical micrograph showing the microstructure near the bottom corner of the tube. Based on the existing nomenclature for FSW/FSP, the microstructure of the processed tube can be classified into processing zone (PZ), thermomechanically affected zone (TMAZ) and base materials (BM), as indicted in figure 3.3a. It is obvious that friction heat and plastic flow generated during FSBE process produce a refined and recrystallized grain structure near the PZ which is close to tool-materials contacting interface; while an elongated and distorted grain structure is

formed in the TMAZ. At locations away from the PZ, initial microstructure is retained due to insufficient amount of strain and plastic flow is introduced during the process. However, it should be noted that the BM is only observed near the bottom corner of the processed tube since it is where a deformation dead-zone is expected. It is also noticed that the PZ in the bottom of the tube exhibits a depth of around 1.5mm, whereas the dynamically recrystallized region in the tube wall is only measured to be 700-800um. Higher magnification micrographs of the PZs located in tube bottom as well as tube wall are shown in figure 3.3b and figure 3.3c, respectively. Despite of the fact that both regions are featured by equiaxed recrystallized grain structure, it is interesting to note that average grain size of the PZ located in tube bottom is determined to be 12.7um using linear intercept method, while in the PZ of the tube wall, average grain size is determined to be 32.5um. It is obvious that grain growth occurs when the initially refined grain structure flows into the tapered region of the tube due to extended exposure to high deformation temperatures. Additionally, it should be emphasized that materials and microstructure located in the taper or the wall of a processed tube can be treated as a later stage of the microstructure observed in tube bottom during FSBE process that is subjected to additional shear strain and heat exposure while flowing along the processing tool.

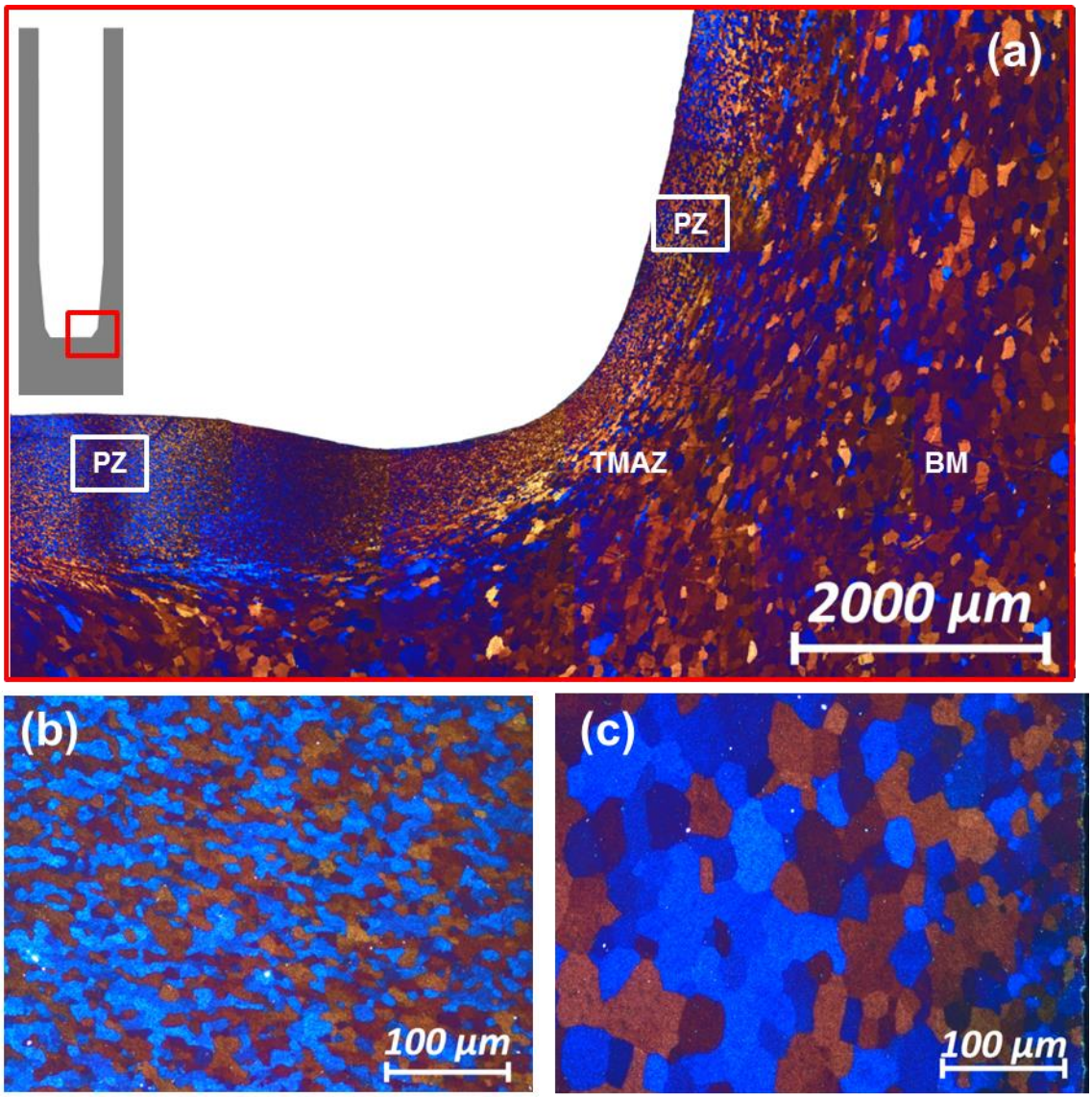

Figure 3.3(a) Microstructure near tube corner (b)-(c) magnified image of the PZ at tube bottom and wall

Optical microstructure across the tube wall at 15mm location is shown in figure 3.4a. The tube wall consists of PZ characterized by fine equiaxed recrystallized grains and TMAZ exhibiting distorted and elongated grain structure along the extrusion

direction due to strong plastic flow and shear deformation. BM region is absent since the thermomechanical effect of the FSBE process penetrated the entire thickness of the tube wall at this location. It is noted that grain structure across the tube wall is not homogeneous since a strain gradient is expected due to the deformation nature of FSBE process. Materials adjacent to the processing tool is subjected to relatively high temperature and high levels of plastic strain compared to those distant from the processing tool, where the thermomechanical effect of the process is not enough to trigger dynamic recrystallization. Under these circumstances, initial grain structure are deformed and elongated following the plastic flow and deformation geometries. In order to quantitatively analyze the grain structure evolution across the tube wall, figure 3.4a is subdivided into four parts, as indicated by the red dotted lines, and named as region i-iv, respectively; average grain size as well as aspect ratio were measured statistically for each region and the results are plotted in figure 3.4b and figure 3.4c. It is noted that the measured average grain size increases monotonously with the distance from analyzed regions to tool-materials interface, while the average aspect ratios of grains within su B region i-iv exhibit a low value of 1.1 at region i, where the PZ is located, and culminates sharply to a plateau of 2.1 to 2.4 once the boundary between PZ and TMAZ is crossed. The penetration of recrystallized zone with an average grain size of 32um is determined to be around 700-800um, similar to the case in figure 3.3a.

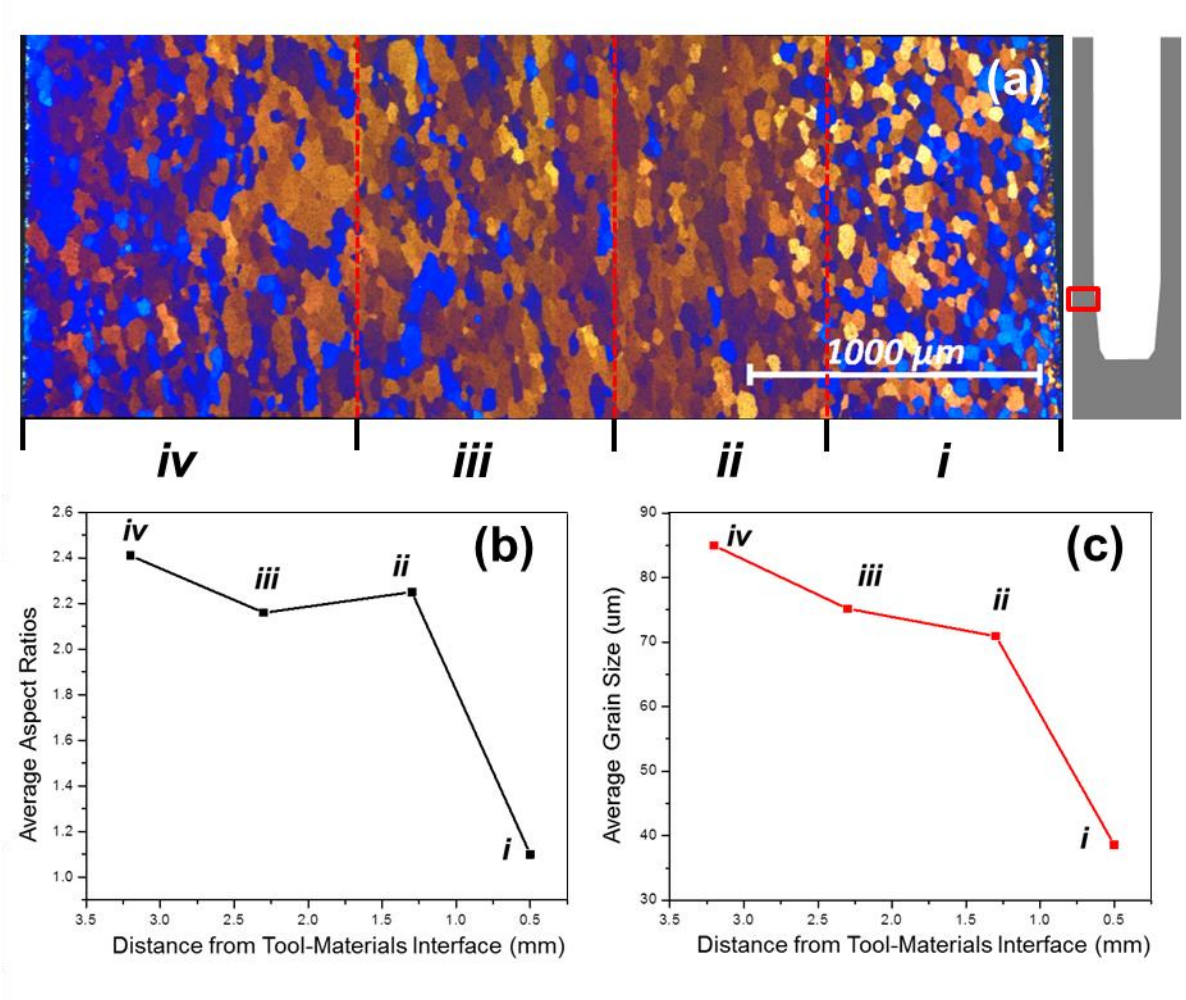

Figure 3.4 (a) Microstructure at 15mm location (b) distribution of average grain size and (c) grain aspect ratios

Figure 3.5 illustrates the microstructure of the tube wall at 30mm location. Similarly, the map shown in figure 3.5a is su Ɓ divided into five regions, labeled as region i-v, and the average grain size as well as aspect ratio is measured for each of them. It should be noted that the PZ in this case consists of two su Ɓ regions (region i and region ii) since both of them are showing distinct characteristics and need to be addressed

separately. As mentioned earlier, the microstructure observed at 30mm location can be regarded as a later stage of 15mm specimen subjected to extended heat exposure and continued straining while flowing along the extrusion direction. By comparing with the case of 15mm location in figure 3.4(a), several major observations can be made: grain growth occurs within the PZ, as illustrated in region ii of figure 3.4a, despite the fact that extra shear strain is supposed to be introduced while material is flowing from 15mm to 30mm locations; grains located in close proximity to the processing tool that are showing equiaxed characteristics in previous stages tend to be sheared, distorted and elongated along the extrusion direction, due to the geometrical requirements of the imposed strain, as indicated in region i of figure 3.4a; the microstructure in the TMAZ seems to be slightly elongated along the extrusion direction compared to 15mm specimen and a peak value of 2.55 of the average grain aspect ratio is noted for region v; additionally, the width of the recrystallized region is measure to be 700-800um, similar to 15mm location. As noted in figure 3.5b, region i that is located within the PZ is featured by grains having a high average aspect ratio of 4.56, which is significantly higher than the value of 2.5 that is measured for the TMAZ; while the equivalent grain size is determined to be 35um, close to the value of the PZ in 15mm case. At the same time, the equiaxed part of the PZ, represented by region ii, exhibits an average aspect ratio of 1.2, suggesting minor distortion along the extrusion direction, and a coarse grain size of 60um. The general trend for the variations of grain aspect ratio across the tube wall consists of a peak value noticed at the region next to the processing tool, which sharply drops to the level standing for a slightly elongated equiaxed grain structure and finally escalate to a relatively stable

value of 2-2.53. Similar to the previous situation, the average grain size for sub-region i to v increases linearly from PZ to TMAZ.

However, significant microstructural changes across the tube wall have been identified at 65mm location, as shown in figure 3.6a. Ultrafined recrystallized grain structure has been formed in the area next to the processing tool and the entire PZ is refined compared to the observations made in previous stages (15mm and 30mm locations); at the same time, the PZ expands to a depth of round 1.5mm, twice as much as the penetration obtained in 15mm and 30mm samples. Additionally, grains within the TMAZ are further stretched along the extrusion direction, featured by even higher aspect ratios, because of the geometrical requirement of the accumulated shear strain and extrusion effects. It is instructive to notice that the PZ should be subdivided into three parts for detailed investigations since complicated grain structure evolution is expected within the PZ and each region is featured by different grain sizes and morphologies, as represented in region i-iii of figure 3.6a. Region i is characterized by ultrafined grain structure, whose exact size can't be resolved properly considering the capacity of optical microscope as well as the fact that cross-polarized operating mode is applied. Distorted and stretched grains are also identified within the PZ, as in the cases of 30mm specimen, and these grains showing an average aspect ratio of 4.64 and grain size of 27um have been classified as region ii of figure 3.6c. Region iii consists of recrystallized equiaxed grains with a relatively coarse grain size of 33um, which is typically observed in the PZ of the tube wall. Finally, region vi and v represent the highly elongated grain structure of the TMAZ with aspect ratios ranging from 4.5 to 6.5. Average grain size and aspect ratios

measured for each sub-region is plotted in figure 3.6b and 3.6c, respectively. In general, grain size increase monotonously across the tube wall, while average grain aspect ratios vary in a periodic low-high-low-high profile. It is crucial to point out that the morphologies and sizes of the ultrafined grains within region i can't be determined precisely from optical microscopy, in such cases, the data plotted in figure 3.6 is based on EBSD analysis.

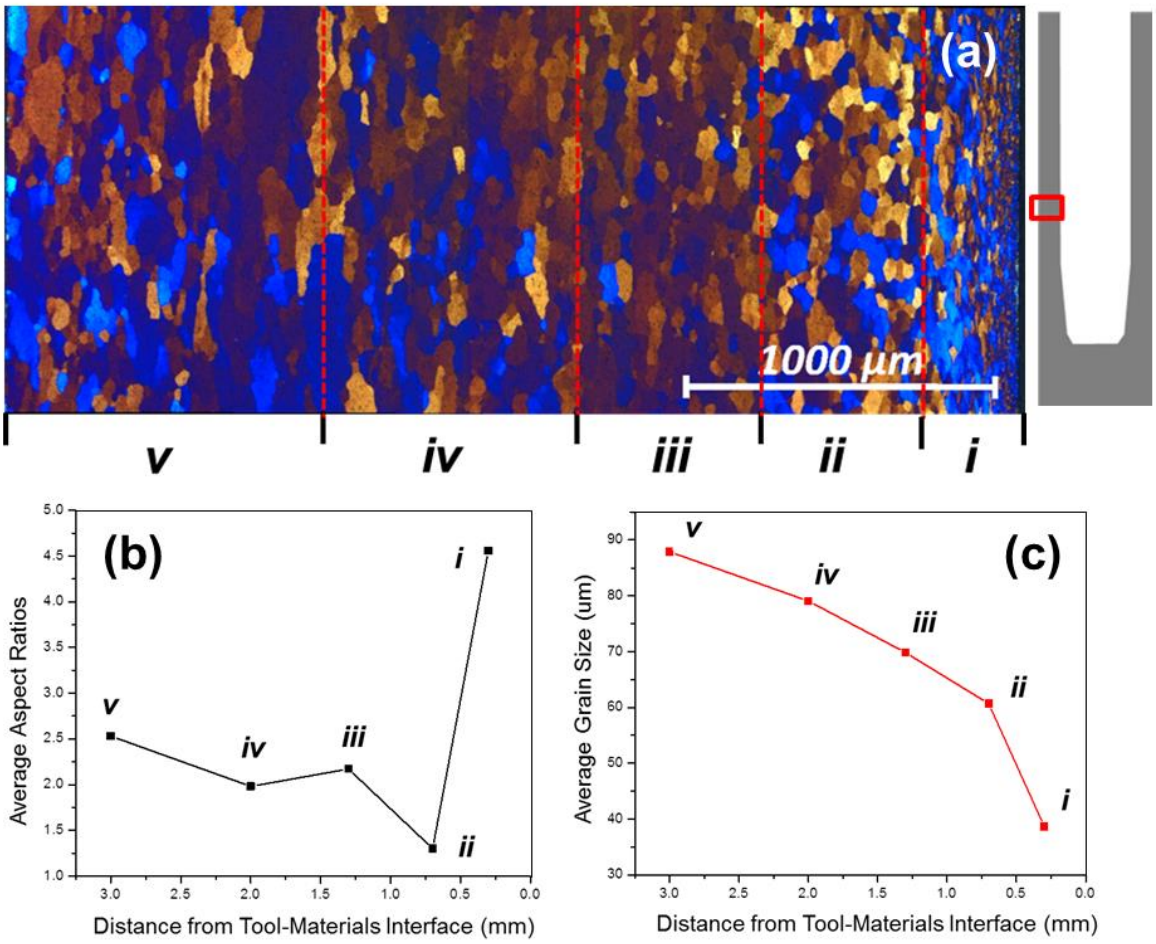

Figure 3.5 (a) Microstructure at 30mm location (b) distribution of average grain size and (c) grain aspect ratios

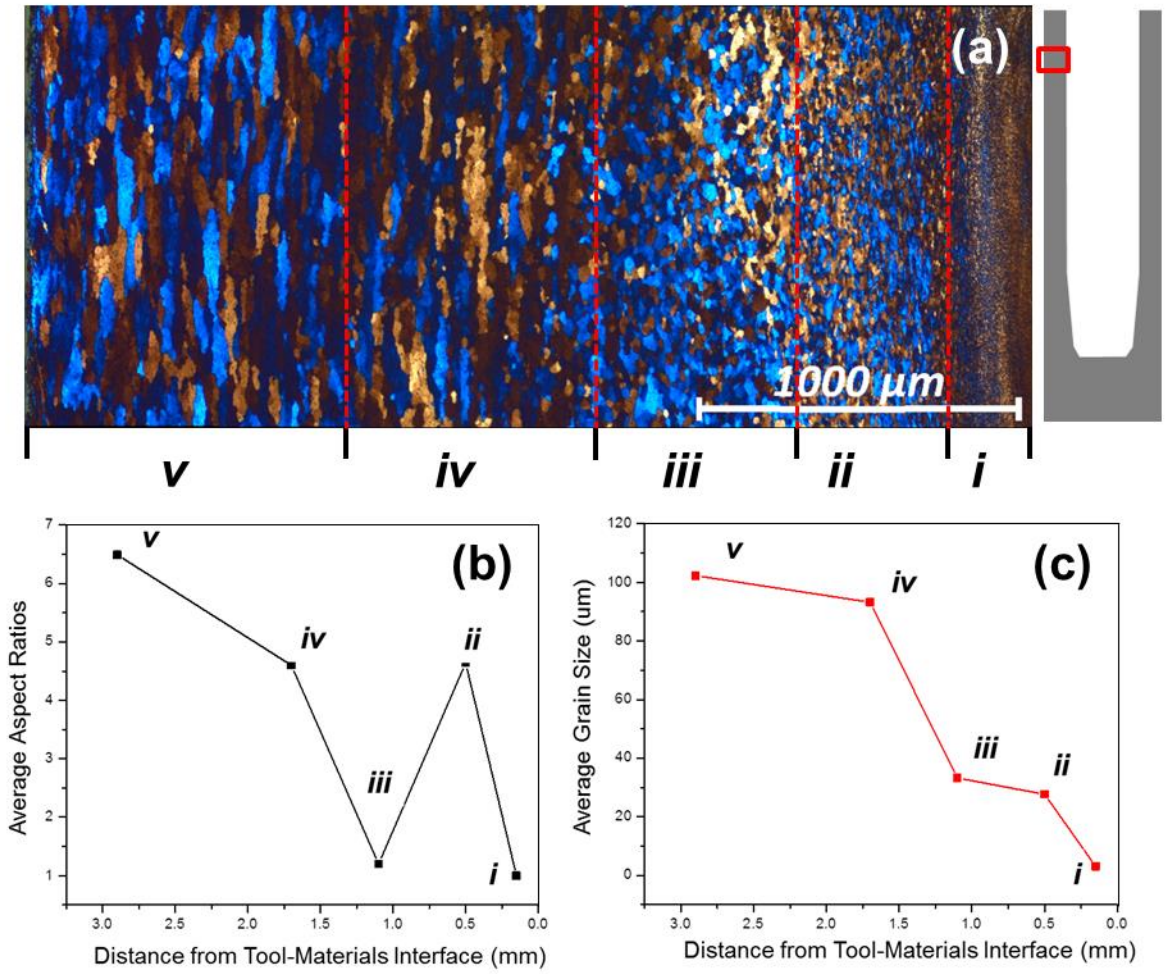

Figure 3.6 (a) Microstructure at 65mm location (b) distribution of average grain size and (c) grain aspect ratios

Considering the deformation nature and flowing characteristics of the FSBE process, materials underneath the tip of the processing tool is strained at high temperature and refined grain structure is formed initially; as the process proceeds, these processed materials are extruded by the processing tool and start to flow through the tapered region

and finally forms the tube wall; while at the same time, the flowing material is subjected to additional shear deformation and thermal exposure, mainly because of its continued contact with the rotating tool. Thus, the microstructure captured near the tapered region of a processed tube can be regarded as a later stage of the microstructure observed in tube bottom that is evolving during the FSBE process. Based on this philosophy, the 15mm specimen is of a later evolutional stage relative to both tube bottom and tapered region, while similar extrapolation can also be made for the microstructure identified at 30mm and 65mm locations. That is to say, the final microstructure captured by the imaging system is not only affected by the current deformation modes and temperatures, but also controlled by its thermal and straining history. It is obvious that strong plastic flow generated in tube bottom by friction stir phenomenon, which is intensified by the forging effect of the processing tool, enables the formation of refined grain structure and a deep penetration of the PZ. While flowing toward the tapered zone, these refined grains with an average size of 12.7um grow to an average value of 35um, even if continued shear strain is imposed. However, it should be noted that, fundamentally, recrystallized grains size is directly correlate to the rate of dislocation generation and annihilation, whose dynamics are controlled by local strain rate and temperatures, respectively. In this case, shear strain rate is decreased near the tapered region since the forging effect is reduced and a strong contact between processed materials and the rotating tool can't be guaranteed; while at the same time, similar deformation temperature is expected as in tube bottom, which tends to overweigh the contribution of the local strain rate and finally coarsen the recrystallized structures. Once the materials flow through the taper, the

forging effect of the tool start to decrease tremendously near the taper and finally disappears, then the corresponding shear strain rate applied to the processed materials solely depends on local contacting conditions, which is supposed to be weak. Since the inner surface of the tube is parallel to the extrusion direction, it is extruded along ED without too much interference with the processing tool once a steady state is achieved. As in the case of 30mm specimen, the majority of the PZ is coarsened because of extra exposure to heat compared to the microstructure identified at 15mm location, while only limited amount of grains adjacent to the processing tool seems to be under deformation and elongated along the extrusion direction. This further testifies our latest discussions that only marginal amount of strain is introduced while the processed materials are flowing along the tube wall. However, the situation is different at very late stage of microstructural evolution, where significant grain refinement by another order of magnitude and a wide PZ with doubled dimensions (around 1.5mm) are achieved at 65mm location. It is believed that tremendously amount of shear strain is applied to the materials at this location because of extremely strong interaction with the processing tool. The root cause of this strong interaction is assumed to be the shrinkage of aluminum alloy due to reduced deformation temperature. Two factors are believed to contribute to the reduced processing temperature near the top part of the tube: first, it is distant from the heat source since the majority part of heat is generated near the bottom and taper of the processing tool; secondly the coolant is applied while the tool is extracted once the processing is finished, thus it would reduce the local temperature of the top part of the tube most instantly and effectively, while the tool is still not fully extracted. Thus, the

synergic effect of ultra-high strain level and low deformation temperature triggers extensive recrystallization across the tube wall, resulting in a deeper penetration of the PZ accompanied by further refinement and the formation of ultrafined grain structures.

Micro-hardness Evaluation and Underlying Mechanisms

Vickers micro-hardness profiles were measured along the centerline of the tube bottom as well as across the tube wall at 15mm, 30mm and 65mm locations for both as-processed and post-process aged tubes, the results are shown in figure 3.7. It is noted that similar locations are chosen in order to correlate the micro-hardness results to optical microstructure. In these figures, x-axis represents the distance from the region being tested to tool-materials interface. The hardness value of the as-received materials is measured to be between 55HV to 60HV while the average value of 58HV is used for constructing the plots. It is apparent from figure 3.7 that Vickers hardness values of the as-processed tubes are consistently lower than that of the as-received materials in all cases, while the extent by which the microhardness values decrease varies at different locations both across and along the tube wall. However, post-process aging at 177℃ for 8 hours restore the micro-hardness values to a level of 75HV to 85 HV, which is considerably higher than that of the as-received materials. It is also noted that the Vickers hardness profiles for artificially aged samples are showing different trends compared to the curves for as-processed condition. Additionally, even at same locations, the HV value across the tube wall varies, especially for the bottom and 65mm specimens. Underlying mechanisms that are responsible for such variations will be discussed based on the microstructure and precipitation behaviors analyzed by TEM.

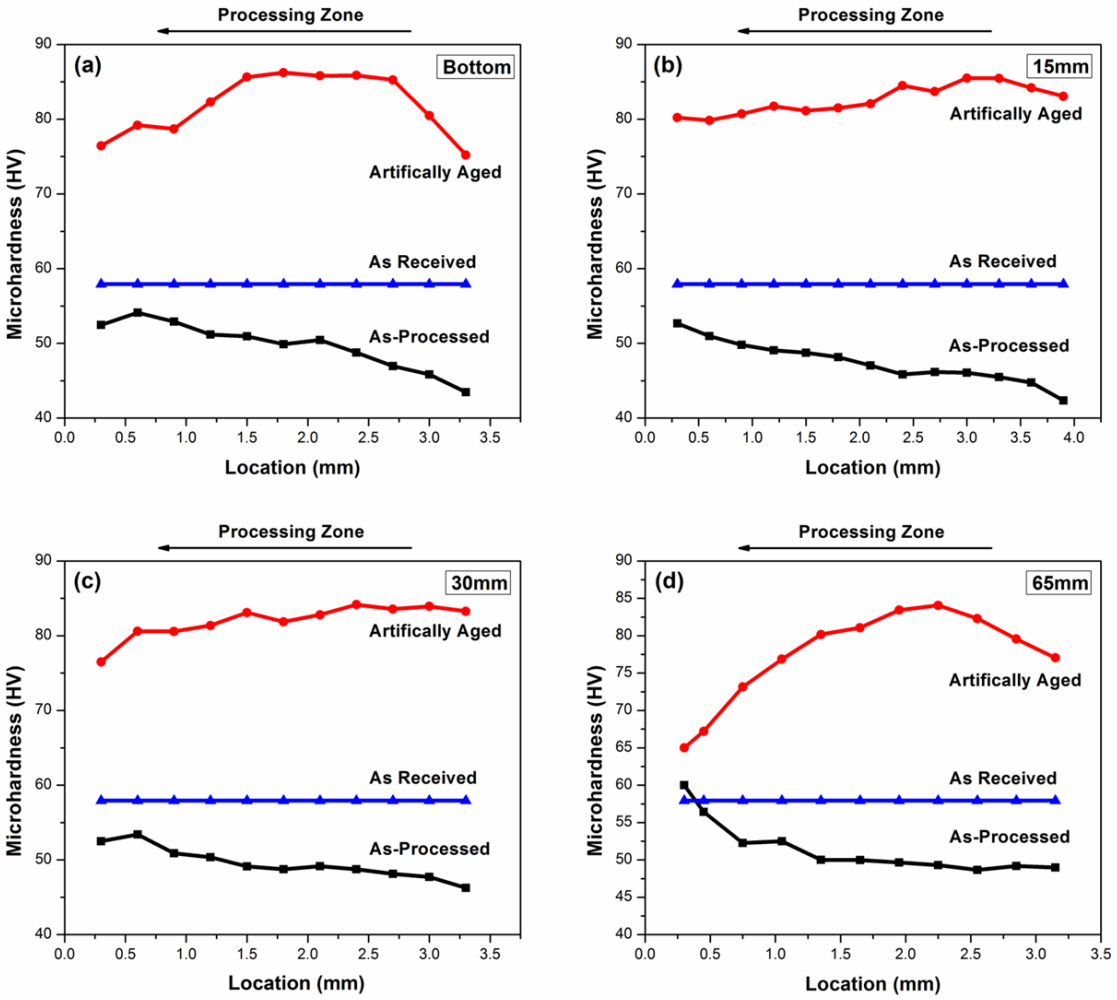

Figure 3.7 Micro-hardness across the tube wall at (a) tube bottom (b) 15mm (c) 30mm and (d) 65mm locations

The hardness profiles of FSW-ed Al-Mg-Si alloys depend predominantly on the precipitation behavior and only slightly on the grain size, as reports by Sato et al. and Ma et al. [14, 15, 72]. While the size, morphology and distribution of the precipitates are mainly controlled by local thermal exposure during the process. It is well established that the precipitation sequence of Al-Mg-Si series is supersaturated solid solution→ dot-like

GP zone→ needle-shaped precipitates (β'') → rod-shaped precipitates (β') → equilibrium β phase[15]. Based on the DCS results reported in previous studies, the dissolution temperature for β'' and β' are determined to be round 250 ℃and 350 ℃ respectively. Complete dissolution of both β' and β'' has been reported for 6063-T5 alloy under typical thermal hysteria experienced in FSW process with a peak temperature of 403℃ [14, 15]. Thus, the extensive softening across the as-processed tube should be associated with the dissolution of hardening precipitates, since the peak temperature of 403C and above can be easily achieved in typical friction stir related process of 6xxx Al alloys.

Figure 3.8 shows TEM images obtained from the as-received alloy as well as the PZ of as-processed tube. The incident beam is aligned to a <100> zone axis of the aluminum matrix. As illustrated in figure 3.8a, the as-received material consists of needle-shaped β'' precipitates that is typically less than 50nm in length and rod-shaped β' with a length between 50-700nm [19, 73]. However, the microstructure of the as-received materials should be interpreted as somewhat being over-aged since coarse β' precipitates are noticed in the micrograph, which is also suggested by the low hardness value of the base metal. A very clean TEM micrograph with only sporadic precipitates, either in the form of pin-dot or rod-shaped, is obtained in the PZ of as-processed materials, as presented in figure 3.8b. This suggests the dissolution of both β' and β'' during the thermal hysteria of FSBE and contribute the reduced hardness value measured in the as-processed AA6063 Al tubes. The formation of pin dot-like GP zones [31] should be attributed to the extended natural aging for several months, while rod-shape precipitates

might be the result of incomplete dissolution of some of the coarse β' phase present in the starting materials since the processing cycles can't provide enough time for complete dissolution of β'. It should be noted that, compared with the previous reports [14, 15, 31], where complete dissolution of β' is achieved under typical FSW thermal cycle, the starting materials employed in the current study is in over-aged condition thus the β' phase is even coarser, which means a longer time is needed to fully dissolve them. Additionally, from the hardness profiles plotted in figure 3.7, a slightly higher hardness value has always been noticed near the PZ under as-processed conditions, as shown by the hardness profiles measured at bottom, 15mm and 30mm samples. This can be explained as: at locations closer to the processing tool, a higher temperature thus stronger dissolution and solid strengthening effect is expected; meanwhile, the grain size is more refined in the region closer to the processing tool because of dynamic recrystallization. An extreme case involves the hardness measured near the PZ of 65mm specimen, where the grain structure is so refined and heavily strained, as confirmed by the EBSD analysis, that the micro-hardness value in as-processed condition is even higher than that of the starting materials.

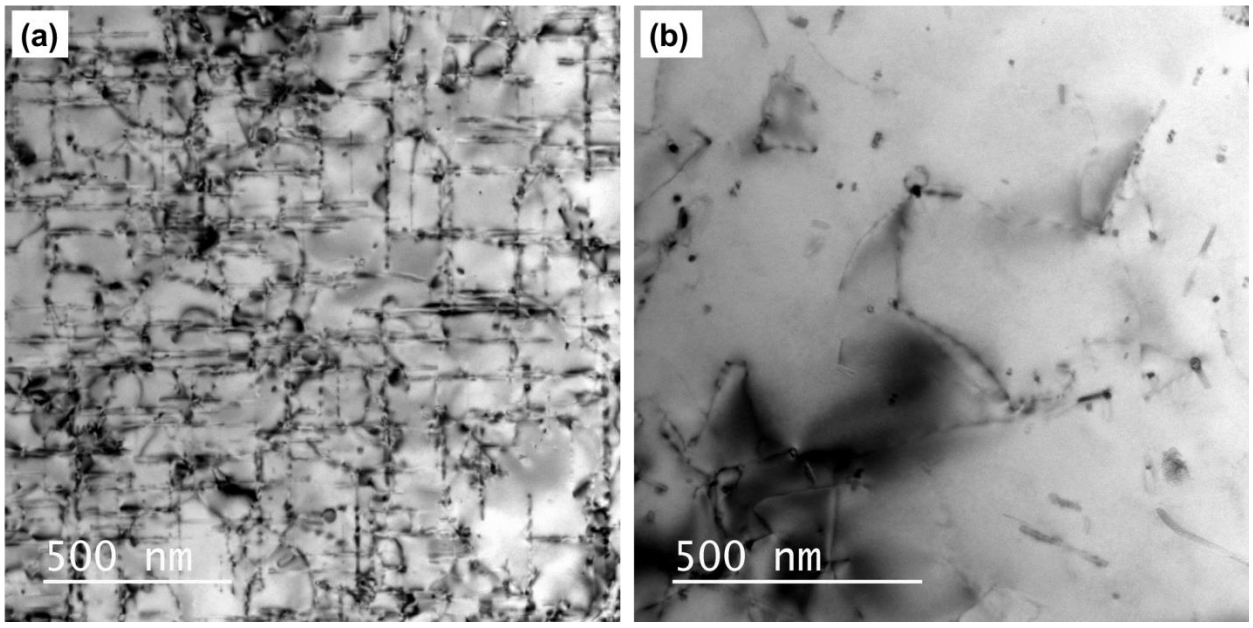

Figure 3.8 TEM micrographs for (a) as-received materials and (b) as-processed specimen

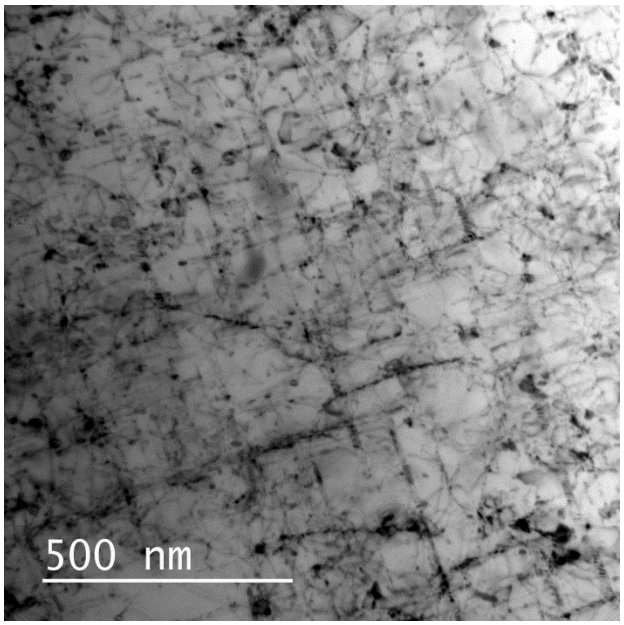

Figure 3.9 TEM micrograph for post-aged sample

Since the FSBE process serves as a solutionizing step that dissolved most of the hardening and non-hardening precipitates, the increase in Vickers hardness that is illustrated in figure 3.7 during post process aging can be expected, which is related to the reprecipitation of solute atoms in the form of hardening precipitates. As reported by Sato et al. [19, 31], extensive reprecipitation of fine needle-shaped β'' are observed during the post-weld aging of AA6063-T5 alloy after FSW. They are of high density and distributed homogeneously in the aluminum matrix, resulting in increased mechanical properties. TEM micrographs of FSBE processed and post aged samples are presented in figure 3.9. It is noticed that the microstructure consists of a mixture of both needle-shaped β'' and rod-shaped β' precipitates, which is typical for a T6 treated 6000 series alloys. However, it is noticed that even if rod-shaped β' are formed during post aging, their sizes are significantly smaller than those β' present in the as-received samples, as shown by figure 3.8a. Thus it is suggested that FSBE process, when combined with a post process artificial aging step, is able to effectively dissolve the coarse precipitates that are present in the initial materials and reprecipitate the solutes as homogeneously distributed fine needle-shaped β'' phase as well as refined β' phase, which finally contributed to the increased mechanical properties. However, as mentioned earlier, the restoration or improvement of the local mechanical properties, represented by Vickers hardness value, because of the reprecipitation of hardening phases is not uniform along the hardness profile shown in figure 3.7. It is observed that achievable HV values near the PZ, where grain size is smaller, are consistently lower compared to the less processed region such as TMAZ and transition region. This phenomenon is opposite to the situation of as

processed tube, where the PZ is showing a higher hardness because of solid solution strengthening and grain refinement. It is point out by Sato [19] that precipitation-free zones (PFZ) and grain boundary precipitations are detected in the region adjacent to the majorities of grain boundaries, which is confirmed by TEM analysis. Ikeno etal [74] have suggested that grain boundary precipitates of Al-Mg_2Si alloy are non-hardening β' phase. That means the formation of PFZs tends to deplete the solutes atoms that are available for reprecipitation of hardening phases and form non-hardening phases at grain boundaries. Also, from a general point of view, the presence of PFZ typically results in inferior mechanical properties of aluminum alloys. The crucial part of this mechanism is the formation of PFZ and grain boundary precipitation is more significant for finer-grained microstructure due to high fraction of grain-boundary area, while its effect is less significant or even minimal for the coarse-grained structures. By applying this well-developed philosophy to our case, it can be easily noticed that finer grain structure near the PZ achieved a lower peak hardness value as a result of grain boundary precipitation and PFZ formation. While for the microstructure near the transition region or TMAZ, this PFZ effect is less prominent because the microstructure of these regions are characterized either by less refined grains or distorted/elongated initial microstructure, as confirmed by the optical micrograph shown in figure 3.3-3.6. Citing 65mm sample as an extreme case again, the hardening response of the corresponding PZ during post aging is the lowest among the entire hardness measurements performed across the tubes, because of the formation of ultrafined grain structure. It is noted from figure 3.7d that the increase is only around 5HV after post process aging, suggesting the significance of grain boundary

precipitation as a function of grain size. An excellent illustration is found in the tube bottom where grain structure and hardness values can be directly correlated. The micro-hardness profiles for the tube bottom are shown for a second time in figure 3.10a to illustrate their relationship to grain structures. It is noted that the first three data points that are circled out by blue corresponds to the refined microstructure shown in figure 3.10b, while the region that is showing increased age hardening response marked by the green circle matches the region where grain structures are transformed from distorted initial grains to refined recrystallized grains, based on their distance to tool/materials interface. Those data points that exhibit peak hardness value and highest age hardening response are correlated to the grain structure of base metal, as illustrated in figure 3.10d. Additionally, apart from the PFZ affected micro-hardness variation, it is noticed that after region d, the micro-hardness profiles shown in figure3.10 start to decrease significantly even if no additional microstructural change is present. This can be explained as: the material that is more than 2.5mm away from the tool/materials interface might experience a lower peak temperature and less aggressive thermal cycle, which can result in overaged microstructure that is characterized by coarse non-hardening precipitates. Over-aging effect can be confirmed from the simultaneous decrease of Vickers hardness for both as processed and post aged samples. However, significant age hardening responses is still noticed while the achievable hardness values are decreasing, indicating the coexistence of solutionizing effect and over-aging. To conclude this part, all these experimental results are explained based on the existing literature rather than our own TEM data.

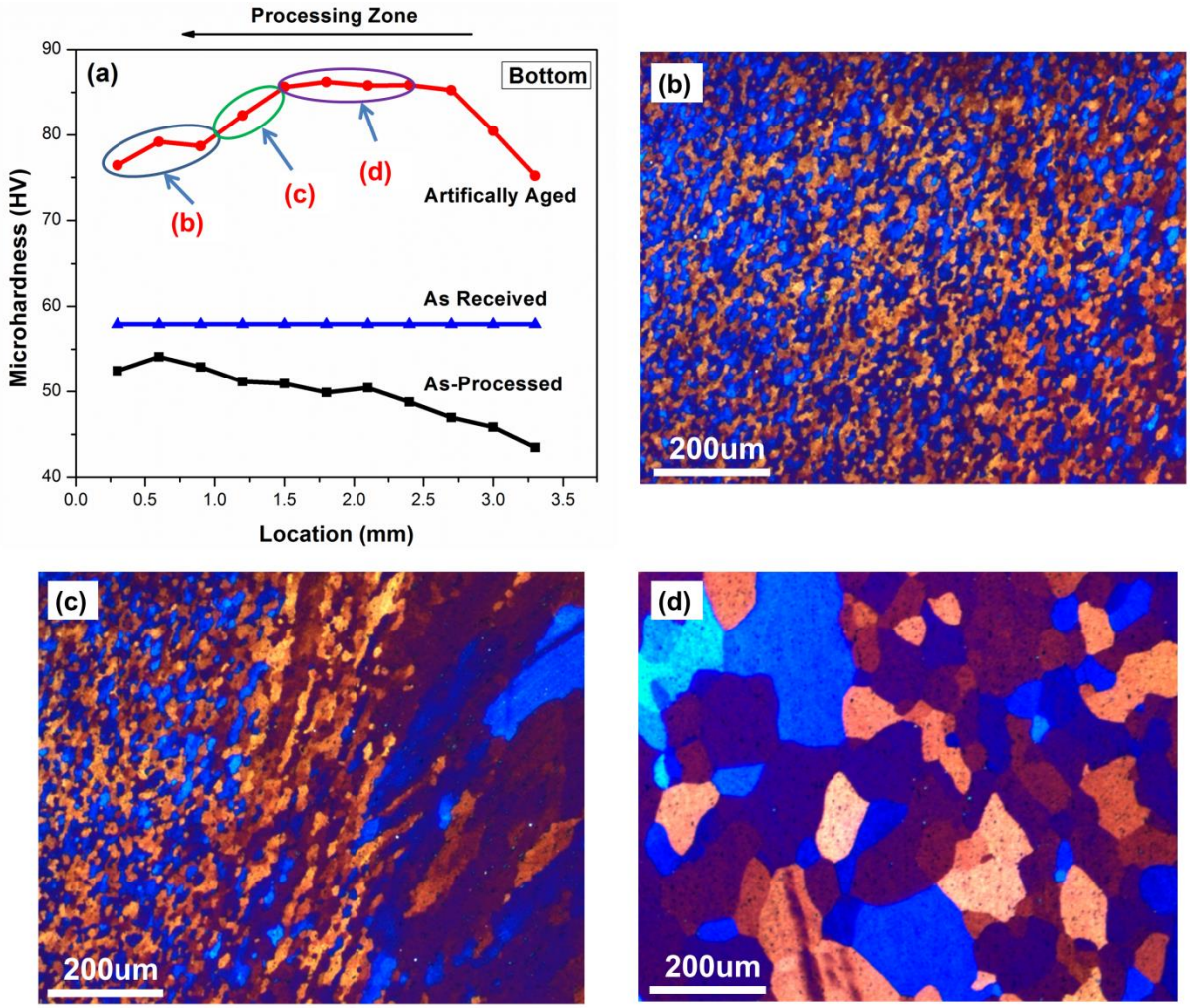

Figure 3.10 (a) Hardness profile at tube bottom and (b)-(d) relevant microstructures

Uniaxial Tension Tests

The tensile properties of as-received as well as processed specimens were also evaluated. For each condition, three samples were tested and average engineering stress-strain curves are presented in figure 3.11. The mechanical properties extracted from the curves are summarized in table 3.1. As-received T5 treated sample shows a moderate yield strength, tensile strength and failure strain of 144Mpa, 185Mpa and 12.3%,

respectively. After FSBE process, as-processed specimen exhibits a decreased yield of 93Mpa, compared to 144Mpa of as-received materials, which is consistent with the results of micro-hardness measurements as well as previous reports regarding FSW/FSP of age-hardenable aluminum alloy [14, 31]. It is generally believed that the strength loss is because of dissolution and growth of strengthening precipitate during thermal cycles introduced by the friction stir related processes [1, 31]. However, the failure strain was increased to 20.8% relative to the value of 12.3% for as-received materials. This phenomenon is not consistent with most works conducted on FSW/FSP of age-hardenable aluminum alloys [20, 21, 32], even non-heat treatable ones [18], where elongation increase has barely being noticed. Post artificial aging treatment significantly enhanced the mechanical properties of as-processed tubes, elevating the yield and tensile strength to 230Mpa and 254Mpa, showing an increase of 147% and 39% respectively. It is obvious that as-processed samples exhibit considerable hardening effects during post-aging, signifying the dominance of dissolution of soluble precipitates during the thermal cycle imposed by FSBE and reprecipitation of dispersed hardening precipitates, as confirmed by the TEM results. Finally, it is interesting to note that, compared with as-received materials, the yield strength of the specimen is increased from 144Mpa to 230Mpa, realize an improvement of 59.7%, the tensile strength is elevated from 185Mpa to 254Mpa with an increase of 37.3%, while the fracture strain remains almost the same, by applying combined FSBE process and artificial aging step. Based on our understanding of the precipitation sequence of AA6063-T5 aluminum alloy under typical thermal cycles of friction stir related process, the superior mechanical properties for

processed and aged samples should be largely due to the dissolution of initial soluble phases and reprecipitation of fine hardening phase during the post heat treatment. It should also be noted that the tensile test results are consistent with the observations made in micro-hardness test as well as TEM analysis, the mechanical properties is largely controlled by precipitation behavior which in turn is dictated by the thermal cycles imposed by FSBE process and post heat treating.

Fracture Locations

Figure 3.12a-c shows the macroscopic fracture morphology for three types of samples. As-received AA6063-T5 sample shows fracture location right in the middle of the gauge, whereas for both as-processed and post-aged samples, fracture predominantly occurs at the top part of the tube, being next to the end of fillet, which corresponds to the region of 50-60mm from tube bottom. It is widely reported that in FSW/FSP of aluminum alloys, fractures can occur in various regions like HAZ, TMAZ, SZ and BM depending on local microstructure and mechanical behaviors resulting from the corresponding thermomechanical processing. Vickers hardness has always been used to explain the fracture location of FSW 6000 alloys, Ma et.al [75] reported the coincidence between fraction location and minimum micro-hardness region near transition zone, signifying strain concentration at softer regions.

In the present study, average micro-hardness values across the tube wall at 15mm, 30mm and 65mm locations have been calculated and present in figure 3.12d. It can be inferred from the previous hardness results across the tube wall that average hardness values of as processed samples always increase monotonously across the tube

wall at different locations, indicates average hardness can't be used to explain the fracture location. It is emphasized in previous section that microstructure change across tube wall at 65mm location is most remarkable with respect to grain size and aspect ratio: the recrystallized region extends to a depth of 1.5mm into tube wall and the TMAZ shows highly elongated grains with a maximum aspect ratio of 6. Figure 3.12d shows the hardness range (difference between highest and lowest hardness value) and standard deviation of hardness values measured across the tube wall at multiple locations, for both as process and post aged conditions. It is noted that at 65mm region, both hardness range and hardness deviation are found to be significantly higher than the values measured for other regions, indicating strong local mechanical properties variation at 65mm location. It is highly possible that the variation of local mechanical properties might be prone to initiate inhomogeneous deformation that result in pre-mature fracture.

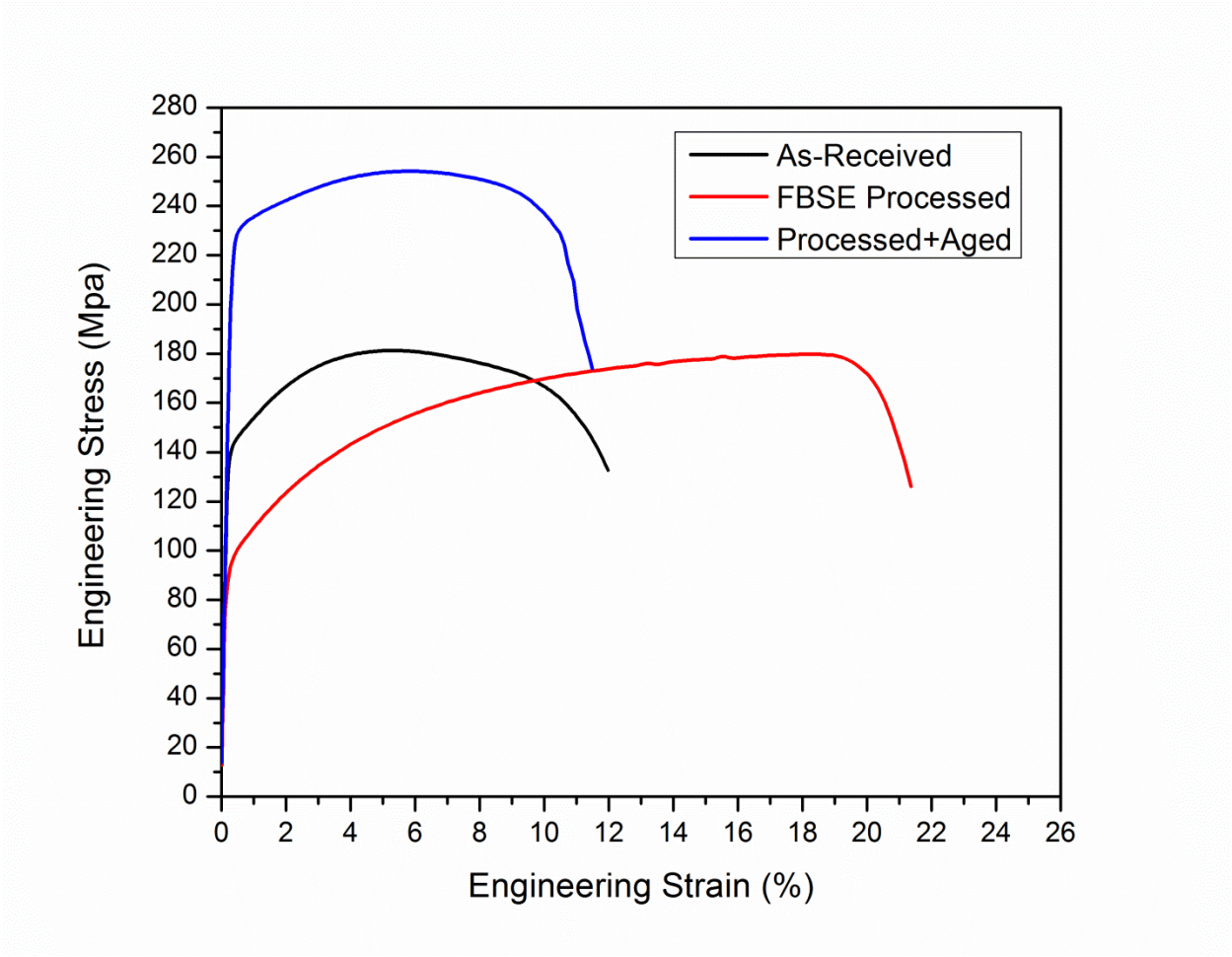

Figure 3.11 Uniaxial tensile tests curves for AA6063 tubes

Table 3.1 Summary for uniaxial tension tests of AA6063 tubes

Sample	YS(Mpa)	UTS(Mpa)	Failure Strain (%)
As-Received	**144**	**185**	**12.3**
FSBE-Processed	**93**	**182**	**20.8**
Processed+Aged	**230**	**254**	**11.8**

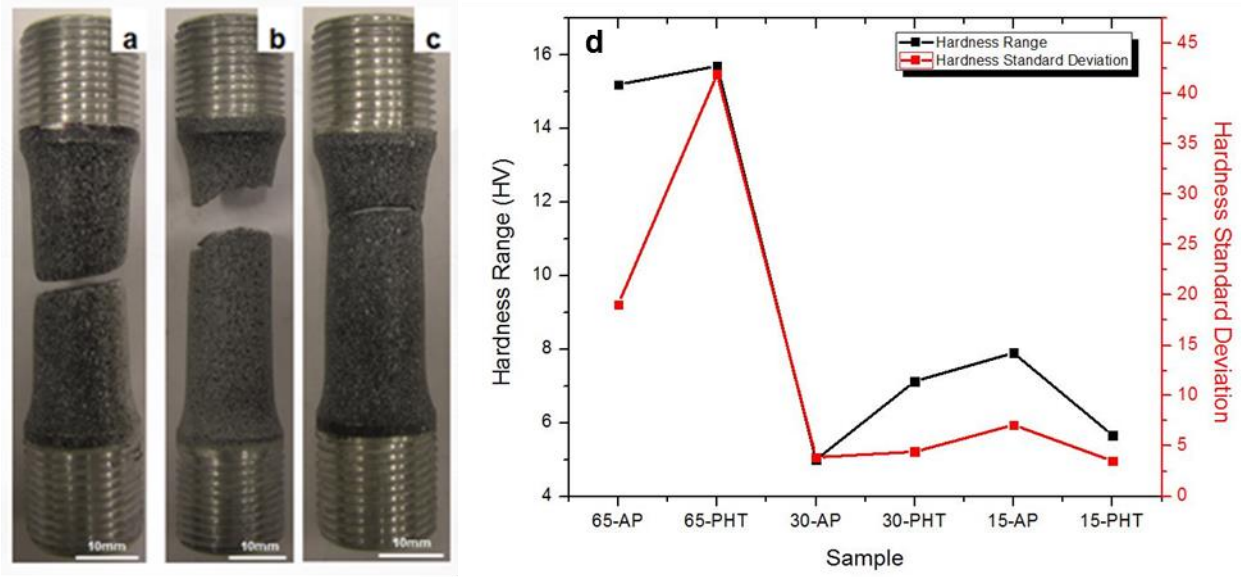

Figure 3.12 Fractured samples for (a) as-received (b) as-processed (c) post-aged and (d) hardness variation along the tube wall

Recrystallization Mechanisms and Discussions

As for the recrystallization analysis with respect to alloy systems that are investigated in the scope of current dissertation, AA6063 alloy will be addressed firstly, simply because the current understanding of Al-Mg-Si series is more mature based on existing literatures and meanwhile it is the alloy system that of our primary focus throughout this dissertation. It has already been clarified that materials underneath the tip of the tool first get in contact with the processing tool and undergoes severe plastic deformation at relatively high temperature. Then with the axial movement of the tool, these processed materials are extruded and start to flow along the processing tool, finally forms the tube wall. Additionally, extra shear deformation and heat exposure are imposed on the flowing materials. That is to say, the recrystallization first occurs in the tube

bottom, while the microstructure observed either near the tube wall or the corner is a result of initial recrystallization at tube bottom and subsequent grain structure evolution under additional thermomechanical effect while flowing along the processing tool. Since the DRX is a dynamic process, whenever the heat and strain level satisfy the thermodynamic and kinetics requirements, DRX will be triggered. That means DRX as well as grain growth might occur while the materials are flowing into tube wall. Thus microstructure formation and corresponding recrystallization behaviors at wall locations can be a little bit more complicated due to its deformation and thermal history. It is also possible that grain size or even micro-texture can be modified by grain growth. With all these reasons, the DRX behavior of the tube bottom sample will be addressed in the first place as a baseline, then DRX phenomenon near the tube wall will also be discussed briefly based on the microstructural information captured by EBSD and the existing understanding of materials flow as well as texture evolution. The EBSD map taken near the centerline of the tube bottom is shown in figure 3.13, with the IPF image colored relative to the shear direction. Grain boundary distribution is shown in figure 3.13b with thin red lines representing low angle grain boundaries (LAGB) having misorientations of 3-15 degrees and thick black lines stand for high angle grain boundaries (HAGB) with more than 15 degree misorientation. Figure 3.13 is constructed mainly used to identify the three major regions where detailed microstructure and recrystallization mechanism discussion will be performed in the following sections.

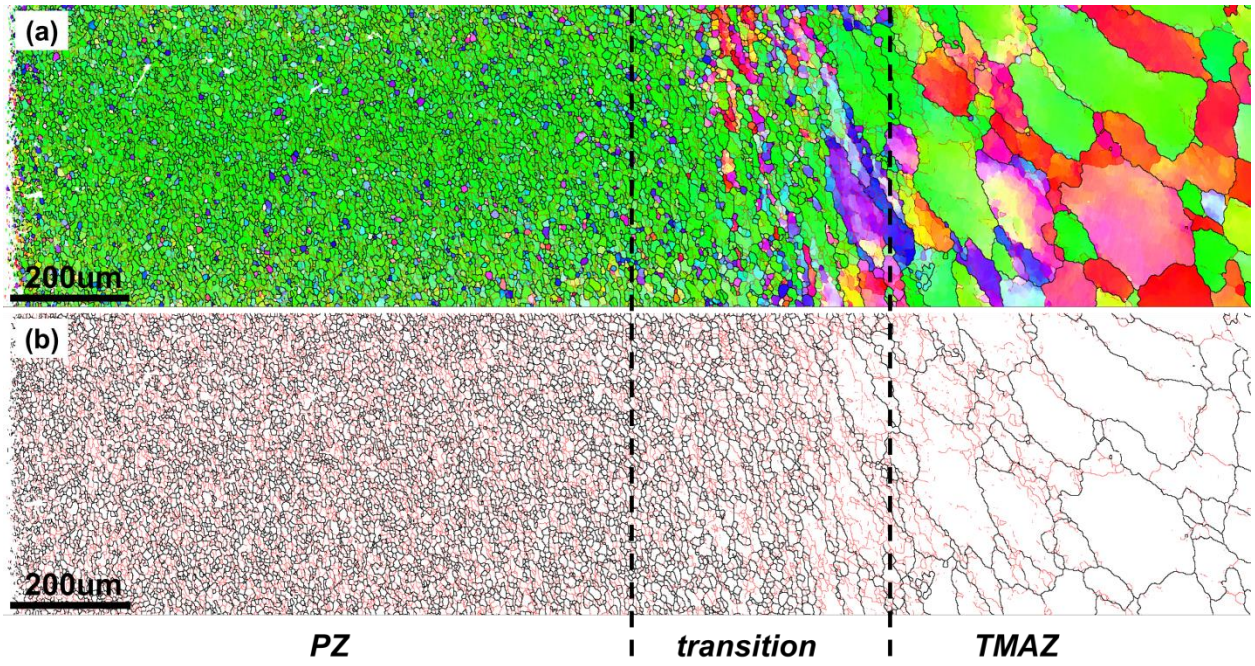

Figure 3.13 (a) IPF image and (b) grain boundary distribution of tube bottom

Recrystallization Mechanism and Microstructural Evolution within the Transition Region of AA6063 Tubes

In this section, grain structure evolution and recrystallization mechanisms will be discussed based on the observations made near the transition region of the tube bottom. Since texture types and relevant evolution pathways are addressed specifically in another chapter, relevant conclusions are going to be directly applied to our present discussions. However, recrystallization mechanisms as well as grain structure evolution pathways are inevitably associated to the grain orientation and texture formation. Based on classical recrystallization theory, microstructural investigations performed by other researchers regarding FSW/FSP and the present author's new understanding learned from the experimental results, several mechanisms that are responsible for grain structure

evolution and dynamic recrystallization will be discussed; at the same time, their respective contributions to the final microstructure as well texture will also be evaluated.

The IPF image of the microstructure near the transition region is shown in figure 3.13a, colored based on pixel's orientation to shear plane normal. The grain boundaries mapping of LAGBs and HAGBs near this region is illustrated in figure 3.13b. It is noted that near the BM side where initial large grains are distorted and stretched by the strain field, LAGBs are mainly distributed near the initial grain boundaries, leaving the grain interiors relatively clean. As mentioned in the previous discussion, LAGBs can accumulated near the grain boundaries and form subgrains, which can further evolve into dynamic recrystallized grains via crystallographic rotation, even under very low levels of strain. As the strain level is increased, the distorted initial grains are highly elongated following the plastic flow as shown in the middle part of figure 3.14a; while at the same time, a major change of grain orientation is noticed. Detailed texture analysis confirmed the formation of A and C components in these elongated grain structures. The elongated grains are characterized by irregular and somewhat serrated grain boundaries, which might suggest grain boundary migration under plastic flow. Profuse LAGBs are generated and distributed homogeneously across the entire elongated grains, even if little LAGBs are present in some regions that might be under minimal strain locally. It is also indicated that LAGBs start to align themselves into the ordered substructures, indicating the formation of subgrains. In the region close to the PZ where additional plastic strain is introduced, elongated structure is refined in size and reoriented away from the transitional C and A components toward more stable B/ $\bar{B}$ types. High fraction of LAGBs

are also observed at this end of the microstructure, most of them forms well defined subgrain boundaries and subdivide the existing refined grain structure, as shown in figure 3.14. Since the major focus of this part is the recrystallization mechanisms and grain structure formation from a microscopic perspective, several recrystallization mechanisms that are involved in the microstructure evolution will be discussed accordingly.

Mechanism 1: it should be noted that mechanism 1 is related to subgrain rotation near original HAGBs in a progressive fashion, which corresponds to the classic theory of CDRX described by Humphreys and Ion [55, 61, 64] . In this case, subgrains near the grain boundaries tend to form new recrystallized grains via progressive lattice rotations, originating from the interaction between grain boundary serrations and deformation substructures. The model for this type of CDRX has been addressed in a previous section. This mechanism will be named as mechanism 1 hereafter throughout this dissertation. As show in figure 3.15, a new small grain surrounded by HAGBs is formed near the grain boundary between grain A and grain B. The grain boundary mapping is presented in figure 3.15b with thin red lines indicating LAGBs with a misorientation angle between 3 to 15 degrees and thick black lines representing boundaries that of higher angle than 15 degrees. From the corresponding misorientation relationship to these two grains, it can be determined that grain A is the initial grain where the new grain comes from since a lower misorientation angle is noticed, as confirmed by the misorientation profile from A-B shown in figure 3.15c. According to the classical theory of CDRX, recrystallized grains can be formed by progressive lattice rotation near the original grain boundaries, thus the newly formed recrystallized grain should exhibit a somewhat lower misorientation with

respect to the mother grains. The scattered PFs for both newly formed grain and the initial grains are constructed and shown in figure 3.15d. The mother grain, i.e. grain A is marked by black circles while the newly formed grain is highlighted by smaller red circles, in order to pinpoint their orientational relationships. It is noticed that the initial grain A is characterized by a typical C orientation while the orientation distribution of the newly formed grain is rotated along the 'Z' axis, which is perpendicular to SD-SPN plane, to some extent when comparing to the ideal C location. However, as mentioned in the texture analysis, grains having C component are supposed to predominantly transform to either B or $\bar{B}$ component by rotating around SD//<110>. Thus, it can be preliminary concluded that the grain formed near grain boundaries via subgrain/lattice rotation might not follow the texture evolution pathways that are controlled by macroscopic deformation geometry. It means the grains formed near GB via classical CDRX mechanism might exhibit orientations that are more dependent on local grain boundary behaviors rather than the macroscopic strain fields imposed by the FSBE process. This theory will be further substantiated by the investigation of recrystallized grain in the PZ.

Another similar set of grains are analyzed and the results are shown in figure 3.16. There is one grain located near the original GB that have already been fully developed and surrounded by HAGBs, while another subgrain marked by black arrow in figure 3.16a is being developed into a separate grain via a similar mechanism. Based on the philosophy of minimal misorientation angle, the mother grain of the recrystallized grain is determined and corresponding orientations distributions are marked on the PFs accordingly. It can be noted from figure 3.16d that the mother grain exhibits an ideal B

orientation with <112>//SPN and <110>//SD, while the recrystallized grain is showing an orientation that is not belong to any ideal shear texture types. As indicated by the red arrows, it seems that the orientation distributions of the newly formed grain are moving away from that of the mother grain and toward a certain direction, resulting in a recrystallized grain with 'unknown orientation'. Combining the present results with the observations made in the previous set of grains, it can be concluded that the grains formed near the GBs via classical CDRX mechanism [68] are not following any specific rules of transformation and their orientation changes as well as the corresponding 'rotation axis' are somewhat random, which is believed to be controlled by the behaviors of grain boundaries. Actually, more grains of this type are analyzed in both the transition region and the PZ, which will be addressed in a future session. However, attempts were made to figure out the underlying rules without luck. It should be noted that decent amount of grains is formed via this mechanism in the transition region, even if only part of them can be proven and defined as a result of this mechanism clearly. Grains formed by this mechanism does affect the overall microstructure and texture to some extent even if the most dominant factor will be discussed later. Additionally, compared with the case of PZ, if seems that more grains are formed via this mechanism in the PZ.

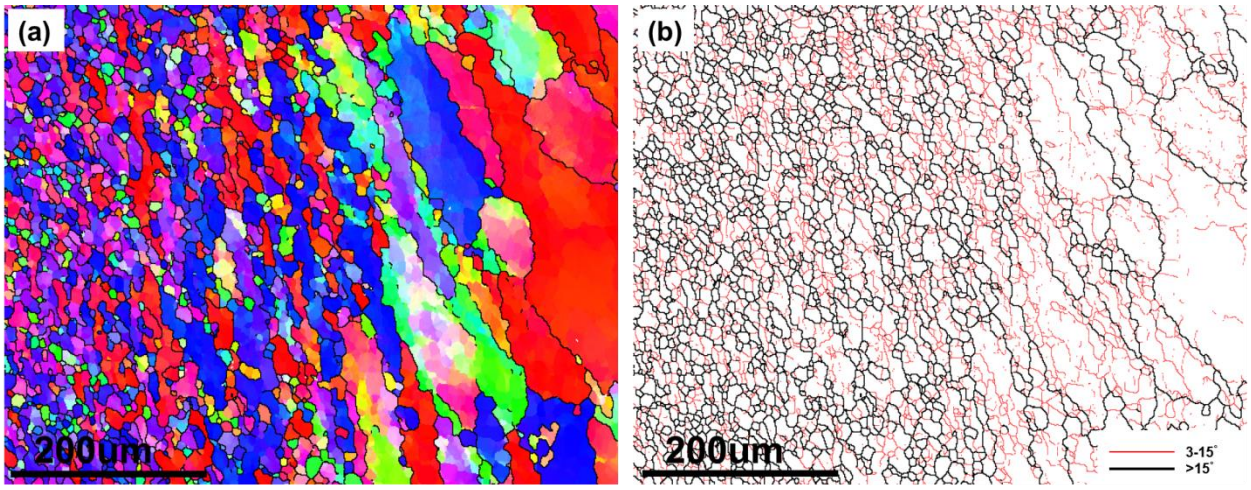

Figure 3.14 (a) IPF image and (b) grain boundary distribution of the transition region

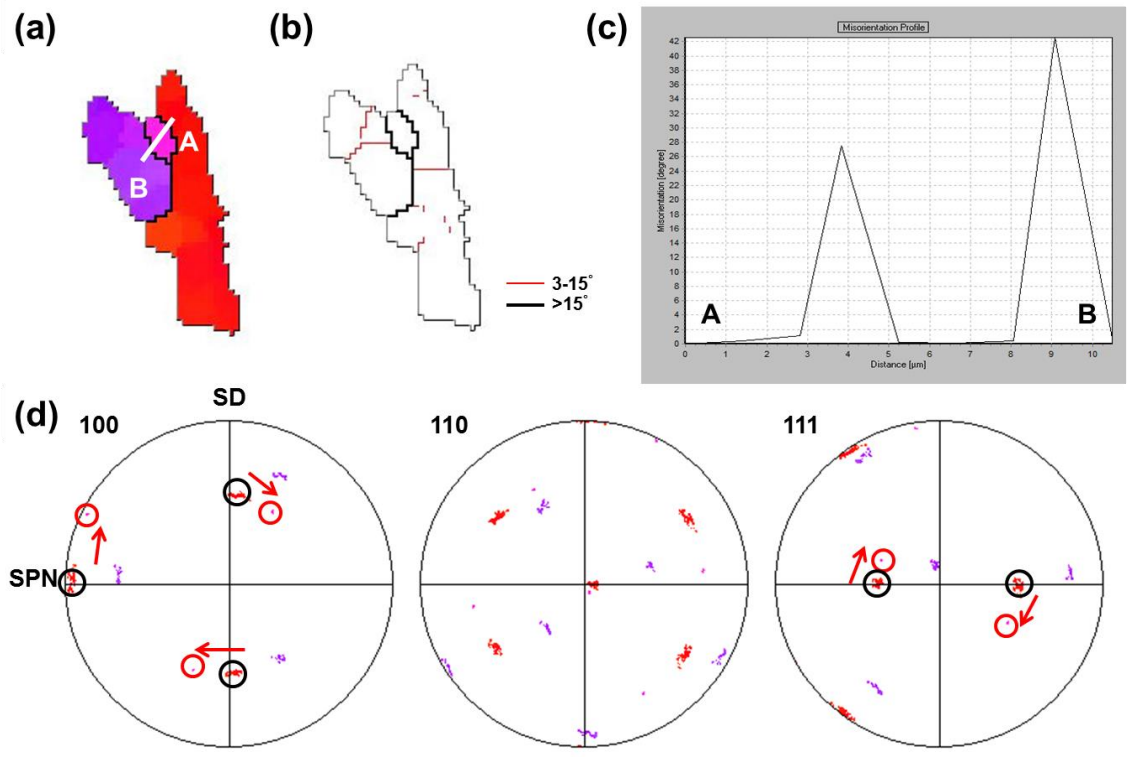

Figure 3.15 (a) IPF image (b) grain boundary distribution (c) misorientation profile along A-B and (d) orientation distribution on pole figures for a selected grain

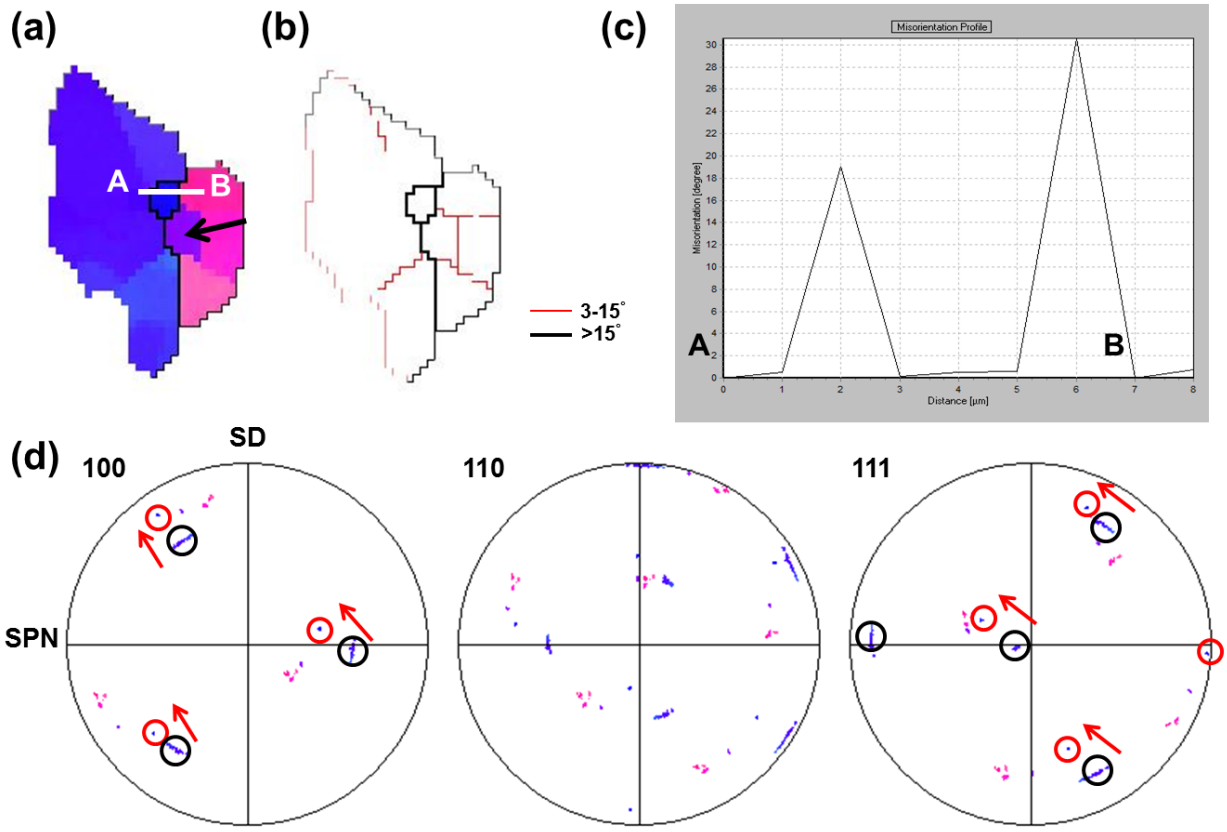

Figure 3.16 (a) IPF image (b) grain boundary distribution (c) misorientation profile along A-B and (d) orientation distribution on pole figures for a group of grains show grain boundary nucleation

Mechanism 2: the second mechanism refers to the formation of new grains within the existing grains, rather than relying on the existing grain boundaries. It is noticed that these types of grain are always very small in size and located near the junction of several LAGBs. It should be mentioned in advance that the effect of this mechanism in the transition region is minimal since only a couple of these grains are observed, whereas grains formed via this mechanism are widely observed inside the PZ. Thus some brief

descriptions and discussions will be performed based on behaviors of these grain, leaving the comprehensive discussions of the second mechanism to be performed in the analysis of grains inside the PZ. As shown in figure 3.17a, a very small grain is generated in the interiors of an existing grain, which is clearly deformed and subdivided. The grain boundaries distribution presented in figure 3.17b clearly indicates that this grain is formed right at the junction of three LAGBs. It is also confirmed by the misorientation profile along A-B that the new grain is defined by HAGBs with misorientation around 21-23 degrees. It seems that these HAGBs are formed by absorbing dislocations and relatively high misorientation levels are build up near the junction of the LAGBs. Apart from the GB, the junction might serve as 'high energy' site that can facilitate the nucleation of new grains. Additionally, the relatively lower misorientation angles signified the fact that these grains are formed via a continuous lattice rotation rather than discontinuous nucleation. The orientation distribution of the mother grain and newly recrystallized grain are also plotted on the PFs, as illustrated in figure 3.17. It is obvious that the orientation distribution of these two grains are very close to each other with around 20-degree difference, also it seems that the new grain is also generated via a rotation mechanism, similar to the CDRX phenomenon at the grain boundaries.

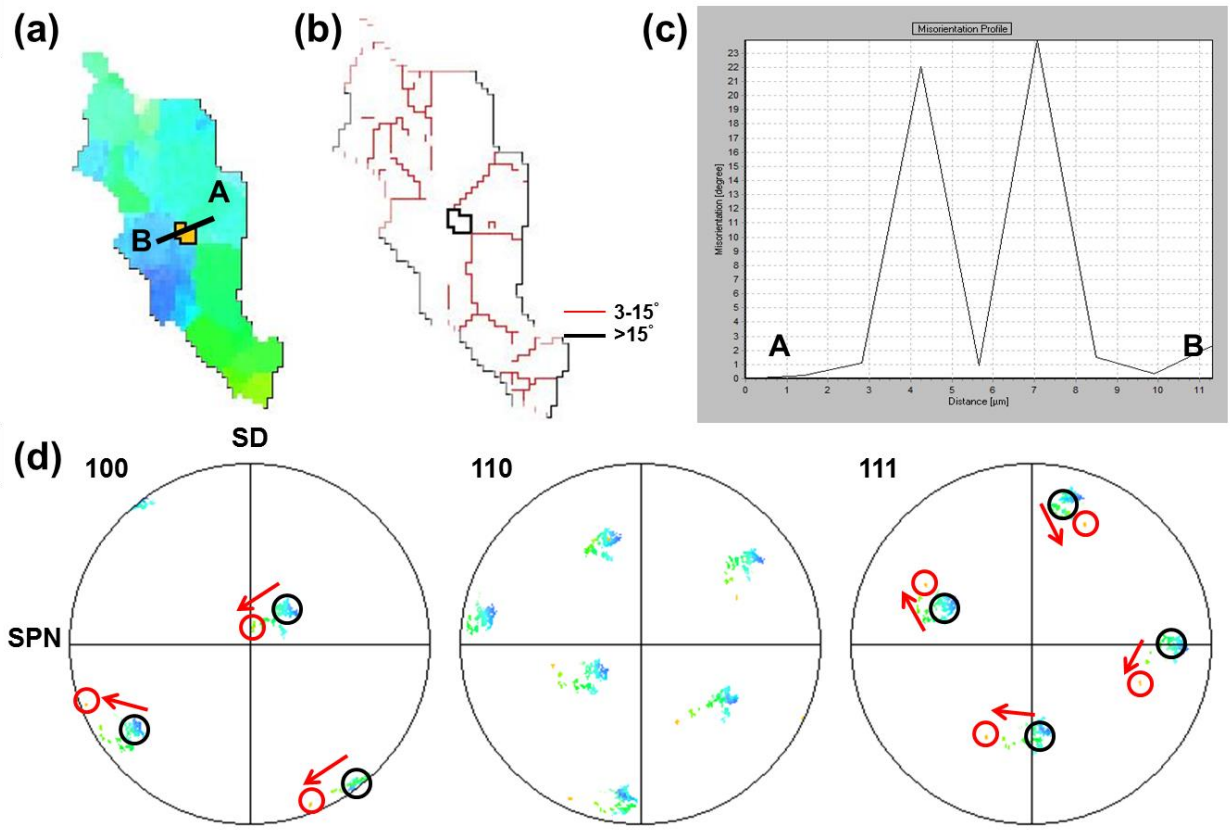

Figure 3.17 (a) IPF image (b) grain boundary distribution (c) misorientation profile along A-B and (d) orientation distribution on pole figures for a selected grain

A second example is shown in figure 3.18. Similarly, this grain is characterized by 'nucleation' at the subgrain boundaries, as represented by the grain boundary mapping in figure 3.18b, whereas the misorientation with respect to the initial grain is determined to be at higher end of 50-60 degrees, as it is well known that the maximum misorientation between any two directions in cubic lattice is 60 degrees due to crystallography symmetry. It is also observed that the initial grain is oriented close to one ideal location of B texture while the newly formed grain corresponds to its alternative, as indicated in

figure 3.18d. It is most likely that new grain is formed by lattice rotation around the ‘Z’ axis near the junction of subgrains. However, it is interesting that such a high misorientation can be developed in the interiors of a deformed grain that is only subdivided slightly and showing scattered distribution of LAGBs. Even if higher density of dislocations and strain gradient is expected at the junctions of subgrains, it seems that such a grain boundary can’t form immediately unless the localized lattice rotation rate is extremely high or the new grain is formed during an earlier stage of deformation. The more interesting part is the orientation of the new grain, which reaches the stable B orientation by the time of being found. However, dynamic nucleation via DDRX is not supported in the present dissertation due to the universal belief of fast DRV rate of aluminum alloys and lack of evidence supporting the nucleation of defect free nuclei within the Al matrix. This type of grain will also be addressed in the case of grain structure formation inside the PZ and more exhaustive discussion will be performed in the corresponding section. It should be emphasized that this mechanism is of minimal influence on the microstructure and texture evolution of the transition region, it is briefly discussed simply for the sake of completeness and serve as the reference for the discussion to be made in the case of PZ, where a lot of these type of grains are found and exhibiting a slightly higher impact on the crystallography texture.

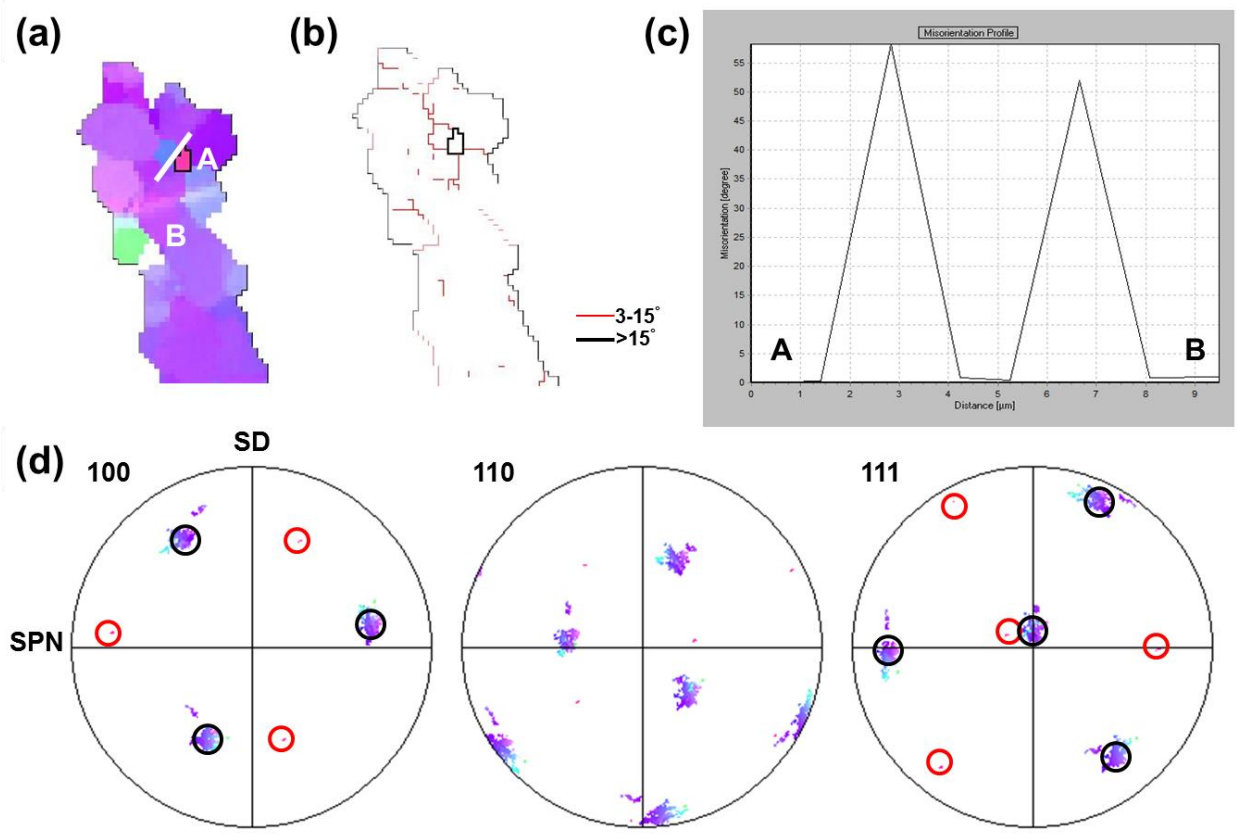

Figure 3.18 (a) IPF image (b) grain boundary distribution (c) misorientation profile along A-B and (d) orientation distribution on pole figures for a selected grain

Mechanism 3: grain subdivision and gradual lattice rotation under straining

This mechanism refers to grain subdivision and progressive lattice rotation across the entire initial grains when subjected to external strains. It is believed to be one of the most important recrystallization mechanism that is actually dominating the grain structure formation or even the texture formation [40, 76], more importantly it coincide with the traditional understanding of recrystallization behaviors of aluminum alloys. However, in a lot of other investigations this mechanism is not supported due either to the observation

of extremely small defect-free nuclei or its incapacity to explain the formation of some HAGBs under certain circumstance[10, 62]. This mechanism is cited as a separate one compared to the first recrystallization mechanism only because the grain subdivision penetrated the entire grains rather than relying on the existing grain boundary. However, underlying physical backgrounds for both of them might be similar which has not been proven yet. In this section, some of the grains that showing distinct transformation characteristics are extracted from the transition region and analyzed separately. The discussion will be performed starting with the existing knowledge and consensus that has been reached regarding the grain subdivision and lattice rotation via a continuous fashion of in FSW/FSP process aluminum alloys, then new observations that are made from the current experimental data will be analyzed and discussed, finally some new ideas and thought will be proposed.

Starting with a large grain that is located near the end of transition region that is characterized by distorted and elongated morphologies, where steep strain gradient is expected since the materials start to be snapped and trapped by the strong plastic flow that is introduced by the rotating tool. The IPF images with respect to SPN, corresponding grain boundary distribution are shown in figure 3.19a and 3.19b, respectively. The first note need to be highlighted is that the grain shown in figure 3.19 is determined to be a single grain based on 15 degree misorietation criterion, even if some HAGBs are developed within the grain during grain structure evolution and reorientation, that is to say even if some part of the grain is developing into a separately grain, it will be analyzed with its mother grain as a whole as long as the grain under transition is not fully

enclosed by HAGBs. Additional evidence that support this point is the scattered orientation distribution shown in figure 3.19d, it is obvious that the entire grain is splitting and transforming in a continuous fashion while some HAGBs are formed. One dominant characteristic of this grain is it tend to split into several blocks that are characterized by distinct orientations, in this case the blocks are of long strips morphologies. As shown in figure 3.19a, a long block showing purple color is formed with in the initial grain; two blocks represented by green showing <110>//SPN are also indicated; additionally, another block located at the middle-bottom part of the grain that is featured by significant orientation spread is also noticed. It can also be observed from the scattered PFs that these blocks are transforming continuously along the PFs and the purple block is orientated to a stable B orientation. The key point here is the initial grain is subdivided in the form of 'blocks' rather than by individual subgrains because of plastic flow and steep strain gradient, during initial stages of deformation. The entire block, as long strip, is reoriented and HAGBs are formed relative to its neighboring blocks, in this case only part of the boundary is featured by HAGBs since they are still under development. At the same time, evidence shows that each block also consists of high content of LAGBs that are arranged orderly into subgrains. However, only some sporadic subgrains can evolve into separate grains at this stage. Misorientation profile along the trace of A-B shows that accumulated misorientation angle up to 35 degrees can be expected without detecting a single grain boundary having misorientation higher than 15 degrees. This clearly supports the CDRX mechanism that grains are subdivided and reoriented continuously along the strain field. It should be noted that A side is definitely

of lower strain level, leaving the region near A close to its initial orientation, while B side if of higher strain due to its proximity to the core of strain field. Interestingly, in other blocks represented by <110>//SPN and <111>//SPN, no such gradual lattice rotation and buildup of misorientation is found, that might suggest these blocks are reoriented to the new orientations as a unit and the entire block is subjected to similar deformation conditions. Thus to briefly summarize these findings: the distorted initial grains are split into several blocks having different orientations, HAGBs tend to form among these blocks and finally resulting individual grains showing long strip morphologies. Within each block, extensive LAGBs and grain subdivision is noticed, however, the corresponding transformation into grains surrounded by HAGBs is barely identified. Based on the PF analysis, the orientation distributions of these blocks are distributed continuously, while individual blocks are not showing extensive orientation spread. Additionally, it should be pointed out that the deformation conditions for each block might not be similar, that result in the strong lattice rotation of part of the grain in the form of strip.

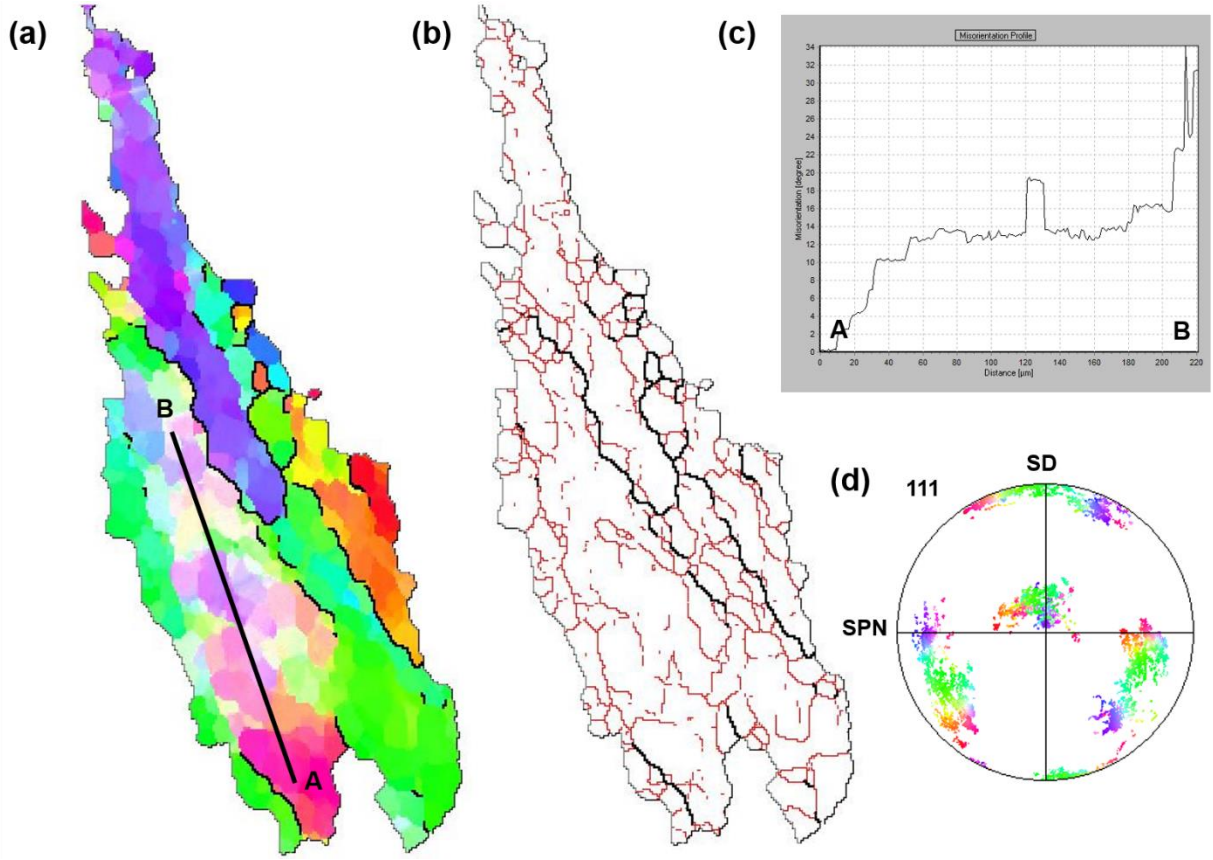

Figure 3.19 (a) IPF image (b) grain boundary distribution (c) cumulative misorientation profile along A-B and (d) orientation distribution on pole figures for a selected grain

As shown in the middle part of figure 3.14, where moderated strain level is expected, elongated grains or group of subgrains characterized by red and blue colors are distributed in an alternate fashion, which are found to corresponds to transitional A and C texture respectively. It is learned from the texture analysis that these C and A components are relatively stable in the early stage transition region where shear strain level is still not very high, while additional shear strains applied at a later stage of deformation will finally transform them into either B or $\bar{B}$ component. These elongated grains actually consist of highly ordered subgrain structures and it seems that they tend to form

individual grains with sizes much larger than the subgrain size. By adopting the nomination strategy applied for the case of figure 3.19, these strips will also be classified as blocks and discussions are performed for individual blocks. One typical block that is showing A type texture, colored by blue, is shown figure 3.20. It can be seen from the map of grain boundary distribution that extensive LAGBs are generated within the block and arranged into ordered subgrains, while only limited amount of LAGBs are involving into HAGBs (mainly featured by misorientation angle slight higher than the threshold value of 15 degrees) because of orientation spread and inhomogeneous deformation. Similar to the blocks mentioned in the previous figure, no significant orientation gradient is expected within these strips, as illustrated by the cumulative misorientation profile from A to B in figure 3.20c, this further suggests that in most blocks, strong orientation gradients are not developed within each block and these block might evolve as an integrated unit. Admittedly, some subgrains are found to be rotated such that they are partially surrounded by HAGBs, the general trend of the entire block is still obvious. As further substantiated by the orientation distribution of the entire block shown in figure 3.20d, no major orientation spread is noticed. One crucial point that needs to be highlighted is this block is surrounded by other blocks that are showing C type orientation, colored by red, as shown by the alternative structure in figure 3.14. It has been noticed that the boundary between the current block and its neighbors are irregular and serrated, so as that of its neighbors. This might suggest the strain induced grain bulge or even migration. At some locations marked by the green arrows in figure grain 3.20a, the block become so thin that it is almost tend to be pinched off by the neighboring grains

because of localized plastic strain and the interactions with its neighbors. The grain shown in figure 3.20 is just intended to represent the elongated blocks that are formed because of the splitting of initial grains, leaving its further development to be discussed later.

An example of the other type of block that is featured by C orientation, colored by red, that is typically located next to the blue blocks with ‘A’ orientation is shown in figure 3.21. It is noticed that this type of block is shorter in size compared to the block belongs to A texture, which might suggest the fact they are relatively unstable and easy to be transformed into other orientations or split into several islands. Similarly, this block is also confirmed to be subdivided into subgrains by LAGBs. However, misorientation profile from A to B only suggest a cumulative misorientation of around 12 degrees, and little HAGB is formed within the block. It should be mentioned that, even if the geometrical effect is playing an important role in stretching the grain into long blocks, its effect on the formation of recrystallized grain is not confirmed. Most of the elongated blocks are showing a larger width than the subgrain size, additionally, no ordered subgrain boundaries are noticed to be aligned almost perpendicular to the original grain boundaries, as described in typical geometric dynamic recrystallization phenomenon. Interestingly, some locations on this block become so thin that some part of the island is almost going to be separated from the block and become a new grain/block, as marked by the green arrow in figure 3.21a. Despite the fact that this marked island near the bottom of the block is going to be pinched off by their neighboring grains, its orientation is still

similar to that of the original block, as confirmed in the scattered PFs shown in figure 3.21d.

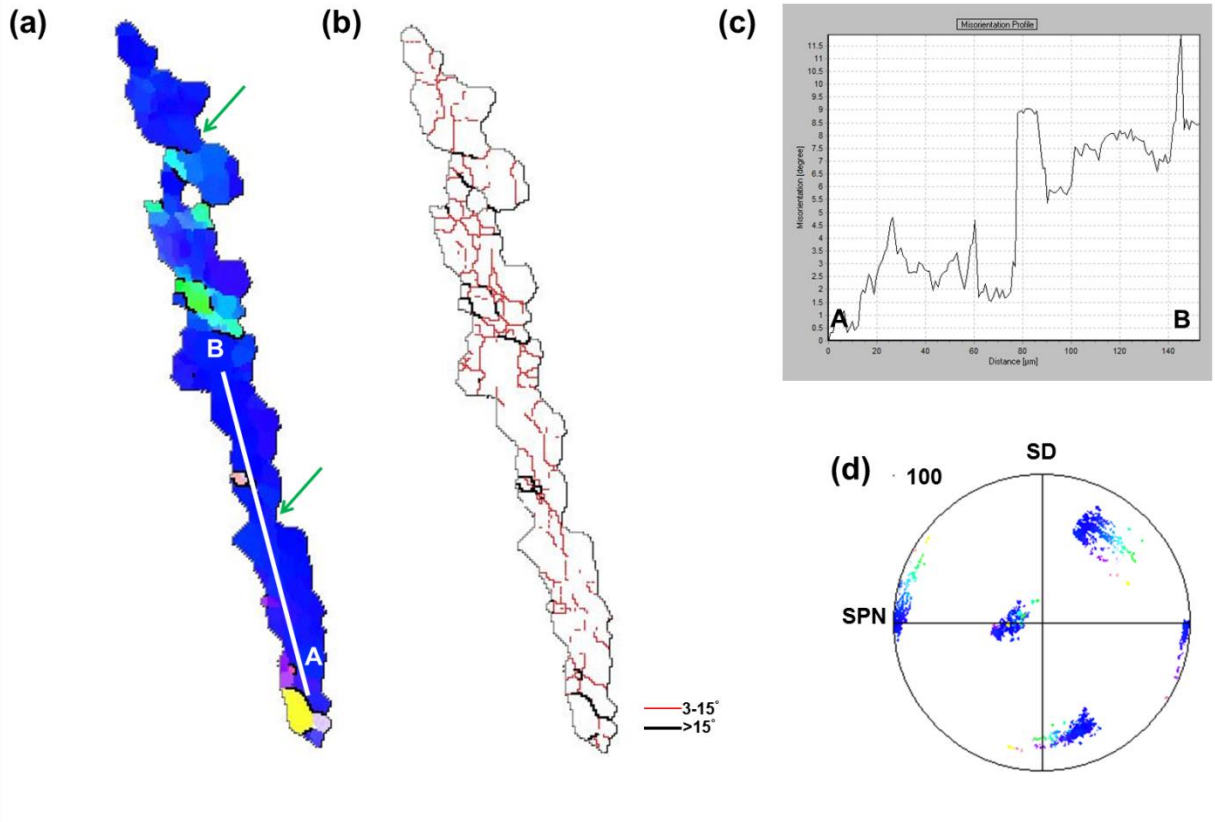

Figure 3.20 (a) IPF image (b) grain boundary distribution (c) cumulative misorientation profile along A-B and (d) orientation distribution on pole figures for an analyzed grain

Further investigation is preformed to clarify this type of 'grain refinement' mechanism by pinching part of an elongated grain off. The same block shown in figure 3.21 will be addressed, while its neighbors are also included accordingly, as shown in figure 3.22. It is noticed from figure 3.22a that apart from the block addressed in figure 3.20, there is another block showing similar orientation lies along the direction of materials flow, by which those blocks are stretched. Accumulative misorientation profile

along A to B indicates that the block observed on the A end is showing similar orientation to the case on the B end, with only less than 10-degree misorientation. This suggest that initially, they should come from a same block showing C texture component, while subsequently split into two blocks during the thermomechanical process. It is interesting to note that the entire red block is neighbored by two blue blocks that are turned out to be of 'A' orientation, the grain boundaries between them is irregular and serrated, leaving some 'necks' on the red block where the two blue neighbors can come together, as indicated by the red arrows. Once the two neighbors start getting in touch with each other, the initial block is split into two blocks or even more. It should be emphasized that these block are not directly related to subgrains since typically the block can be either large or small, can be highly elongated or relatively equiaxed and they are typically of a much larger size compared to subgrain size. The red block that is pinched off by its neighboring blue blocks should mainly be related to the strain induced grain boundary migration as well as localized grain structure evolution such as rotation or translation of the entire or part of the block under shear. This procedure is cited as a crucial mechanism that is responsible for the grain refinement in the transition region.

With these cases, the pinch off process of the blocks is addressed whereas no obvious orientation change is identified, which should be attributed to the relatively low strain level and grains showing C and A type texture can be crystallographically stable. As discussed in the chapter addressing crystallographic texture, stable B/$\bar{B}$ are going to be formed in the PZ from the transition components, thus the orientation changes of these

blocks that are exhibiting transition textures need to be discussed too. A block of grains that is under higher levels of strain is extracted from the transition region that is closer to the PZ, as illustrated in figure 3.23. It is noticed that two sub-blocks are developed with distinct orientation change, these blocks, located at two ends of the block being investigated are highlighted in the grain boundary mapping of figure 3.23b and figure 3.23c, respectively. The scattered PF of the entire block shown in figure 3.23d suggests that this block is initially of C type texture colored by red, while the texture evolution occurs via rotation along the SD, as predicted in the texture analysis. However, it is very interesting to note that the C component is rotated toward two directions, both clockwise and anticlockwise, forming both B and $\bar{B}$ type texture, rather than dedicated transformation into a single component of B. Additionally, this block can be treated as an individual grain that is just distorted and elongated into irregular shape. This will provide strong evidence to the notion that a grain characterized by C orientation can evolve into either B or $\bar{B}$ texture component via rotation along <110>//SD. In the extreme case shown in figure 3.23, C-B and C- $\bar{B}$ transformation happens on two ends of the elongated grain, respectively, which is confirmed in the PFs constructed exclusively for these blocks shown in figure 3.23e-f. The orientation distribution of the block that is highlighted in figure 3.23b is plotted in figure 3.23e, it is obvious that the entire block is transformed into B orientation even if a deviation about 10 degrees is observed. While another block showing distinct orientation change that corresponds to the $\bar{B}$ orientation is presented by the scattered PFs in figure 3.23f. From the foregoing analysis, it can be concluded that when blocks having transitional orientations of C or A are developed into

more stable textures, the orientation change and texture evolution occurs still in the form of sub-blocks, i.e. a group of subgrains, rather than by gradual rotation of individual subgrains. It should be noted that, under addition shear straining, it is highly possible that these two sub-blocks that are showing stable orientations can be pinched off by its neighbors following the pinch off mechanism; while another possibility arise that the middle part of the block that is still showing C orientation tends to be transformed into either B or $\bar{B}$ texture component, which can result in a grain with weird shape while showing stable shear orientation. This type of grains turned out to be widely observed in the PZ and become stable under intense shear strain. In this case since two different texture components have already been formed, it turned out to be at least two grains anyways.

A second example showing similar phenomenon is shown in figure 3.24. This block with initial grain orientation of C is exhibiting a very complicated shape because of the strain induced boundary migration and interactions with its neighboring grain under straining. It seems like that several 'neck' regions are developing into pinch-off locations, as marked by the black arrows in figure 3.24a. One block that consists of several subgrains is showing distinct orientation change, misorientation profile along A-B within this block indicated a strong orientation gradient up to 35 degrees. This suggests that the reorientation of the block relative to its initial orientation is still via a progressive mechanism. Combining the present blocks with distinct orientation change as well as those observations made from earlier discussions, where only pinch-off is noticed without any major orientation variation, it can be briefly concluded that grains are subdivided and

rotated in the form of blocks, rather than by individual grain or subgrain. These blocks can be different in sizes and morphologies. They are formed as long as the interaction of grains near the grain boundaries come to a critical point that can result in the pinching off of grain or the local strain field is high enough to reorient the lattice and result in HAGBs

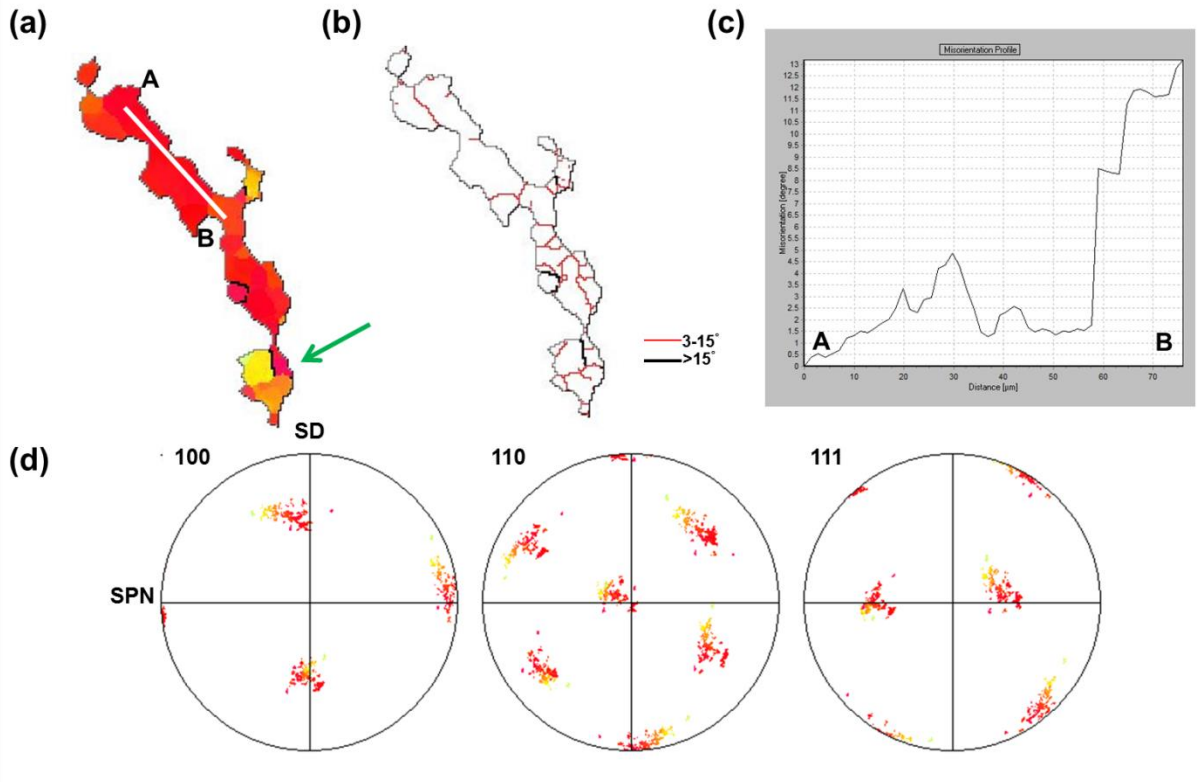

Figure 3.21 (a) IPF image (b) grain boundary distribution (c) cumulative misorientation profile along A-B and (d) orientation distribution on pole figures for a selected grain

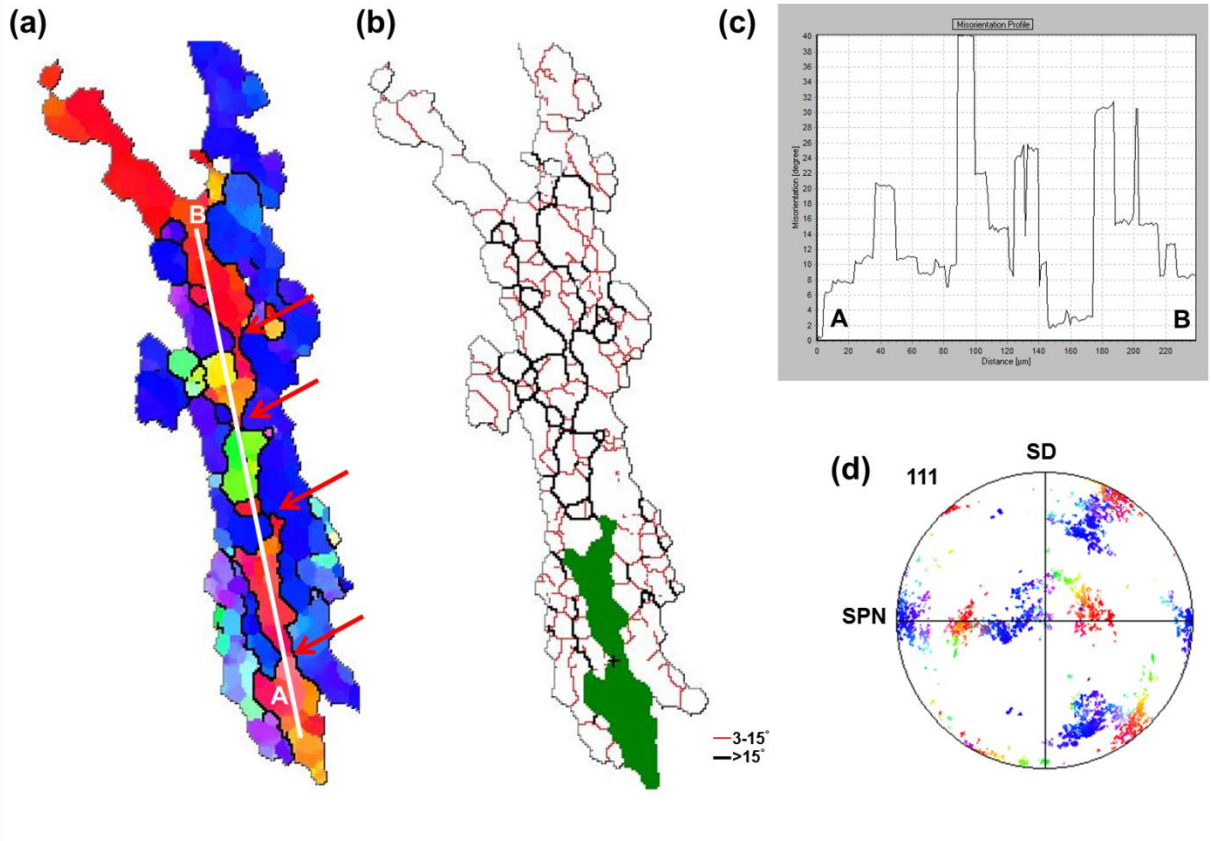

Figure 3.22 (a) IPF image (b) grain boundary distribution (c) cumulative misorientation profile along A-B and (d) orientation distribution on pole figures for a group of grains with the center grain being pinched off by its neighbors

.

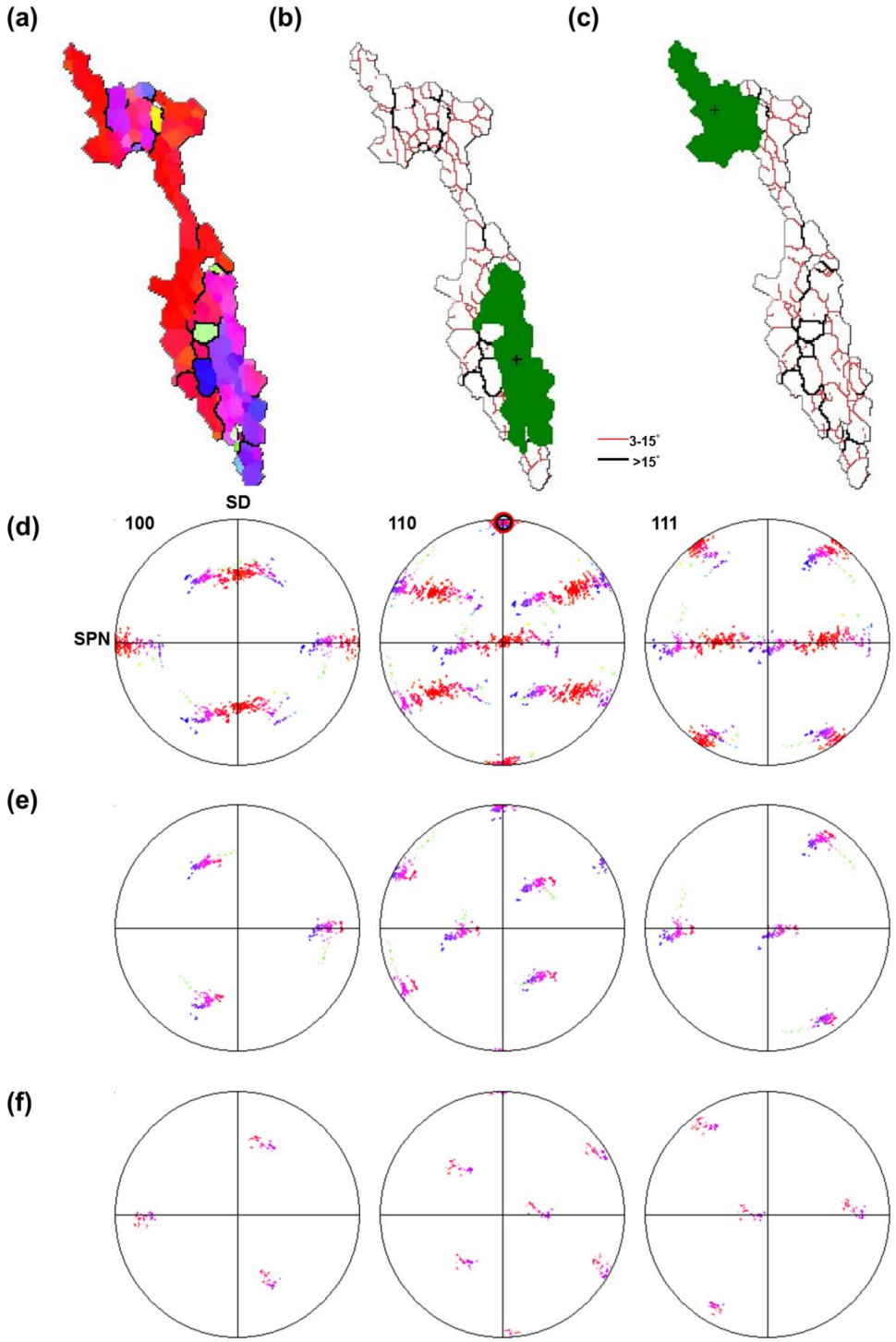

Figure 3.23 IPF images of (a) selected grain (b)-(c) selected blocks and (d)-(f) orientation distribution on pole figures for each block

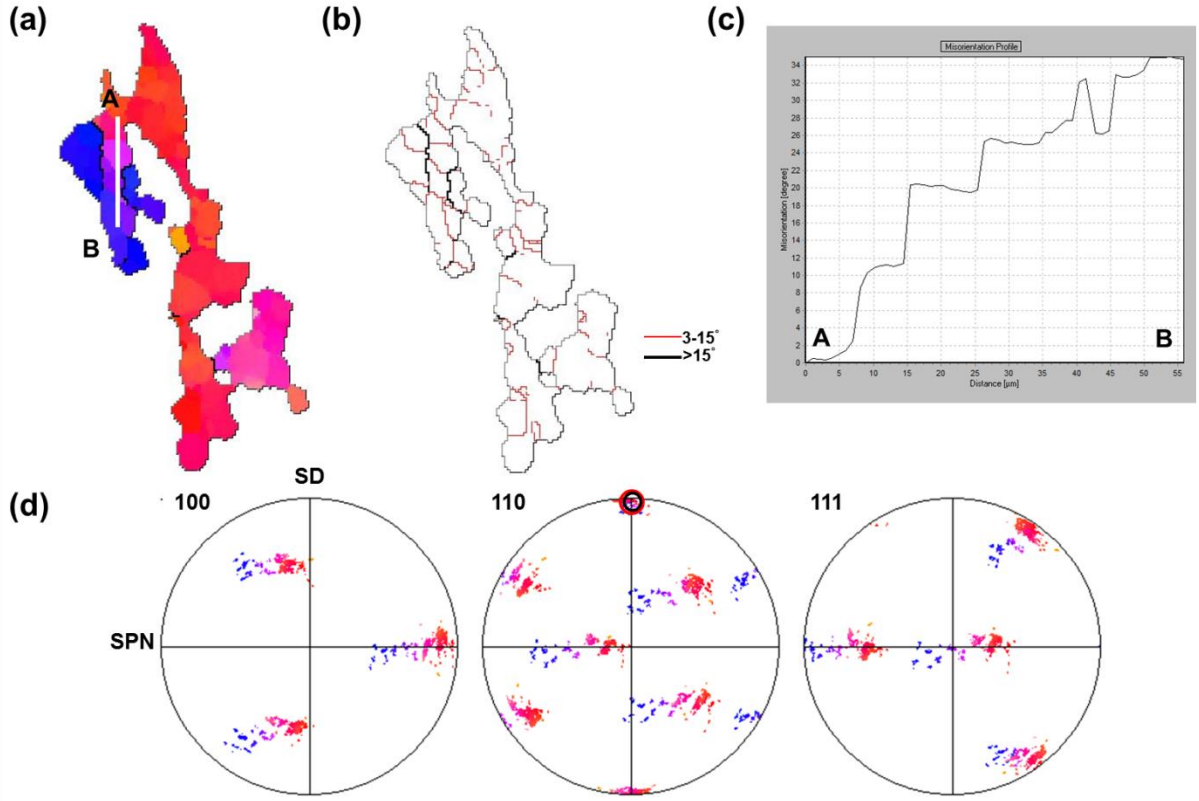

Figure 3.24 (a) IPF image (b) grain boundary distribution (c) accumulative misorientation profile along A-B and (d) orientation distribution on pole figures of a selected grain

Another critical aspect need to be addressed is: the block behavior is well defined and the grain blocks are extensively observed in the transition region, with later investigation performed in the PZ, it turn out that the majority of grains within the PZ are actually these type of blocks with complicated shapes rather than well-defined grains with regular morphologies; some individual grains surrounded by HAGBs that are showing the shape of typical equiaxed or slightly elongated grains are also noticed and their origins as well as the corresponding forming mechanism should also be discussed. It is noted that a lot of individual grains are formed near the original grain boundaries via

the first recrystallization mechanism, even if their initial size is relatively small, post-formation growth is expected under extended high temperature deformation and finally individual grains with various sizes can be formed. At the same time, during the pinch-off procedure, blocks of grain can be dissociated from their mother grains; however, it is still possible that the blocks that are pinched off by neighboring grains are very small in size, consisting of only one or two subgrains, which can be finally identified as isolated grains. An excellent example is shown in figure 3.25. This figure illustrates primarily a pair of grain blocks that are highly deformed and evolving both crystallographically and geometrically. It can be noticed that one block consists of a part colored by red or purple on the left side of the microstructure shown in figure 3.25a, the purple part is transforming into an individual block while it has not been fully encompassed by HAGBs yet; another block is featured by blue, corresponding to A texture component. In both blocks, extensive LAGBs are noticed, while at the same time, a lot of them are developing into HAGB as indicated by the green arrows, also confirmed by the grain boundary distribution shown in figure 3.25b. The major focus of the present discussion is the two grains pointed out by red arrows near the bottom of the microstructure shown in figure 3.25a, as well as the blue block that is located in the very bottom of the entire microstructure. It is noticed that the blue block near the bottom is separated by these two highlighted grains from its parent block while these two grains are isolated by the blue blocks. Accumulative misorientation profiles are constructed along A-B and A'-B' and the results are presented in figure 3.25c and figure 3.25d, respectively. It is noticed that the isolated grain at 'A' end is of similar orientation to the block on 'B' end with only 5-

degree misorientation being present; while for the case of A'-B', the accumulative misorientation turned out to be around 10 degrees, suggesting the fact that the blue block near the bottom is of similar origin with the major blue block on the right side. With these results and the observation made in figure 3.24, it can be easily noted that those two separate grains are pinched off by the blue block from the initial long block while at the same time blue blocks are pinched off into two smaller blocks by these two grains. The possibility of forming individual grains by this pinching off mechanism is illustrated by the present set of grains. Thus the isolated grains observed in the microstructure of the PZ can be either explained as grains formed near the grain boundaries via CDRX or originated from the pinching off procedures. Additional set of grains showing the formation of individual grains by the pinching off procedure is also shown in figure 3.26. The isolated grain marked by B is confirmed to come from block A based on the cumulative misorientation analysis. It seems that grain B is just pinched off by the neighboring block showing predominantly C texture component from the mother grain and still has an extremely small contact point. With this case, it is also testified that small grains can also be pinched off from the periphery of the initial block rather than only from either the top or the bottom of a specific block.

With the analysis and discussion preformed in this section, several key points can be summarized as follows:

1, newly recrystallized grains can be formed via grain boundaries serration and localized lattice rotation near the existing grain boundaries, this mechanism is ever-lasting during the entire recrystallization analysis. However, their contribution to the final

microstructure and texture is determined to be insignificant, at least in the case of AA6063 tubes.

2, the block theory is proposed and used to explain the grain refinement as well as grain reorientation rather than individual subgrains.

3, one block that consists of many subgrains can be pinched off by their neighbors during grain structure evolution as an integrated unit; at the same time, lattice reorientation also occurs in blocks via a similar fashion.

4, the block can be as small as a single subgrain and as large as tens of subgrains, its morphology can be either highly elongated or close to equiaxed

5, extensive LAGB and ordered subgrain formation is noticed within the grain structure, while only limited amount of subgrain boundaries are evolved into HAGBs.

6, the pinching off process is similar to the process of GDX, however, it can't be defined as GDX for the moment

7, our contributions: propose the importance of block behavior rather than individual subgrains during both grain refinement and texture development; refined grain structure is not formed via gradual lattice rotation of subgrains across the entire microstructure, as suggested in a lot of existing publications, rather, grain blocks are playing an important role which is assisted by the geometric effect of the deformation; even if some individual grains can be formed via the first mechanism and pinching off of a small part of a block, the contribution to the final microstructure and texture is turned out to be small.

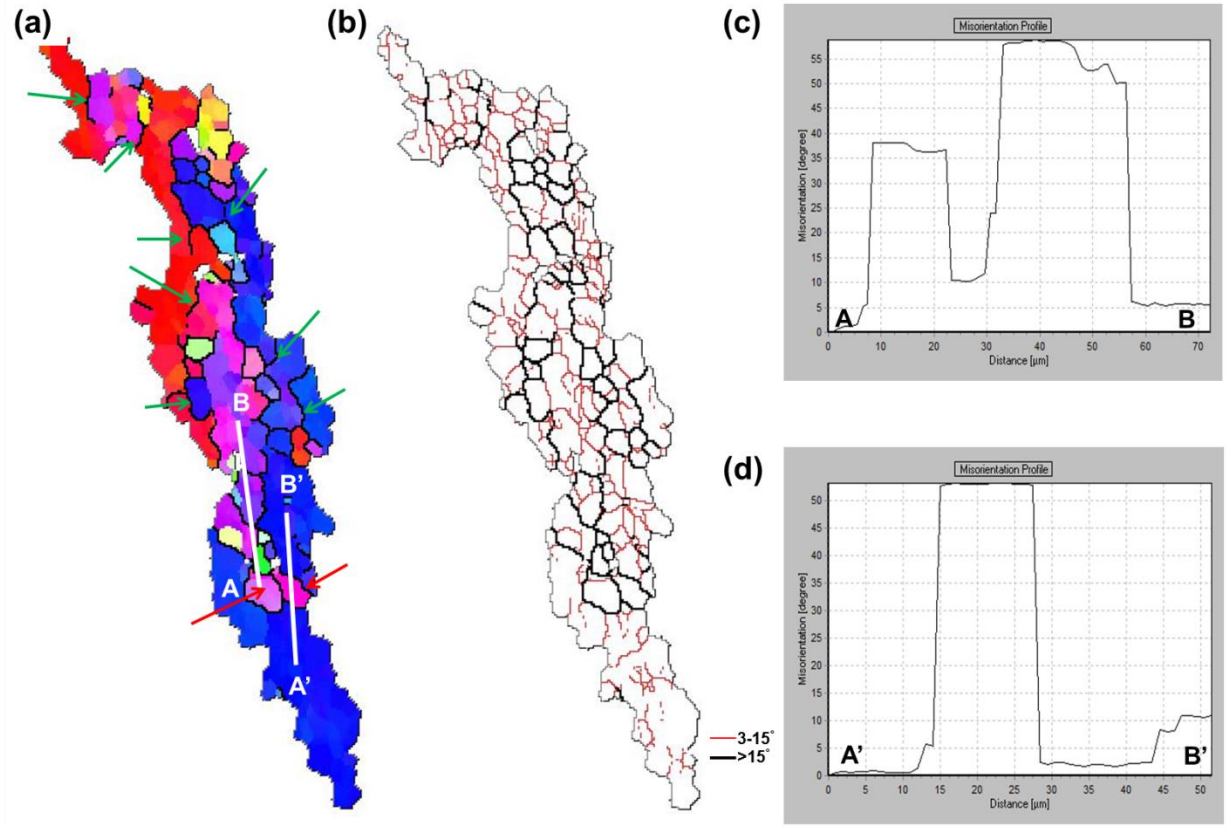

Figure 3.25 (a) IPF image (b) grain boundary distribution (c) misorientation profile along A-B, A'-B' and (d) Orientation distribution on pole figures for an elongated grain undergoing subdivision

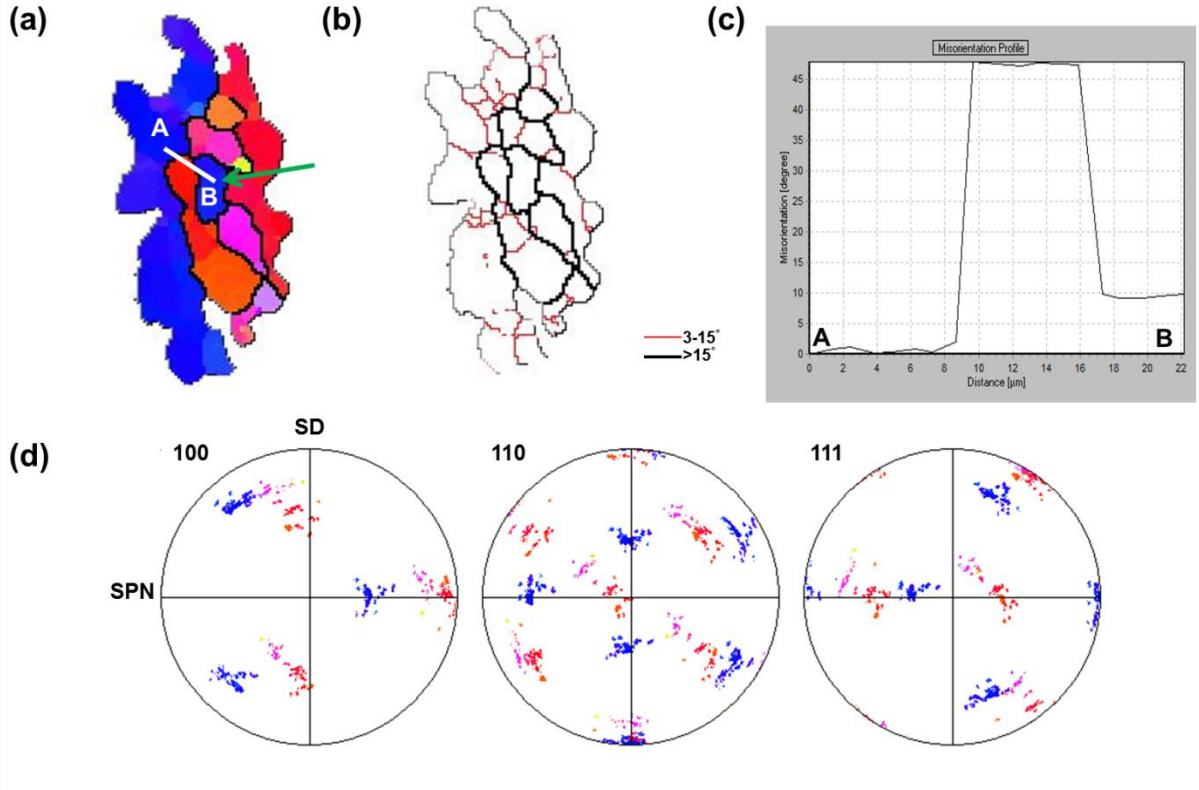

Figure 3.26 (a) IPF image (b) grain boundary distribution (c) misorientation profile along A-B and (d) orientation distribution on pole figures for a group of grains

Recrystallization Mechanism and Microstructural Evolution within the Processing Zone of AA6063 Tubes

In this section, the observations made inside the PZ of the tube bottom will be analyzed and discussed based on the EBSD results. The discussion will be mainly focused on the grain structure evolution by dynamic recrystallization process as well as its relationship to the orientation change of newly formed grains or subgrains, in an attempt to understand the mechanism involved during the FSBE process. The detailed texture analysis has been addressed in a separate chapter, thus no extra explanation is going to be performed regarding the basic texture evolution; rather, major conclusions

will be adopted directly for the purpose of understanding recrystallization mechanisms and its connection to grain orientations. Similarly, newly formed grains by DRX will be analyzed at a local scale by addressing its relationship to their mother grains and neighboring grains. Thus several mechanisms will be proposed and the corresponding experimental observations are demonstrated together with in depth misorientation and orientation analysis. The analyzed grains will be categorized based on the site of formation, i.e. in the grain interiors, near grain boundaries or even close to subgrain boundaries.

Mechanism1**:** similar to the discussions about the transition region, the first mechanism involves the subgrain/grain formation near previous high angle grain boundaries. As described in the classical theory of CDRX proposed by Humphreys and Ion [55, 61, 64], misorientations tend to build up at grain boundaries and form LAGBs, then, new grains are formed by progressive subgrain and lattice rotation under straining. This type of CDRX is typically observed at low strain levels, as shown in the previous case of regions close to BM side, which is slightly deformed by the plastic flow. However, the newly formed grains that originate from this mechanism are also observed inside the PZ, where high shear strain and strain rate is expected.

A few examples following this mechanism will be analyzed, together with their orientational relationship to mother grains and neighbor grains. A typical example is shown in figure 3.27, a fully recrystallized grain surrounded by HAGBs is formed near the grain boundary between grain A and B, showing a different orientation from that of both neighboring grains. The HAGBs with misorientation larger than 15 degrees is

depicted by thick black lines while the LAGBs with more than 3-degree misorientation are represented by redline. The misorientation profile from A to B illustrated in figure c shows a lower misorientation on the side of grain A, indicating the fact that grain A should be the original grain where the newly formed grain evolved from. The corresponding orientations of both newly formed grain as well as its mother grain (grain A) are circled out by red and black circles in the PFs shown in figure 3.27d. Based on our understating of the shear type texture and deformation geometry of the FSBE process, both grain A and grain B corresponds to an ideal shear type orientation of B an $\bar{B}$ component showing <110>//SD and <112>//SPN. However, the new grain exhibits an orientation that seems like being rotated along the direction close to but not exactly perpendicular to the SD-SPN plane, relative to its mother grain, as shown in figure 3.27d. This observation matches well with the CDRX mechanism that subgrain evolves into grains via local lattice rotation. Additionally, it also signifies the fact that grains formed by this mechanism is not showing similar orientation to their mother grain, in our case, it might serve as a disruptive role to the ideal B/ $\bar{B}$ texture under shear deformation.

Similar observations can be made from another recrystallized grain that is shown in figure 3.28. Based on the misorientation relationship, grain A is identified as the original grain of the newly formed grain. The recrystallized grain exhibits a rotational relationship with the original grain, suggesting the mechanism of lattice rotation at initial grain boundary, as illustrated in the PFs. From the (100) PF shown in figure 3.28d, it seems like the rotation axis is close to the ‘Z’ axis that is perpendicular to SD-SPN plane, similar to the previous grain. However, the relatively large deviation of orientation

distribution in (111) PF contradict this assumption, thus it is assumed that by what way the newly formed grain rotated might depend on the local deformation conditions as well as grain boundary behaviors. Additionally, another grain formed via a similar process is illustrated in figure 3.28. It is noticed that the two nearby grains next to the newly formed grain exhibit an ideal B and $\bar{B}$ orientation, respectively, whereas the new grain is not showing any orientations related to shear texture components. It is noticed that the orientation of the new grain is rotated around a certain axis from its original grain, which is grain A. It is for sure the rotation axis is not associated with the macroscopic coordinate system or the shear reference frame; rather, it should be determined by the local deformation at the grain boundary. Unfortunately, the exact crystallographic direction of the rotation axis can't be determined for the time being.

Interestingly, another grain that is formed following the regime of progressive lattice rotation of subgrains near grain boundary shown in figure 3.29 suggests that, the rotation axis can be coincide with certain macroscopic directions. In this case, it is obvious that the grain is formed by rotating around SD from its initial grain, i.e. grain A, which is showing an orientation close to ideal B, as presented in figure 3.29d. The corresponding orientation distribution for the newly formed grain is circled out as red in the PFs, while black circles are used to identify the orientation of its mother grains. Because the evolution occurs by rotating around the SD, the fixed pole that corresponds to <110>//SD is represented by black circles overlaying with red ones. The results drawn from this set of grain mainly explained the possibility that rotation axis of the newly formed grain can be aligned to the SD or other directions related to shear reference frame

or macroscopic coordinate systems. Additionally, the situation that two separate grains formed near the grain boundary of a same set of initial grains is shown in figure 3.30. It is obvious that these two grains are formed along a same initial GB that is of high misorientations. Grain A is determined as the initial grain for both newly formed grains since a low misorientation level is measured on the side of grain A, based on the philosophy these grains are evolved gradually from the initial grain. It is noted that only misorientation profile across A-B is illustrated, profile along A'-B' is extremely similar thus not shown here. As presented in the scatter PFs in figure 3.30d, the orientation of the initial grain, grain associated to A-B and A'-B' are circled out by black, red and light blue, respectively. It is obvious that the two newly formed grains are not evolving along a similar pathway, grain associated to A-B is rotating along the ideal 'Z' direction anticlockwise, as evidenced by the overlapped circle near the center pole of (111) PF; while the orientation distribution of the grain corresponds to A'-B' profile seems like being shifted compared to the case of initial grain. Thus is can be concluded that, subgrains developed near a same initial GB can evolve following different routes, in our case, the rotation axis related to the subgrain rotation mechanism varies.

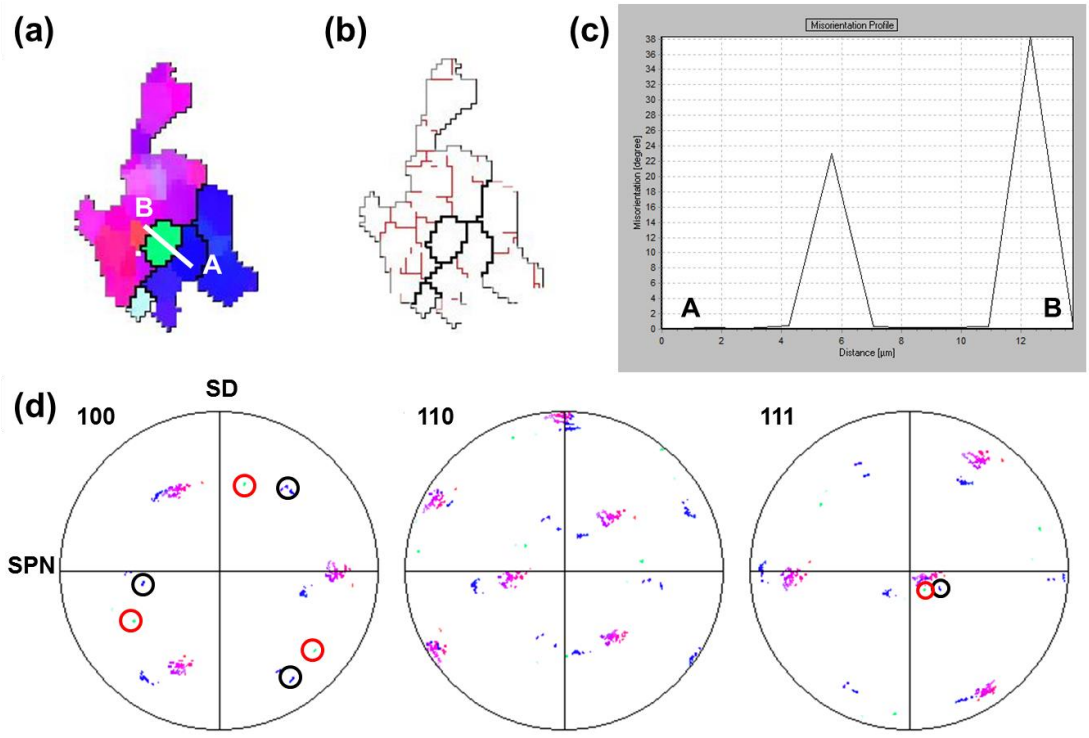

Figure 3.27 (a) IPF image (b) grain boundary distribution (c) misorientation profile along A-B and (d) orientation distribution on pole figures for a set of grains

In the current investigation, more than 20 of such grains formed near previous grain boundaries are evaluated, they are exclusively exhibiting a relatively low level of misorientations (less than 35 degrees) with respect to their mother grains. It is possible that those grains formed via this mechanism grow and keep changing their orientations under thermomechanical processing to such an extent that it is very hard to be identified from their mother grains. The author believe this should barely happen since little grains are observed near grain boundary that is showing very high misorientations to its neighbors, and at the same time a characteristic of well-defined relatively small grains. It

should also be mentioned that majority grains within the PZ are actually not highly refined, rather they are subdivided into distinct subgrains with some boundaries evolve into HAGB but typically less than 30 degrees. That means considering 15 degree misorientation as the threshold for HAGBs, the highly distorted and subdivided initial grains inside the PZ can be an order of magnitude larger than the newly recrystallized nears near their GBs. Thus it is unlikely that the newly formed recrystallized grains by subgrain rotation can grow by such an extent. To summarize, the grains formed near the GBs are typically showing lower misorientations relative to their mother grains. Since most of the grains that consist of this microstructure are showing ideal B/$\bar{B}$ orientation, the newly formed grains tend to serve as a disruptive factor that is scattering the ideal B/$\bar{B}$ components.

Unfortunately, only several of the detailed grains can be presented in this dissertation. However, the primary conclusions will be drawn based on both the discussions made in this section and those grains that are not shown here.

1, Recrystallized grains following the classical subgrain/lattice rotation mechanism are observed near the original grain boundaries, no distinct evolutional trends with respect to grain reorientation and rotation axis are noticed; even with same neighboring grains, two grains formed near the GBs via this mechanism are showing disparate evolutional characteristics.

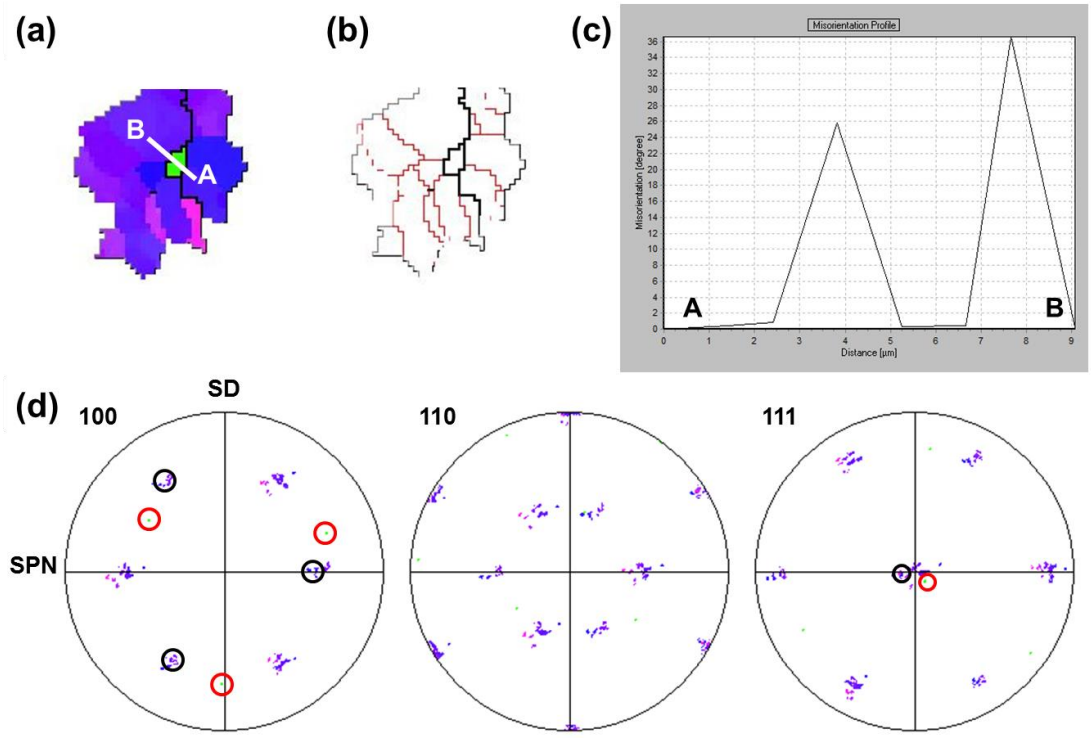

Figure 3.28 (a) IPF image (b) grain boundary distribution (c) misorientation profile along A-B and (d) Orientation distribution on pole figures for an analyzed grain

2, the rotation axis by which grains are evolved can either be coincided with certain directions associated with macroscopic coordinate systems of shear reference frame or being random.

3, grains formed via the present mechanism exhibits relatively lower angle misorientations with respect to the related initial grains, regardless of their orientations.

4, since most of the grains pre-exist in the PZ are showing orientations of ideal B/ B̄ texture, the newly formed grains via this mechanism will always generate new grains that

are not showing B/ B̄ texture components. Thus this mechanism might serve as a disruptive force for the texture formation of stable B/ B̄ under high strain levels.

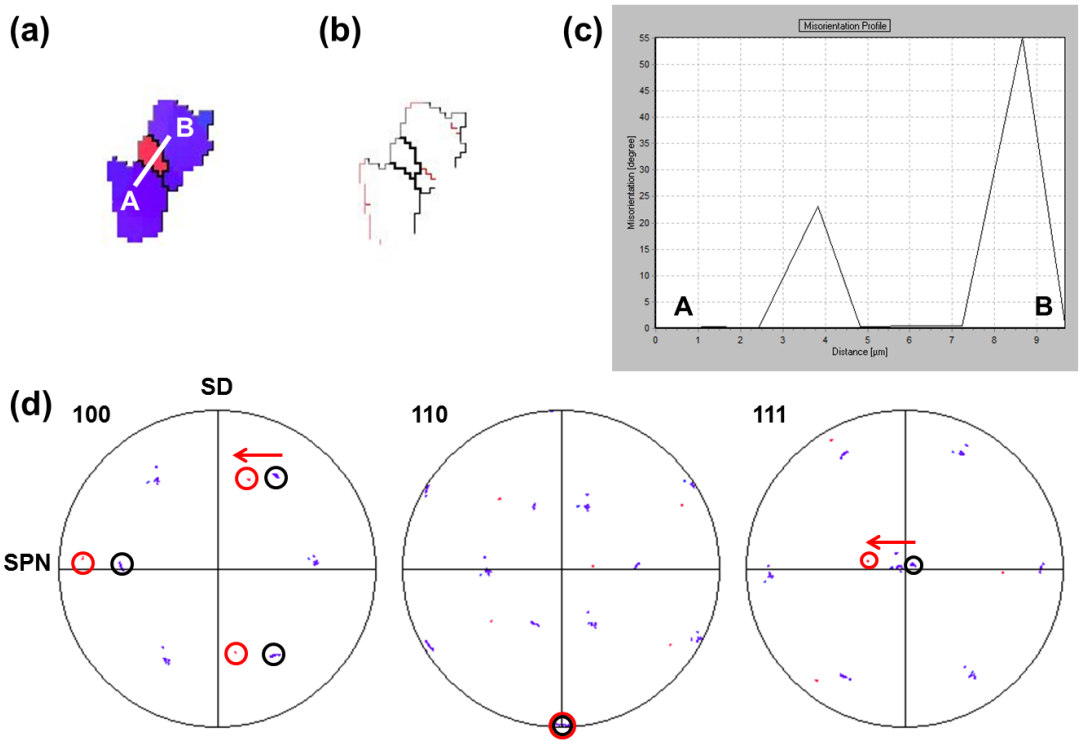

Figure 3.29 (a) IPF image (b) Grain boundary distribution (c) misorientation profile along A-B and (d) orientation distribution on pole figures for one set of grains

5, among several recrystallization mechanisms involved in the PZ, this grain boundary rotation mechanism is not playing a major role in determining the final microstructure and texture.

6, our contribution: typically, the orientation of grains formed near grain boundary are not specifically addressed especially during FSW/FSP process of aluminum alloys, a detailed investigation on the behaviors of subgrain/grain formed near grain

boundaries is performed with special attention paid to the rotation axis and the trend of the grain reorientation.

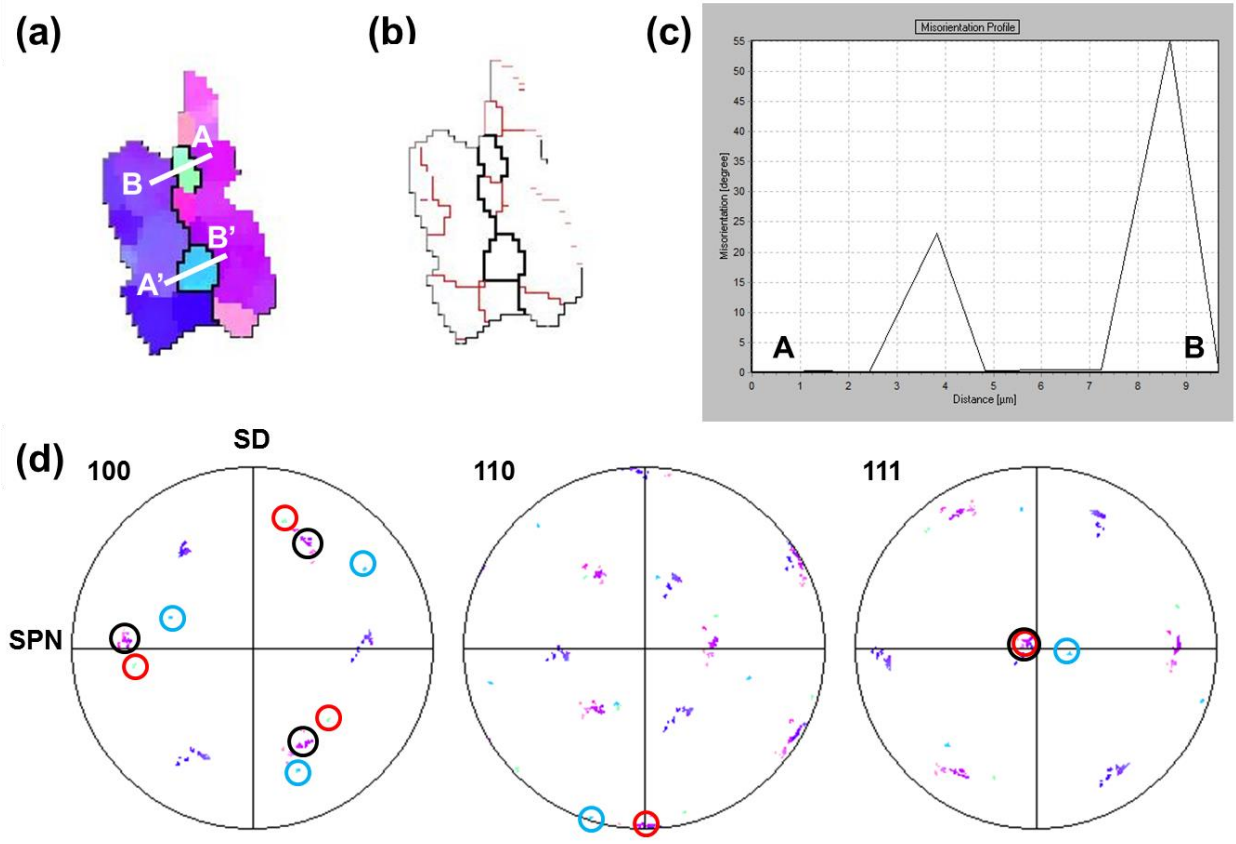

Figure 3.30 (a) IPF image (b) grain boundary distribution (c) misorientation profile along A-B and (d) orientation distribution on pole figures for selected grains

Mechanism 2: this recrystallization mechanism involves the formation of HAGB in the interiors of either initial or deformed grains, one dominating characteristic of this type of grains is they are showing very high misorientations to the mother grain in the range of 50-60 degrees, which contradict the typical belief of gradual grain rotation and

subdivision; additionally, these grains are connected to their mother grains by LAGBs with misorientations lower than 15 degrees and looks like formed at the junctions of several subgrains; finally, these grains are exhibiting a special relationship to their mother grains in the sense of grain orientations.

A typical example is shown in figure 3.31, it can be seen that an individual grain away from the previous grain boundaries is generated within the existing grain, which undergoes grain subdivision and dynamic recovery. It is also noted that several subgrains are formed inside the grain being investigated and the recrystallized grain sit right at the junction of four subgrains. Misorientation profile along A-B shown in figure 3.31c indicated that very high misorientation of around 50-60 degrees is formed between the recrystallized grain and its mother grain. As represented in the PFs shown in figure 3.31d, orientation distribution of the newly formed grain is around 50-60 degree from that of the mother grain, notably, around the 'Z' axis. The projection of recrystallized grain on the PFs is circled out by red while black circles are used to highlight the orientation of the mother grain. It is very interesting to note that while the mother grains show an ideal B shear orientation, as expected and addressed from the texture analysis; surprisingly the newly recrystallized grain exhibits a near ideal $\bar{B}$ orientation, the equivalent component of B! And this is not coincidence, more than 20 grains are actually analyzed one by one following the procedure applied in figure 3.31. The grains recrystallized in the interior of an existing grain exclusively exhibit orientations that corresponds to either B or $\bar{B}$ component, while the mother grain shows their equivalent alternative. In some cases, the orientation distribution is not located exactly at the ideal location, however, it can still be

identified as B/$\bar{B}$ components with some deviations, which is inherent since both recrystallized grains and mother grains are undergoing progressive lattice rotations. Also, the high level misorientation of 50-60 degrees can be explained via this texture relationship since the ideal misorientation between the B and $\bar{B}$ component is 60 degrees around 'Z' axis. Now the questions are why these types of grain are formed and by what mechanisms they are generated? Since the mother grain consist predominantly of su$\bar{B}$ regions that are separated by LAGBs, which coincide with the prevalent standpoint of the microstructure and micro-texture evolution of aluminum alloy during FSP/FSP by grain subdivision and dynamic recovery [40, 55, 68]. It seems hard to understand why these very high angle boundaries are generated inside the grain without any transitions. If grain subdivision and gradual lattice transition is the mechanism, there should be some boundaries exhibiting intermediate misorientation levels like 30-40 degrees, which are not observed in most cases at the PZ.

Based on the existing literature, it seems that DDRX [55, 62, 70] might be the controlling mechanism that is responsible for the formation of such HAGBs, since only discontinuous nucleation is able to generate a new grain with high misorientation to its neighbors immediately. However, based on the definition of DDRX, the nuclei are typically surrounded by HAGBs, which is only defined as more than 15 degrees; while the misorientation level of the recrystallized grains in the present case consistently showing a misorientation angle of 50-60 degrees. Additionally, nucleation site for DDRX is typically related to grain boundaries or highly strained microstructure features [55, 57], since the dislocation density and driving force for nucleation is definitely higher than the

grain interior, especially no large particle or shear bands are formed inside the grains. That means it is less likely that DDRX is triggered in grain interiors where the driving force is low. Another argument is, DDRX is generally believed to generate random or cube-oriented grains in aluminum alloy [10, 17, 62, 70], which can't explain the consistent observation of grain orientation close to B/$\bar{B}$ shear component. Last but not least, DDRX is really not a preferred mechanism for the DRX of aluminum alloys during any processing that is performed at high temperatures solely because of fast recovery rate and its incapacity to accumulate enough stored energy for discontinuous nucleation and growth. Thus, to summarize, it seems unlikely that the DDRX is the underlying mechanism associated with the new grain formation in the grain interiors.

Another possible reason for the formation of such recrystallized grains might be closely related to the observation that these grains are always observed at the junction of several subgrains that are defined by LAGBs (at least 3 subgrains but in most cases 4 are noticed). It is likely that at the junction of several subgrains, local strain or misorientation field can generate a high driving force for the formation of such boundaries of very high misorientation with the mother grain. Even if it is for sure that such recrystallized grains are always observed near the junction of several subgrains, the direct relationship can't be built without further evidence provided. Also, the same problem arises: assuming the local HAGB are formed at the junctions of subgrains, it is still not necessary to show a B or $\bar{B}$ orientation, which is observed almost in very single grain. This come to another question, is it possible that the HAGB formed in these cases are not in the very high range of 50-60 degrees at the very beginning, but transformed quickly to the alternative

B/$\bar{B}$ orientation that is stable [42, 43, 52]. Remember, material inside the PZ is subject to intense plastic deformation, which means the grain subdivision process can develop very fast. This reasoning seems reasonable since the matrix grain is showing either a B or $\bar{B}$ orientation and they are already treated as stable, if a grain with certain orientations are formed within the initial grain, is can be immediately transformed to either B or $\bar{B}$ orientation depends on its relevant stability under the intense shear deformation. That is to say, if a HAGB showing intermediate misorientation level with respect to the surrounding grains/subgrains is formed, the associated new grain is not of a stable orientation under current shear strain, it will be transformed to a stable B/$\bar{B}$ component very quickly, which result in either a LAGB less than 15 degree or HAGB within the range of 50-60 degrees. Similarly, the extensive observation of LAGB in the interior of grains is mainly because of its stable orientation under external deformation. The LAGBs are formed either from the previous straining or as a result of the fluctuation of local deformation.

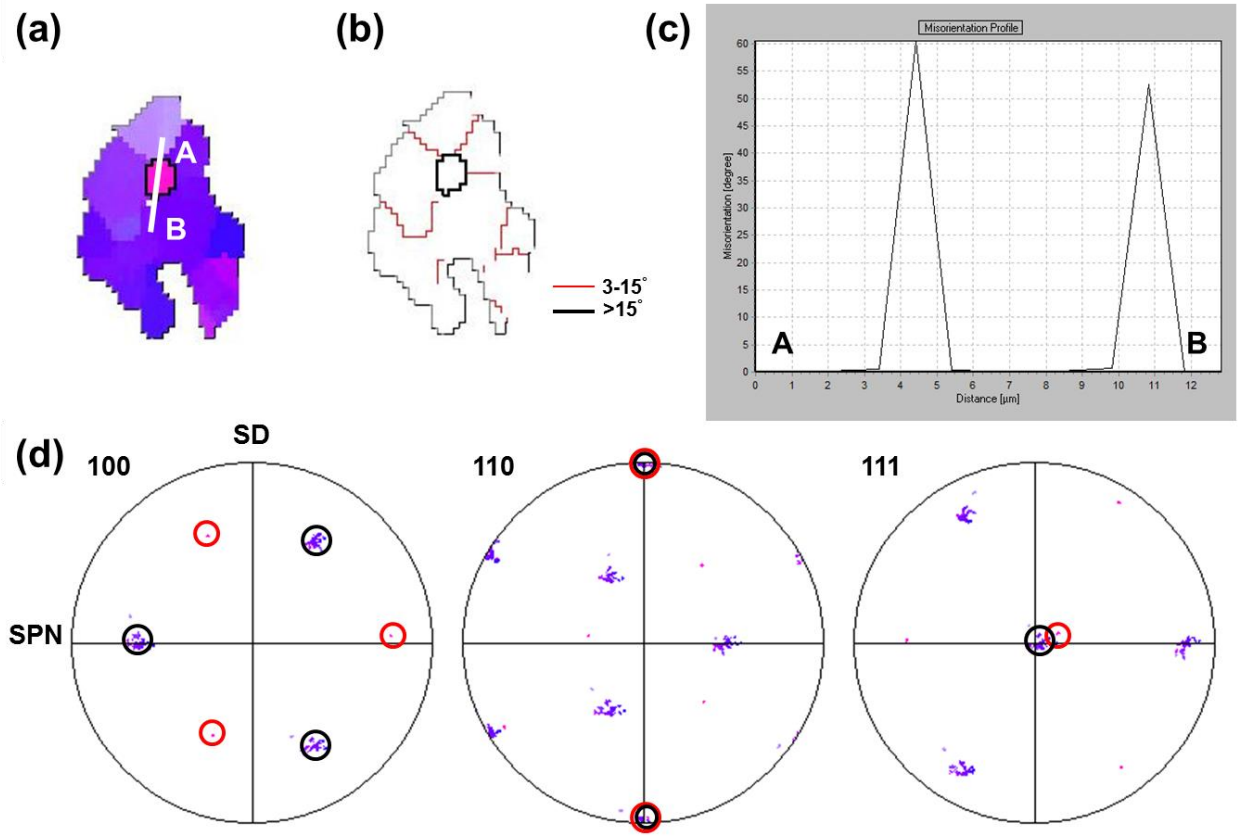

Figure 3.31 (a) IPF image (b) grain boundary distribution (c) misorientation profile along A-B and (d) orientation distribution on pole figures for a selected grain

Another example is shown in figure 3.32, similar observations regarding misorientation and texture components can be made. It is obvious that both the newly recrystallized grain and the mother grain are showing ideal <110>//SD and <112>//SPN and corresponds to the two components of ideal B/$\bar{B}$ respectively. The misorientation profile consists of two peaks showing a value of around 55 degrees. As noticed in (110) and (111) PF, the overlay circles indicate the rotation occurs predominantly around nominal 'Z' axis. However, it should be noted that even if the distribution of <110>

directions are exactly the same for two types of grains, that does not mean it is fixed during the transformation; rather, their distributions are on top of each other simply because of the symmetry of FCC lattice structure.

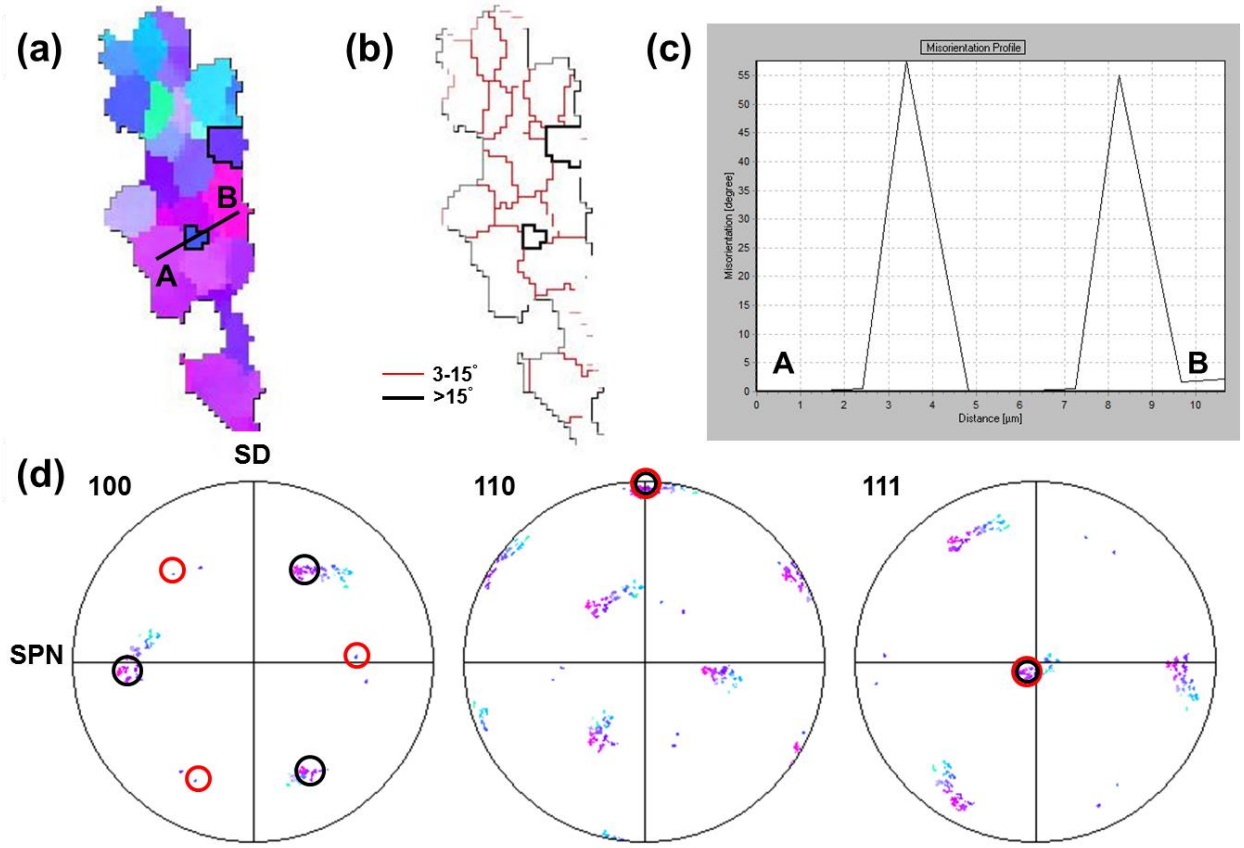

Figure 3.32 (a) IPF image (b) grain boundary distribution (c) misorientation profile along A-B and (d) orientation distribution on pole figures for an analyzed grain

One more example with two recrystallized grain formed inside a mother grain is illustrated in figure 3.33. It seems that this type of recrystallization site is not uncommon under current processing condition, even more than one grains can be formed within the interior of the mother grain. With this case, two recrystallized grains are formed at two

different sites that located at the junction of four subgrains, as shown in figure 3.33a-b. Misorientation profiles along A-B and A'-B' across both grains are illustrated in figure 3.33c, high misorientations angles of 55-60 degrees are observed for the larger grain while a slightly lower value of 40-50 degree is noticed for the smaller grain. In the PF analysis shown in figure 3.33d, the red circles are used to identify the orientation distribution of larger recrystallized grain on the PFs, while the light blue circles indicate those for the smaller grain. It is obvious that the smaller grain associated with A'-B' profile is actually a little bit away from the ideal orientation associated with stable shear components. Thus, when combining these observations with previous discussions regarding the possible mechanisms that are responsible for the formation of grains exhibiting such high misorientations with respect to their parent grains, it can be inferred that these grain are originated from a specific subgrain or part of an existing subgrain that tends to develop HAGB with relatively high misorientation, for example near junctions of several subgrains; the developed HAGBs are not stable since the associated grains are not showing stable orientations under shear deformation. Then these unstable grains tend to be transformed to ideal B or $\bar{B}$ components by lattice rotations, leaving the initially generated HAGBs near the recrystallized grain hard to be identified. From a logical point of view, the projected unstable grains initially formed at subgrain junctions can be either transformed to the orientation similar to its mother grain or to its alternative, depending on the grain orientation and local deformation geometry. Thus for those tend to transformed to its mother grains' orientation, it will be simply identified as subgrains, similar to other subgrains. Those grains that are evolving into the alternative orientation,

like in the case of the smaller recrystallized grain shown in figure 3.33a, can be captured, and serve as the evidence for the proposed mechanism responsible for the formation of recrystallized grains.

The major findings and discussions regarding the second mechanism can be summarized as:

1, grains recrystallized in the interiors of existing grains are observed, this is a new mechanism that haven't been reported in the microstructural evolution of FSW/FSP of aluminum alloys.

2, these grains are always nucleated at the junctions of three or more subgrains that are separated by LAGBs.

3, misorientations between this type of grains and their mother grains are always of very high angles, around 50-60 degrees.

4, interestingly the newly recrystallized grains are always oriented according to one of the B or $\overline{\mathrm{B}}$ shear component, while their mother grains are characterized by its equivalents.

5, it is unlikely that DDRX is responsible for the formation of such recrystallized grains for several reasons; it seems like lattice rotation is still controlling the formation of such grains. However, in this case, the lattice rotation might occur fast and the newly formed grains are reoriented to a stable orientation very quickly under intense shear deformation.

6, the formation of recrystallized grain in the grain interiors should be playing a more important role than the grain subdivision at GBs in determining the final microstructure and texture of the PZ.

7, our contribution: new mechanism is proposed and preliminary explanation and discussion are performed; however further analysis via advance technique and more systematic and comprehensive discussion is still needed.

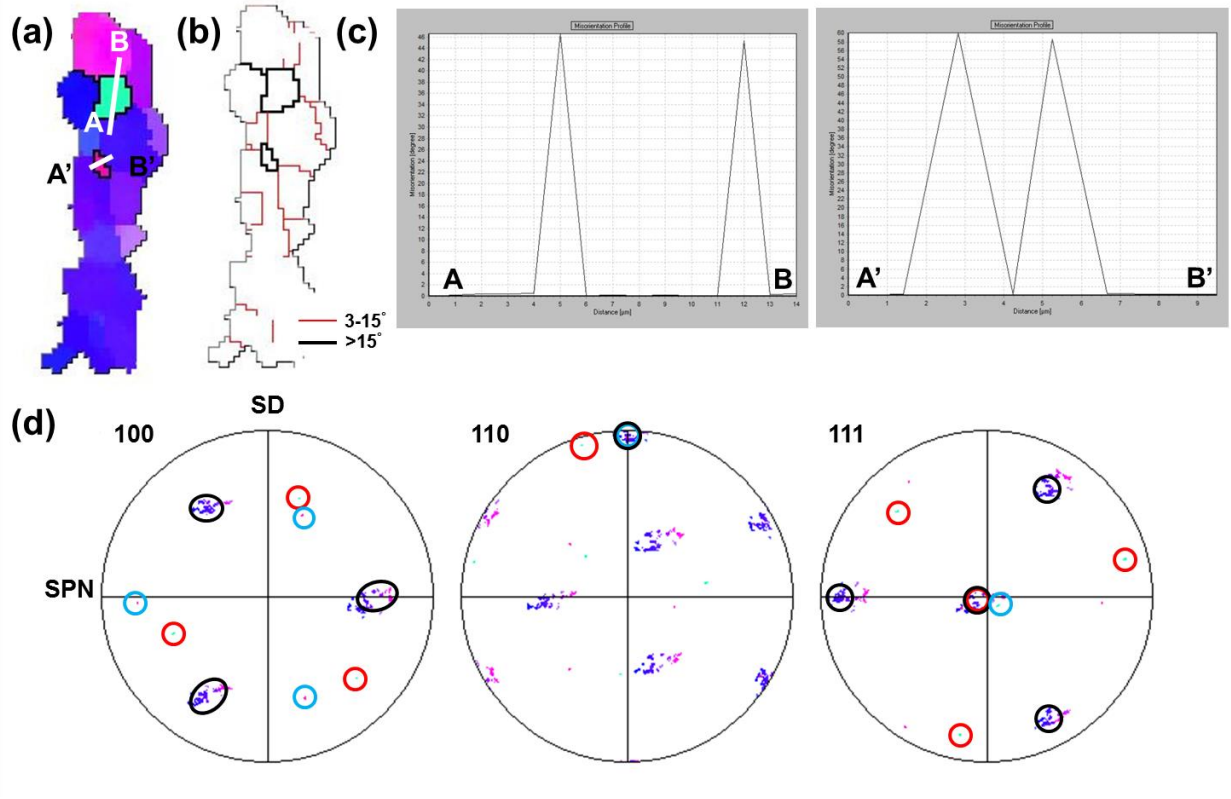

Figure 3.33 (a) IPF image (b) grain boundary distribution (c) misorientation profile along A-B, A'-B' and (d) orientation distribution on pole figures for a selected grain

Mechanism 3: grain subdivision and progressive subgrain rotation.

This mechanism is the one that is widely reported in literatures and believed to be the dominating mechanism responsible for the recrystallization and texture formation of FSW/FSP processed aluminum alloys[11, 42, 43, 52]. It involves the grain subdivision under deformation and progressive subgrain rotations across initial grains. It should be noted that the only difference between this mechanism and the first mechanism is grain subdivision happens across the entire grains rather than localized at grain boundaries, as illustrated in figure 3.34. They are treated as different mechanism simply because the previous one doesn't necessary generate grains exhibiting shear type textures, while the later mechanism is always associated to the stable $B/\bar{B}$ texture as in the present case. Detailed analysis regarding this mechanism has already been performed in the analysis of grain structure near the transition. Thus, for the time being, only new observations and some difference will be address briefly. As shown in figure 3.34, a relatively large grain showing ideal shear-related orientation within the PZ is analyzed. Based on the existing scientific reports, grains formed within the stir zone are typically characterized by equiaxed morphology. However, in our case, highly subdivided large grains with elongated or complex morphology are observed in the PZ of tube bottom, where refined equiaxed grains are expected. It is strange but also interesting, the most straightforward reason for this phenomenon might be insufficient plastic deformation compared to the case of FSW/FSP, resulting in the partially refined microstructure. Another possible explanation is also proposed according to the corresponding grain refinement mechanism as well texture development. It is obvious that the grain shown in figure 3.34 shows an

orientation corresponding to the ideal B texture, indicating it is of a very stable orientation under external strain. Extensive subgrains/LAGB formation in the grain interiors and the orientation spread because of variation/fluctuation of local straining conditions are noticed from the corresponding PFs, suggesting this grain is still undergoing subdivision and orientation change; however, since the entire grain is of a stable orientation, it is less likely a high angle grain boundary is formed and become a new grain. As elaborated in the second mechanism, if a local HAGB is formed by progressive lattice rotation, it will either be transformed to another stable grain orientation that is alternative to its mother grain, resulting in a very high misorientation angle of around 50-60 degrees, or it is less stable and tends to form a subgrain during later deformation (the possibility of this reverse procedure need to be further clarified). Additionally, grain structure evolution and orientation change should be fast under such high levels of strain and strain rate underneath the processing tool, which seems to be contradictory to the existence of large and distorted grains that consists of extensive subgrains. Based on all these observations, we believe orientation pinning might be playing a crucial role, which refers to the fact that certain grains have already develop stable orientations can be resistance to further subdividing thus the development of HAGBs, despite of the fact that the existing grain is still of a large dimension and contains extensive LAGBs.

Another larger grain that contains extensive LAGBs as well as newly formed grains in its interiors is illustrated in figure 3.35. LAGBs within misorientation range of 3-15 degrees are shown by red lines, black lines are used to identify the HAGBs showing

misorientations of 15-50 degrees; finally, thick blues lines are used to highlight those boundaries exhibiting misorientation level higher than 50 degrees. Several notable observations can be made based on results illustrated in figure 3.35. First, the entire grain is surrounded mainly by those boundaries with very high misorientation angles of more than 50 degrees, as indicated by the blue lines. Additionally, grain orientation analysis shows that this grain belongs to one component of $\bar{B}/B$ while most of its neighboring grains are oriented following the corresponding alternative equivalents, which is also in very good agreement with our previous discussions about the relationship between texture components and grain boundaries with high misorientation angles of 50-60 degrees. Similar analysis was carried out on around 15 such grains and similar trends have been suggested. Thus is it concluded that grains showing one stable shear component are typically surround by grains exhibiting the alternative orientation of the ideal shear texture.

Second, orientation pinning is also noticed as in the case of previous grain since extensive LAGBs with misorientation angle less than 15 degrees are noticed from figure 3.35b. However, in this case, some LAGBs have already been transformed into HAGBs with misorientation angles between 15-50 degrees by progressive lattice rotation, as shown in figure 3.35b. In reality, most of the black lines are turned out to be at the lower end of around 15-25 degrees. It is believed that orientation pinning is playing a strong effect on the formation of new grains from a larger mother grain that is stable from a crystallographic perspective; while some HAGBs can still be formed with misorientation angles at the lower end, which might be attributed to the variation of local deformation

geometries as well as local dislocation build-ups. These observations also substantiate our previous assumption that grain boundaries with intermediate misorientation are hardly noticed due to orientation pinning and their stability under intense shear deformation.

Third, newly recrystallized grains are formed in the interiors of the existing grain via the second mechanism, as reported and discussed earlier, showing HAGBs of more than 50 degrees and corresponding orientations. However, two distinct feathers are noticed in the present analysis in addition to the previous discussions. As shown in figure 3.35a, these grains are marked as No.1, corresponding GB are highlighted by the thick blue lines in the GB analysis of figure 3.35b. It seems that these grains can be further subdivided under deformation and even generate grains with HAGBs of around 15-20 degrees. This suggest the fact that grains formed in the interiors of initial grain are stable and have the potential of being further subdivided under deformation and produce new grains. However, it should be emphasized that this phenomenon is only observed in the newly recrystallized grains having larger grain size. Also, it turned out that some new evidence, even if it is not very strong, supporting the notion that mechanism 2 is related to lattice rotation rather than DDRX is noticed. As marked by the green arrow, the GB of grain group 1 that is formed via mechanism 2, is partially characterized by a boundary of lower misorientation angle, which is determined to be around 45 degrees in this case, even if the majority part of the GB is of high misorientation angle. This would further support the fact that these grains are formed by lattice rotation, grain reorientation is transient and hard to be captured. Finally, some grains separated by HAGB of around 15-20 degrees are also formed via continuous rotation, as marked by No.2 in figure 3.35a.

The orientation analysis of these grains shows that they are very close to the ideal orientation of stable shear component, just barely within typical deviation of standard orientation that can be defined as a specific texture, as shown by the black marks of figure 3.35a. It is obvious from the plotted PFs that the orientation of the initial grain is scattered mainly around <110>//SD due to grain subdivision and change of local deformation geometry. Grain group 2 happen to be located at one end of the scatterings thus the HAGBs can be formed. However, their stability under additional deformation is not clear.

A critical reasoning regarding the relationship between grain refinement and reorientation can be proposed as follows. It is believed that on one hand, the initial grains showing <100> fiber textures inherently tend to reorient themselves toward the ideal location of shear texture under shear strain. On another hand, grain subdivision occurs mainly because of variations of local deformation conditions, thus different slip systems are activated, resulting in orientation spread across the initial grain and generation of LAGBs as well as subgrains. These two aspects can be treated as being closely related, however, it is unwise to claim that grain reorientation depends on subdivision and grain refinement, even if it might be true that grain subdivision can facilitate the textural evolution process. In another word, grain refinement is mainly a result of inhomogeneous deformation whereas texture evolution is controlled by the type and geometries of macroscopic deformation. The recrystallization is mainly connected to the grain refinement and in some cases might provide indications to the texture change. They can be connected to some extent but seems to be more of independent processes. In our case,

the grains of AA6063 alloy have a very strong tendency of transforming to shear type texture, as shown in the analysis performed near transition region. Under moderate levels of strain, texture changes from distorted fiber texture to transitional types then reaches stable component in a very short distance when the strain level is increased near the transition region. It occurs either by lattice rotation of the entire big grain as a whole or the reorientation of the assembly of small subgrains. Think about an extreme case, if the initial material consists of refined grains that are showing similar size to the achievable subgrain size under the strain rate level of the PZ. The grain subdivision might be minimal while the final texture of stable shear type will most likely be observed. Additionally, further grain subdivision is inhibited by the stable orientation of the mother grain, even if it can be very large in size, which should be not expected due to high shear strain level in this case. Thus it is believed that orientation pinning is dominating the grain refinement process once stable texture is formed under such situations. Some literature cited grain subdivision and progressive lattice rotation that is typical for CDRX as the evidence or support for the formation of ideal shear texture. Based on the knowledge and findings of the present dissertation, grain subdivision and lattice rotation is a necessary factor for the formation of ideal shear texture rather than a sufficient one. In later cases of AA7075 alloys, the formation of ideal shear type texture is not observed due to its sluggish reaction to external shear even if extensive grain subdivision and LAGBs formation are observed across the grains.

Additional information regarding grain subdivision and formation of HAGBs in a relatively large grain is shown in figure 3.36. It is observed that five grains defined by

HAGBs are formed near the subgrain junctions following mechanism 2. The corresponding orientation distributions are also shown in the PFs of figure 3.36c. It is confirmed that these grains are also showing stable B/$\bar{B}$ components even if they are still of small dimensions. It is also note from the boundary mapping shown in figure 3.36b that the entire grain is mainly defined by grain boundaries of more than 50 degrees misorientations, while those HAGBs formed within the grain is either of high end or low end of the HAGB definition. Interestingly, some GBs with intermediate misorientation of as low as 35 degrees are observed, as highlighted by the three arrows in figure 3.36b. They are also part of the small grains formed near the junction of subgrains. That means, grain boundaries with intermediate misorientation levels can be formed during the formation of such grains that are finally identified as exhibiting equivalent alternative orientation with respect to their mother grains

To summarize the mechanism 3, several key points are noted:

1, Grain subdivision and formation of LAGBs are observed extensively within the PZ due to orientation spread resulted from inhomogeneous deformation at local scale; however, it seems like most of these subgrains are not developed into HAGBs even under high strain and strain rate near the PZ.

2, Decent amount of highly distorted large grains with grain size more than 50um showing complex shapes are observed within the PZ, they are typically characterized by grain boundaries having very high misorientation angles or 50-60 degrees. Orientation analysis shows that these grains are normally belongs to one shear component of B/$\bar{B}$ while their neighbors are characterized by the equivalent alternatives

3, Orientation pinning is proposed as the major reason for the observation of larger grains showing stable grain orientations under shear conditions rather than insufficient strain level. It is believed that extensive LAGBs within the large grains are noticed because of orientation pinning, which means the entire grain have already been transformed to an ideal B/$\bar{B}$ orientation that is believed to be stable, thus it is less likely that new HAGBs that is only of misorentations slightly higher than 15 degrees criterions can be formed since it will most likely be associated to a unstable orientation, unless GBs of 55-60 degrees are formed as proposed by mechanism 2, which is not universally indicated base on our EBSD analysis.

4, Some HAGBs are also observed within the larger grains; however, most of them are showing misorientation levels of 15-20 degrees. Based on the PF analysis, theses grains barely cross the 15degree threshold that can be defined as HAGBs and they are still within the normal deviation level of 15 degrees for standard ideal texture. However, their stability under additional straining is unknown. They might continue reorienting themselves to a higher misorientation levels, which is actually hard because the resulting grain will be of an unstable orientation under such deformation geometries. Also, these grains with HAGB of 15-20 degrees might evolve back to LAGBs, becoming subgrains. Even if no relevant evidence is shown to support this mechanism, it is highly possible from a perspective of grain orientation stability and the possibility of dislocation annihilation if inverse lattice rotation is applied at high temperatures.

5, Evidence that is supporting the lattice rotation nature of mechanism 2 is also noticed, it is of a fast transition process and hard to be captured.

6, Critical discussions regarding grain refining process and grain reorientation are performed. It is believed that these two processes are not really strictly related. Grain subdivision might be able to facilitate the texture development. It is not necessary for the grain reorientation. The capacity of reorienting and transforming to shear type texture under straining might be inherent to a specific material, which is related to the alloy content.

7, Contribution: the splitting of B/$\bar{B}$ has not been analyzed in detail in a grain structure level, especially associated to recrystallization mechanism, based on existing literatures. Classic theory regarding the splitting of B/$\bar{B}$ component is simply described as splitting under high strain levels [45, 47] without microstructure support. In our analysis, it is observed that the splitting can follow two pathways. First, during the initial formation of stable shear texture near the transition regions, grains tend to be reoriented based on its initial orientation and local deformation conditions. Thus some grains, or more precisely some part of these grains, are transformed to B component while others evolved into $\bar{B}$, as detailed in the texture analysis part and also in a previous grain structure analysis; second, with the new phenomenon recrystallization mechanism 2 noticed in the PZ, alternative texture type can also be formed within the grain via this mechanism. This is definitely a distinctly new proposal.

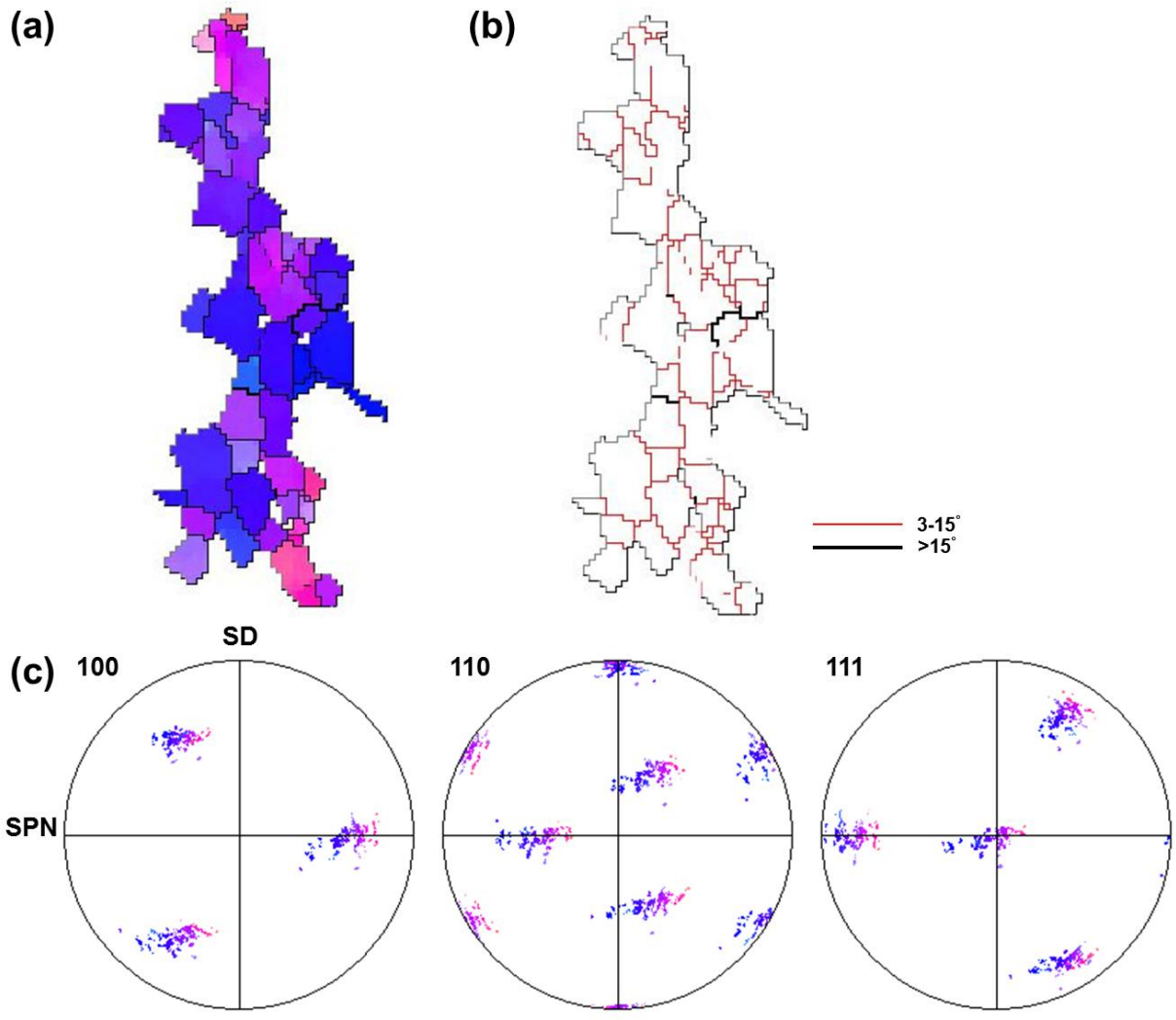

Figure 3.34 (a) IPF image (b) grain boundary distribution and (c) orientation distribution on pole figures for an analyzed grain

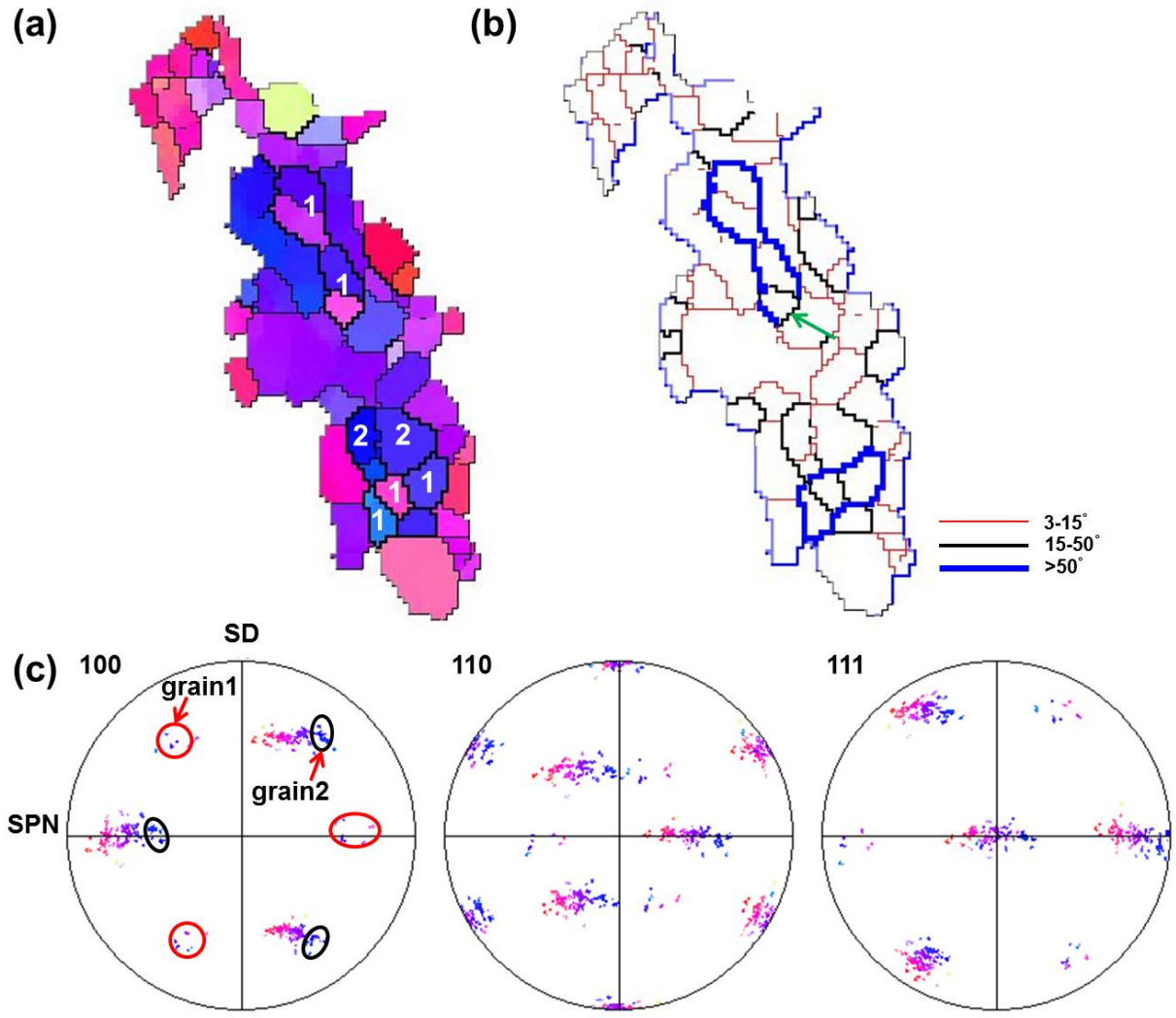

Figure 3.35 (a) IPF image (b) grain boundary distribution and (c) orientation distribution on pole figures for a selected grain

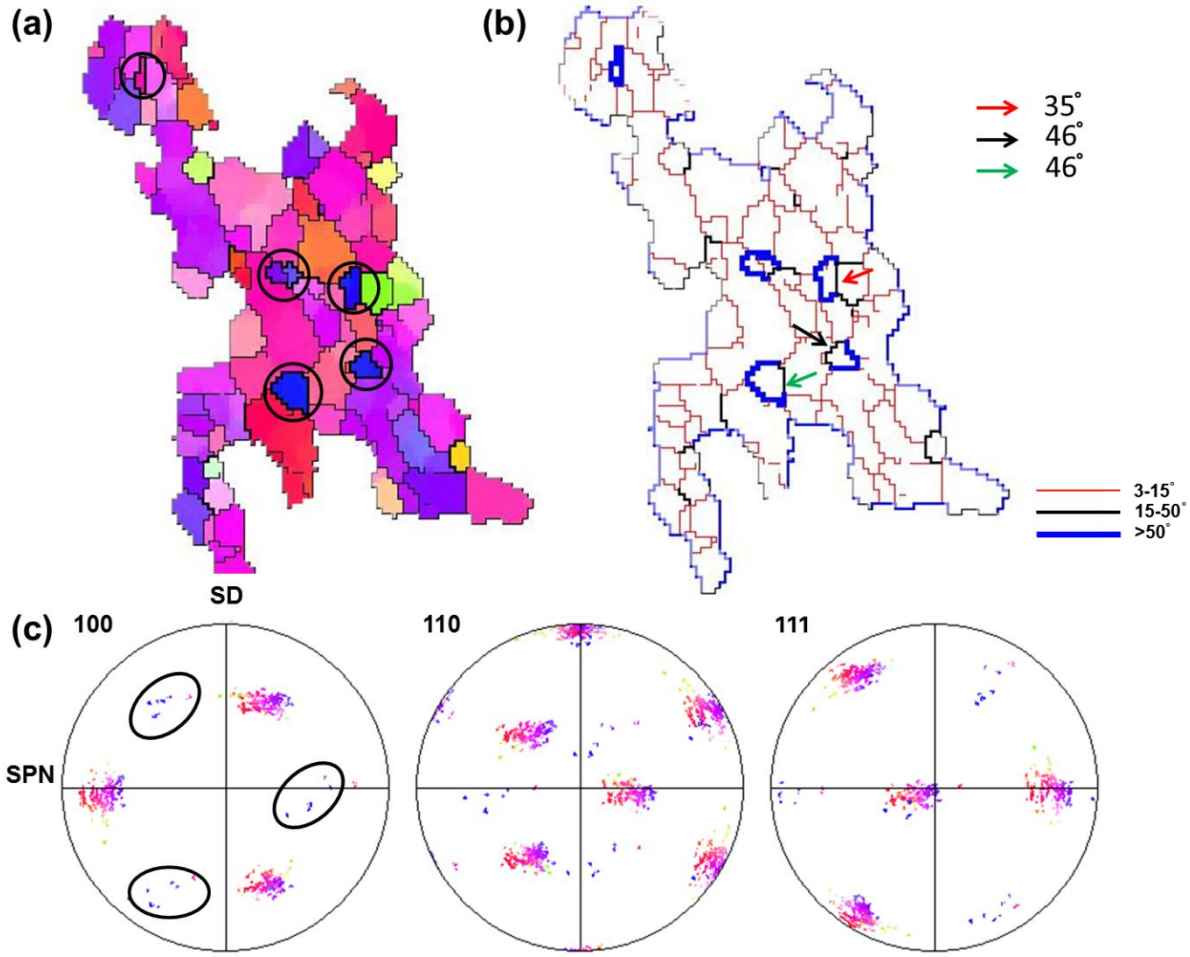

Figure 3.36 (a) IPF image (b) grain boundary distribution and (c) orientation distribution on pole figures for a grain being analyzed

Discussions regarding the microstructure near tube bottom have been performed systematically in a grain by grain fashion. However, it should also be emphasized that the tube bottom only serves as a starting point for the microstructure and micro-texture evolution during the entire FSBE process. Since materials located near tube bottom are firstly get deformed and recrystallized, then these processed materials will start to flow around the processing tool into the tube wall, during which extra thermal exposure and

plastic deformation is applied. However, it should be noted that materials near the tube bottom is under very strong simple shear; while flowing to the tube wall, the deformation geometry or shear reference frame start to change continuously, which might change the microstructure that has already reached a stable state in the previous step, for example in the tube bottom. Additionally, when flowing into the tube wall, materials are subject to lower strain rate, i.e. lower rate of dislocation generation, which might result in grain growth under additional heat exposure. At the same time, micro-texture can be weakened due to the fact that plastic flow is not as intense as that of the tube bottom; more importantly the stable and strong B/$\bar{B}$ texture formed in the tube bottom can be altered because of the deformation condition variation and thus providing opportunities for the formation of grains showing other orientation. The current draft is not intended to address every single detail of the recrystallization and grain structure evolution mechanisms across the entire tube since that will be tedious and lengthy. Thus the case of 10mm wall location will only be presented briefly to discuss the transition of LAGBs into HAGB from a very general point of view rather than via a grain by grain analysis. The microstructure and corresponding grain boundary distribution is illustrated in figure 3.37. It is roughly divided into TMAZ, transition region and PZ. It is noticed that the TMAZ consists of deformed and elongated grains with networks of LAGBs, while approaching the transition region, the amount of LAGBs is observed to increase sharply and ordered subgrain structures are formed in the elongated grain structure. Surprisingly, beyond a certain watershed, as represented by the blue dashed line in figure 3.37, the amount of LAGBs decreases significantly to a lowest level within the entire map. It is also noticed

that the grains structure on another side of the watershed characterized predominantly by HAGB and equiaxed morphologies. The transition is so sharp that the elongated grain structure consists of profuse subgrains transformed to equiaxed grains almost instantaneously. It is also noted that the grains on the equiaxed side is of similar size to the subgrains observed near the unrecrystallized side with some minor grain growth. All these evidence points to the recrystallization mechanism of continuous lattice rotation and progressive development of subgrain boundaries into HAGBs across the entire deformed grain structure, which is consistent with the prevalent consensus regarding the grain structure development in FSW/FSP processed aluminum alloys. However, the block behavior is not noticed, suggesting the fact that DRX mechanism might be different in the tube wall. Another very interesting phenomenon is the distorted initial grains showing <100> close to 'Z' axis, represented by red color is changed to the C type transitional texture that is represented by green color, once the watershed is crossed. This observation, when combined with the results about grain structure evolution and the sharp transition from LAGBs to HAGBs almost eliminate the possibility of DDRX since there is no way transitional texture is formed by DDRX. This might provide some further indications for the statement made by Suhuddin et al. [62] , the transition can be sharp if there is a sharp transition with respect to the strain and strain field, a sharp orientation change is also possible under these situations without borrowing the mechanisms that are related to the DDRX.

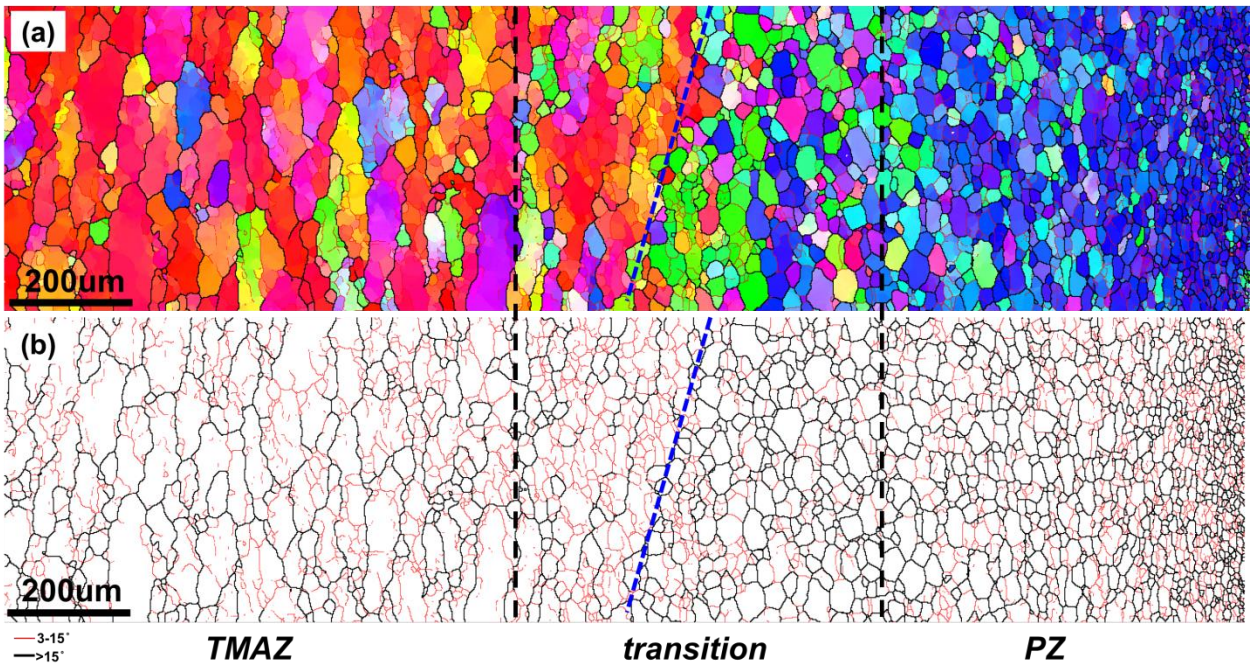

Figure 3.37 (a) IPF image (b) Grain boundary mapping of 10mm location across the tube wall

CHAPTER FOUR

MICRO-TEXTURE EVOLUTION OF AA6063-T5 ALLOY DURING FRICTION STIR BACK EXTRUSION

In the previous chapter, microstructure evolution, especially grain structure evolution and refinement mechanisms involved during FSBE have been systematically investigated at multiple locations along the processed tube, optical microscopy and EBSD scan are performed across the entire thickness of the tube wall; microstructure evolution is dominated by the deformation geometries of the process and also controlled by local temperature and straining history.

Apart from microstructure and grain structure, another important aspect that always draws extensive scientific interest is crystallographic texture, which is typically believed to be the controlling factor for plastic anisotropy. In real world industry applications, texture result from aluminum rolling is responsible for the earring formation during subsequent deep drawing process; in a lot of cases, strong basal texture in hexagonal structured alloys greatly limit the formability of the HCP alloys and render these materials significant tension-compression asymmetry; a further example involves the fact that cube/Goss type texture formation is critical to guarantee the minimal magnetic loss in silicon iron used for manufacturing transformers. Extensive research and experimental measurements have been conducted to unveil the mechanisms responsible for the formation of certain types of texture in order to build up the relationship between texture formation and processing conditions as well as the heat treatment, to help building models capable of predicting texture evolution under certain conditions. Crystallographic

texture is traditionally measured by X-ray diffraction (XRD) and represented by stereographic projections called pole figures. With the invention and commercialization of EBSD systems, it become possible to measure the texture in very small regions (from nm to mm scales) and crystallographic texture can be directly related to specific microstructural features such as grains, grain boundaries or even phases. EBSD is especially useful to measure and identify texture change in microscopically small regions that is beyond the resolution and capacities of XRD. A good example is materials with gradient crystallographic and grain structures with sub-micro dimensions. In the cases of FSW/FSP, the weld zone and TMAZ are typically of a dimension of a few millimeters depending on the shoulder and pin size, however, significant micro-texture variation has already been observed and documented in a lot of publications [43, 45, 50, 54, 62, 77] both within and across these regions by EBSD. Since the processed materials undergo severe plastic deformation and strong materials flow simultaneously during friction stir process, the final texture is predominantly controlled by the plastic flow. In previous reports [42], shear type texture is reported in both cubic and hexagonal materials, in another word, the formed texture can be reasonably interpreted by shear type textures. Additionally, the special texture formed during friction stir process can also be used as starting materials for investigating deformation behavior of grains with certain special orientations or misorientations with their neighbors. For example, Xin et al. [78] fabricated very strong initial texture in magnesium alloys via FSW with grain misorientation axis predominantly located near <0001>, upon subsequent deformation,

mechanical twins initiate inside one grain can propagate into the second grain, or even more grains.

In a word, texture evolution and investigation is extremely important and necessary from both scientific and practical perspectives. In current research, the FSBE process itself is relatively new, existing reports regarding the micro-texture of processed tube are very limited; despite the fact that the process is based on friction stir phenomenon, the materials flow and deformation geometry is different from FSW/FSP. In this chapter, micro-texture measurements will first be performed on multiple locations along the cross section of the tube via EBSD, each scan typically starts from the very end of the PZ and extend all the way to the end of TMAZ, as shown in figure 4.1. Then the micro-texture evolution regarding the texture type and forming mechanisms will be discussed based on the deformation geometries induced by FSBE. A comparative discussion will also be conducted between micro-textures formed during FSBE and ideal shear texture, a series of rigid body rotations will also be performed on measured texture data to match the ideal shear texture type, revealing the shear reference frame deviation from ideal situations, which can further enhance the understating of deformation geometry and materials flow of the FSBE process. Also, a simple model is proposed to explain the deviation of measured texture data from ideal shear types.

Texture Evolution at Tube Bottom

Texture in the PZ of Tube Bottom

Micro-texture in the bottom of the tube, as shown in figure 4.1 will first be analyzed since the deformation mode is relatively simple. A large EBSD scan extending from the tool-materials interface all the way to the base metal is performed, as shown in figure 4.2. Detailed micro-texture analysis will be performed on subsets taken from PZ, transition region and BM, respectively. The mechanism of texture change from initial texture to final texture type in the PZ will also be discussed.

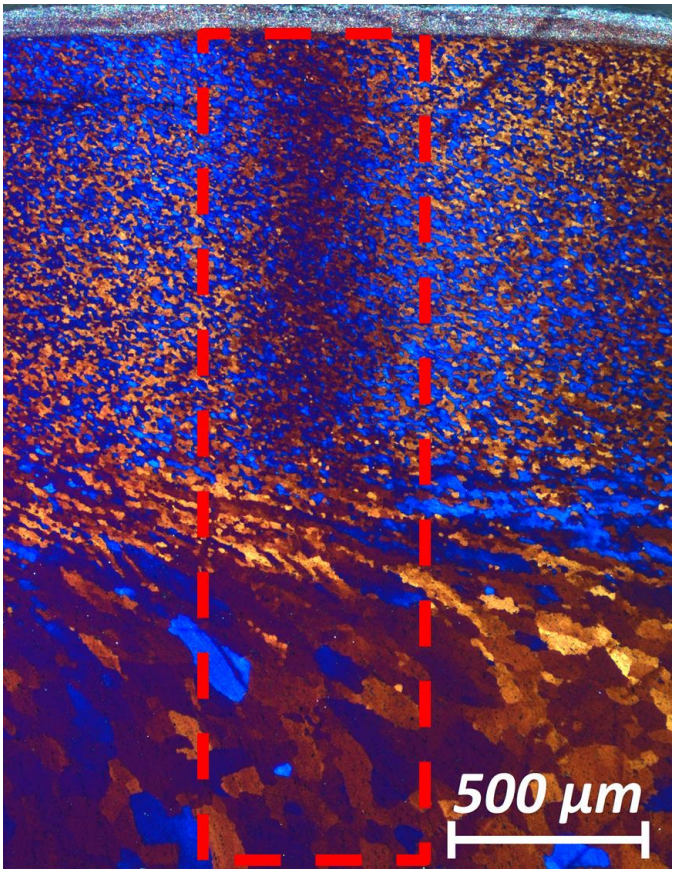

Figure 4.1 Optical micrograph of the region being analyzed at tube bottom

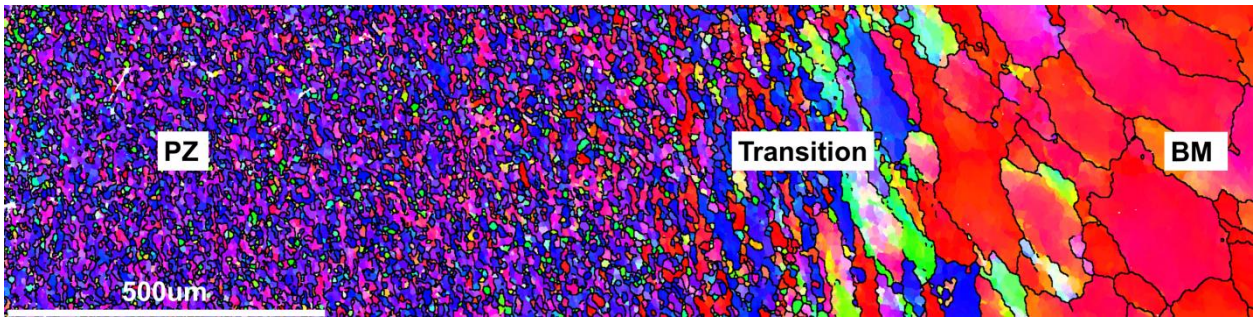

Figure 4.2 IPF image of the region to be analyzed near tube bottom

The IPF image and texture results in the PZ of tube bottom is shown in figure 4.3 with the ‘center’ indicating regions that are close to the centerline of the extrusion. This sample is divided into four parts and the texture results for each su B region are reported separately. It should be noted that pole figures of shear texture are typically represented in the reference frame of shear plane normal (SPN)-shear direction (SD) and typically this reference frame does not coincide with macroscopic specimen coordinate system, especially in the case of friction stir process where multiple deformation frameworks coexist and superimpose on each other. Under current situation, two major deformation modes coexist, the major one is severe shear deformation from the processing tool while another mode is the compression from the tool while the extrusion is performed. However, extrusion effect should be minimal in the PZ since the amount of shear deformation should be significantly higher than that of the compression. Considering the compression effect is negligible, the SPN of the PZ should always be parallel to the extrusion axis while the shear direction is tangent to the surface of the processing tool and can rotate around the tool. Depending on the region to be analyzed, the SD can be rotated up to 90 degrees. In order to show the rotation, PFs for four different regions are

only represented in the reference frame of ideal situation near the center. It can be seen that a strong B/$\bar{B}$ texture is observed in region i showing <110> // SD and <112>// SPN. Region ii-iv also show similar B/$\bar{B}$ type texture components, however it seems that for these samples, the entire pole figures are rotated to different extents, predominantly around the direction of extrusion axis, i.e. SPN. Further analysis shows that rotations of 7 degrees, 10 degrees and 17 degrees around extrusion axis are able to align the pole figures of region ii-iv to the ideal cases of i, respectively. It can be inferred that the shear reference frame is simply rotated around the extrusion direction to various extents, depending on the location of analyzed region with respect to the centerline of the tube. B/$\bar{B}$ type texture is located on the B fiber of the orientation space and originally be identified as stable shear type texture of FCC metals during torsion tests at high strain levels [33-37]. During FSW/FSP, it is also reported stable B fiber texture is observed in the PZ of aluminum alloys where materials undergoes severe plastic deformation, especially for those materials that are relatively resistant to dynamic recrystallization [40, 76]. The strong ideal texture B/$\bar{B}$ type texture measured in the tube bottom shows that shear deformation is dominant and the materials are either relatively resistant to dynamic recovery or the duration of thermos exposure is not enough for distinct static recovery/recrystallization and texture change.

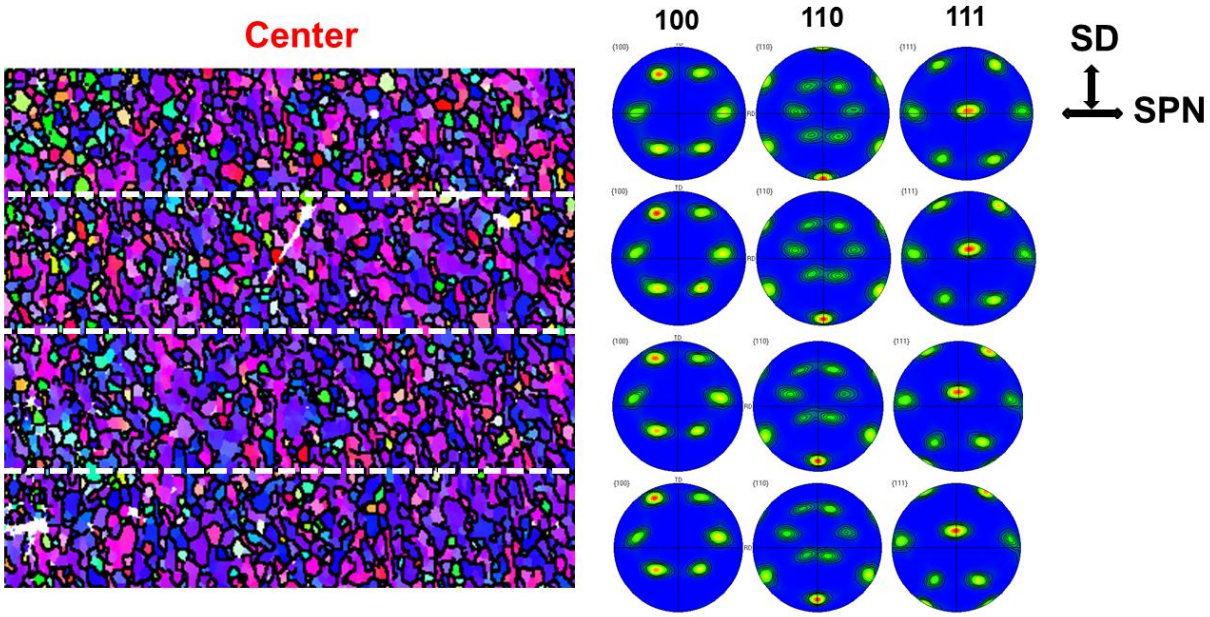

Figure 4.3 IPF image and corresponding pole figures showing the gradual texture variation

Texture Evolution in the Transition Region

EBSD measured IPF images and PFs of the transition region indicated in figure 4.1 is shown in figure 4.3. The microstructure is colored with respect to SPN in figure 4.4a based on the orientation triangular shown in the insert, and the microstructure in figure 4.4b is colored based on the orientation relationship between each pixel and the SD. That is to say any red pixels in figure 4.3a correspond to an orientation with <100> aligned close to SPN, whereas a red pixel in figure 4.3b indicated a crystallographic orientation with <100> close to SD. Similarly, the situation for <110> and <111> can be extrapolated based on this principle. From figure 4.4a, it can be seen that the microstructure predominantly consists of two major components with <100> or

<111 >directions aligned to SPN, shown by red and blue grains, respectively. However, figure 4.3b indicates a very strong component with <110> direction aligned with SD, which can also be confirmed by the pole figures in figure 4.4c, where a strong pole is observed near the SD of (110) pole figure. By scrutinizing the PFs in figure 4.4c, it can be found that the entire PFs are rotated around the strongest (110) pole located near the SD location in (110) PF, as shown in (100) and (111) PF. The distribution density of <111> direction represented in (111) PF is spread along the equator, with some relatively strong poles. The orientation distribution in (100) PF is also showing three relatively strong poles but also stretched by around 70 degrees along the SD. To summarize, the transition region is characterized by a texture type with <110>//SD, which is well known as B fiber texture observed in shear deformation of FCC metals. However, stable B/B texture components have not been observed, indicating a marginal amount of shear strain is applied in the transition region. It can also be concluded that during shear deformation, the <110> direction is first aligned to SD while texture is evolving along the B fiber to final stable components.

To further analyze the evolutional sequence and mechanisms of micro-texture formation near transition region, the red grains and blues grain in figure 4.4a are extracted into two subsets with IPF figures and corresponding PFs shown in figure 4.5. It should me mentioned that these two types of grains showing distinct texture types takes more than 80% area fraction of the entire map, left-over grains that are not showing any specific types of textures will be analyze later. As illustrated in figure 4.5a, those grains extracted from the transition region showing <100> direction parallel to SPN turn out to

be ideal C type texture, evidenced by the PFs in figure 4.5a. C type texture is believed to be a transition texture of FCC metals under moderate shear deformation, with <110>//SD and <100>//SPN. It is located on the B fiber and its appearance is confirmed by multiple investigations during shear deformation and FSW/FSP of aluminum alloys [43, 45, 71]. Generally speaking, C component is not stable and tend to be transformed to stable B/$\bar{B}$ types with <112>//SPN under further deformation. Grains belong to another component showing <111>//SPN is extracted as a new subset as shown in figure 4.5b, corresponding PFs are shown in figure 5.4d. From these PFs, it is observed that grains in this subset also show <110>//SD in a similar fashion as in the previous subset, which belongs to B fiber; however, the distribution of <111> directions is closely aligned to SPN, showing <111>//SPN and <110>//SD, which corresponds to type A shear texture [35, 37]. Type A is also a typical shear texture observed in FCC metals, the special part of A texture is it belongs to both A fiber and B fiber simultaneously. However, A type texture is rarely observed and reported in FSW/FSP of aluminum alloys [43, 52]. Based on the observations made near the transition region and PZ, it can be concluded that A type and C type texture serve as precursors to the stable B/$\bar{B}$ texture. The major mechanism involved is the <110> directions of the initial microstructure start to aligned to SD immediately under strain by grain reorientation and this process is almost finished near the transition region where the amount of shear strain is moderate; however, even if <001> and <111> directions are rotated to SPN during deformation, their nature is transitional and will be further evolved to <112>//SPN under additional shear strain. As indicated by figure 4.4 c, it seems that the entire PFs are stretched around <110>//SD and

the orientation density is distributed along the horizontal direction of the PFs, while the <110>//SD pole on (110) PF is strong and stable. This will further confirm the proposed mechanism that after reaching <110>//SD, the texture in transition region mainly evolves by rotation around <110>//SD. At this point, it is very hard to tell whether C forms first then transform to A or vice versa, or even there is any dependence between them, since no strong evidence is provided to confirm any of these possibilities. Based on previous research on FSW/FSP, it seems like C type texture is generally report as transition texture while A type is not always observed.

A bold postulation is C type forms at an earlier stage based on the fact that the initial texture type of this 6063 alloy is <100> fiber, as mentioned in the previous chapter, which means <100> direction is already aligned close to SPN in the beginning, thus it might be less resistant for grains trying to align their <110> direction to SD by rotating around the <001>//SPN that is already crystallography favorable. It is also possible that A texture is less stable under relatively lower strain level thus it is not widely observed in literature. Nevertheless, it is still unclear whether there are any direct relationships between the formation of C and A texture.

An interesting observation is it seems like two components of B start to form in transition region as shown in figure 4.4c; however, based on the location and rotation tendency of A texture, it can only transform into one component of B by rotating around SD as observed in figure 4.5d. Then the question is what is the forming mechanism for another derivative of B i.e. $\bar{B}$? Since both B components are still under transition and not fully developed, it is less possible that two equivalent components are formed by splitting

one of them that is already mature, which is typically observed under high strain [45]. Thus, it is highly possible that another component of B alternative is formed by C. As mentioned previously, a dominant transition texture component of A type has a strong tendency of transforming to only one specific B component. By observing the pole figures in figure 4.5c and figure 4.5d, it is found that if component A is transformed into B type by rotating the entire pole figures for around 20 degrees around SD in anticlockwise fashion, $\bar{B}$ texture can be formed by rotating the entire PFs of C texture by rotating around 30 degrees in a similarly anticlockwise way. If the PFs exhibiting C type are going to evolve by rotating around SD clockwise, two components of B can't be formed.

Thus, a projection is, A texture transform into B component exclusively, while $\bar{B}$ mainly come from C texture. The orientation distribution function is plotted in figure 4.6 to further analyze the texture components present in the transition region as shown in figure 4.4. It should be mentioned that orientation distribution functions (ODF) calculation is based on Gaussian estimation method, rather than typical series expansion method, because the latter method always takes sample and crystallography symmetry into account thus extra poles are generated in the ODF figure, which can complicate the identification of texture components in the present analysis. Also, least possible sample symmetry is also adopted to simplify the orientation distribution in the Euler space, enabling easy identification of texture components. Figure 4.6a and figure 4.6b show the ODF cross section at phil2=0 and phil2=45 degrees for the entire transition region shown in figure 4.4, while figure 4.6c-d and figure 4.6e-f illustrated the ODF distribution for

subset extracted near the ideal A and C types of texture, as same subset as those taken in figure 4.5. The reason why subsets are taken near the ideal orientations of A and C on PFs is trying to capture the evolution tendency of the A and C type texture. By comparing with the standard location of typical shear texture in phil2=0 and phil2=45 cross section shown in figure 4.6g, it is observed that the entire transition region is showing distinct C and A- components, A1* is also identified but very weak, which is not found in PF analysis. As shown in figure 4.6b, a strong A- component is evolving into $\bar{B}$. At the same time, it looks like C component is evolving into B and $\bar{B}$ simultaneously. Figure 4.6b-e represents the ODF distributions of the grains exhibiting orientations close to C texture, as mentioned earlier. It can be seen that C component is moving along phil=0 and phil=180 at phil2=45 cross section whereas orientation distribution at locations of (120, 54.7, 45) and (60, 54.7, 45) are not found in the phil2=45degrees section. That means the C-B/$\bar{B}$ transformation might still be under early stage of the development, the assumption that certain B component is formed by C can't be substantiated for the time being. Whereas in figure 4.6c and figure 4.6f, a strong A- type texture is observed and it is showing strong tendency of transforming exclusively into $\bar{B}$, at the same time a weak A texture is developing into B. Minor A texture is also observed transforming into weak B. Two derivatives of B components are generally believed to form under high shear strain level by splitting one specific component into two [45, 46, 52], which should not be the case here since the shear deformation in transition region is relatively low. To summarize: A- showing strong tendency of transforming into $\bar{B}$, a weak component of A

is also evolving into B while C texture seems like transforming into both B and $\bar{B}$, but it can't be verified until further analysis is performed.

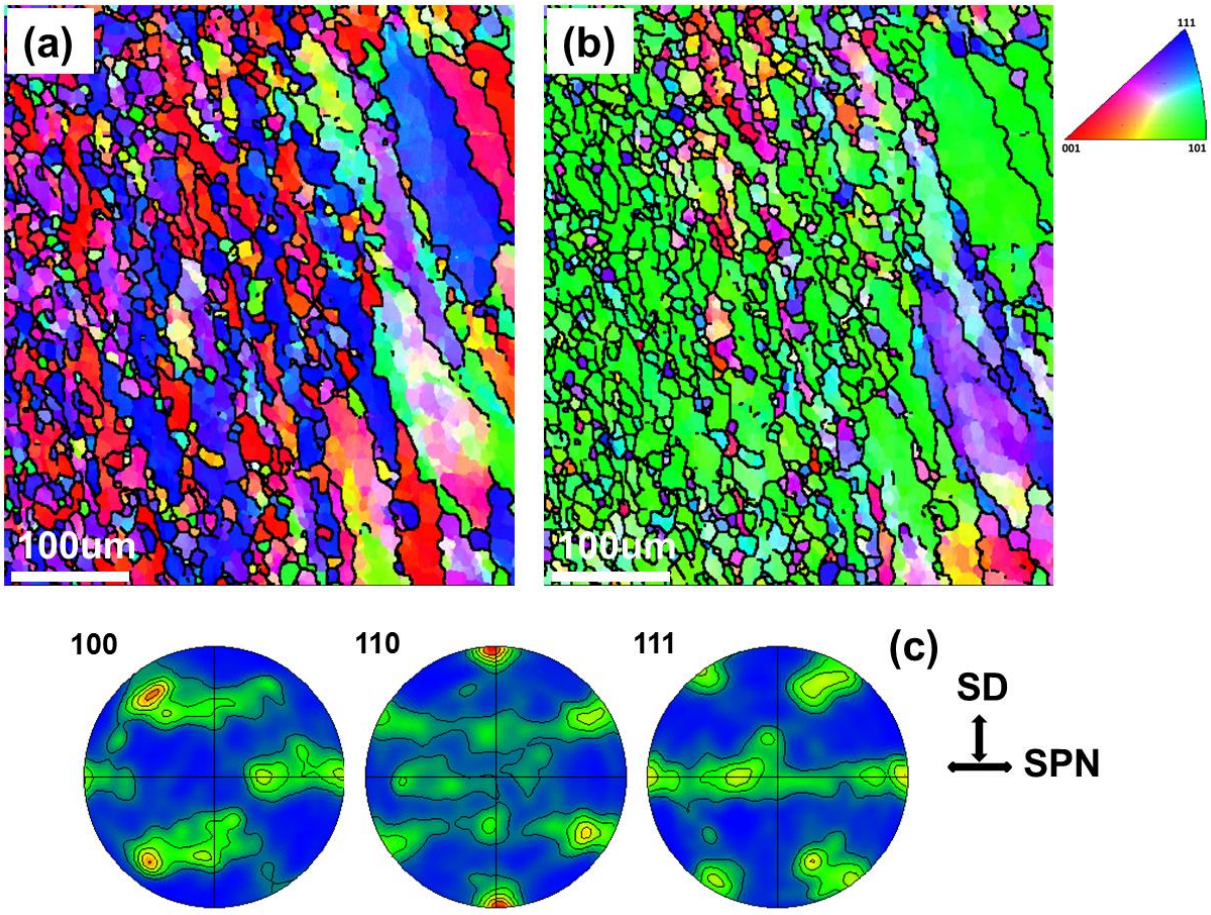

Figure 4.4 (a) (b) IPF image and (c) Pole figures of the transition region

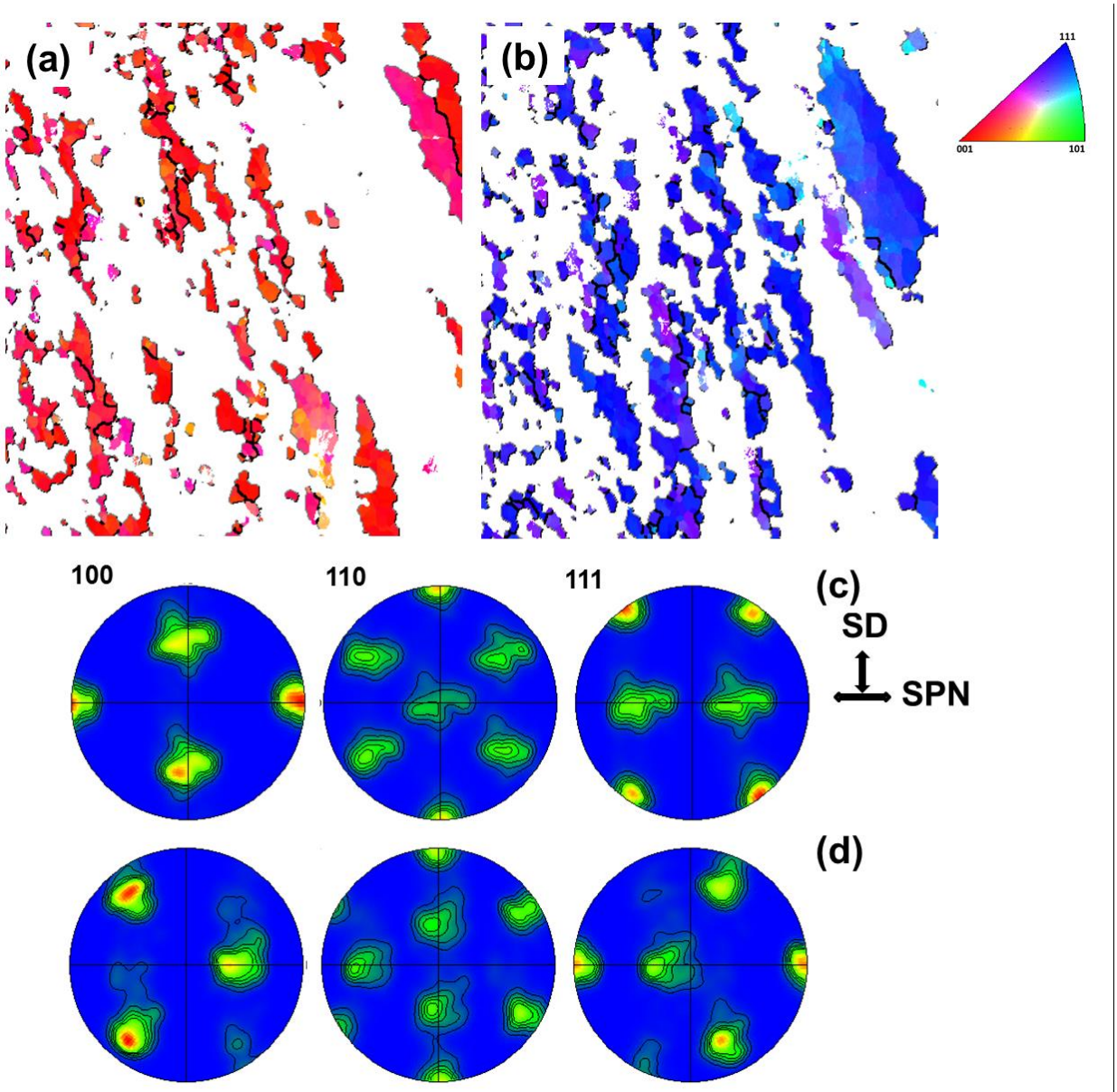

Figure 4.5 (a) (b) IPF image and (c) (d) Pole figures for the two components showing <100>//SPN and <111>//SPN

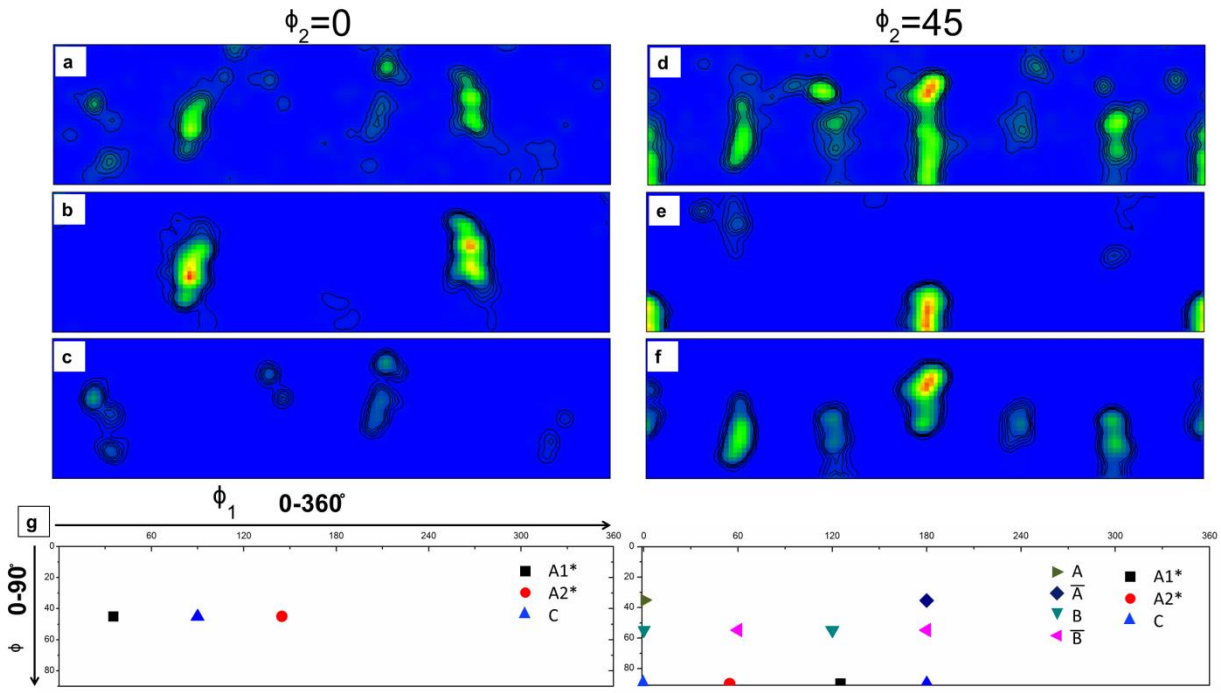

Figure 4.6 ODF figures for (a) the entire region shown in figure 4.5 (b) subset1 (c) subset 2 of figure 4.5 and (d) ideal locations of shear texture on ODF

To better understand the forming mechanism of B/ B̄ texture, a subset next to the transition region is taken on the PZ side since the development of shear texture is more mature. As shown in figure 4.7. IPF images with respect to SPN and SD are shown in figure 4.7a and figure 4.7b respectively, the PFs are also plotted in the shear reference frame of SD-SPN. It can be seen that <110> direction of the subset is predominantly aligned to SD and the texture is showing well defined B/ B̄ texture. However, two components are not aligned perfectly to <112>//SPN, indicating the texture is still transforming into B/ B̄. It should be noted that the deviation of texture observed in figure 4.7 from ideal texture should not be attributed to the rigid body rotation originating from

the locations of the analyzed samples relative to the centerline. If the sample measured is not in the center, the rigid body rotation of the PFs should be around SPN, which have already been fixed in the PFs of figure 4.7c, rather than SD.

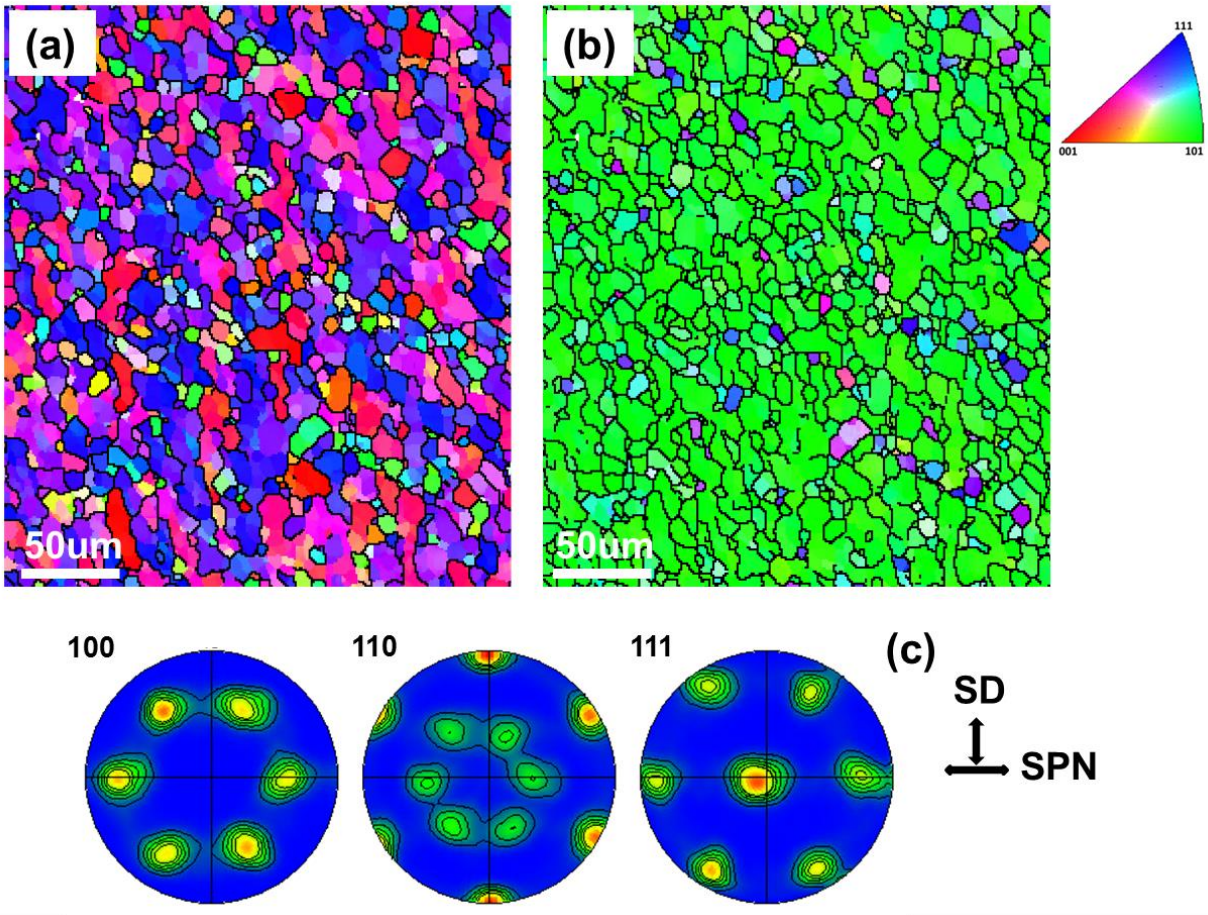

Figure 4.7 (a) (b) IPF image and (c) Pole figures of the map

To enable in depth analysis, two subsets are taken based on the scanned region shown in figure 4.7c in a similar fashion as in the transition region, by selecting those grains belongs to B and $\bar{B}$ component respectively. That is to say, grains near B and $\bar{B}$ texture components will be selected and analyzed separately to figure out their precursors during transition and the traces of texture development. It should be noted that in the

transition region, as mentioned previously, subsets are selected based on pre-mature/unstable texture components to identify their evolutional trend; whereas in this region closer to PZ, relatively mature texture components are selected and extracted separately to deduct their precedent texture types. The corresponding IPF microstructure and PFs of the two subsets are shown in figure 4.8. It should be mentioned again that the two subsets take around 95% area fraction of the entire maps thus there shouldn't be any change any noticeable texture component is ignored. It can be observed in figure 4.8a that grains related to this component is showing red color, i.e. <100>//SPN, suggesting C type texture; whereas in figure 4.8b grains are showing blue color, suggesting <111>//SPN, which is mostly likely related to A- component. Two alternatives of B are clearly demonstrated in figure 4.8c and 4.8d respectively, (111) poles are not perfectly aligned to the center of (111) PFs, indicating <112> direction is not fully aligned to the SPN, which means the texture is still under development even if the formation of stable B/$\bar{B}$ texture is almost achieved.

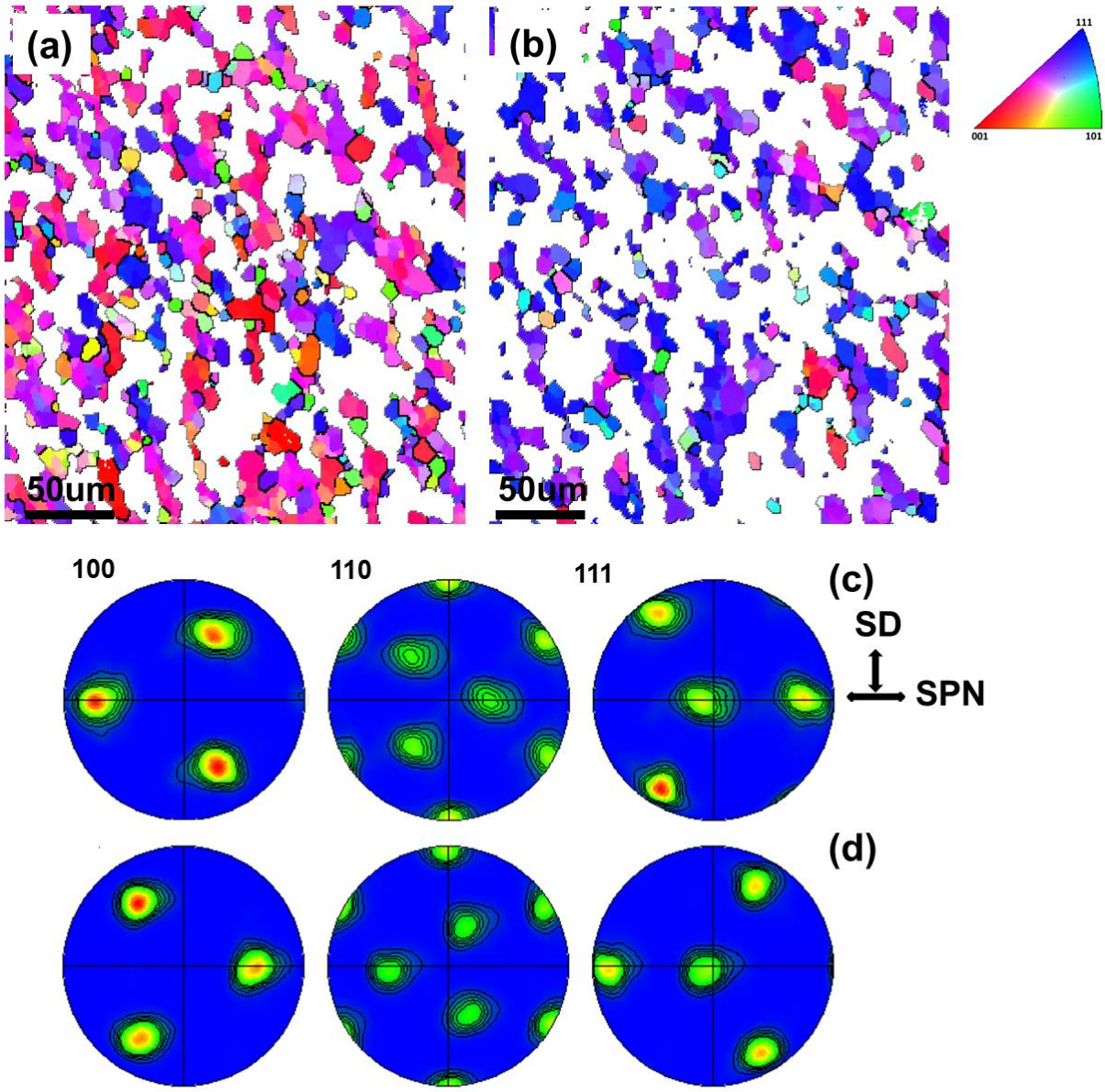

Figure 4.8 (a) (b) IPF image and (c) (d) pole figures for the two components showing <100>//SPN and <111>//SPN

ODF analysis is also performed for this subset and the result is shown in figure 4.9, figure 4.9a and figure 4.9d shows the orientation distribution of the entire region. It can be seen that C component is very weak, whereas B and $\bar{B}$ are almost fully developed.

It is observed at phil1=0 and phil1=180degrees locations in phil2=45degree cross section, $\bar{B}$ is mainly developed from the A- near phil1=180 whereas B component seems like developed mainly from C since the orientation distribution at phil1=0 is more closely located near phil=90degrees. A small tail is also observed near C-B location, which might suggest the transformation of A to B simultaneously, as observed in the ODF of transition region. The ODF results of subset containing mainly B component is shown in figure 4.9b and 4.9d. It can be seen that C component is detected at both phil2=0 and phil2=45 but relatively weak. The presence of C texture suggest that B component should be mainly developed from C, and a transition is observed near phil1=0. The observation made in the current cases is different from the subset taken near the ideal C component in the transition region, as shown in figure 4.6e, regarding C texture evolution. Previous result shows that C might evolve into both components of B/$\bar{B}$ texture at the same time, while it seems that only one component of B is related to C texture based on the present analysis. This discrepancy might be explained by the fact that C component is evolving into both types of B texture as proposed in the previous discussions. However, one component is fully developed during deformation, leaving no signs or traces showing the relationships. This postulation is further supported by the ODF figures in figure 4.9c and figure 4.9f, where C component is not observed in the subset showing mainly $\bar{B}$ texture. From fig4.9c and 4.9f, it can be seen that, the formation of $\bar{B}$ is closely related to A- texture, which matched the observation made in the transition regarding A- texture. In combination with the result in transition region, the ODF analysis in the figure 4.8 can be summarized as following: A- texture is predominantly transformed into $\bar{B}$ component; C

texture might evolve into both B and $\bar{B}$, however, only B components showing traces close to the ideal orientation of C texture, suggesting that C- $\bar{B}$ might be possible and mature earlier thus leaves no evidence of transformation; minor A and A2* component is also identified.

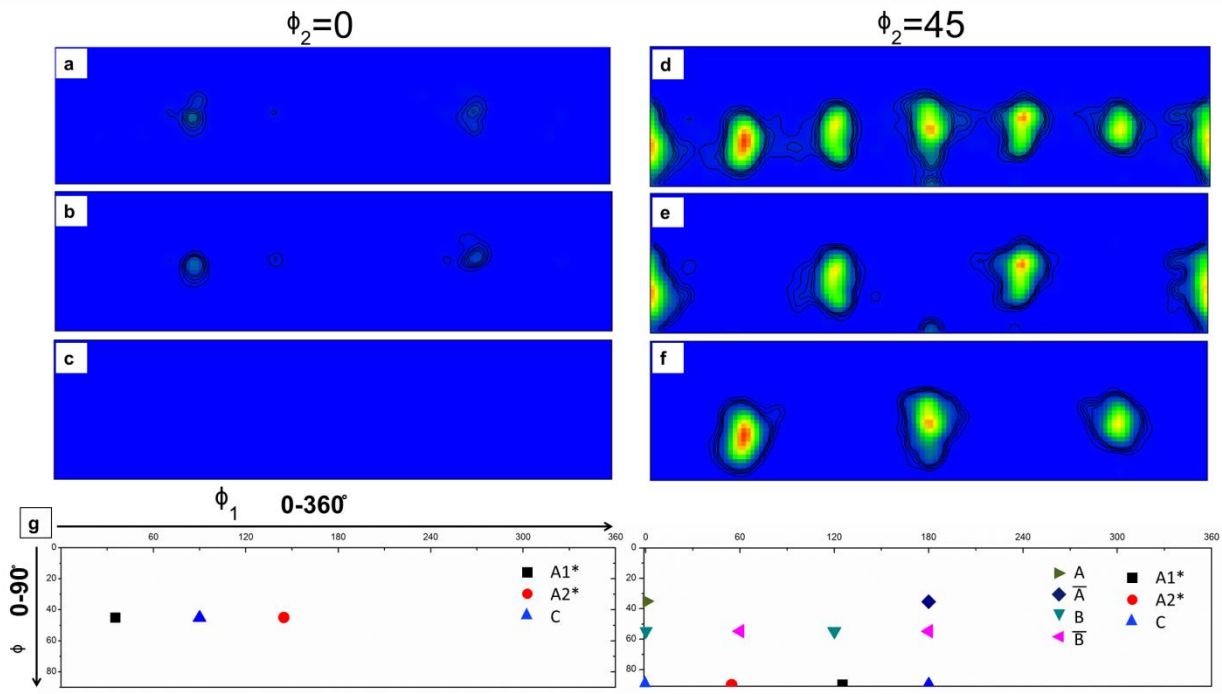

Figure 4.9 ODF figures for (a) the entire region shown in figure 4.5 (b) subset1 (c) subset 2 of figure 4.5 and (d) ideal locations of shear texture on ODF

Texture Evolution near Base Metal-Transition Region

In this section, grains structure and orientations near the interface between the base metal and transition region will be discussed in a grain by grain fashion to facilitate step-further investigations. Grain by grain analysis will enable the identification of the orientation split and grain reorientation of initial grain structure, and thus a better understanding the mechanism of texture evolution can be achieved.

The microstructure near the transition-BM interface is shown in figure 4.10, grains are labeled by number from 1 to 10 and their orientations change will be discussed separately. It should me mentioned that the IPF figure is plotted with respect to the SPN, i.e. extrusion direction and the initial texture is measured as <100> fiber texture with <100> parallel to the extrusion direction. Thus most grains close to the BM side are showing red color. Also, only grains showing distinct orientation change or split will be discussed.

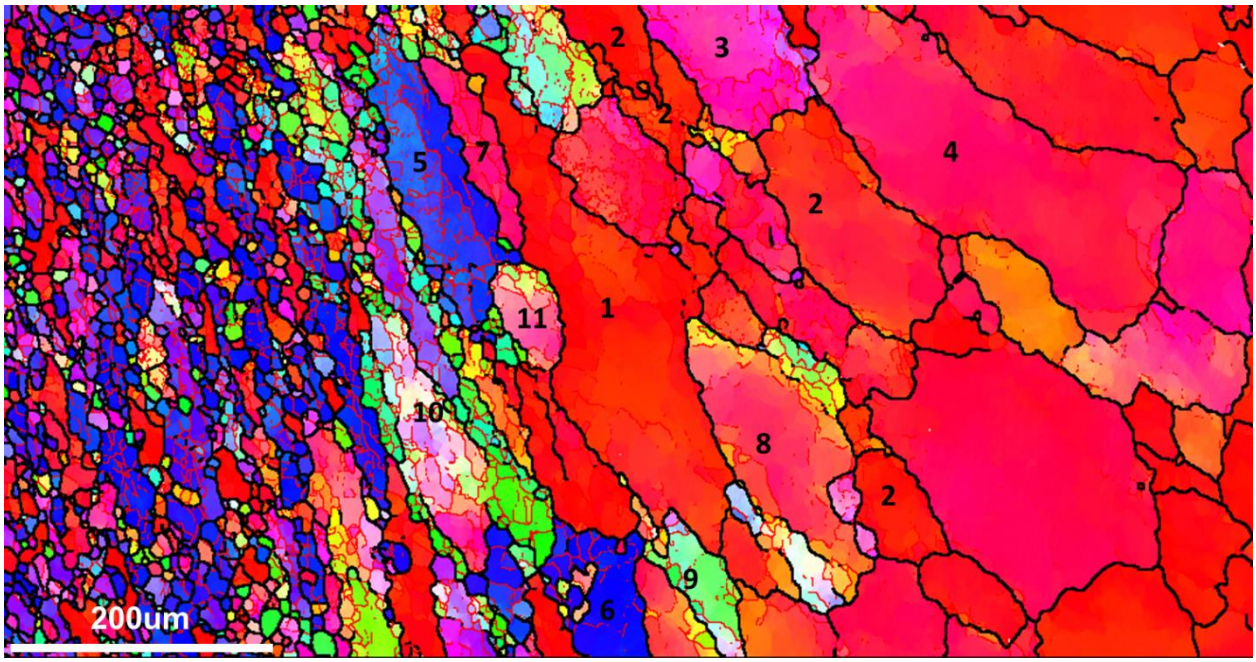

Figure 4.10 Grains to be analyzed separately

Grains labeled number 1-3 are plotted in figure 4.11 with respect to both the SPN and SD and the corresponding orientations of each pixel are plotted in PFs, based on the IPF-SD images. It can be observed in figure 4.11a that grain 1 exhibits orientation with <100> close to SPN while <110> direction is evolving toward SD, as depicted in the (110)

PF where orientation distribution is moving towards SD. It is also noted that, during the reorientation of grain 1, regions near the grain center or further away from the strain field is less deformed, thus showing orientations closer to its initial values; whereas regions closer to the strain fields or near the grain boundaries showing <110> more closely oriented to SD. As observed in the IPF images in figure 4.11a, the <100> direction of the analyzed grain is not showing significant spread whereas the distribution of <110> direction is moving toward the SD by grain splitting and reorientation, especially near the grain boundaries, where plastic strain is easily to accumulate. It can be concluded briefly that under small amount of strain, grains are aligning their <110> to SD and the <100> direction is keeping relatively constant, at least for those grains whose initial orientations are characterized by <100> close to SPN. The grains labels number 2 is not a single grain, rather, they are a group of grains showing similar behaviors as shown in figure 4.11b. These grains are not showing any significant orientation spread and reorientation with a relatively stable orientation of <110>//SD and <100>//SPN, which is the C component. It is assumed that the initial orientation of these grains are close to the C texture and experience marginal amount of shear deformation, C orientation is relatively stable at this stage. Thus no distinct grain reorientation is observed for grain2 and they are keeping their initial orientations at relatively low strain level. Grain labeled number 3 is analyzed and shown figure 4.11c, it should be noted that grain 3 is only subjected to very small amount of deformation since the grain is not distorted both geometrically and crystallographically. However, it can be seen that the <100> direction of the grain is not perfectly aligned to SPN, as shown by (100) PF, indicating the fact that the initial grain

orientation of grain 3 is deviated from <100>//SPN. By observing the regions near the grain boundaries, it seems that the <110> direction is aligning toward SD whereas no trend of <100> moving back to SPN is observed, i.e. evolving into C component, this phenomenon provides an important implication that initial grains with <100> fiber texture are not necessarily reorient into C texture first then transform to stable B/ $\bar{B}$ under extended deformation; rather, it might be possible that the grain can directly evolve into B/ $\bar{B}$. Grain 4 in figure 4.11d is showing a similar trend as in the case of grain3, but deformed to an even lower strain level. Thus it is assumed that the controlling factor is the initial grain orientation, as observed in grain 1-3; the strain compatibilities induced by the orientations and deformation behaviors of neighboring grains is also effecting the activation of slip systems thus grain reorientation; however, not enough data is provided to relate this mechanism to texture evolution in the present study. With the previous statements, a general conclusion is: grains can evolve directly into B or via transitional texture components like C depending on its initial orientation and local deformation geometry.

The analysis of grain 5-7 is shown in figure4.12. It can be observed that grain 5 and grain 6 are exhibiting similar behaviors with their <110> parallel to SD and <111> aligned to SPN, matching the A- texture. Grain 5 and grain 6 are further deformed and elongated compared to the previous analyzed grain 1-4, especially grain 6. However, the clear transition from initial fiber orientation to A- and the subsequent evolution into $\bar{B}$ is not captured at the grain level. It is believed that grains with initial fiber texture will align their <110> directions to SPN under deformation and the reorientation of crystallography

plane to SPN is of lower priority, thus the transformation into <110>//SD will be performed on the path that will show least resistance, leaving some grains first goes to A type texture rather than directly transforming into stable B/ $\bar{B}$. That is to say, grains with different initial orientations might involve into B/ $\bar{B}$ texture on different routes because of disparate resistance. Grain 7 shows <110>//SD while no specific crystallography direction is demonstrated to be related to SPN, however, it is believed that this grain is under transition from C orientation to B by rotating around the <110>//SPN direction, which can match our previous PF and ODF analysis very well. Another piece of evidence is that grain 7 is next to grain1, who is showing splitting and reorientation tendency toward C texture, on the side that is under higher strain level; thus it is highly possible that grain 7 and grain 1 used to share the same matrix, grain 1 is orientating towards C locations under strain while grain 7 is further deformed and become an individual grain, and at the same time start to transform to B orientation. Also no direct evidence showing the formation of grain 7 is provided since a new grain can be formed readily near the transition region, even if by grain split and reorientations rather than nucleation and grain growth, and leaves no information about its previous orientation and from which matrix it come from.

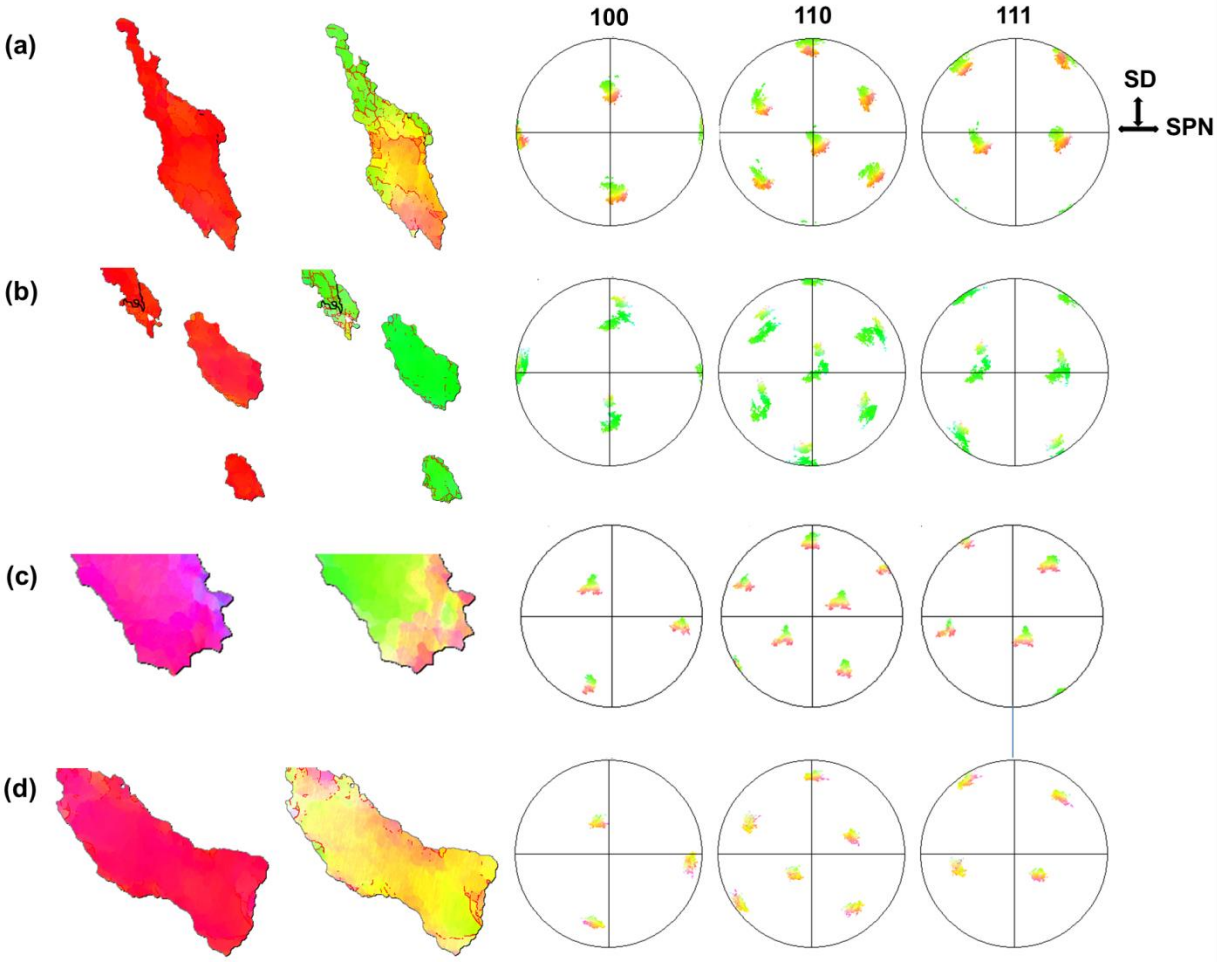

Figure 4.11 IPF images and relevant pole figures for different grains to be analyzed

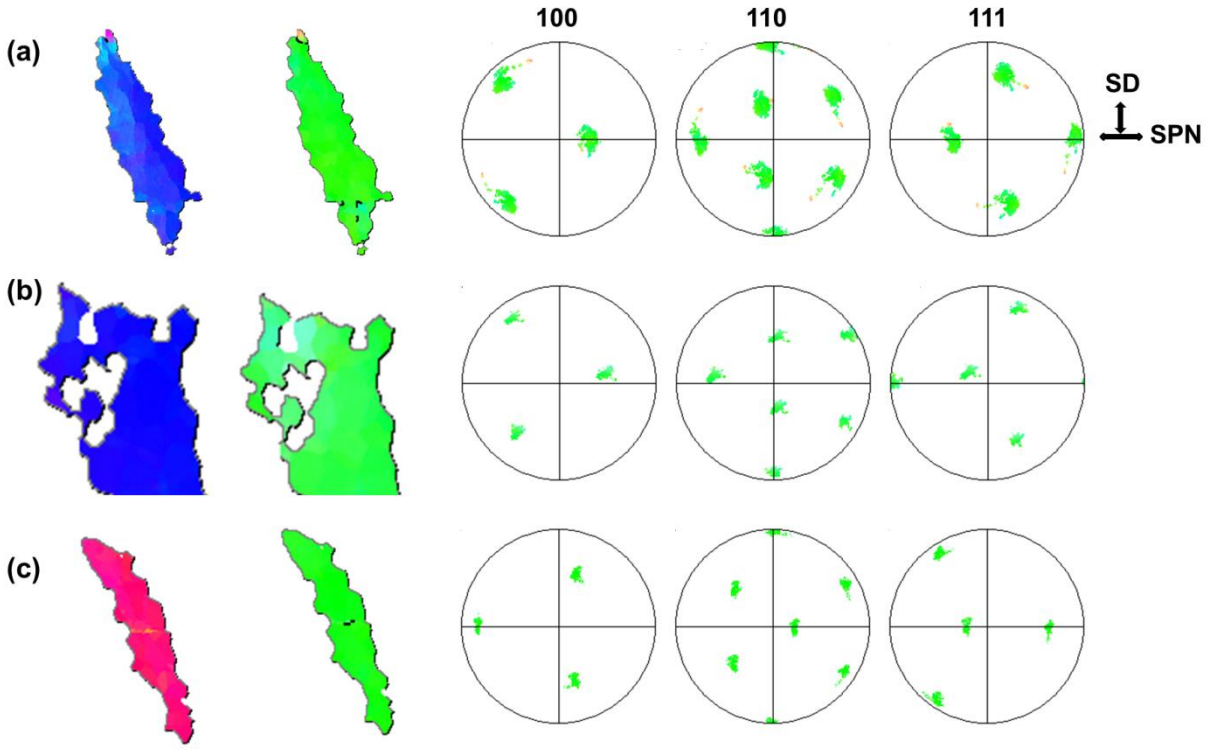

Figure 4.12 IPF images and relevant pole figures for a group of grains to be analyzed

Orientation and grain structure analysis are also performed on grains numbered 8-11, as shown in figure 4.13. The PFs in this figure are plotted and colored based on the pixel's orientational relationship to SPN. It is observed that these grains are aligning their <110> direction parallel to SPN and surprisingly the <110> direction is not rotated to the SPN even if moderate deformation is expected, as confirmed by the LAGB inside these grains. This trend can be observed clearly and especially in figure 4.13a and figure 4.13c for grain 8 and 10, as indicated by the red arrow, highly deformed region of these grains are aligning their <110> directions to SPN, whereas it seems that <111> is moving to SD. Thus a weird transitional texture component with assumed orientation of <110>//SPN and <111>//SD is expected. By comparing with ideal shear texture types in the literature

[35, 37], it is called E or E- texture, however, not too much information regarding this type has been reported in the literature. In the previous texture analysis performed in the transition region and PZ, this component is not identified, thus it is believed that this component should be transient by nature and immediately transform to other components under deformation. The forming mechanism of E component is unclear since no relevant reports have been found and the local deformation field might be the major reason for its appearance.

To summarize the grain orientation analysis in this session, several key observations can be demonstrated:

1, most grains showing <001> aligned to SPN before deformation due to the initial <001> fiber texture. Alignment of <110> direction to SD is of highest priority.

3, during the transition of <110>//SD, either <100> stay at the SPN or <111> can be rotated to SD, forming C or A type texture as transitional texture.

4, in some grains with initial orientation or deformation field that shows greater resistance to the formation of C or A, a directly transition of corresponding <112> to SPN while <110> is rotated to SD can be expected.

5, E type texture is also observed and this component is not found in the previous analysis, or in most relevant peer reviewed papers.

6, several possible texture evolution routes are proposed as: fiber to C to B, fiber to A to B, fiber to E to B, the dominant factor that can affect the exact route a certain grain will follow involves its initial grain orientation and local deformation field.

7, grain by grain analysis performed in this part matched the previous PF and ODF analysis regarding the texture evolution very well except that E component is not found in previous discussions.

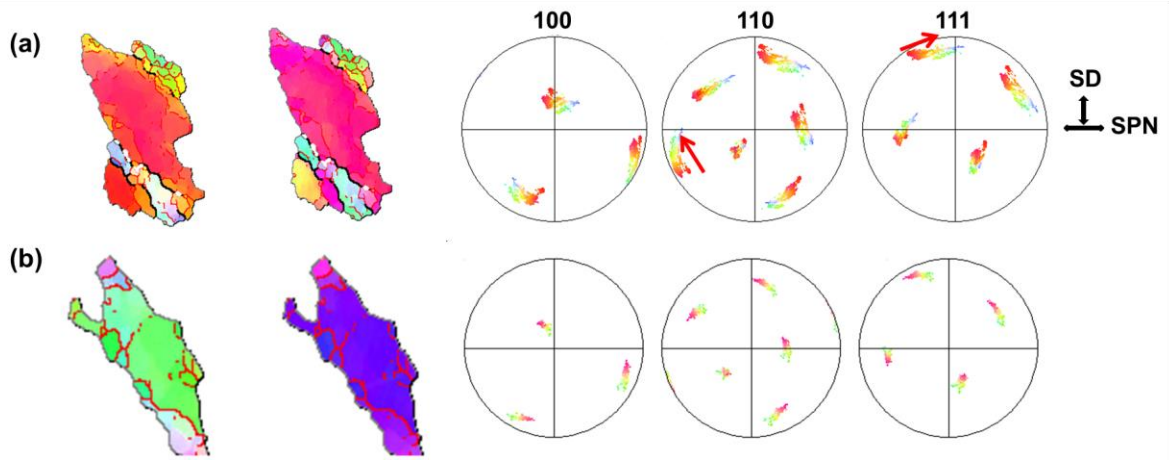

Figure 4.13 IPF images and corresponding pole figures for a group of grains to be analyzed

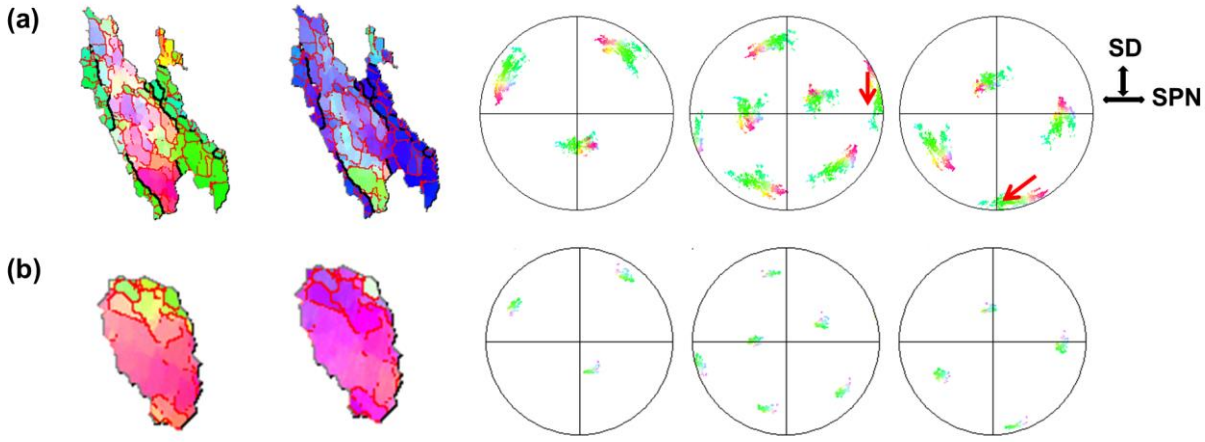

Figure 4.14 IPF images and relevant pole figures for another group of grains to be analyzed

Texture Evolution near Tube Corner

As addressed in the previous chapter, material under the tool is heated and processed then extruded, during which materials flow upwards from the bottom through the corner and finally forms the tube wall. Even if deformation mode and materials flow is relatively simple in the bottom region, as elaborated in the previous section, not every detail regarding crystallography texture and materials flow can be fully understood. While the materials flow into tube wall, texture evolution could be more complicated for a couple of reasons: 1) there will be a major change in the deformation framework of the dominant shear straining from the tool rotation; 2) another shear mode is involved originating from the axial movement of the processing tool, called axial shear hereafter; 3) the micro-texture evolution at later stages, i.e. near the wall or anywhere away from the tool bottom, might be affected by its previous deformation history since a certain type of texture has already been developed in an earlier stage. Thus in this section, the micro-texture evolution near the bottom corner will be report and analyzed systematically. The behavior of corner region is of great importance since it serves as a transition from the bottom to the wall, corresponding micro-texture investigation will not only provide crucial information regarding how the textures in the bottom are developed into other types in the wall, but also signify the materials transportation and deformation geometry variation during this process.

As the results shown in the previous discussion, when the materials is deformed underneath the tool, local shear directions constantly change and distribute along the

rotating tool, while the SPN is remained stable. The trick is if the tube is perfectly sectioned in the middle into halves, there will be minimal shear deformation in the center by theory since the linear velocity of the processing tool is almost zero, and the SD for the entire sample will be perfectly perpendicular to the surface of the cross section, this situation is shown in the illustration of figure 4.14a. However, in reality, it is not possible to have a sample perfectly cut in the center and at the same time, the processing is a relatively dynamic activity and tool itself can be deformed and deflected during the processing due to limited rigidity. Thus by assuming the ideal situation can't be reached and there is always off-centering and deflection, the distribution of the SD is shown in fig4.14b. The discussion in this section will only be based on this more realistic circumstance.

The bottom corner region scanned by EBSD is shown in figure 4.15. To better investigate the behavior of the micro-texture change, this map is further subdivided into several sub-regions and numbered as 1-11. The texture analysis for each region will be performed and reported as pole figures. The sub1 is taken as an example showing the methodology used here to analyze the micro-texture in the corner.

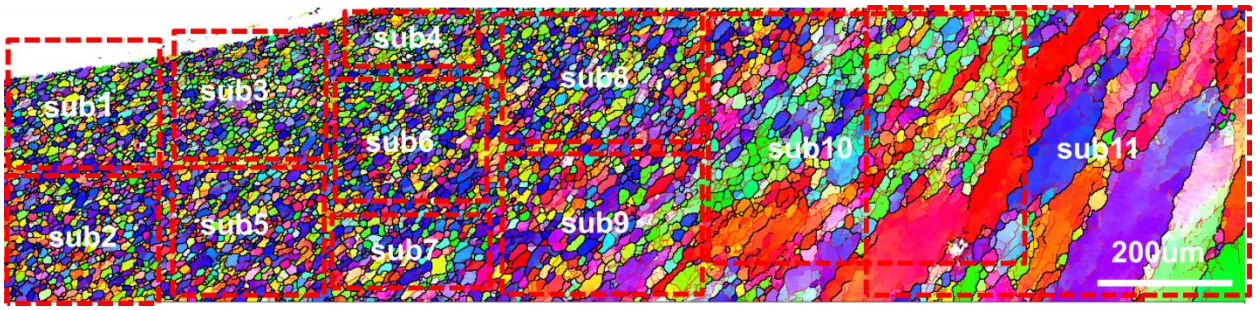

Figure 4.15 IPF image near the tube corner and the subset selection

From now on, PFs will be plotted in the shear reference frame of the wall as a starting point, rather than the framework used previously to analyze the samples near the bottom region. The illustration of the differences between the reference frames for bottom and wall locations are shown in fig4.16, the SPN is rotated 90 degrees whereas the SD shows a difference between 0 to 90 degrees depending on the analyzed region. The shear reference frame of the bottom region will be called framework1 and the one for the wall will be called framework2 hereafter. The reason why framework2 is used as reference is that the SD near the corner is supposed to be closely aligned to the SD on the wall and the SD is of highest importance and priority in the entire texture analysis. In this case, the analysis and results of the corner region can be also used to build a direct relationship with the future analysis and discussions to be performed on the wall regions.

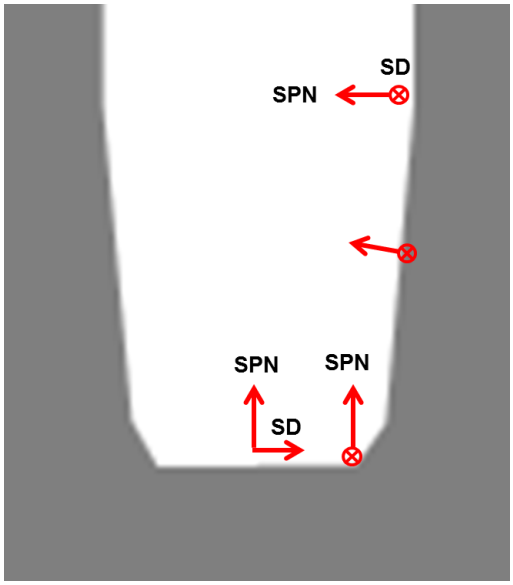

Figure 4.16 Illustration of deformation geometry variations along the tube

The PFs for sub1 are show in figure 4.17. It is noticed that by plotting the PFs in the framework2, the distribution of SD has already been aligned to the ideal location, while SPN is showing a relatively large deviation. By looking at the frameworks shown in figure 4.16, the SD near the corner region should be the same as the case in the wall location. However, the SPN will be mainly affected by the curvature of the tool near the corner since the SPN is supposed to be perpendicular to the tangent plane at each specific location. That is to say the local shear reference frame of sub1 mainly shows a deviation regarding SPN compared with framework2. Thus a post rigid body rotation is applied on the PFs in figure 4.17a along a specific macroscopic axis, in this case ND, to align the SPN to the ideal location in framework2. The resulting PFs are shown in figure 4.17b after a rigid body rotation of 57 degrees, a strong B/$\bar{B}$ fiber shear texture is observed, which is expected near the PZ under intense shear deformation. This result indicates the local shear reference frame of sub1 is rotated by 57 degrees along the ND in the macroscopic coordinate system with respect to framework2. To summarize, the SD near the corner have already aligned to the macroscopic ND, which is also believed to be the direction where the SD of samples taken from wall region aligned to; the SPN seems to be mainly related to the local curvature of the tool-materials interface.

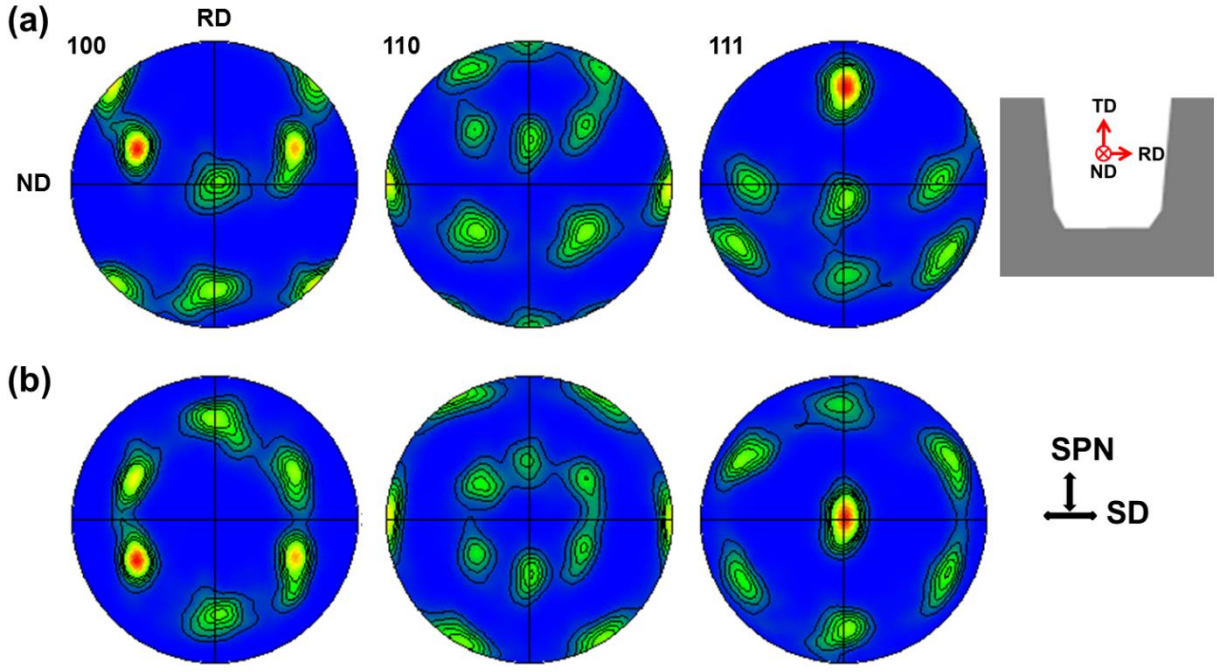

Figure 4.17 Pole figures for sub1 (a) before and (b) after rigid body rotations

Similarly, rigid body rotation will also be applied to other sub-regions labeled 2-9 to align the measured texture components to their local shear reference frameworks, and the result will simply be reported in terms of the amount of rigid body rotation needed as well as the final texture represented in PFs. It should be noted that in sub-region1, apart from the 57 degree rotations applied around ND, a 3-degree rotation is also applied around TD to align the SD in the PF to its ideal locations. In spirit of explaining the mechanism in a simple and effective way the extra small rotation round TD is not mentioned earlier. However, in the following analysis, the rotation along TD and ND will be explicitly labeled. For the sub-regions close to the processing zone, the B/$\bar{\text{B}}$ texture should be expected due to high levels of shear strain. As in the cases of sub-regions labelled 2-4, the measured PFs are rotated following the fashion described earlier and the

resulting PFs and the amount of rigid body rotations are shown in figure 4.18. It can be seen that similar to the case of sub-region 1, 55-58-degree deviation is observed for the SPN with respect to the framework 2, which is supposed to be related mainly to the curvature near the corner; while 2-5 degree rotation is also applied on the measure PFs along TD to align the SD to the local shear reference frame. It is noted that there is only minimal change of required rotations among these sub regions, indicating that the local shear reference frames for sub-region 1-4 is relatively constant. And texture types in these regions mainly showing stable B/ B̄ shear texture, and the only difference compared to early result in the PZ is that the local shear reference frames are rotated significantly because of the deformation geometry.

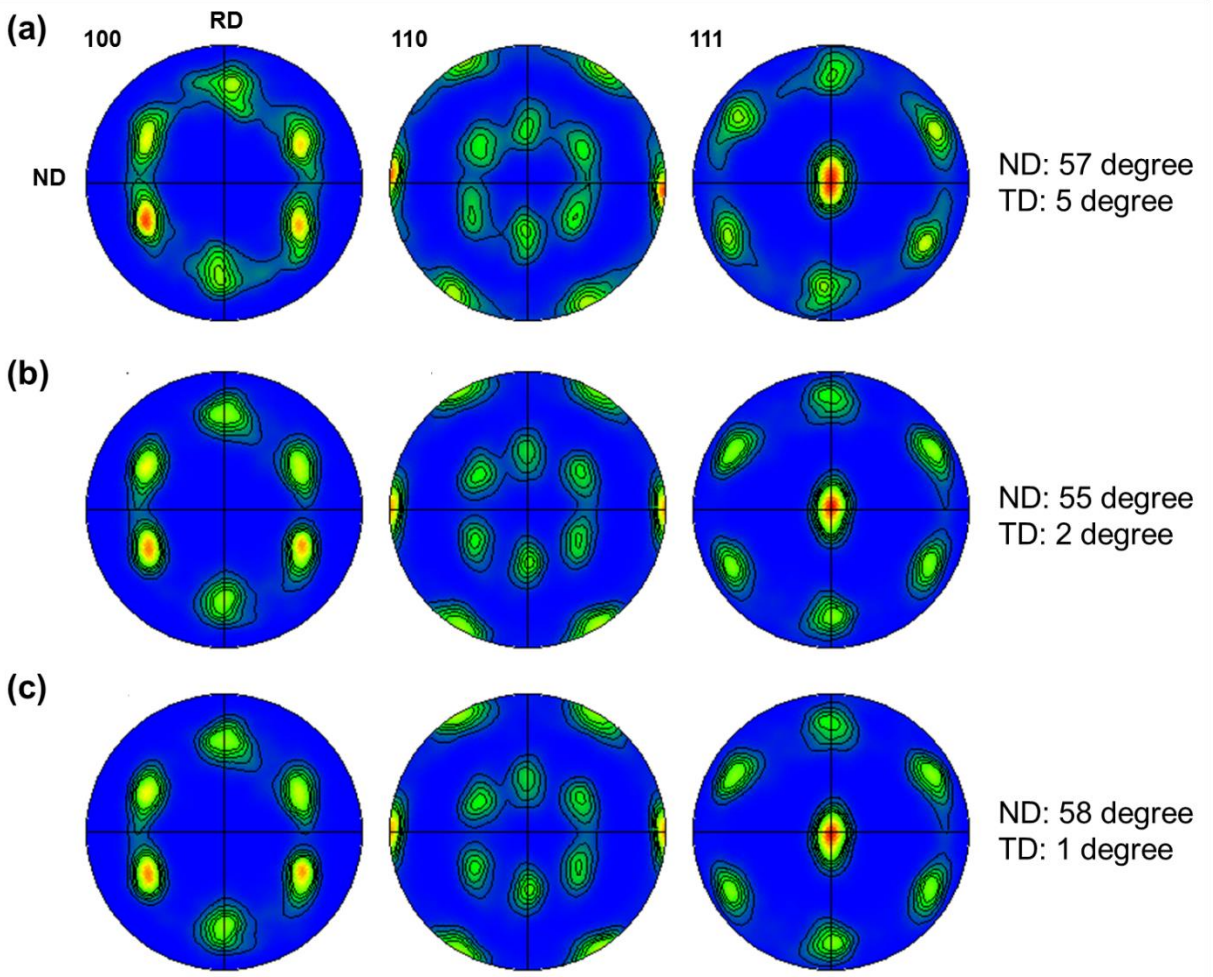

Figure 4.18 Pole figures for sub-regions 2-4

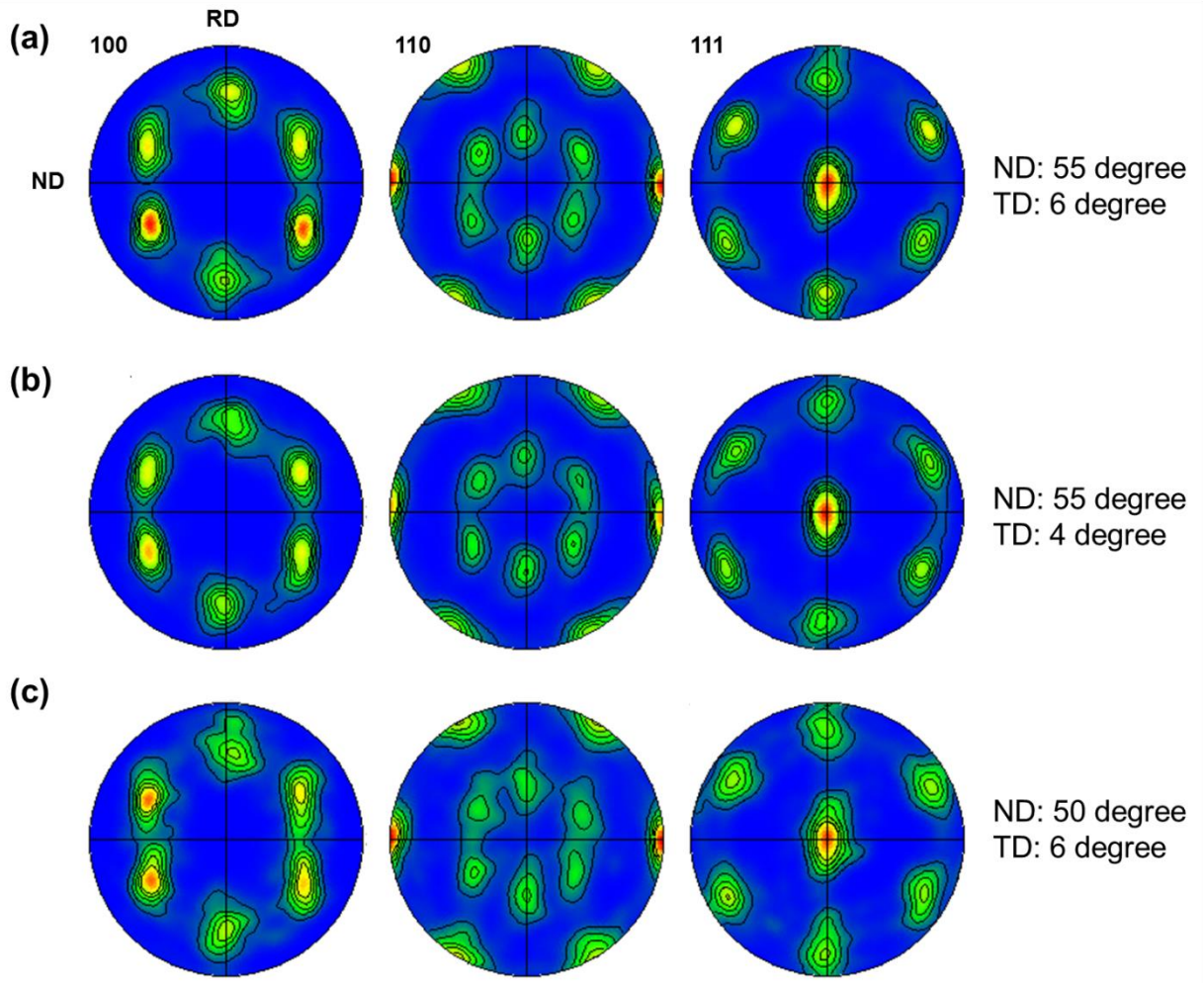

Figure 4.19 Pole figures for sub-regions 5-7

Micro-texture in sub-regions labeled 5-7 are also analyzed in a similar fashion. It should be noted that this group of subsets are further away from the very end of the processing zone, i.e. tool-materials interface, compared to sub-region 1-4, thus it is possible that the deformation geometry and amount of shear strain differs slightly. However, these regions should still be fully located inside the PZ and exhibit stable shear texture rather than transition texture types since the corresponding grain structure is

identified as typical refined microstructure observed in friction stir related processes, meanwhile these sub-regions are located around 500um away from the transition region, as shown in figure 4.15. The texture results of sub-regions labeled 5-7 plotted in their local shear reference after rigid body rotations are shown in figure 4.19. It is noticed that B/$\bar{B}$ texture is still the dominant component in all three sub-regions, as expected. However, it seems that the texture in sub-region 7 is relatively weak and spread, indicating its close proximity to the transition region. It is also observed the amount of rotations around ND needed to align the measured data to local shear reference frame is slightly less than the cases in sub-region 1-4, whereas the rotation around TD shows a higher value of 4-6 degrees. It might because sub-region 5-7 is not under extreme shear deformation thus the evolution of SD is lagged behind a little bit since the SD is changed continuously from the center to the edge of the bottom sample. Insufficient shear deformation and penetration might delay the evolution of SD to align perfectly to the SD in the local shear reference frame. On another side, the amount of rotation applied on the ND shows a lower value compared to the cases in sub-region 1-4, this might be attributed to the fact that materials further away from the tool-materials interface is more likely being affected by the materials flow since less shear deformation is expected. To summarize briefly the results for sub-region 5-7: B/$\bar{B}$ type shear texture is still dominant, rotation needed along TD and ND to align the measured PF to local shear reference frame differs slightly compared to sub-region 1-4, sub7 should be close to the transition region because of showing scattered texture.

In the following part the sub-region 8 and sub-region 9 located close to the transition region will be analyzed. By observing the figure 4.15, it seems that sub8 is close to transition region but still on the PZ side whereas sub9 should be mainly located at the transition region with elongated and not fully developed grain structure. Thus the rigid body rotation applied to the measured PFs of sub8 is still based on the assumption that stable B/ B̄ components are the dominant texture while this scheme won't be used for sub-region 9 since transitional texture is expected in this sub-region. The amount of rotations applied to the sub-region 9 will be close to those used in sub-region 7 and 8 since they are next to each other thus the deformation geometries should be similar. The texture will not only be represented in the form of PFs in their local shear reference frame, but also be analyzed in ODF. The results for sub-region 8 are shown in figure 4.20, the rigid body rotation required to align to the local shear reference is found to be 45-degree around ND and 5 degrees around TD, based on the orientation of stable B/ B̄ shear texture. It should be noted that the amount of rotation applied along TD is further reduced to 45 degrees, while the rotation needed on ND is relatively constant. As illustrated in the PFs, the B fiber texture is not as strong as those of previous subsets and the poles are relatively scattering around the ideal locations and stretched along a specific direction. It is believed that this sub-region is close to the transition region and some unstable transitional texture component should be present. This brings our investigations further into the ODF analysis, as shown in figure 4.20b and figure 4.20c. At the section phil2=0, C component and A1* component can be clearly observed, which can further be substantiated in the section of phil2=45 degree. At phil2=45 degrees, it is clear shown

that the A, A1* and C components are showing up as transitional texture types while transforming into dominant B/$\bar{B}$ texture.

The PF and ODF study will also be performed on the sub-region 9 which is believed to be located near the transitional region; however, the amount the rigid body rotation needed for this subset will be pre-determined based on the results in other regions and chosen to be 45 degrees along TD and 7 degrees along ND. It can be seen in figure 4.21a that the texture near sub-region 9 is distorted and the orientation distribution on the PFs is relatively scattering; at the same time, the poles on the PFs seem like being stretched along RD. It is certain that extensive texture transformation is expected at this location and further analysis is performed aided by ODF. As shown in figure 4.20b and figure 4.20c, relatively strong C component is present as observed in the cross section of phil2=0, while relatively weak B and $\bar{B}$ components and significant transitional texture types are observed in the section of phil2=45. Thus can be concluded that sub-region 9 mainly demonstrates transitional texture types as detailed in the previous section, at the same time the rigid body rotations need to apply to these measure data in order to match local shear reference is slightly different compared with those sub-regions close to the PZ. This might be attributed the fact that material near the transition region are less deform thus more likely affected by the materials flow or even the deformation history.

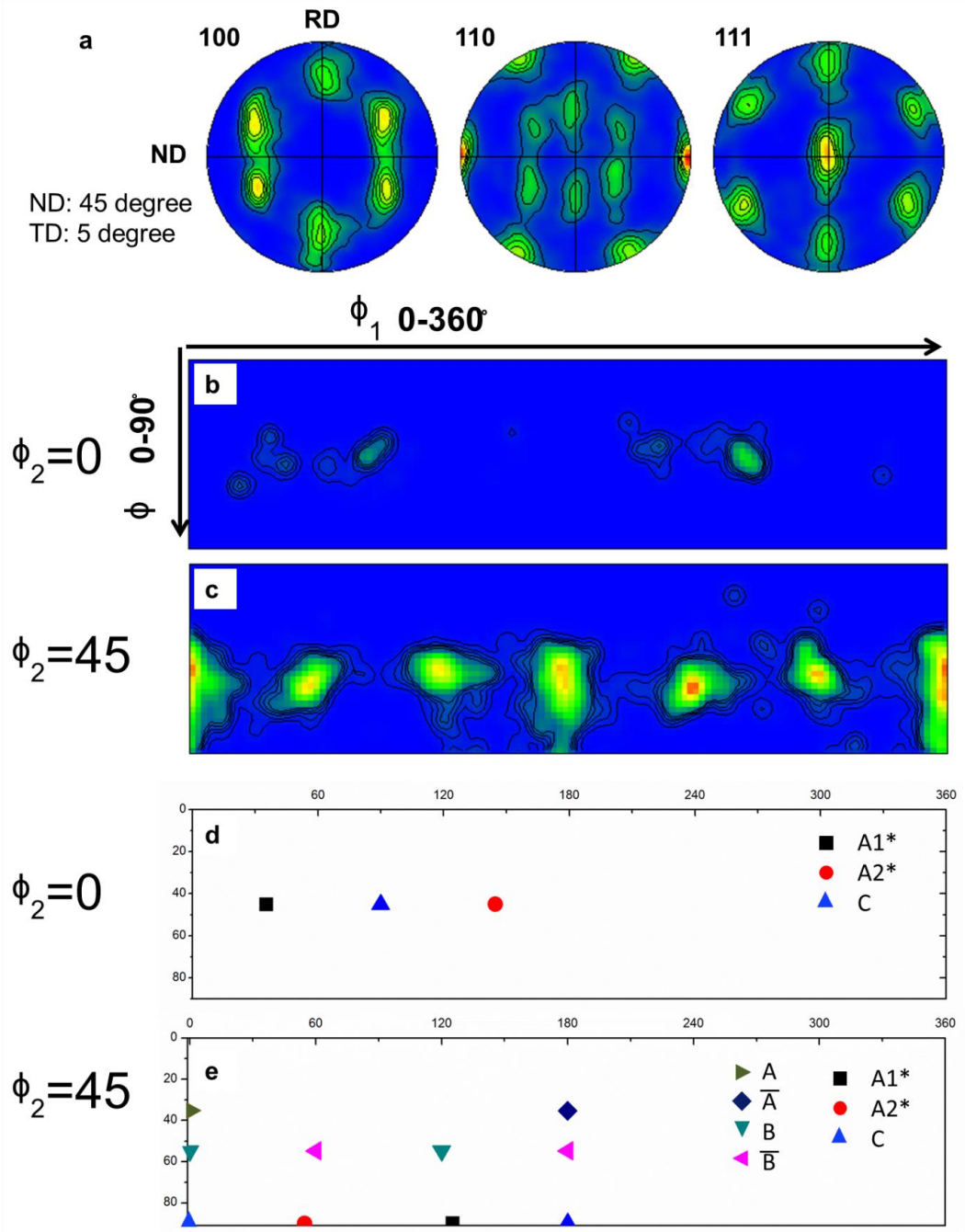

Figure 4.20 (a) Pole figure (b)-(c) ODF figure for sub8 and (e)-(f) ideal locations of shear components in ODF figure

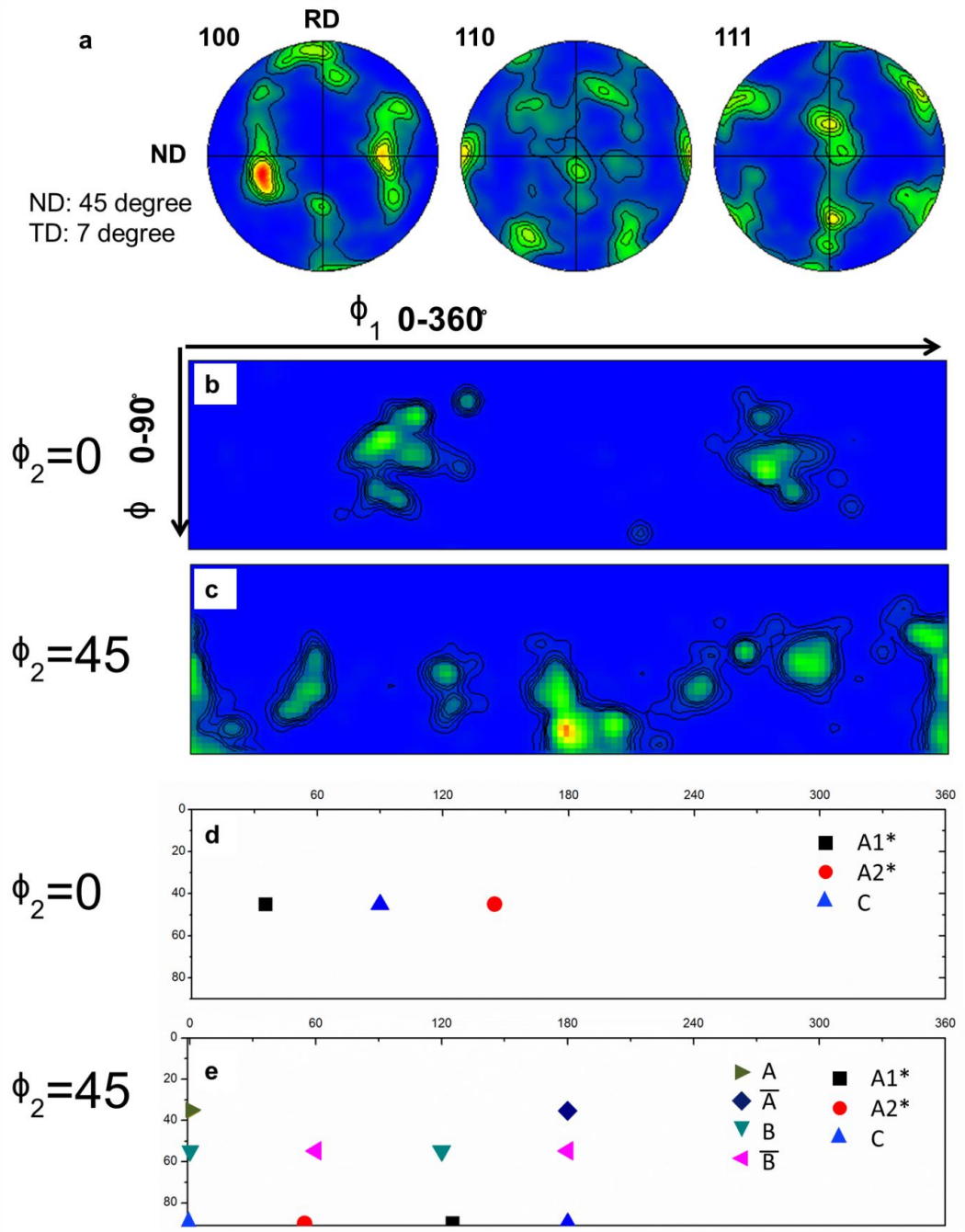

Figure 4.21(a) Pole figure (b)-(c) ODF figure for sub9 and (e)-(f) ideal locations of shear components in ODF figure

In this session, primary findings can be summarized as:

1, the texture type near the corner region is still showing strong B/$\bar{B}$ fiber component, while the shear reference frame will not match any macroscopic coordinate systems

2, rigid body rotations are performed on the measured texture data to reflect the texture component in local shear reference frame, the amount of rotations performed are mainly related to the geometry of the contact surface at the tool-materials interface

3, the amount of rotations need to align the SD are relatively constant in multiple sub-regions in the PZ, while to align SPN to its ideal location, less rotation is needed for sub-regions away from the PZ, i.e. near the transition region.

4, at the sub-regions further away from the PZ or even close to the base metals, mechanism other than shear deformation such as materials flow, axial shear, extrusion, and compression might start playing a noticeable effect on the deformation geometry thus micro-texture evolution. Thus it is very hard to estimate the contribution of each factor and the local deformation geometry can't be determined precisely. At this point, this part will be discussed and analyzed in future works.

To further substantiate the observation that local deformation geometry is mainly affected by the geometry of the tool-materials contact interface, another region next to the area shown in figure 4.15 but closer to the wall is also scanned by EBSD and the result will be discussed accordingly. It should be noted that in figure 4.15, the interface between the friction stir tool and materials being processed is relatively smooth thus no significant change of SPN is observed; however, in the following map, systematic variation in the

SPN should be expected along the PZ since the interface is relatively steep. As shown in figure 4.22 four sub-regions along the PZ are analyzed separately, and the measured PFs will undergo rigid body rotations in order to align themselves to the local shear reference frame. Similar to the methodologies used in the previous samples located in the corner, the PFs and texture results will only be presented in their local shear reference frame and the amount of rigid body rotations applied. As illustrated in figure 4.22, the texture type observed in sub-region1 to sub-region4 still showing stable B/$\bar{B}$ type shear texture, indicating the dominant effect of shear strain from the tool rotation. As mentioned earlier, the tube wall is subjected to lower amount of shear strain and this should be the major factor contributing to the weak texture in sub-region4. The amount of rigid body rotation applied on measured texture data of each sub-region in order to project the results in local shear reference frame is also summarized in figure 4.22. Regarding the amount of rotation around ND, a clear trend with continuously decreasing value from 48 degrees to 34 degrees is shown. Since at sub-region 4, the orientation of tool-materials interface, i.e. local SPN is aligned closer to the SPN of the PZ in the wall, resulting in less rigid body rotation around ND. While at sub-region 1, which is relatively distant from the end of the corner or the wall, more rotations around ND is needed to align to the local SPN. At the same time, minimal rigid body rotations are needed to align the SD to local shear reference frame, since the SD in the coordinate systems is almost parallel to the SD in the local shear reference frame for these sub-regions.

To sum up the entire discussions regarding micro-texture evolution near the tube corner. It is scientifically interesting and important to understand in the sense that the

microstructure and micro-texture development is not fully understood yet for this new FSBE process. From a more practical perspective, the behaviors of the micro-texture in the corner serve as a significant connection between the materials behaviors in the bottom of the tube and tube wall, where the micro-texture and microstructure would dominate the macroscopic mechanical properties of the tube. In the following section, micro-texture in the tube wall will be investigated, not only the result in this part will provide crucial information about the texture on the tube wall but also the current methodologies will be applied.

Figure 4.22 IPF image and subset selection near tube corner

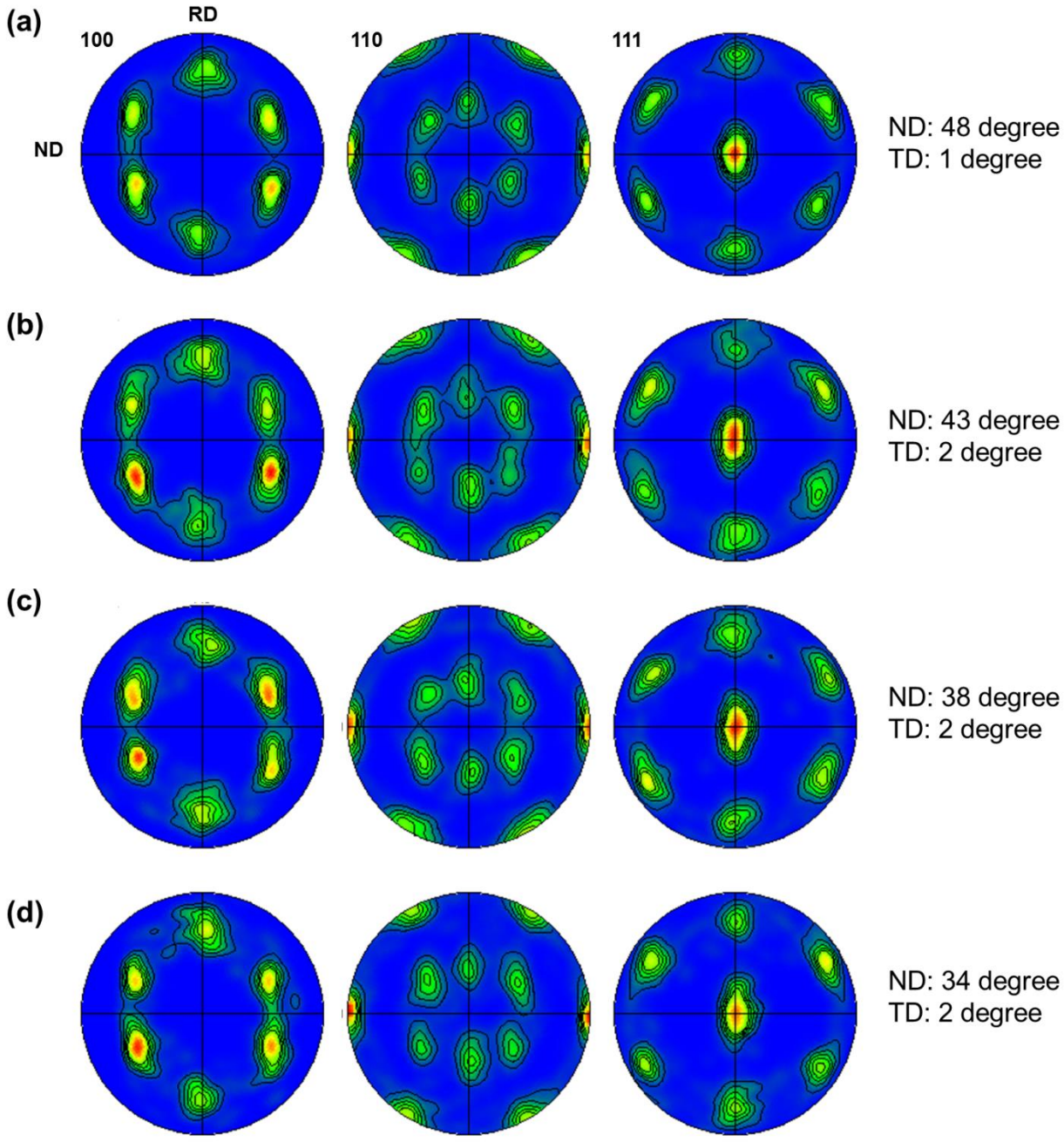

Figure 4.23 Pole figures for subset1-4 in figure 4.22

Texture Evolution on Tube Wall

Before starting the texture analysis on the tube wall, some major distinctions between wall locations and tube bottom regarding the shear strain and deformation geometries should be reviewed:

1, a major change in the local shear reference frame is expected, as shown in figure 4.16

2, materials in tube bottom flows upward and forms the tube wall while being deformed, thus resulting micro-texture and microstructure is a function of both current straining modes and deformation history. In this case, the shear texture in tube wall is formed from a similar mature shear texture type but in a difference shear reference, rather than directly from initial fiber texture

3, lower shear strain level, or more precisely, strain rate is expected in the tube wall. At tube bottom or even tube corner, materials are pushed and compressed mechanically by the processing tool while subjected to shear straining, whereas at tube wall the materials is flowing upward and the shear strain level is mainly determined by the contact condition at the tool-materials interface

4, multiple deformation modes are contributing to the final texture, for example, axial shear start playing an important role, the extrusion effect and materials flow will also influence the texture in the TMAZ where shear strain is minimal.

5, continuous materials transportation around the rotating tool is expected thus the entire pole figures might be transported around the rotation axis accordingly. It is also believed that effect of materials transportation on the resulting texture might be minimal

in the PZ, especially close to tool/materials interface where shear deformation is dominant

Texture Evolution at 15mm Location

In this section texture evolution across the tube wall at sample machined 15mm from the bottom of the tube will be analyzed and the EBSD scan is perform across the tube wall on the cross section similar to the one in previous discussion. It is noted that, by assuming the dominant deformation mode is shearing from the tool rotation, the RD should be perpendicular to SPN while ND should be parallel to SD. Thus in the following discussion, the measured texture data will be directly projected on the PFs with coordinate system of RD-TD-ND without any rigid body rotations. Also, the PFs will mainly be constructed in RD-ND plane and viewed from TD, that is to say TD and also the direction perpendicular to SD-SPN plane will always be located in the center of the PFs in our study. This direction will also be called Z, forming the systems of Z-SD-SPN. There are a couple of reasons for using this strategy:

1, the view of PFs with the direction perpendicular to SD-SPN in the center of the PFs is widely adopted in the literature, both in the texture analysis of torsion and FSW of aluminum alloys. The results in our work can be directly compared to those in the literature and any difference or problems can be immediately identified.

2, it enables better identification of the shear texture components. If a B texture is expected with <110>//SD and <112>//SPN, the 111 pole will be automatically aligned to the Z direction and a strong 111 pole will be observed in the center of (111) PF. If the C component is formed, the 110 direction will also be observed in the center of (110) PF.

This framework seems to be the best orientation to analyze shear texture component compared to the other two.

3, additionally, since materials transportation around the rotating tool is possible, the entire PFs will also be rotated around the rotation axis of the tool, which is the TD in macroscopic coordinate system. It is not clear to what extent the materials at a specific location is affect by this effect (it varied position by deposition depend on the local deformation geometry), thus the best way or most rational method of analyzing crystallographic texture in these situations might be plotting the PFs on the surface perpendicular to the rotating and transporting axis. This axis should be relatively stable under deformation and materials transportation around the tool. A quick example involves if a C type texture is transforming into B/$\bar{B}$, ideally the distribution of the 110 direction should be relatively constant. However, it is highly possible that under the current deformation field and materials flow, the shear reference frame is further rotated due to the materials transportation while the texture is evolving, switching the <110> direction to another position or even forms a certain distribution around the TD. In this case, plotting PFs on planes other than RD-ND may result in two sets patterns, rendering the PFs hard to read and analyze.

4, finally, the initial fiber texture of as received materials with <100>//TD will further justify the adoption of the current method. By projecting the measured texture data on the RD-ND plane, the initial fiber texture will show strong pole in the center of (100) PF, transition texture type C shows up in the center of (110) pole while stable B/$\bar{B}$ texture result in a strong concentration in the center of (111) pole. Another item that will

further benefit our analysis is by combing the IPF image with respect to TD and PF plot, grains close to initial fibers will show red, while grains exhibiting green and blue color are most likely associated to the C and B type texture.

The EBSD scan at the 15mm wall is shown in figure 4.23 and the grains are colored base on its orientation relative to the TD. This entire map is further subdivided into three regions called: TMAZ or close to BM, transition region and PZ. It can be observed in the TMAZ, most grains are showing <100> parallel to the TD, which corresponds to the initial fiber texture with, while in the transition region, grains exhibiting <110>//TD show up, representing by the green color. Finally, the PZ showing predominantly <111>//TD (blue grains), signifying the stable B/$\bar{B}$ texture, which is expected because of the high shear strain level near the PZ. Specific types of texture can't be determined at this point since only the crystallographic directions relative to TD is represented in the IPF figure while other directions are not considered, the following part will analyze the texture components and their evolution in detail via PFs in each region.

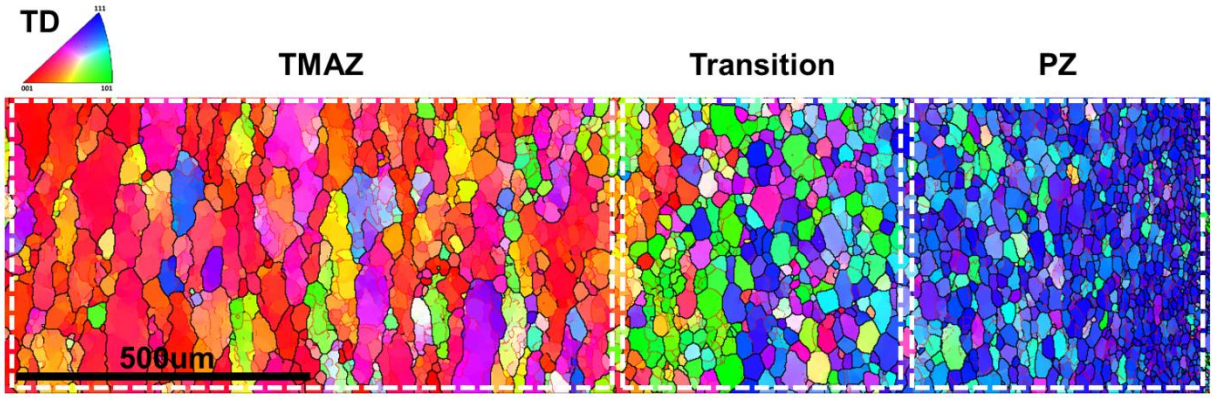

Figure 4.24 IPF image of 15mm specimen

The pole figures for the TAMZ region is shown in figure 4.25. It is very interesting to note that initial fiber texture with <100> direction randomly distributed around the extrusion direction evolve into a texture type with the <100> direction mainly distributed at certain locations on the pole figures; as observed in the 100 pole in figure 4.25a, four major poles around the TD are observed rather than an even distribution of initial fiber. At the same time, it seems that the center pole of (100) pole figure switch off the center, where it is located initially. The microstructure in this region is characterized by coarse and elongated grains with extensive low angle grain boundaries and substructures. Thus, material in this region is only subjected to limited amount of shear strain, which is not even enough to trigger significant amount of dynamic recrystallization. Thus the way the micro-texture develops in this region might be related to the combined effect of small amount of shear deformation and extrusion effect. The pole figures are also constructed by projecting each pixel in figure 4.24 and the color of the grain can be directly connected to its position on the pole figures. It can be seen in the (100) PF in figure 4.25b, the center pole of 100 is moving away from the center and evolving into the first quadrant, forming grains showing <110> close to TD and <111> close to TD respectively, illustrated by the green and blue grains. As mention earlier, the green grain showing <110>//TD might be related to the C component while <111>//TD should be connected to the formation of B/$\bar{B}$ texture to some extent.

It should be noted that in the TMAZ region, small amount of shear strain is expected, thus there should be little tendency of forming stable B/$\bar{B}$ texture, even if in

some cases, the grain structure will evolve into B/$\bar{B}$ directly under marginal amount of shear deformation without going through the transitional texture types like C or A*

In order to analyze the texture transformation of the grains showing <110> and <111> close to TD, they are extracted from and pole figures are constructed exclusively for them. As shown in figure 4.26, the grains showing 110 close to TD are extracted and the pole figures constructed for these grains are shown in figure 4.26b; for reference, the PFs for the entire TMAZ region is shown again in figure 4.26c. By observing the PFs for the extracted grains in figure 4.26b, it seems that it is showing a somewhat C component which might still under transformation in a rotated shear reference frame along TD. If this component is transforming into C component mainly under shear deformation, the SPN and SD can be assumed as indicated in by the arrow in figure 4.26b. Interesting, by comparing with the texture for the entire TMAZ region in figure 4.26c, it seems that this texture type come from the texture in TMAZ by rotating around a specific direction in the (100) PF, as shown by the red line, and most importantly this rotating axis is aligned to the assumed SPN direction of the assumed C texture type that is still under transformation. Thus the preliminary conclusion can be draw, the observed C component is still under development and it might come from some of the grains in the TMAZ showing orientations close to cube or rotated cube texture by rotating around a specific direction, and this direction is fixed during the transformation; by analyzing the assumed C texture, the projected SPN happen to be the rotating axis; by adopting the general texture transformation mechanism under shear discussed in the texture analysis of the bottom region, the current observations can be interpreted as grains showing <100>

aligned to SPN tend to transform their orientations into C component under shear deformation, i.e. aligning the <110> to SD, by rotating around the SPN; the shear reference frame at the TMAZ is not coincide with the macroscopic coordinating system, confirming the previous claim that the continuous materials transportation might rotate the shear reference frame around TD, in this case the shear reference is rotated by about 30 degrees. Last but not least, the C component is still under transition, the circled 110 pole should be aligned to SD under further deformation.

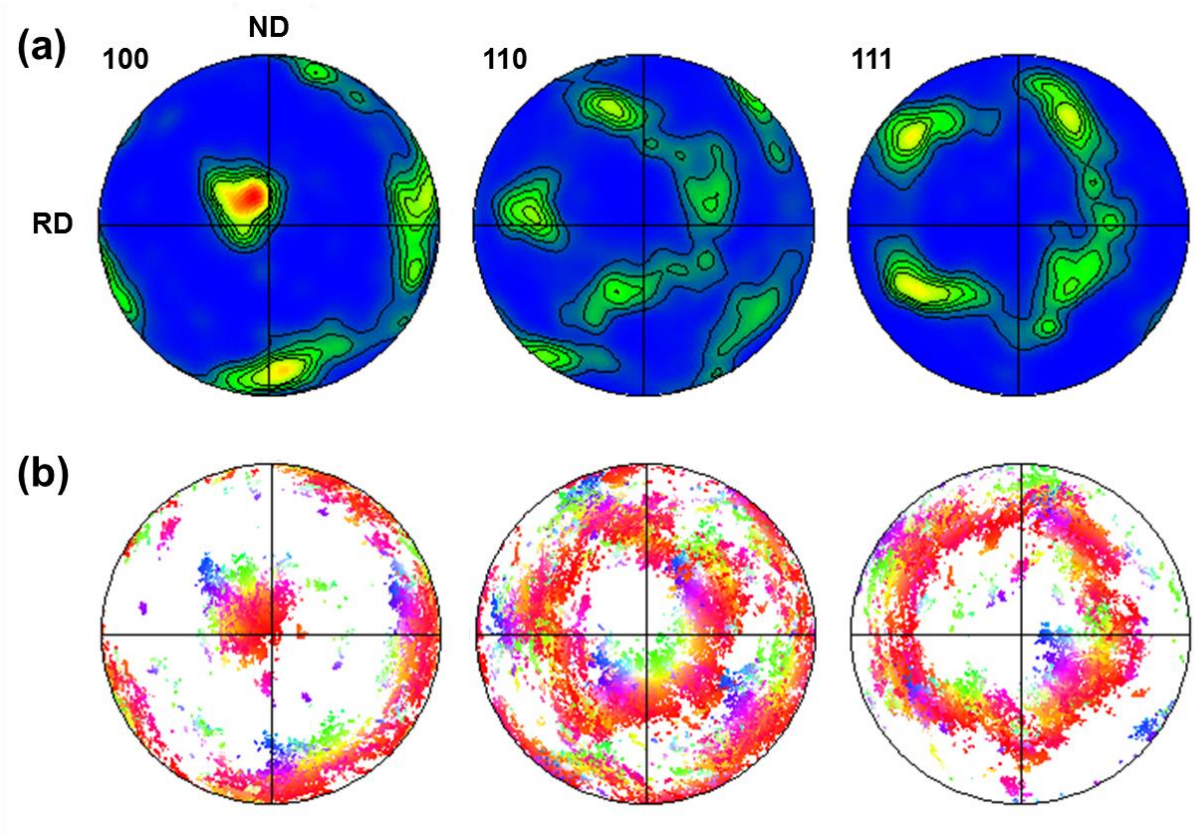

Figure 4.25 Pole figures for the TMAZ region at 15mm location

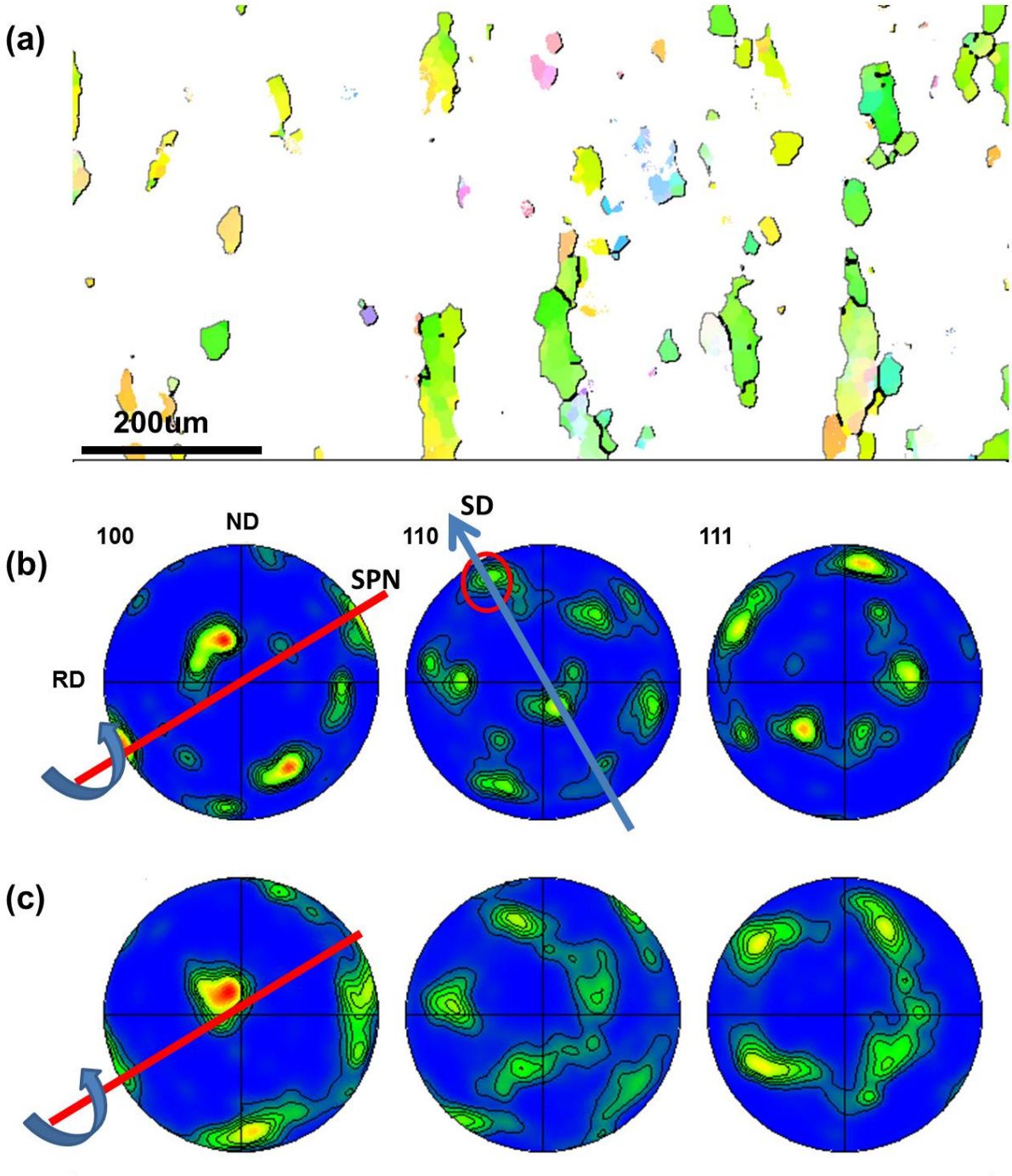

Figure 4.26 (a) IPF image for grains showing <111>//Z axis (b) pole figures for green grains and (c) pole figure for the entire TMAZ

It is also noted in figure 4.25b that decent amount of grains showing orientations with <111> close to TD are present in the TMAZ. Based on the assumption that these grain tend to evolve into B/$\bar{B}$ type texture, they are extracted and PFs are constructed solely for these grains. The results are shown in figure 4.27 and the PFs for the entire TMAZ are also attached in figure 4.27c for better illustration and comparison. By adopting the similar philosophy utilized for the case in grains showing C texture, it seems that texture/PFs of these grains are transformed from the texture shown in figure 4.27b by rotating along a specific direction as shown in figure 4.27b. By comparing with the results and discussion in the section addressing how the texture are transformed into A component and then possibly B texture in the tube bottom, it is believed that transitional A type texture is formed by rotating around the axis shown in figure 4.27b and it is assumed that if the shear deformation is the major strain mode, this rotation axis should be the shear direction and the A component is formed by rotating around <110> direction which has already been aligned to SD. As mentioned in the previous session, some grains are not forming C component because their initial orientations are more favorable for the development of A component. This texture evolution mode observed in the TMAZ can match the observations made in the tube bottom, that is to say, some grains are still evolving into A texture under shear deformation in the wall region. It should be noted that the A texture is still under development and a couple of degrees of further rotations around the SD could align the PF to its ideal location. Nevertheless, A component is believed to be transient by nature and very hard to capture when it is located in its ideal orientation since it transforms into other component under further deformation. It is also

needed to mention that the shear reference frame will not coincide with the shear reference frame for those grains developing C type texture. It seems that continues materials transportation result in the change in the shear reference frame in the TMAZ, but the trend is hard to capture at this point.

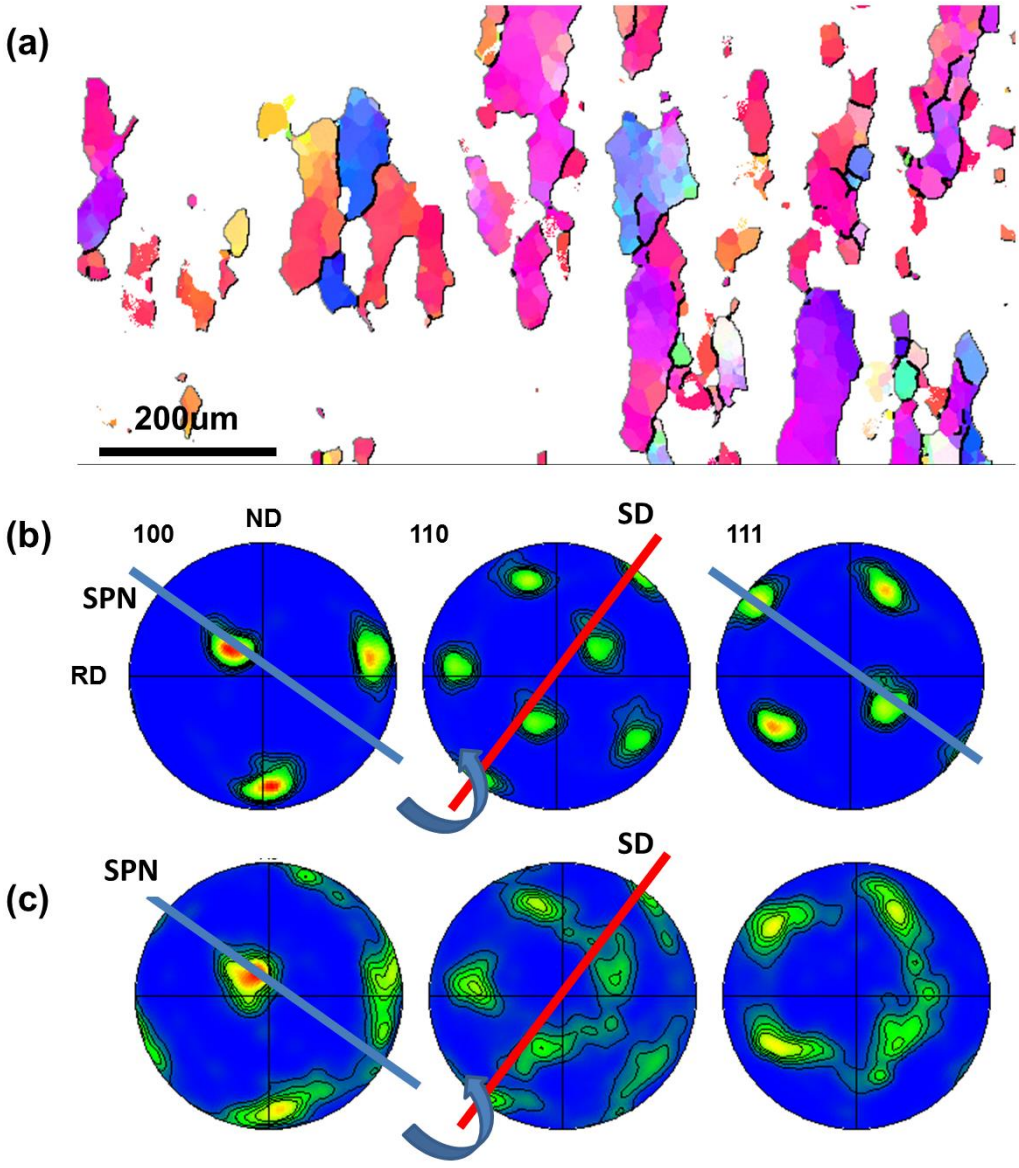

Figure 4.27 (a) IPF image for selected grains (b) pole figure for selected grains and (c) pole figures for the entire TMAZ

Following the TMAZ region, the texture evolution of the transition part of the 15mm sample will be addressed. As show in figure 4.28c, the texture is relatively weak and not showing any specific components, the poles in figure 4.28c are relatively scattering and elongated, indicating significant texture transformation in this region. Microstructure in this region is characterized by elongated grains showing reduced aspect ratios and a large portion of fully recrystallized small grains with equiaxed morphology. That means the amount of shear deformation is higher compared to the TMAZ and significant deformation gradient is expected at this location. It it still very interesting that certain poles are relatively stable in the (110) PF while other poles seem like elongated along a certain direction, especially the (110) pole and (111) pole. Grains showing <110>//TD and <111>//TD will also be extracted based on the PFs in figure 4.28b and analyzed separately. Since the grain showing <100>//TD has already been addressed in detail and those grains are showing similar trend in this region, it will not be discussed for the second time. The current focus is the relationship between grains showing <110>//TD and <111>//TD and their evolutional mechanism.

The IPF figures with respect to the TD for both grains showing <110> close to TD and <111> close to TD are shown in figure 4.29a and figure 4.29b, respectively. It is noted that grains with <110>//TD are located close to the TMAZ while <111>//TD is close to the PZ side, where higher shear strain is expected. The PFs for the grains showing <110>//TD is expected to be a C type texture that might still under development with a rotated shear reference frame around TD, as discussed in the sample located at TMAZ. However, the PFs for these grains shown in figure 4.29c exhibit two components

that both resemble C type texture with one of them aligned almost identical to the C component observed in the TMAZ in figure 4.26, which is believed to be formed by rotating around SPN. The projected shear direction for the first component is labeled as SD1 and its corresponding shear reference frame is the same as the one in TMAZ. However, it seems that the second component with shear direction labeled as SD2 is showing stronger texture intensity. The shear reference frame characterized by SD2 is rotated clockwise around TD from the one for SD1 by around 45 degrees, which is believed to be the result of materials transportation originating from the rotating tool. And this clockwise nature from SD1 to SD2 is the same way as the processing tool spins. The second component with SD2 as shear direction is of great importance since it is closed related to the formation of B texture, as indicated in figure 4.29c and figure 4.29d. It seems that the grains showing <111> close to TD are showing a texture type that is involving into one texture component of B/B, and this component that is still under development come from the C component related to SD2 by rotating around the SD2. It is inferred from figure 4.29c and figure 4.29d that the two poles aligned on the SD2 for both set of pole figures are located at the same position and being stable during the texture transformation. Another observation involved that the way the orientation distributions are stretched on the PFs as indicated in figure 4.28c seems to correspond to the rotation along SD2. Thus the C component that is rotated and aligned to the shear reference frame associated to SD2 transform into one component of B texture by rotating the entire PF along <110>//SD, which is confirmed in the previous section and also observed in literatures [35, 36, 46]. Since on B fiber, shear texture components can

transform into each other while keeping <110> direction relatively constant and parallel to SD. Additionally, the (111) PF in figure 4.29c shows that the developing B fiber texture start splitting into two components with the second one being relatively weak. This might be attributed to the mechanism detailed in the texture evolution in tube bottom, while C texture transform into one component of B, its alternative component might be formed from A type texture. It is less likely that a stable B component split into two since this mechanism is always associated with high shear strain.

Regarding the shear reference frame, it seems that the reference frame associated with SD1 coincide with the framework related to the formation of C texture in TMAZ. Thus the C component related to the SD1 might come from the grains that are developed in the TMAZ while still present in the transition region. The second component of C represented by the SD2 should come from the rigid body rotation of the previous texture since more materials transportation around the rotating tool is expected, which will realign the shear reference. Another interesting observation is that the framework associated with SD2 is aligned with the shear frame of C-A transformation discussed in figure 4.27. However, it should be noted that the B component formed here is not via A as a transitional component, rather it's a more direct C-B transformation in a rotated framework.

To summarized, the texture evolution in the TMAZ and transition region follow two routes: cube/rotated cube to C to rotated C to B (it is hard to find a proper name for the deformed fiber texture thus cube/rotated cue is employed); Cube/rotated cube-A-B, even if the A-B transformation is not observed here. For the shear reference frame, it

seems that in early stage of deformation. The framework connected to SD1 should be mainly associated with texture development under relatively low amount of deformation, especially in the TMAZ; whereas under further shear strain and materials transportation around the processing tool, the framework is rotated around TD and form the framework associated to SD2, where C-B evolution happens. However, all these reference frames are not perfectly aligned to the macroscopic RD, ND direction mainly because of relatively low amount of shear deformation while materials transportation is present and functioning as an important factor.

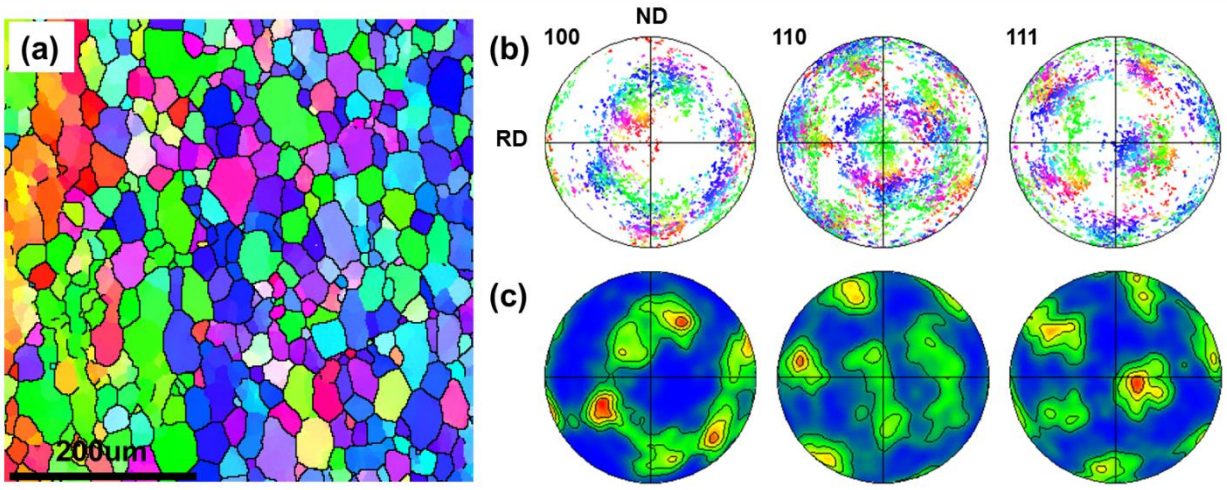

Figure 4.28 (a) IPF image (b) scattered pole figures and (c) contoured pole figures for the transition region of 15mm sample

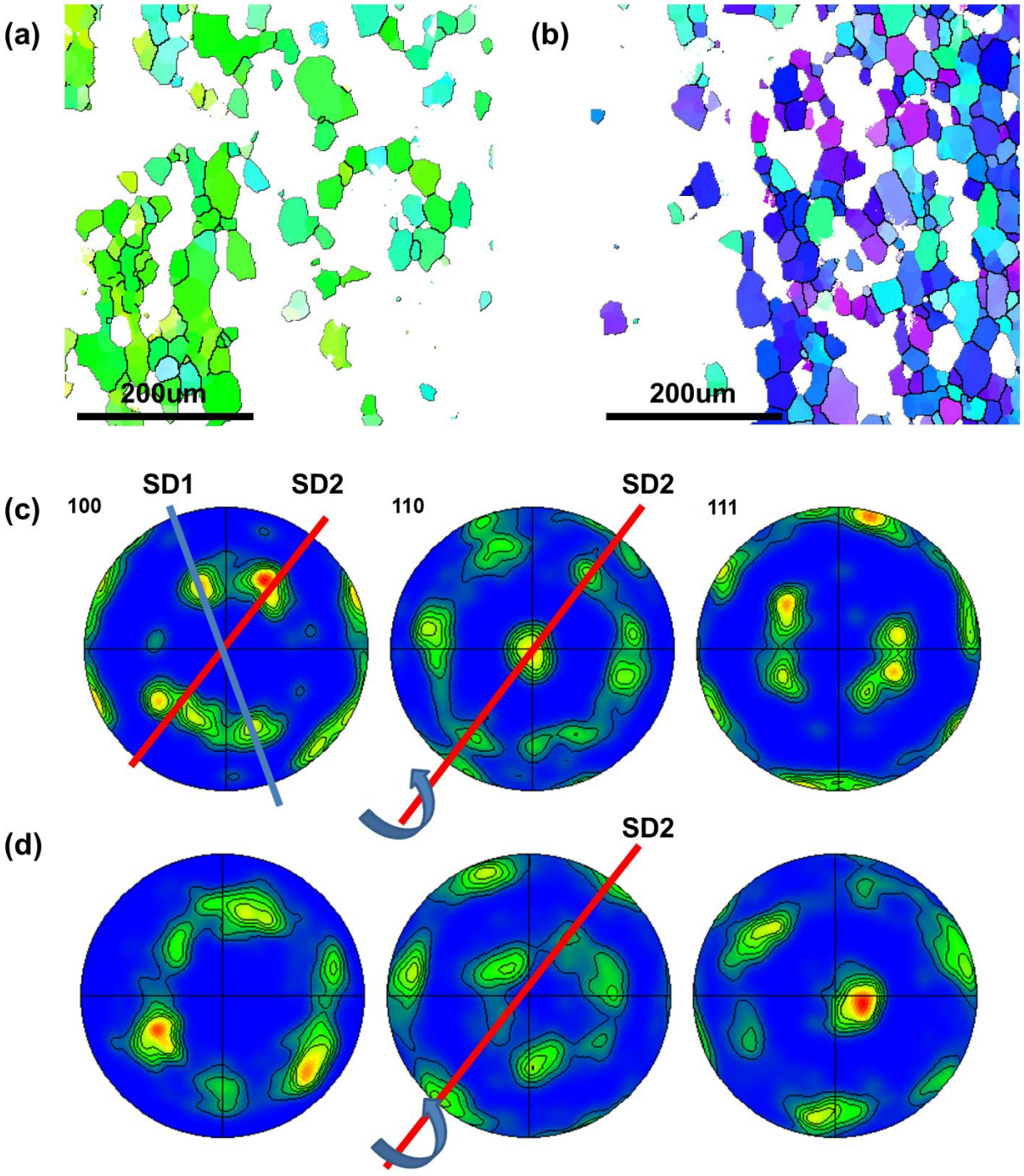

Figure 4.29 IPF image for selected grains showing (a) transitional texture and (b) B/ B̄ texture and (c)-(d) corresponding pole figures

In the PZ, microstructure is characterized by refined and equiaxed recrystallized grains. It can be seen from figure 4.30 most of these grains are showing <111>//TD, indicating a stable B/$\bar{B}$ texture type. As shown in the PFs, two components of B fiber texture are formed with <110> aligned to SD and <112> aligned to SPN. However, the texture is not as strong as in the case of previous sample from tube bottom and orientation distribution at each pole is relatively scattering. As observed in the figure 4.30c, the poles are not very sharp and seem to be elongated around the TD. Ideally this region is only located within 500um from the tool-materials interface and should be mainly dominated by the shear deformation. By comparing with the texture in tube bottom where a PZ with a depth of more than 1mm and relatively strong B/$\bar{B}$ texture is observed, even assuming the materials in the bottom into two walls and the amount of processed grains should be split by two, a general conclusion is that the deformation in the wall might be less severe and the axial shear might be playing a role in affecting the texture evolution. At the same time some grain growth is observed and it might affect the texture, as pointed out by Suhuddin et al. [62], significant texture change is observed because of in situ annealing during the process.

As mentioned earlier, multiple mechanisms might be playing a role in controlling the micro-texture of the PZ, such as axial shear, in situ annealing and rotation of the shear reference frame because of materials transportation around the tool simultaneously. Also the depth of PZ at this location is only around 500um compared to 1300um in the tube bottom, indicating less circumferential shear deformation is applied, thus the texture within the PZ might be under continued transformation rather than reach a stable B/$\bar{B}$

component. To better analyze the texture evolution of the PZ, it is further divided into several sub-regions, i.e. the map shown in figure 4.30a will be divided into eight parts vertically with spacing of 60-65um and the PFs for each part will be plotted accordingly. The constructed PFs for the eight sub-regions are shown in figure 4.31. As shown in figure 4.31a, the sub-region next to the transition exhibits almost exact the same PFs as in the transition region illustrated in figure 4.29d, which is believed to be transformed from C component in rotated shear reference frame. At the same time the equivalent part of B texture, i.e. $\bar{B}$ is also observed but very weak, it might either come from the evolution of A texture as mentioned in previous section or evolved from the existing part of B because of the axial rotation. Once the materials undergo further shear deformation, as illustrated in figure 4.31 b-d, it seems that the entire PFs are rotating around their centers, and at the same time the center pole of (111) PF is slightly getting closer to TD. This suggests that while the material is deformed by circumferential shear, the grains are also transported in a rigid body way around the rotating axis, resulting in the fact that the entire pole figures are rotated axially. Another important note is that the center pole of (111) is getting closer and closer to the TD, suggesting the tendency that the texture is evolving toward the ideal location of B/$\bar{B}$ texture component while under continuous materials transportation and change of shear reference frame. alternative is very weak; in the sub-region slightly deformed in the next step, it seems that the orientation distribution of <111> directions around the center pole in figure 4.21b is scattering and stretched around the TD; while in the next step of deformation as illustrated in fig4.21c, surprisingly two components of B start showing similar intensity. This suggests that the materials transportation around the

rotating axis might be contributing to the formation of $\bar{B}$ alternative by mechanically moving some grains to certain orientations on PFs, where the $\bar{B}$ alternative can be relatively stable under its instantaneously shear reference frame rather than relying on crystallographic slip. When the materials is further deformed, as illustrated in figure 4.31d-h, the entire pole figure keep evolving in a similar fashion by axially rotating around TD in a clockwise fashion while <111> is aligned to TD and <110> align to ND, respectively. Finally stable and sharp B/$\bar{B}$ texture with <110>//SD and (111) parallel to SPN is observed in the sub-regions very close to the tool-materials interface. It can also be easily recognized that during the later stage of deformation, B and $\bar{B}$ components are well developed with similar intensities as shown in figure 4.21f-h.

To briefly summarize the texture evolution in the PZ of 15mm sample, the behavior of the texture evolution can be categorized into two branches:

1, first part is about the rigid body rotation and materials transportation around the rotating tool, the entire pole figures are rotated clockwise, same as the way that processing tool rotates; because of the deformation nature of FSBE process, materials being processed are dragged and transported around the processing tool while at the same time being pushed and flow upward towards the top of the tube. Thus a spiral nature of materials flow is expected and the grains are transported in a rigid body way, resulting in the rigid body rotation of the PFs and the shear reference frame accordingly. It should be noted that the spiral fashion is mainly about rotation around TD and marginally flowing along TD, which is regarded as disturbance and will also be named as axial shear. The

effect of axial shear is more dominant in later samples and its effect will be addressed in detail in the next session regarding the samples of 30mm and 65mm.

2, the second branch is about shear deformation, fundamental driving force of the formation of B/$\bar{B}$ fiber texture is the shear deformation from rotating tool. Materials flow and transportation can't transform C type texture or any forms into B texture. Ideally if enough shear deformation is applied, even if some rigid body rotation around TD and some disturbance from the axial movement of the tool are involved, the grains should be immediately realigned to the orientations that correspond to the ideal shear texture with minimal offsets. Also, the C type texture will transform into B/$\bar{B}$ with a narrow transition region and the materials start showing stable B/$\bar{B}$ texture, as shown in the tube bottom in fig 4.3. However, the shear deformation in the tube wall is not enough to transform the transitional texture component into stable texture type right after the transition region and align the <110> to SD against the materials transportation until it is very close to the tool-materials interface. The amount shear applied to the materials at this location should be much less than the case in the tube bottom, since in the bottom materials is forged, stirred and thus severely deformed whereas in the tube wall, the amount of shear deformation is mainly relied on the contact condition of the tool materials interface without significant forging effect. The axial shear or axial material flow will also tend to move the ideal shear texture out of plane in the PFs, but should be of a minimal extent.

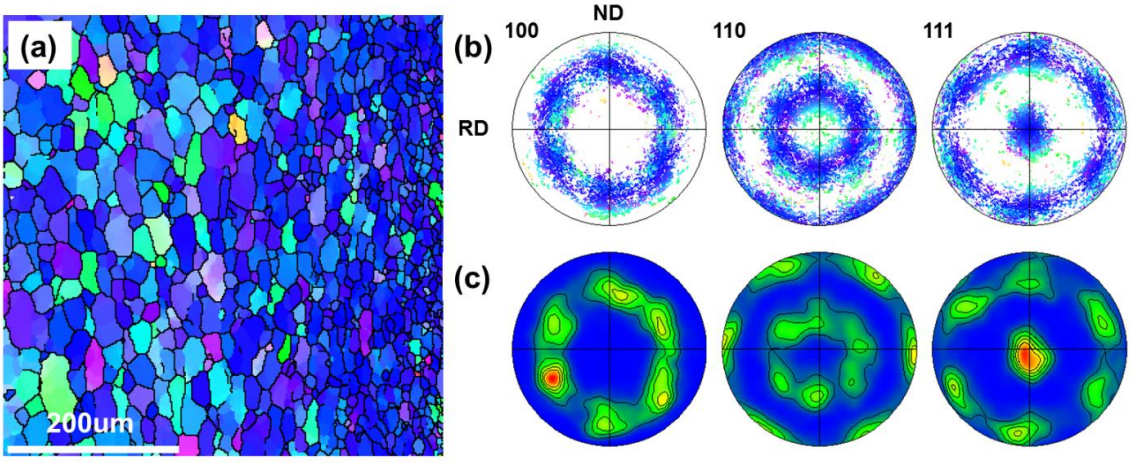

Figure 4.30 (a) IPF image (b) scattered pole figures and (c) contoured pole figures for the processing zone of 15mm sample

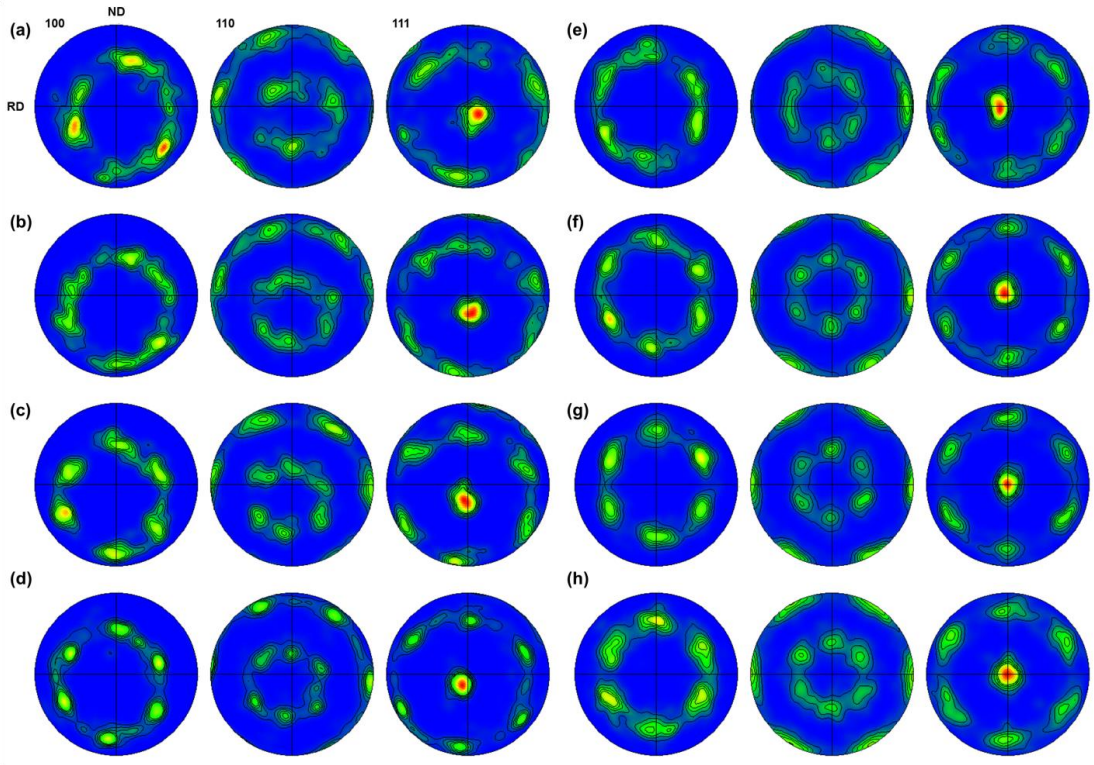

Fig 4.31 (a)-(h) texture evolution across the processing zone of 15mm sample

To summarize the texture evolution of the 15mm samples, several key points are observed and discussed:

1, the microstructure and micro-texture evolution of the 15mm sample is based on the micro-texture that is pre-formed in the tube bottom and tube corner, that is to say, deformation history is playing an important role and the preformed texture in an earlier step is regarded as initial texture in the current situation.

2, generally speaking, texture evolution at this location follows similar mechanisms as observed in the tube bottom, both the activity of C component and A components are observed as transition texture.

3, less shear deformation or strain rate is expected at this location, the amount of shear deformation mainly related to the contacting condition of the tool-materials interface.

4, the effect of materials transportation and thus the rigid body rotations of the measured PFs are more prominent because of the spiral materials flow and the lack of shear deformation.

Texture Evolution of 30mm Specimen

As the process continues, materials located in the tube bottom are extruded then flows into the tube wall and finally reaches the top of the tube. During this process, the processed materials, either heavy deformed by friction stir thus greatly refined as in PZ or marginally strained as in the TMAZ, are further deformed by the rotating tool, that is to say, the materials is under continued shear deformation while flowing into tube wall. Meanwhile, the entire tube is being twisted in a spiral fashion during the extrusion

process. This flow behavior would change the micro-texture by transporting the local shear reference frame and applying deformation in the axial direction. Additionally, extended heat exposure is also expected and possibly result in grain growth and texture variation.

As mentioned in the previous chapter, the 30mm sample can be treated as 15mm sample that is extruded and developed in a further step of the process. However, at 30mm location, grain growth is observed rather than refining, indicating the fact that extended exposure to heat result in dynamic recovery and grain growth of the microstructure, and the shear strain applied to the materials is insufficient to further refine or even maintain the microstructure.

Before addressing the micro-texture evolution of the 30mm sample, a couple of key points of will be proposed base on the deformation condition and relevance to other samples:

1, comparing with the 15mm sample, no significant amount of subsequent shear deformation is applied to the materials, as confirmed by the coarsened microstructure. Grain refinement is observed in the region very close to the tool-materials interface but the penetration and the effect is limited.

2, the spiral flowing nature of the tube will start playing an important role in controlling the micro-texture evolution by transporting the materials in a similar fashion thus rotating the local deformation geometry. The axial component will even make the stable B/$\bar{B}$ textures being hard to recognize.

3, the measured texture is expected to be weak and scattering due to low strain level.

4, extended exposure to high temperature will also change the microstructure and micro-texture, especially when the rate of straining is low.

The IPF image of the 30mm sample with respect to TD is plotted in figure 4.32. This map is also divided into TMAZ, transition region and PZ. However, it can be seen that grain growth occurs across the entire map, with only very limited refinement near the tool materials interface, compared to the 15mm sample. The texture should also be interpreted based on the texture observed in the 15mm sample, and major differences should be recognized and interpreted properly.

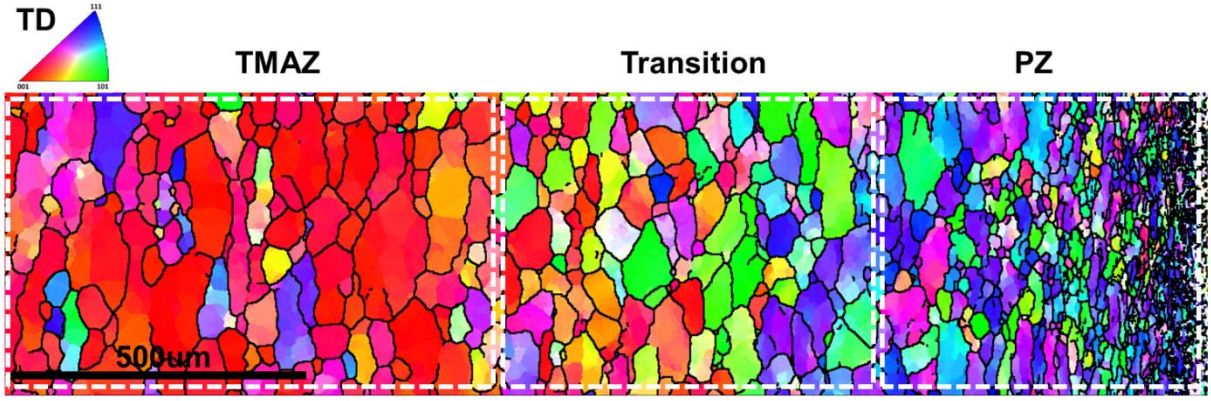

Figure 4.32 IPF image of 30mm region

Starting with the texture in the TMAZ, as observed in figure 4.33, the micro-texture of the entire TMAZ region exhibits a relatively ideal fiber texture, similar to the as-received materials, while the TMAZ in the 15mm sample shows a distorted cube/rotated cube component with the strong 100 pole off center by around 15 degrees

and moving to the first quadrant. This might because of the in situ annealing which can result in the formation of the cube texture [62] and it seems that deformation in the TMAZ of this sample is minimal, which can be substantiated by the coarsened grain structure and grains showing lower aspect ratios compared to the TMAZ of 15mm sample, where most grains are deformed and elongated. Additionally, the LAGBs density in this region is also very low, suggesting an annealed microstructure. No grains showing <110>//TD or any indication of the formation of C texture is found, but surprisingly some grains showing <111> close to TD are observed. Based on the previous discussion, the formation of <111> direction aligned to TD might be an indication of the transformation to B/$\bar{B}$ texture in a rotated shear reference frame. As mentioned in the texture analysis of the tube bottom, some grain with favorable orientation can directly evolve into B/$\bar{B}$ components under deformation. To study the behaviors of these grains more clearly, they are extracted and analyzed separately.

The orientation distribution of the extracted grains is plotted in the PFs as indicated in figure 4.34b, and the PFs of the entire TMAZ region is also attached in figure 4.34c for comparative study. As indicated in the PFs, the assumed SPN is labelled. This SPN is determined by adopting the conclusion in the 15um and bottom sample that during early stage of deformation, grains will orientate themselves by rotating around the SPN. As shown in the PFs of the figure 4.33 b-c, the extracted component seems sharing a same 110 pole along the SPN. Another very important reason for identifying this marked direction as SPN is actually back-extrapolated based on the following analysis, which will be addressed very soon. Now, based on the SPN assumed or determined to

some extent, the extracted component actually exhibits E/E- components with <111> parallel to SD and (110) plane perpendicular to SPN. This component is actually observed in the tube bottom under slight deformation, which might be the case here since even no observable transition texture of C component is found. The discussion about the texture formation in the TMAZ is only briefly investigated and the texture evolution next to the TMAZ, i.e. transition region will be addressed.

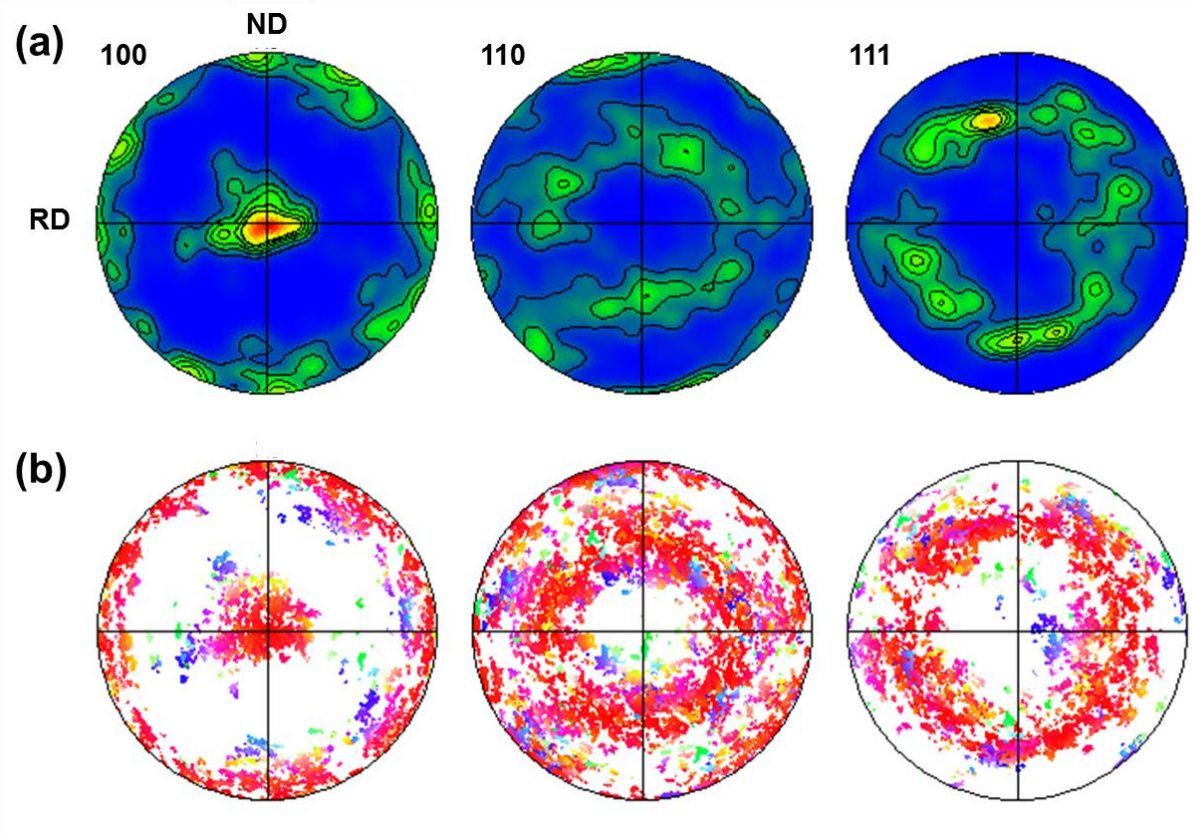

Figure 4.33 Micro-texture of the TMAZ region of 30mm sample

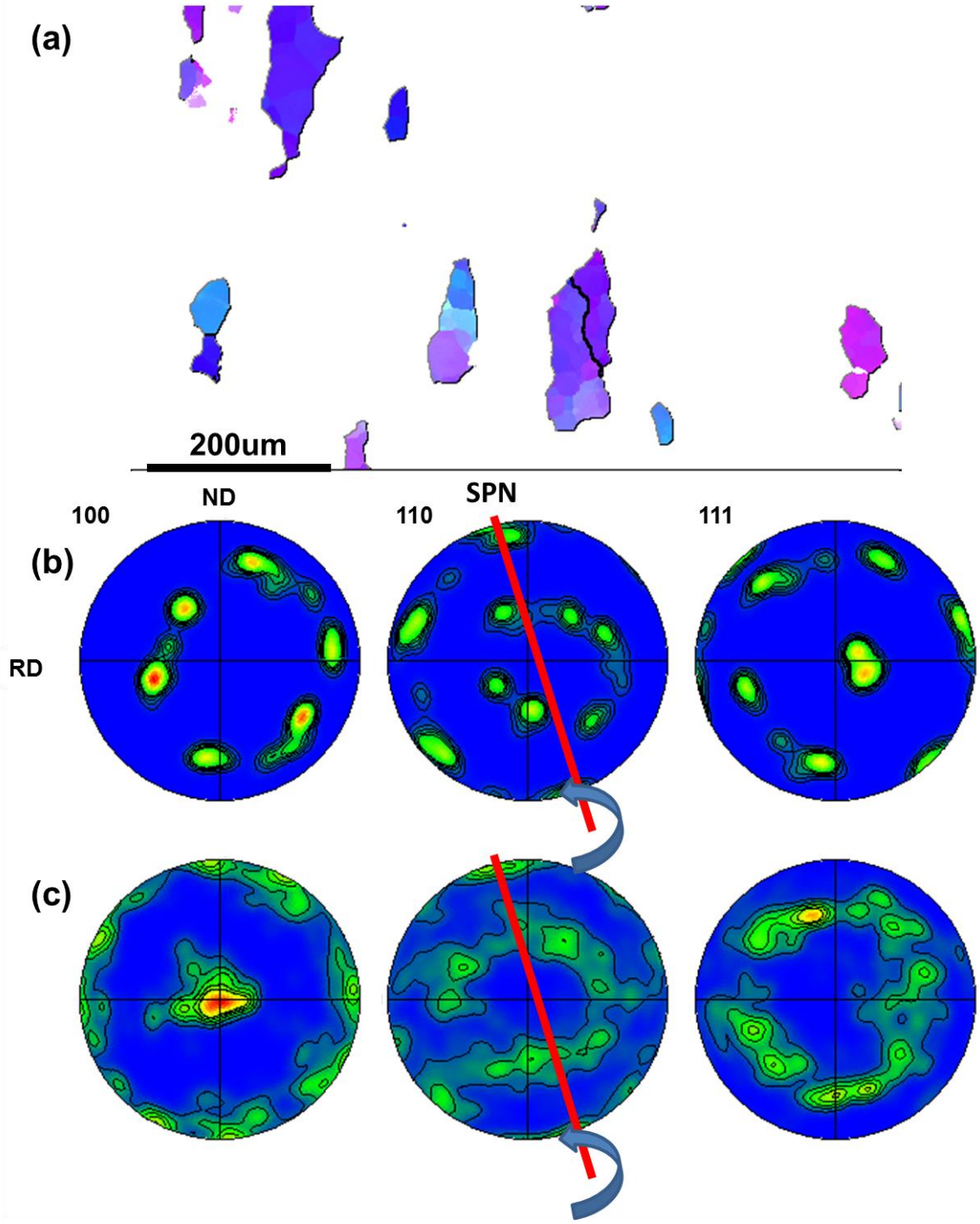

Figure 4.34 (a) IPF image (b) pole figures of the selected grains and (c) pole figures for the TMAZ of 30mm sample

The IPF image regarding TD for the transition region is shown in figure 4.35a, corresponding scattered PFs shows two prominent components of <100>//TD and <110>//TD. As in the previous sample, unstable transition texture should be expected in this region. By observing the contoured PFs in figure 4.35c, it is founded that the entire PFs are scattering and the orientation distribution is spread everywhere, with the exception that <100>//ND in the 100 PF is strong and being relatively constant. Thus it can be deducted that the <100> direction is relatively stable during the texture evolution at this stage, and this phenomenon is notified when the C component is formed by the rotation of PFs around <100>//SPN, as in the case of the transition region at 15mm sample. It can also be projected that the pole showing high intensity should be the SPN of the local shear reference frame. To further identify the evolution mechanism and verify the assumption made regarding the SPN. Grains showing <100> close to TD and <110>//TD are extracted and discussed separately, the results are shown in figure 4.36. It can be observed that from the PFs in fig c that grains showing 100//TD shows a similar texture type as in the TMAZ; while it seems like that the PFs are stretched around the direction that is believed to be SPN. The grains showing <110> aligned to TD exhibit a C texture with the same SPN, thus it can be concluded that C component is formed via a similar fashion in the transition region as in previous samples, by rotating around the SPN of the local shear reference frame that most <100> direction have already aligned to. It should be noted that the entire shear reference in the transition region is rotated clockwise by around 10 degrees compared to the frameworks in TMAZ, which corresponds to the materials flow and transportation.

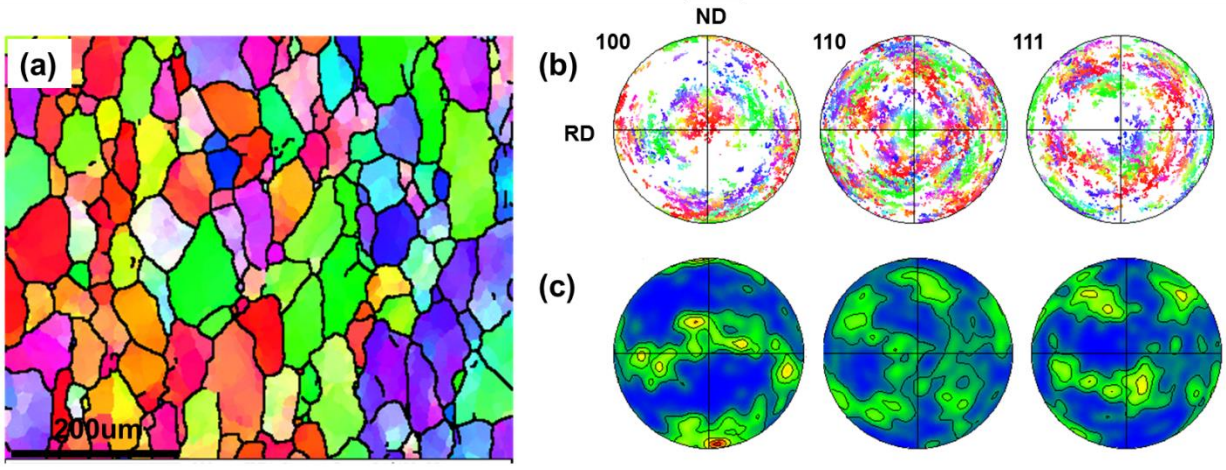

Figure 4.35 (a) IPF image (b) scattered pole figures and (c) contoured pole figures for the transition region at 30mm location

The IPF image of the PZ and corresponding PFs are shown in figure 4.37, it can be observed from the IPF image that grains are elongated along the extrusion direction and most grains are not showing ideal <111>//TD. Pole figures in figure 4.37b shows a texture component resembles the off centered B/$\bar{B}$ types. Interesting, the center pole of the (111) PF is moving around TD, or more accurately in a spiral fashion. This might indicate the assumption that the micro-texture evolution in this sample is mainly controlled by the materials transportation around the processing tool, which is also moving in a spiral way technically.

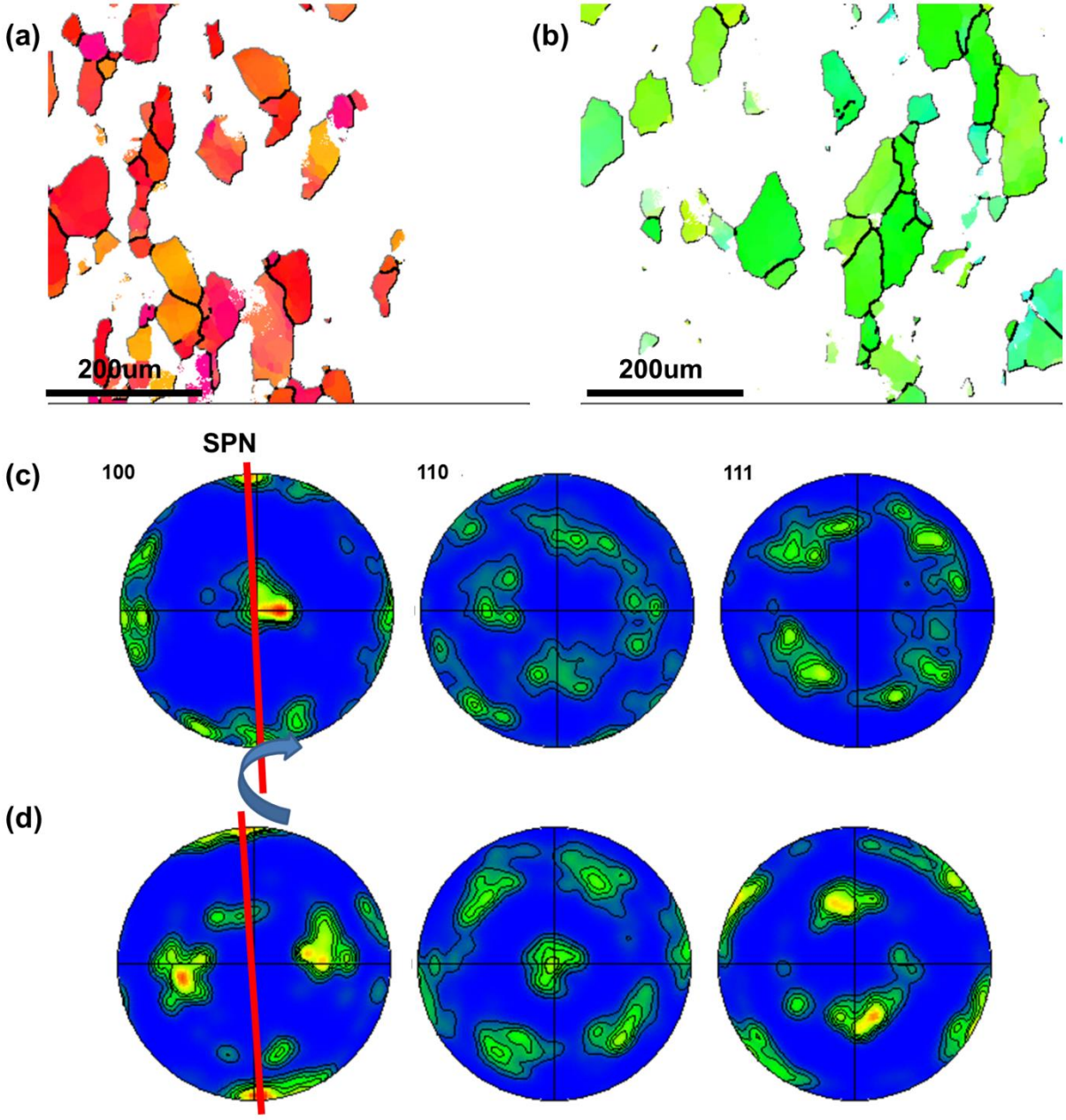

Figure 4.36 IPF image for selected grains showing (a) distorted fiber texture and (b) C texture and (c)-(d) corresponding pole figures

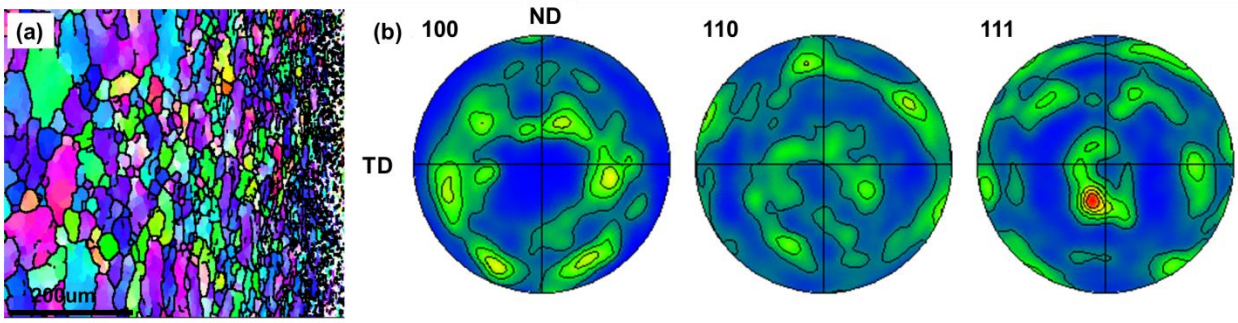

Figure 4.37 (a) IPF image and (b) pole figures for the processing zone at 30mm location

Thus it is necessary to subdivide the EBSD scan of PZ into several segments to better visualize the texture change from the side close to the transition region to the side close to the materials-tool interface. Six subsets are made and the corresponding PFs are plotted in figure 4.38, all the PFs are plotted in RD-ND-TD coordinating systems without any imposed rigid body rotations. It is observed that the orientation distribution of crystallographic directions in these PFs shown in figure 4.38a-e are not localized, sharp and stable, rather, they are scattered and rotated around the center of the PFs, forming a ring around the center of the PFs. It is also believed that these rings should be distributed around the center of the PFs, i.e. the TD, not the center pole of (111) because the center pole of (111) is also rotated and stretched accordingly. However, apart from the scattering characteristics and the off centering nature of the entire pole figures (off centering might mainly come from the transition from C and affect by the axial flow to a less extent) , it seems that the B/$\bar{B}$ components are still observable as well as the transformation from intermediate texture component, even if they are rotated continuously due to the materials flow. Since the 30mm samples can be treated as 15mm

sample that is further processed, the B/$\bar{B}$ textures should be expected in the PZ especially near the tool-materials interface, despite the fact that the texture is more diffuse due to the flowing characteristic of the FSBE process and extended exposure to heat. At the same time, by observing the PFs in fig4.38 and comparing with the result near the PZ-transition region, it can be easily concluded that the texture in the PZ is transformed from C, shown in figure 4.38a, and evolving into B/$\bar{B}$ fiber under further development, shown in figure 4.38 b-f, while the local shear reference frameworks are rotated continuously in a clockwise fashion at the same time. It should also be noted that, despite of the reference frame change, the subset near the tool-materials interface shows SD//TD (ideal location) for both 15mm and 30mm samples, indicating that the relatively strong shear deformation contributes to the alignment of SD. In the case of 15mm sample, strong B/$\bar{B}$ texture is formed; while for 30mm sample, the expect B/$\bar{B}$ component is distorted with the <112> direction slightly away from the SPN.

Regarding the materials transportation and local shear reference frames, the PFs in the 30mm sample is rotated continuously and to a similar extent as in 15mm sample, indicating equivalent materials transportation around the tool. The proposed SD of local shear reference frame for each set of PFs is indicated by the red line in figure 4.38. It should be noted that there is a difference in the 'phase' between 30mm and 15mm sample. For example, the proposed SD near the transition region of 15mm is around 45 degrees off the ideal shear direction, which is RD, while in 30mm sample the assumed SD is aligned close to the RD, as shown in figure 4.37 and figure 4.38a. However, this does not mean that the shear deformation applied to the local materials exhibits such a

SD, rather, it is actually resulted from the materials flow that happen to transport the materials that is deformed in a previous step and has already developed a similar texture into the location that is being analyzed. This might also explain the ‘phase’ difference between 15mm sample and 30mm samples with respect to the SDs and they are believed to be at the different stages during the entire process. Interestingly, the texture close to the tool materials interface starting showing a similar B/ B̄ component even if the case in 30mm sample is still scattering the SPN is aligned perfectly, this still suggest that the materials close to the tool is subject to relatively strong deformation that tend to transform the SD and SPN to its ideal location of the deformation geometry.

To briefly summarize the texture evolution for 30mm sample and its relevance as well as difference compared to 15mm sample, several key points are noted:

1, basically the 30mm sample is of a later stage of 15mm sample that is further developed during the entire FSBE process, that means, 15mm sample is subjected to further straining and materials transportation and forms the microstructure observed in 30mm sample

2, the major reason for the scattered texture should be marginal amount of shear deformation is applied when the materials flow from 15mm to 30mm location. While at the same time relatively strong B/ B̄ component that is already formed in the previous step is moved around by the rotating tool. On top of that, dynamic recovery and grain growth is also observed due to the lack of deformation while the material is exposed to heat, this will also modify the micro-texture.

3, Despite of the texture observed in 30mm sample is scattered and weak, fundamentally it is still showing similar texture components as in the case of 15mm sample. Major difference lies in the texture component is more affect by the spiral materials flow, which becomes more prominent due to the lack of continued shear deformation.

4, for both 30mm and 15mm samples, the local shear reference framework is rotated continuously around TD in a spiral fashion. This effect is more prominent in the 30mm sample. Additionally, the proposed local SDs in each subset of 30mm sample is not identical to the case of 15mm sample, this should be attributed to the fact that the spiral materials flow is accumulative and the two samples are at the different stages of the process, thus a 'phase offset' is expected.

5, the spiral flow or materials transportation consists of axial rotation and axial movement with the former one resulting in the rotation of shear reference frame around the TD while the later component moves the texture out of RD-ND plane, as in the case of figure 4.38f. Extra care should be taken when the axial movement is considered since the shear frame might be changed in an out of plane fashion to the extent that another texture component is observed, while in reality that happens only because of the rigid body movement of the shear framework.

6, texture components observed in the segments close to the tool-materials interface is close to the ideal B texture because of relatively high strain levels.

To briefly summarize the texture results and discussion of 30mm sample, 30mm sample can be regarded as the successor of 15mm sample that is subject to additional

deformation, materials flow and thermal exposure. Also texture observed at 30mm sample is all based on and evolved from the types that are already formed in the previous step, i.e. at 15mm location. Heat exposure result in grain growth across the tube wall, but its effect on micro-texture is only noticeable in the TMAZ (might because of the minimal stain level). Materials flow and transportation is playing an dominant role in controlling the micro-texture and the local shear reference, especially in the PZ and transition, since no major shear strain is expected other than the region that is very close to tool-materials interface.

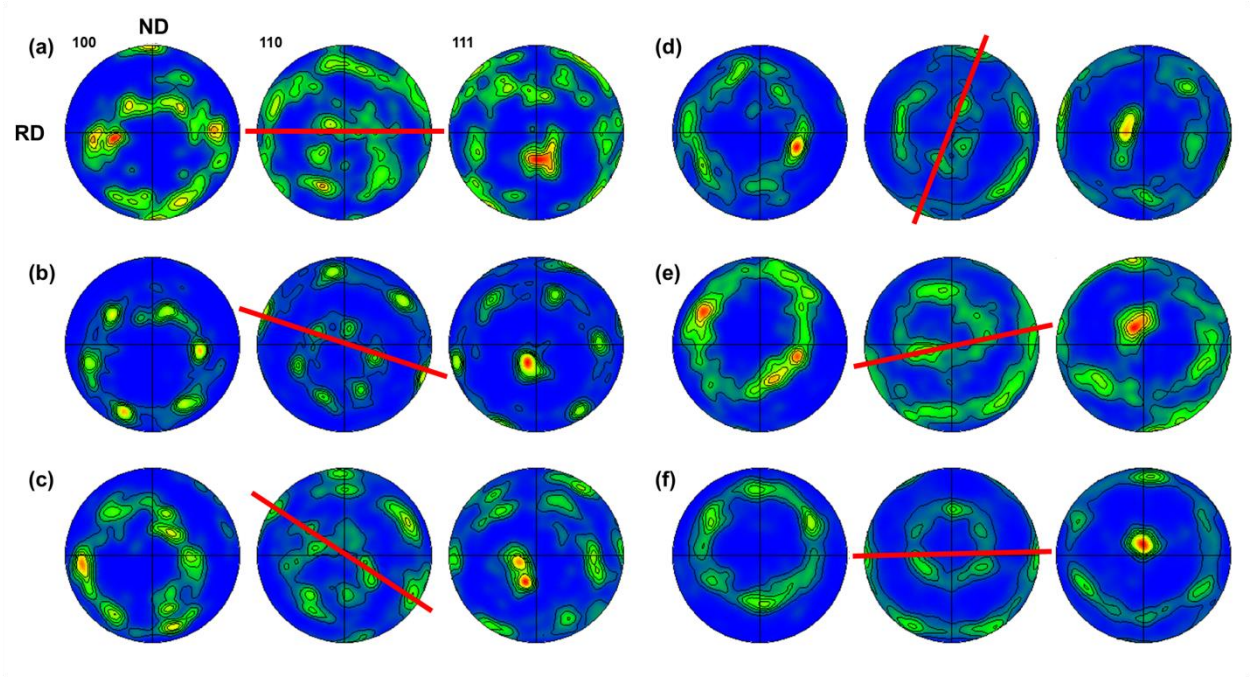

Figure 4.38 (a)-(f) Texture evolution within the processing zone of 30mm sample

Texture Evolution at 65mm Location

As discussed in the 30mm specimen, materials initially located at the tube bottom are friction stirred in the beginning then flows into the tube wall. While the material is

extruded, the microstructure that is formed in the previous step will be subject to further deformation. At the same time the micro-texture evolution will also be affected by the materials flow since the spiral characteristic of the tube forming will move the processed materials and the texture component accordingly, which is interpreted as changes of shear reference frame due to materials transportation.

In the case of 30mm sample, when compared with 15mm specimen, continued shear deformation from the processing tool only affect limited amount of materials located close to the tool-materials interface. Also, grain growth is also observed across the scanned region, indicating extra exposure to heat while marginal amount of deformation is applied to refine the microstructure. Thus the spiral materials flow is playing an important role in controlling the formation of micro-texture. Generally speaking, when the material flows from 15mm to 30mm location, minimum shear deformation is applied while materials flow is relatively important to interpret the micro-texture evolution.

However, the 65mm sample is believed to be different regarding the deformation history, thermal history, microstructures as well as micro-texture evolution. As detailed in the previous chapter, the microstructure of the 65mm sample is significantly refined during later stage of deformation while flowing from 30mm to 65mm location. The grain structure located inside the PZ is refined by up to another order of magnitude and the entire PZ is penetrated deeper into the TMAZ, as measured in the previous section. It is believed that large amount of shear strain is introduced during the later stage of deformation because of the strong tool-materials contact resulting from materials

shrinkage. At the same time, materials transportation should also be playing a major role in contributing to the variation of local deformation frameworks since the spiral materials flow is cumulative. Thus distinct texture development associated with the process should be expected.

In the following part, EBSD scans are performed across the tube wall located 65mm from the tube bottom, TAMZ, transition region as well as PZ will be analyzed and mechanisms of texture transformation will be discussed based on PF/orientation analysis and comparison with previous results. Several EBSD scans are performed on 65mm sample and their corresponding locations on the tube wall is illustrated in figure 4.39. Due to the fact that characteristic dimensions of the microstructure at each location (TMAZ, transition, PF) can be different, several EBSD maps are acquired next to each other with different step size to maximize the efficiency of the machine. As indicated in figure 4.39, four EBSD scans are made on 65mm specimen across the tube wall, with the scan labeled No.1 performed predominantly located inside the TMAZ, while the scan 2 included the transition region and PZ, region 3 and region 4 are two extra smaller scans that use a finer step size since the microstructure at the later stage of 2 starts to be refined to a further step as observed by the optical microscopy.

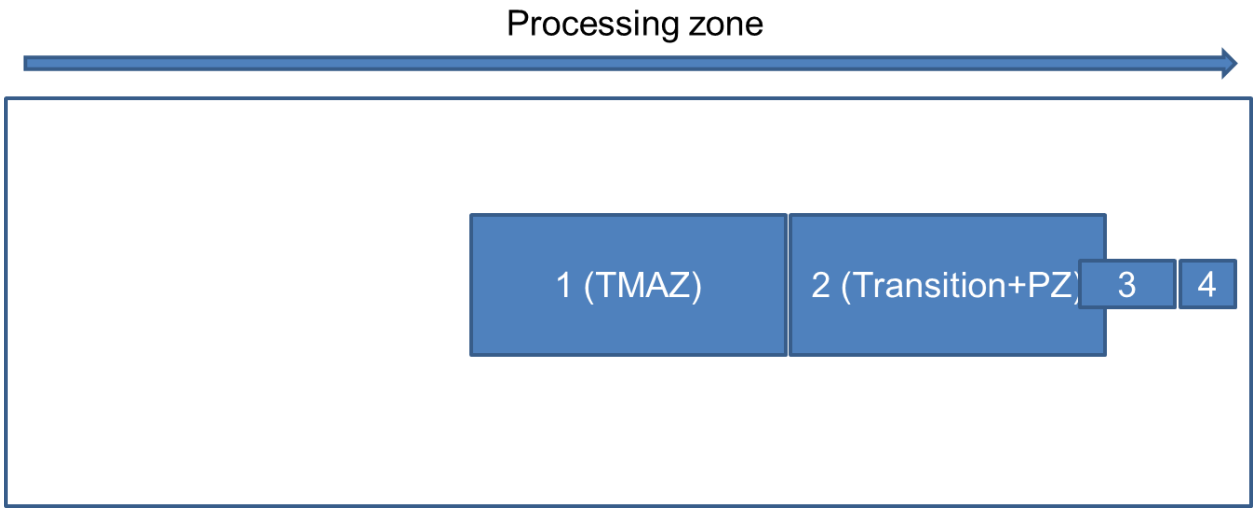

Figure 4.39 Distribution of analyzed regions for 65mm specimen

Before the investigation of texture evolution at this location, something that should always be kept in mind is: materials located at 65mm wall mostly come from the materials that are originally located in 30mm and 15mm regions in earlier stages of processing. That is to say, 30mm specimen is subject to extra shear deformation while flowing to 65mm region. The strain level of this extra shear is believed to be relatively low, as confirmed by the microstructure results obtained at 30mm location. At the same time, compared with previous analysis performed at 30mm wall, the effect of spiral materials transportation should be at least at the same level, or most probably, more dominant in controlling the texture change.

The IPF image of the TMAZ region is shown in figure 4.40 and each pixel is colored with respect to TD. It can be observed that most grains are showing <100> aligned close to TD with elongated grain structure, suggesting typical grain orientation and microstructure of TMAZ. While some grains exhibiting <110>//TD are also

observed, suggesting the possible formation of C component. It should be noted that the grains showing <110>//TD are mainly distributed next to the transition region, where the strain level is higher; meanwhile these grains are refined from their precursors via continuous dynamic recrystallization, as indicated by their decreased grain size and aspect ratios. Additionally, grains showing <111> close to TD, which typically suggests the formation or transition into B/$\bar{B}$, is also observed. To investigate the formation of these texture components, detailed discussion will be performed by subtracting and investigating certain sub-regions or grains showing a distinct type of texture, orientation or transformation. Meanwhile, analysis for these sub-regions will not only be performed independently, their connections and differences will be addressed at the same time.

A very important note is that if the texture evolution is interpreted by means of shear deformation or shear texture, the local shear reference should be predetermined either from the deformation geometry or deducted from the combination of measured texture and the current knowledge regarding the materials and process. In our cases, the exact local shear reference deformation frameworks are hard to be capture directly since the materials flow and extrusion is continuous and changes with the amount of strain, the local shear reference frame will be deducted, as in the cases of the 15mm and 30mm specimens. In the TMAZ region, no significant difference regarding materials transportation should be expected since the strain level is low, grains are most probably transported all together into a similar framework, which is the case of 15mm and 30mm specimens and will also be substantiated in the upcoming analysis of the current 65 sample.

By observing the scatter PFs of the entire region, it can be clearly seen that the grains showing <100>//TD, colored by the red, which corresponds to the initial fiber texture that is developed into a component that resembles cube/rotated cube under low shear strain and extrusion, are evolving toward two directions as illustrated in the (100) PF of figure 4.40, indicated by the two black arrows in figure 4.40b, these two tendencies turned out to be predominant mechanisms of texture evolution in the TAMZ and transition region, which will be detailed in the later discussion. The contoured PF in figure 4.40c also confirm the similar trend, the center pole (001) PF is stretched along both RD and ND with the component along RD is stronger. Grains showing <110>//TD colored as green are actually showing a typical C component with a rotated shear reference frame around TD by 80-85 degrees. With this shear framework, the local SD should be 5-10 degrees off ND and this framework will be tentatively used as the shear reference frame for the entire TMAZ. As also mentioned in the previous paragraph, the grains exhibiting C texture are located closer to the transition region. Based on the discussion and conclusion drew from previous samples, it is believed that the C component is formed mainly by transforming the distorted initial fiber texture around SPN. Grain showing <100> aligned close to SPN in the local shear reference can evolve into C texture component by rotating around <100>//SPN, this should not be any rigid body rotation, rather the reorientation is related to the crystallographic slipping and the statement regarding rotation is just used to show the transformation of PFs in a more direct sense. It should also be noted that, those grain transforming into C component does not necessary showing <100>//SPN ideally, since they are still under the stage of grain

reorientation, the grains showing <100> aligned close to the SPN are most likely transformed into C component due to the minimal resistance to grain reorientation, as elaborated in the bottom sample. Additionally, it is almost certain that the movement of center pole of 100 toward ND is associated to the formation of C component, which will be further substantiated in the texture analysis of the grains showing <110>//TD. Grain showing <111>//TD, which signifies the formation of B/ $\bar{B}$ component, are also observed, however, their <111> directions are not even align to the TD very well, as shown in the <111> PF of figure 4.40b. It should be noted that even if there a tendency of forming B/ $\bar{B}$ component, they are not supposed to be strong or even close to its ideal location due to limited amount of shear strain.

Concluded from the contoured PFs shown in figure 4.40c, the dominant texture in the TMAZ is still distorted cube/rotated cube texture while the C, B or A components are not really obvious at this point since they are relatively weak. Due to the importance of these texture types, even if they are not very strong in the TMAZ, in understanding the texture evolution of the entire process, the TMAZ map is subdivided into several subsets and analyzed individually. The subsets are taken based on the principle that it can represent the formation or evolution of a typical texture component, either transitional or stable, rather than physically divided the map into several regions close to each other. The abovementioned shear reference frame will be adopted in the following part.

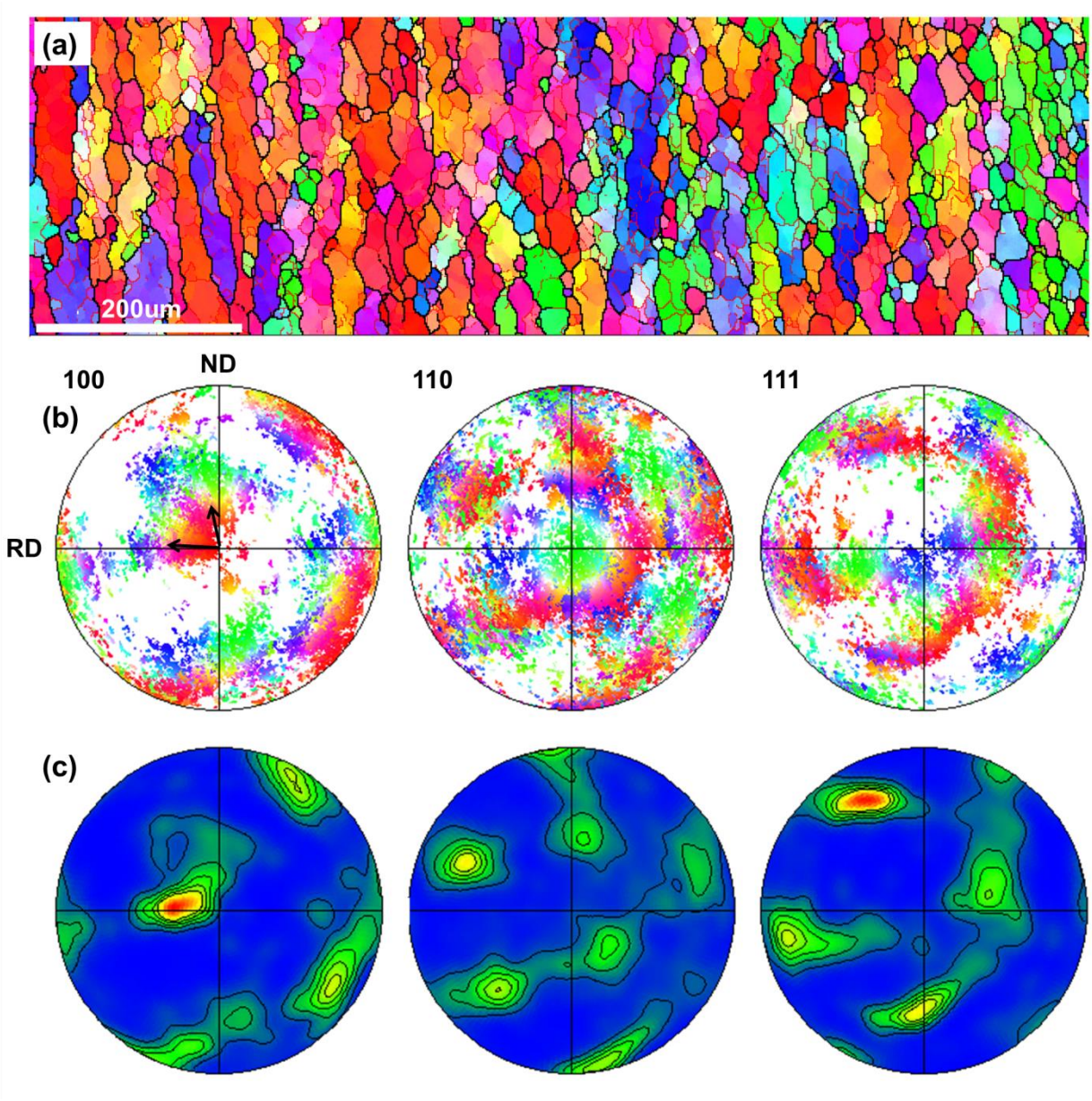

Figure 4.40 (a) IPF image (b) scattered pole figures and (c) contoured pole figures for TMAZ at 65mm location

This first subset is subtracted from the left end of the TMAZ where the strain level is believed to be low. The cube/rotated cube component with <100> close to TD is transformed into a component with <111> close to TD via the 'first path' as shown in figure 4.40. However, further scrutinization indicates that <111> direction is almost parallel to the RD and its equivalent is still around 20 degrees off from the center of (111) pole. Adopting the shear reference frame determined in earlier discussion, with the SD is shown by the red line in the 110 pole of figure4.41b, it is very interesting to observe that this component showing <111>//RD is actually the A component with <111> parallel to SPN and <110> aligned to SD, which has been reported in all of the previous sample and believed to serve as the transition texture of B. The formation of A component involves crystallographic rotation around the SD, as observed in figure 4.41 B c, the 110 poles located on the SD are relatively fixed during the transformation into A texture. Thus in the current situation, the explanation should be, the distorted fiber/cube texture is actually evolving into A component, which is typically a precursor to B texture. However, the formation of B close to its ideal location is not indicated bases on current shear reference frame since the shear strain is very low. Another important observation involves the formation of C component is not observed in this region, which might suggest that the formation of B texture via A component is more favorable at relatively lower strain level while the path through C is more realistic at higher strain level. To confirm this statement and also investigate the 'second' path, another subset is taken from the TMAZ map that is close to the transition region, the results are shown in figure 4.42.

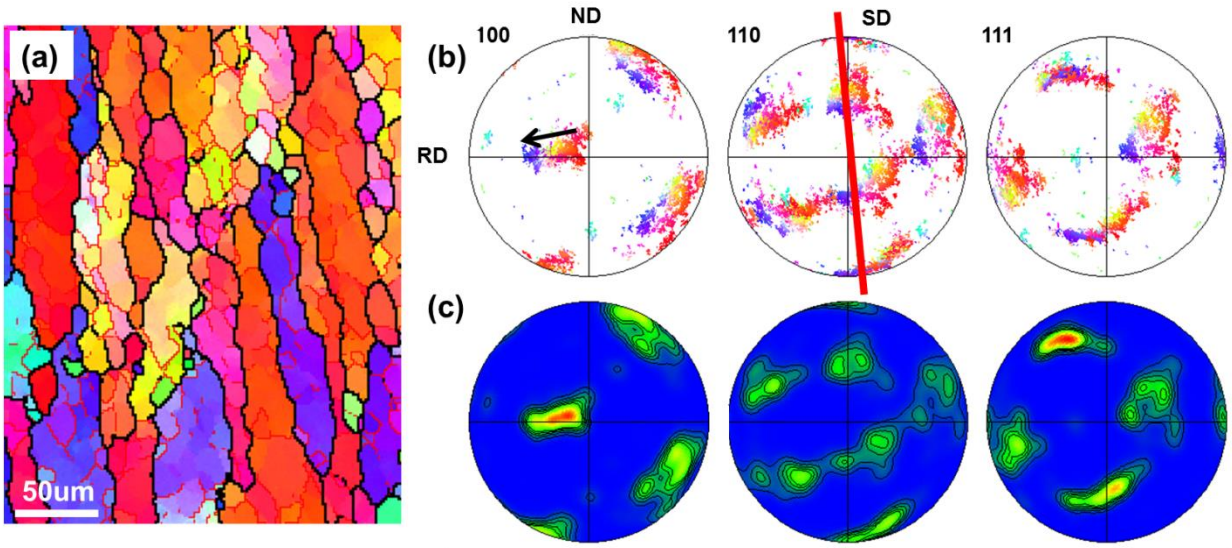

Figure 4.41 (a) IPF image (b) scattered pole figures and (c) contoured pole figures for selected region within the TMAZ of 65mm sample

It can be seen either from the IPF figure or pole figures that C component is the dominant texture type at this region, which is close to the transition, while other components still present but are relatively weak. Meanwhile, a distinct observation made from the figure 4.42b is that the shear reference frame of this C component still coincides with the frameworks of the subset address in figure 4.41, which is about 800um away from the current subset. That is to say, the shear reference framework is relatively constant within the entire TMAZ region, even if a strain gradient might exist across the TMAZ. During the FSBE process, the entire TMAZ region is subject to relatively low shear strain level, and the temperature distribution across the tube wall should be relatively constant due to the excellent conductivity of aluminum, thus the materials

across the TMAZ region might flow in a similar pace. Also this C component is not ideal even if in the local shear reference frame thus it is still under transition.

By observing the scattered orientation distribution of each pixel in the PFs, it is noticed that the grains showing <110>//TD are evolving into the C component by rotating around SPN, as indicated in the scatter pole figures, i.e. the center pole of 001 move toward ND and forms one 100 pole of the C component while the 100 pole close to RD is relatively stable during the transition. This transformation is also discussed in previous samples since some grains already shows <100>//SPN, when subject to moderate strain level, the grain will preferentially align the <110>//SD to SD while keeping the SPN stable. Thus it looks like that the C component is formed from the rotated cube texture by a 'rotation' around the SPN, however, this rotation is of crystallography nature and different from the rigid body rotation of shear reference frame resulting from materials flow. Thus the general result is, the second branch in fig4.40b involves the formation of C component via a rotation around the <100>//SPN, similar to the results of previous samples. However, a strong 110 pole that is very stable during the transformation is observed located in the second quadrant of the (110) PF, and it looks like the entire PFs are rotated around this <110> direction. At the same time this 110 pole does not coincide with any macroscopic ND, TD or RD, as show in figure 4.42c. If this is the case, there might be a different mechanism responsible for the formation of C texture other than the conclusions drew regarding the formation of C texture based on previous samples.

Since the mechanism that grains with their <100> direction already aligned to the SPN can be transformed into C component by rotating around <100>//SPN in the local

shear reference frame is seemingly plausible as indicated in the figure 4.22 and being proven in our previous discussion, a further step analysis will be performed to figure out whether the new methodology is a more reasonable explanation for the formation of C component under current situation. To achieve this, grains that are believed to be involved in the transition are extracted to form a subset and their behaviors on the PFs will be analyzed. Since branch 1 and branch 2 transformations coexist in this map, grains that are evolving into A component as well as those showing <111> close to TD are excluded from the subset. The IPF image and the corresponding PFs are shown in figure 4.43. As observed in the PFs, the 110 pole in the second quadrant of (110) PF is very strong and being constant during the transformation. Orientation distribution on (110) PF seems like being stretched and rotated around this fixed 110 pole. While for (100) PF, the center pole of 100 is actually evolving vertically on the PF, while the entire pole figures are rotated around the fix 110 pole in the second quadrant. Another important notification is that another 100 pole consists of the C texture located in the fourth quadrant of the (100) PF is actually not evolved vertically along the ND, which is the case is the C component is formed while the <100>//SPN is fixed, rather this 110 pole is actually evolved from the third quadrant as shown by the lower arrow in (100) PF, and a clear trace around 45 degrees with respect to RD is noticed. The detailed reason why this specific <110> is relatively constant is unknown at this point, however, it should be related to the crystallographic nature of slipping, when the shipping occurs exclusively on a specific (110) planes, its highly possible that the orientation of this (110) plane is relatively stable on the PFs. Detailed analysis should be performed to unveil this

mechanism in future work. This suggest that the C texture formation might not be based on the crystallographic rotation along SPN in current case, rather transformation from distorted initial texture to C component is related to the activity of a specific set of (110) slip planes. As evidence by the (110) PFs of selected grain that are believe to be under transformation to C component, the location of one specific 110 pole is fixed while all other poles are rotated around it. However, that does not mean the mechanism proposed based on previous result is incorrect, rather, because of the complicated and changing deformation geometries of the process and that the effect of deformation history on the materials reaction to further straining, the formation mechanism of C texture proposed earlier is not very appropriate to explain the observation made for the current sample.

It is also noted that, apart from the formation of C type texture, the previous mechanism of ‘route1’ is also present in the current region that is close to the transition, indicating the mechanism of the transformation from into B component via A is functioning across the entire TMAZ. Thus the ‘route 1’ is observed across the TMAZ while the ‘route 2’ is only observed in the part of TMAZ that is close to transition region where strain level is relatively high, as confirmed by the formation of C component.

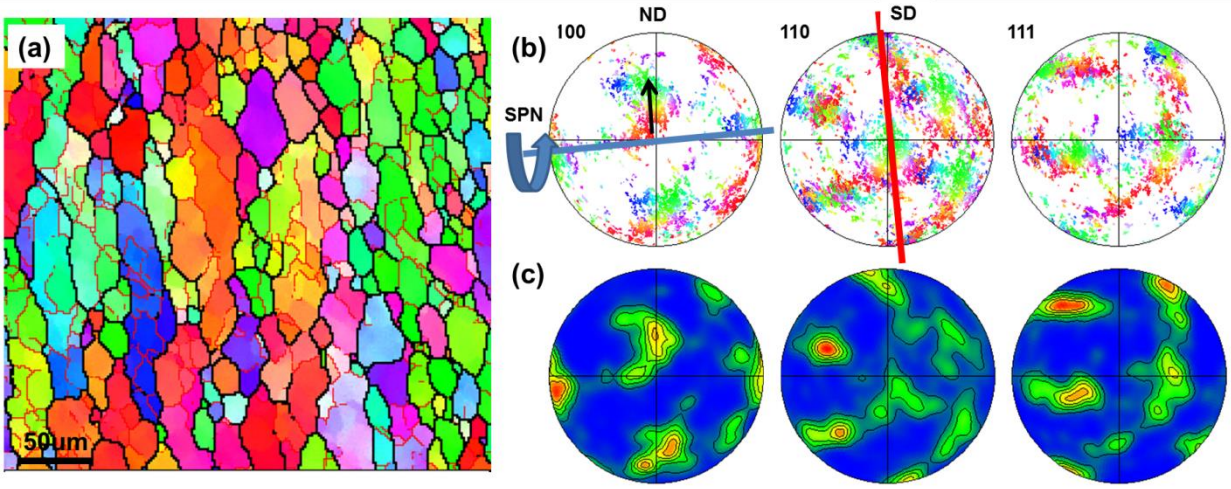

Figure 4.42 (a) IPF image (b) scattered pole figures and (c) contoured pole figures for selected region near the transition zone of 65mm location

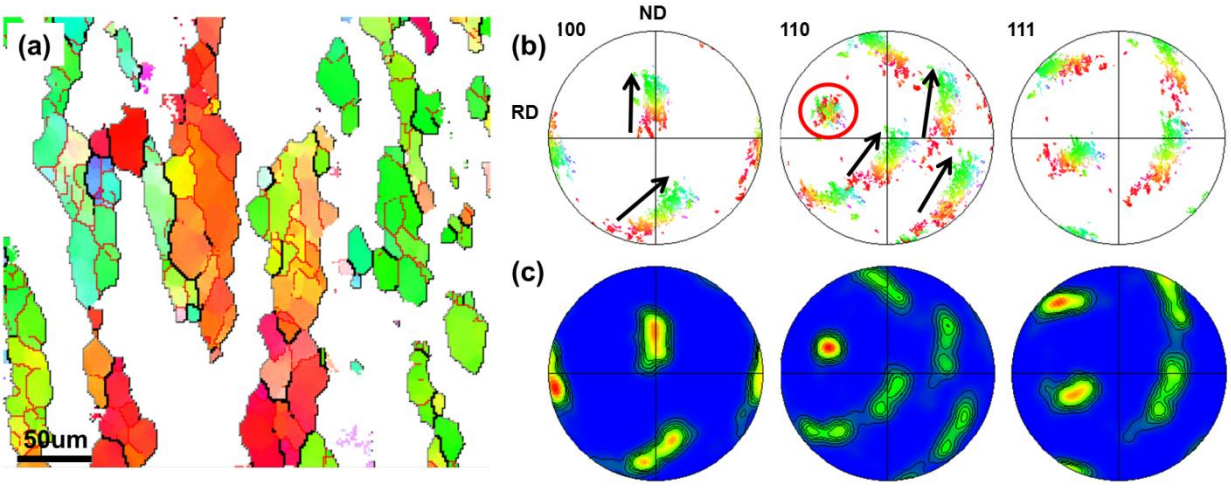

Figure 4.43 (a) IPF image (b) Scattered pole figures and (c) Contoured pole figure for selected grains near the transition zone 65mm sample

Regarding the grains showing <111> close to TD, they will be analyzed on a grain by grain basis since only a couple of them are observed in this subset. Two grains

are extracted from the map and PFs are plotted based on the orientation of each pixel. It can be seen form figure 4.44 that the grains showing <111>//TD are mainly evolved from the C component via crystallographic rotation around the SD in local shear reference frame. Especially the grain in figure 4.44b, it is obvious that the grain is moving away from the C component and transform into $\bar{B}$ around the <110>//SD. However, the part of the grain that is showing orientation close to C texture has already moved away from its ideal location. Unfortunately, we couldn't capture s single grain that is showing the entire reorientation process from C to $\bar{B}$ since the AA6063 aluminum is not very resistant to dynamic recovery. However, typically the formation of B/ $\bar{B}$ component in the TMAZ is not observed due to low strain level, grains exhibit favorable orientations or subject to high local shear strain actually involved into B component via C texture. But this contribution should be minimal since only several of this type of grains is observed.

Two major pathways for the texture evolution of the TMAZ has already been addressed, some minor texture component that is present in figure 4.40 will also be briefly discussed solely for the purpose of completeness and comprehensiveness of the current research. As shown in figure 4.45, the local shear reference frame is relatively constant by identifying the C component and its SD. Also, the texture component corresponds to the two pathways that have already been addressed, i.e. the formation of A and C component, will not be further discussed. Another texture type showing <111>//TD is observed with its center pole of 111 located in the third quadrant rather than the first quadrant, which is believed to be the major trend as discussed in the last sub-region close to the transition. Actually it is found that the existence of this

component is mainly associated to one specific grain, this grain is extracted and plotted in figure 4.46.

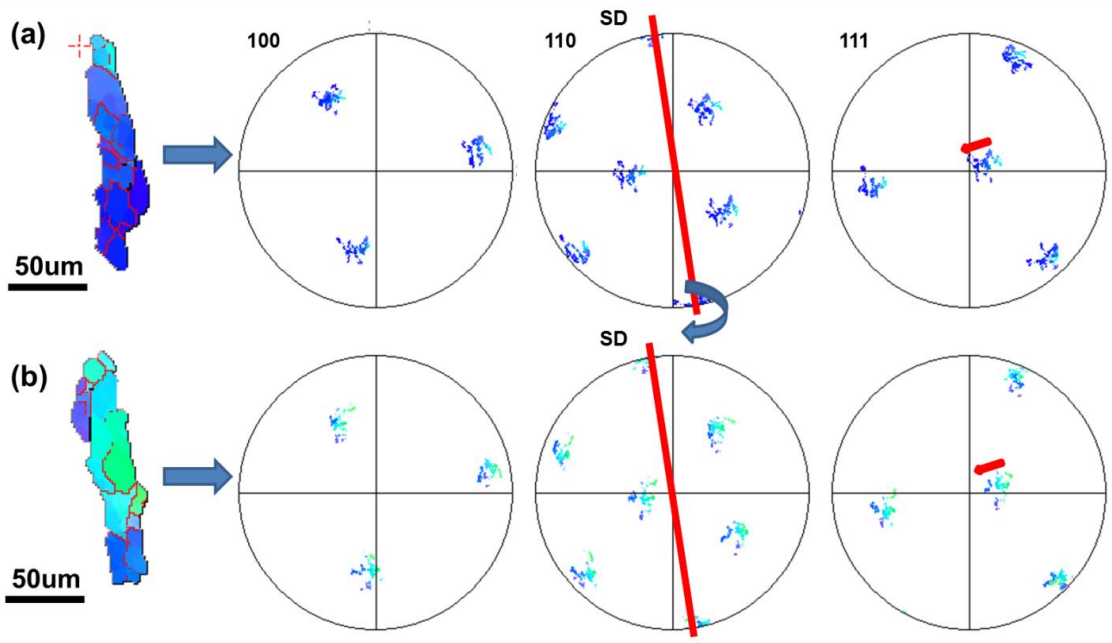

Figure 4.44 (a) IPF image and (b) orientation distributions on pole figures for two selected grains

It is clearly shown that the initial orientation of this specific grain is related to the twist cube texture and seems like evolving into one component of B texture without passing by and known intermediate orientation especially C component, while aligning <111> toward TD, one 110 pole marked by the red pole is actually fixed. This naturally makes us come to the assumption that this direction might be associated to the local SD. If this direction is presumed to be SD, the red/purple pixel can be immediately interpreted as A orientation in the local shear reference, while the pixel showing <111>//TD of the grain are correlated to the B type orientation. If this is the case, the local shear reference

frame is around 50 degrees off from the prevalent shear reference framework that is proposed for the entire TMAZ. Thus the possible explanation involves: first this transformation mechanism in another deformation framework is of minimal effect since only one such grain is observed, it become evident due to its size; second, the FSBE process is a relatively dynamic process involves continuous shear deformation, materials transportation and complex materials flow, it is possible that some grains are supposed to be belong to another framework are transported to the current shear reference in an out-of-pace fashion. Additionally, this out-of-pace framework will reappear and be address in the next session with respect to the transition region. It is indicated that this framework is not showing up by accident, on the contrary, it might signify another important mechanism of texture evolution, even if its effect might be marginal. Another type of grains exhibiting <111> close to TD as well as their neighboring grains is shown in figure 4.47. It seems like this component comes from the C component by evolving toward a different direction as in the major C- $\bar{B}$ texture evolution. However, the evidence for this type of transformation is insufficient and the mechanism is still under investigation.

To briefly summarize the texture evolution of the TMAZ, several key points should be noted:

1, the local shear reference frame across the entire TMAZ is not changed markedly, despite of the continuous materials transportation, the materials of the entire TMAZ should be transported in a similar pace and result in the constant shear framework.

2, two major pathways of the texture evolution with respect to the distorted initial fiber texture are: forming A component first then B and transforming into C texture then $\bar{B}$ texture.

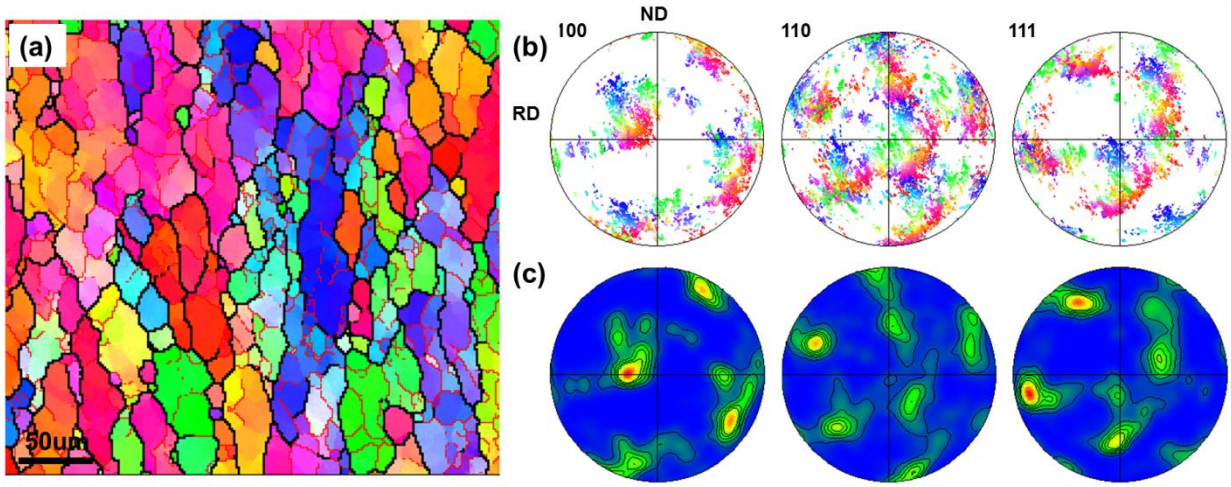

Figure 4.45 (a) IPF image (b) scattered pole figures and (c) contoured pole figures for selected region at 65mm location

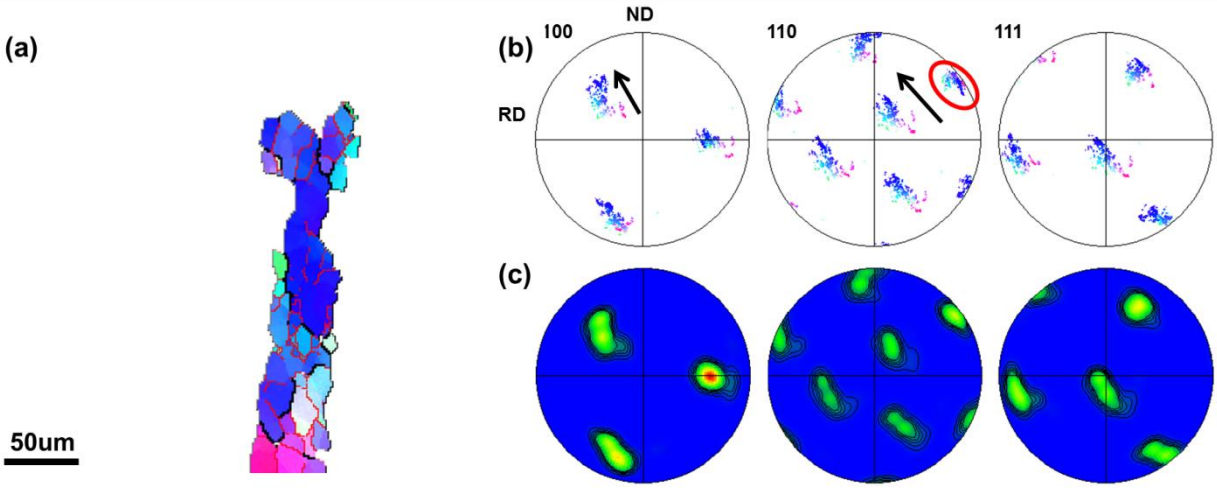

Figure 4.46 (a) IPF image (b) scattered pole figures and (c) contoured pole figures for selected grains at 65mm location

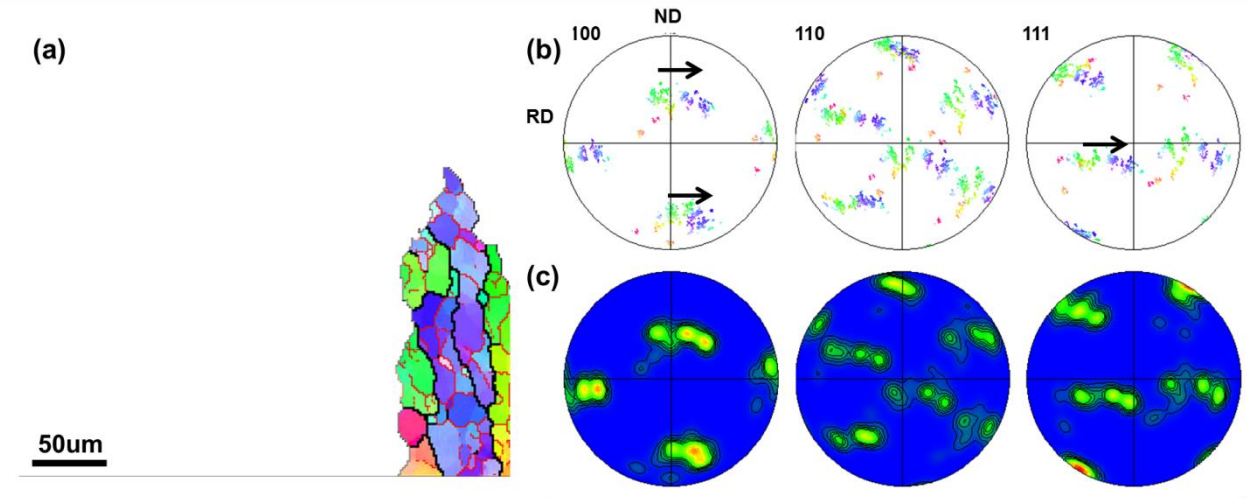

Figure 4.47 (a) IPF image (b) scattered pole figures and (c) contoured pole figures for selected grains at 65mm location

3, the first type of transition via A texture is observe across the TMAZ while the second pathways involve the C type texture is only observed on the side close to transition region, where strain level is a relatively higher.

4, the A component observed in previous samples is weak, however in the current situation, its showing similar strength as of C component or ever higher.

5, the formation mechanism of C texture is following another route, which is believed to be related to certain slip systems, rather than the previous philosophy that C component mainly forms by rotating around the <100>//SPN.

In the following section, the map2 of figure 4.39 will be addressed, this map will be the most critical part of the texture analysis of 65mm specimen since it both the transition region and most of the PZ will be addressed with distinct texture evolution. As illustrated in figure4.48, the IPF image with respect to TD shows significant texture

change and grain size variation. The left end of the map showing <110>//TD and <100>//TD colored by green and red is believed to be the transition region, which is closely next to the TMAZ map discussed in the last section. The middle part of the map showing <111> aligned to TD most likely exhibit a B/$\bar{B}$ texture based on previous observations and discussions and also it is subjected to higher strain level in the PZ, which can be confirmed by the high density of LAGB and refined grain size compared to the transition region. However, the interesting part is, under ever higher stain level, the grain structure is further refined down to 1-2, while at the same time the established B/$\bar{B}$ (assumed for now) components seems like being transformed into components that is showing <110>//TD and <100> //TD. The exact texture types that are showing these orientations can't be determined for the time being but it seems like to be the reappearance of C component under extreme shear deformation; and more importantly, the local shear reference frame related to this 'reappearance' need to be either determined or deducted since it can be a controlling factor in identifying the exact texture type. By observing the PFs shown in figure 4.48b and figure 4.48c, no distinct texture component can be observed, most of the orientation distributions in all PFs are scattered and stretched. Since the texture is under transformation across this map while the local shear reference frame might vary continuously inside the PZ at the same time, as concluded from previous sample, the texture components formed under different stages located in various shear reference frame are stack on top of each other, making the entire PF illegible. Thus the entire maps will be divided into basically 8 subsets as shown by the white rectangles in figure 4.48a and the texture analysis is going to be performed for each

of them to better understand the micro-texture evolution across the transition-PZ under incremental shear deformation and materials flow.

The first subset is taken from the region that is located near the transition-PZ interface, its IPF image and corresponding PFs are shown in figure 4.49. It can be seen that the entire poles figures are transforming into ideal B/$\bar{B}$ fiber texture while the reference frame work is still believed to be similar to the one observed in TMAZ since it seems that the SD marked by the red line in the (110) PF of figure 4.49c is fixed during the texture evolution. Thus there is no major change in the local shear reference framework of the transition region, which is also proved to be true based on the sample analyzed in previous discussions. It is also noted that the two component of B fiber is formed simultaneously based on the local shear reference framework, with $\bar{B}$ texture being relatively weak and B texture being stronger. Based on our latest discussion, while the transition texture is under development with the location of SD on PFs being relatively fixed, the C component is forming $\bar{B}$ while A component transforms into B. It can also be observed in the (111) PF of figure 4.49c that, even if the stable B/$\bar{B}$ component at its ideal location is not formed at this stage, it is clearly shown that two of them are formed with one being relatively weak. Based on the two pathways of the texture evolution discussed in the TMAZ region and the observation that the shear reference frame is still almost constant, it can be concluded that the $\bar{B}$ mainly come from the C component while the stronger B alternative should be transformed from the A texture, as circled out by the white and red circles in (111) PF respectively. It should be noted that the texture evolves while <110>//SD is stable, the direct consequence of C

component rotated around the 110 pole that is parallel to SD is the formation of $\bar{B}$ rather than B since a significantly higher amount of reorientation is needed to align the C component to B based on the observation made in the PF of figure 4.49b and figure 4.49c that the entire pole figures are rotated around the SD in an anticlockwise fashion. At the same time the formation of B from A component should be achieved via a similar anticlockwise crystallographic rotation around the <110>//SD. Actually the PFs measure for this subset are not exhibiting any ideal B/$\bar{B}$ texture, rather it is showing the trend toward what the existing component are transforming into. Up to this point the discussions are still made base on the predetermined local shear reference frameworks of the TMAZ, however according to our previous conclusion regarding the microstructure and micro-texture change, the local shear reference framework starts to orient continuously after the transition region because of the strong shear strain and materials flow. Thus the analysis performed for the following subsets will be based on deformation frameworks that changes systematically.

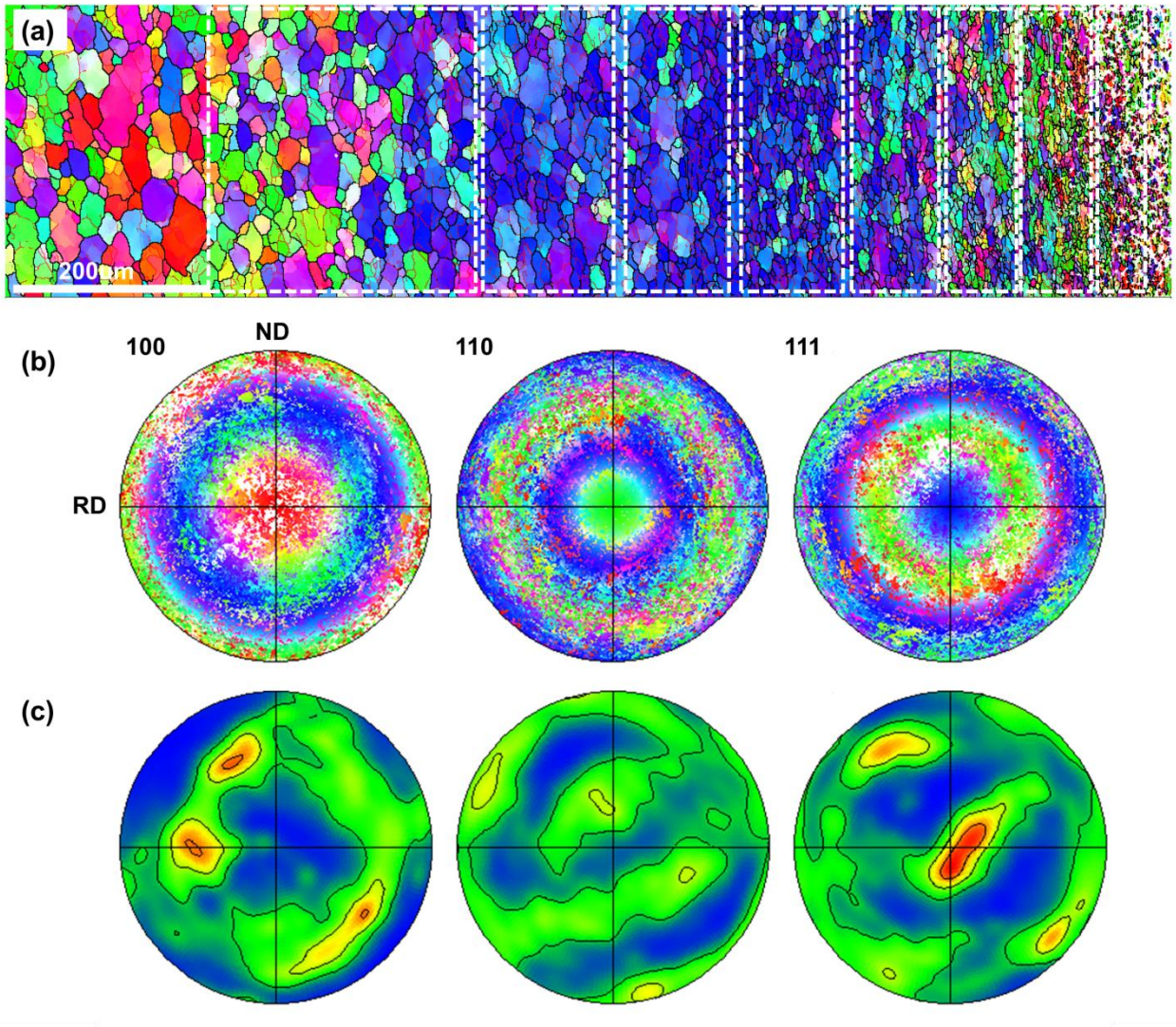

Figure 4.48 (a) IPF image (b) scattered pole figures and (c) contoured pole figures for region 2

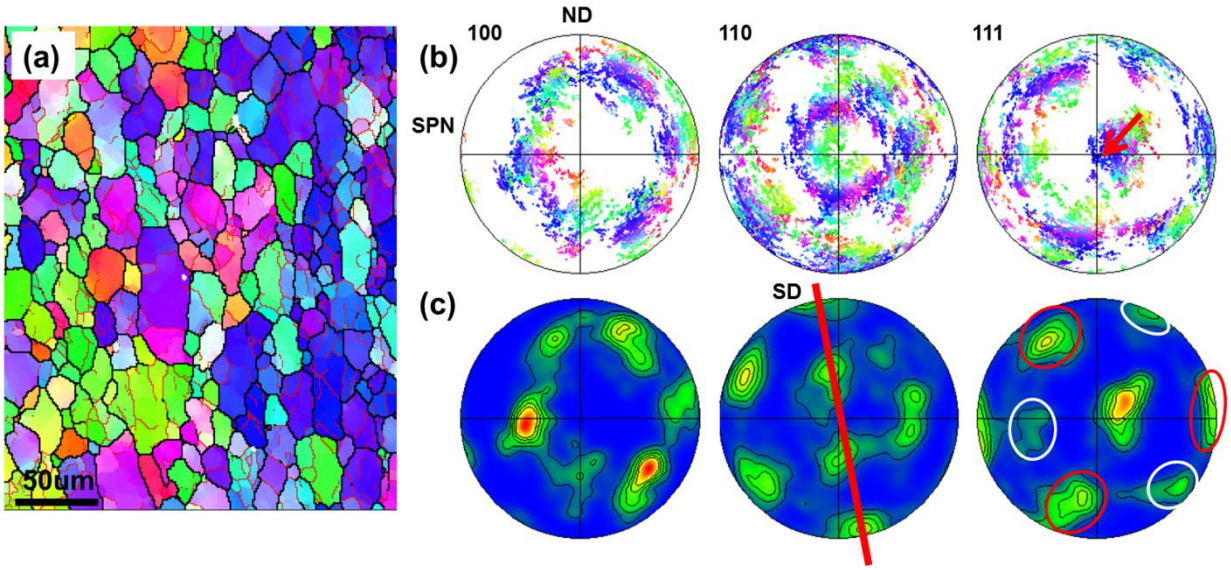

Figure 4.49 (a) IPF image (b) scattered pole figures and (c) contoured pole figures for selected grains at 65mm location of region 2

Constructed pole figures for sub-region 2-5 in figure 4.49a are shown in figure 4.50a-d. It can be seen from the PFs shown in figure 4.51a for the sub-region next to the transition region, as soon as the incipient B/$\bar{B}$ components are formed from A and C texture, the clear definition between the two B component disappear immediately under further deformation. The six (111) poles around the center pole of (111) PF are not showing disparate characteristics, rather they are connected together and forming a fiber type feature. Based on previous conclusion, materials located inside the PZ will be subjected to continuous materials transportation mainly around the rotating axis of the processing tool, thus the local deformation geometries might be transported around TD in a similar characteristic. Thus the spread orientation distribution around the center of the PF might be related to the materials transportation around TD that results in the

continuous rotation of the entire PFs. At the same time, since the center pole of 111 is located closely to TD, it is still showing a relatively higher strength even if it might also be distorted and stretch around TD. However, that doesn't suggest the center pole is relatively constant, the stretch of the center pole is less prominent due to its close proximity to the rotation axis, which simply make it hard to capture by vision. Additionally, if comparison is made among subsets, it is clearly observed that the entire pole figures are rotated clockwise around TD while the center pole of (111) is getting close to the ideal location of B/$\bar{B}$ texture, as indicated in figure 4.50a-d. This will further confirm the philosophy that the grains inside the PZ are transported continuously around the processing tool that result in the rotations of local shear reference frame, thus the texture shown in PFs. It should also be noted that while the materials inside the PZ are transported due to materials flow, the center pole of 111 is aligning close to the TD, which suggests the formation of ideal B/$\bar{B}$ texture type, as shown in figure 4.50c. However ideal B/$\bar{B}$ components are not formed under present circumstance mainly because of two reasons: the shear strain originating from the tool rotation is not high enough to fully transform the transition texture into ideal B/C- types; the axial component of the spiral materials flow disturb the formation of ideal B/$\bar{B}$ component by applying an out-of-plane movement on the local shear reference frame. Regarding the first reason, it is believed that the sub region 2-5 that are located inside the PZ is not subject to high strain level since it is around 1mm from the tool-materials interface, where it is found to be the TMAZ or transition region in other samples like 15mm and 30mm. The second reason involves the spiral nature of materials transportation. This effect is prominent

when the rate of shear straining is low since high strain rate can contribute to the formation of ideal texture component via crystallographic slipping. However, it is also true that materials transportation is more intense when getting closer to tool-materials interface. Thus both factors might be contributing to the non-ideal shear texture. On top of that, rotation around the TD is prevalent in current analysis. Additionally, it is interesting to note that, under further deformation and texture evolution, the center pole of (111) shown in figure 4.50d is moved away from TD, departing the ideal location of B/$\bar{B}$. This might suggest that the materials transportation starts playing a dominant role and offsetting the effect of increasing amount of shear strain or more precisely, the strain rate.

By observing the IPF image of the entire map shown in figure 4.48a, it is very interesting to note that beyond subset 6, the grains seem to be elongated along the extrusion direction, exhibiting a higher aspect ratio, while at the same time grain structure are further refined. Additionally, the IPF image in fig4.48a shows that the elongated and refined grains are showing <110>//TD and <100>//TD. This might indicate the formation of C component and <100> fiber or cube component based on the current understanding of shear reference frame. However, it is generally believed that the B/$\bar{B}$ component is relatively stable under shear deformation and being reported in several works regarding friction stir as the final texture [11, 40, 43, 46, 71]. It is strange if the C component is formed from B/$\bar{B}$ texture, even if the B/$\bar{B}$ component formed has not reached to their ideal locations on the PFs. If that is case, the possible explanation might be the stability of B/$\bar{B}$ component is affect by local deformation or its non-ideal nature. As reported by

Toth et al. [36, 37], it is pointed out that no shear texture component is persistent under strain-sensitivity conditions. Another possible answer for the reappearance of <110>//TD might be the significant change of local shear reference frame under intense materials flow which can be potentially capable of transporting the stable B/$\bar{B}$ components into another reference frame, while observed from the PFs based on the TD-ND-RD systems, the <110> or <100> directions are aligned to TD .Regarding the component showing <100>//TD, typically it is regarded as recovered microstructure under extensive heat exposure due to either dynamic or static recovery. However, this should not be the case here since a high density of LAGB is identified inside those grains showing <100>//TD and they are highly stretched along the TD. To further investigated this trend and better understand the micro-texture evolution at this region showing <110>//TD and <100>//TD with elongated microstructure. Three more subsets are taken as shown in fig4.48a and labeled as sub6-8. The corresponding PFs for each sub-region are plotted in figure 4.51. The microstructure will not be detailed for the time being.

As shown in the PFs of figure 4.52a for sub-region 6 that is next to the sub-region 5, it is noticed that the center pole of (111) PF is moving further away from the ideal location of TD, based on the observation made for the last sub-region. While at the same time, other six (111) poles are well defined rather than being spread and scattered. Actually the texture component observed in figure 4.51a can be readily identified as B/$\bar{B}$ type texture that is projected into a different shear reference frame, which is not only rotated around TD, but also around either RD/ND with respect to TD-ND-RD framework. The rotation around TD will be named as in plane rotation with the ‘plane’

referred to RD-ND plane since the texture component shown in PFs will only be rotated with respect to the center of the PFs if the shear reference frame is changed in this fashion. On the other hand, if the shear reference frame is rotated around RD or ND, visually it looks like the texture components represents by the PFs are being moved out from the RD-ND plane. Even if it's actually not possible that any specific orientation can be moved out from any PFs, this terminology will be adopted for easier representation and recognition of the variation of local shear reference frame.

Regarding the texture observed in figure 4.51a, two important aspects should be addressed. The first one is the formation of the two distinct B and $\bar{B}$ components rather than highly stretched and spread orientation distribution in PFs as shown in figure 4.50d, even if the deformation framework is rotated via an out-of-plane fashion. This phenomenon can be interpreted as the increased amount of shear strain or higher strain rate near these regions, since the clear defined B and $\bar{B}$ texture types should be the result of high strain level, especially the continuous materials transportation is enforced. While the shear strain rate is relatively low as in the cases of sub2-5 shown in figure 4.50a-d, the pole figures are stretched and elongated around TD. Similar observations are also made from previous specimens especially the 30mm sample, when the level of shear straining (precisely the strain rate) is low the texture is diffuse and the effect of materials transportation is more dominant, while the materials located close to the tool-materials interface is showing almost ideal B/$\bar{B}$ type due to high strain rate. This philosophy can be summarized as when the rate of straining is low, the formed texture exhibits a diffused characteristic and the materials transportation is playing a dominant role, while under

high strain rate, texture components showing distinct orientations can be expected. The second item need to be addressed is the variation of the shear reference frame. The out-of-plane component of the shear reference frame change is related to the axial movement of the spiral materials flow while the in-plane changes is mainly connected to the tool rotation. Admittedly both effects contribute to the final texture that is observed in the PFs with TD-ND-RD coordinate system, their individual contributions can be different under different deformation conditions or their relative locations to tool-materials interface. Typically, the effect of axial component is not playing the major role due to the dominant effect of materials transportation around the tool. Based on the samples analyzed in previous sessions, the effect of axial movement is only apparent when the shear strain rate is low, as in the case of 30mm specimen. However, it should be noted that the axial component is ever-lasting regardless of its effect and contribution. Normally it serves as the disturbance to the formation of ideal B/$\bar{B}$ components. In current case, it seems that the axial movement plays such a significant effect on deviating the texture that the center pole of 111 evolving toward TD under further straining is moved away by the axial component of materials flow. Considering the previous discussion that higher strain rate is also expected at this region, it sounds contradictory that the micro-texture is controlled by both high strain level and intense axial materials flow, since typically only one of them is dominant while another one is playing a minor role based on our previous analysis and understandings. By analyzing the microstructure near this region, is it shown that the grain structures are not only further refined at this region but also deformed and elongated along axial direction, as indicted in figure 4.48a. It is interesting that the

elongated microstructure corresponds to the abovementioned texture very well. Thus the higher strain rate is further substantiated by the refined grain structure and elongated characteristic of the grain structure, additionally the out of plane evolution/movement of the texture components plotted on the PFs might be related to the geometrical nature of the deformation condition. As illustrated by the elongated microstructure, there should be an intense axial flow of materials locally for some reasons in addition to the circumferential shear strain. This flow would strongly move the entire PFs in an out-of-plane fashion instantaneously. Additionally, and interestingly, this deviated texture corresponds to the microstructure that is showing <110>//TD and <100>//TD. Based on the discussion above, it is highly possible that these grains should be related to the reorientation of the shear reference frames. Finally, a model for the texture evolution will be proposed to explain the texture behaviors. However, it will be explained later once the texture evolution across the wall is identified. Under further straining and materials flow, the entire PFs continue rotating around TD in a clockwise way while the center pole of 111 is moving further away from TD, as illustrated in figure 4.48b, which corresponds to the microstructure of sub-region7. At the same time, six (111) poles around the center are still well defined and exhibiting localized characteristics. These observations indicate the continued rotation of the shear reference frameworks with the trend that the circumferential component rotates the entire PFs clockwise while the axial component is distracting the center pole of (111), or move the PFs out of plane. Sub-region located even closer to the tool-materials interface, i.e. sub-region 8 is analyzed and the corresponding PFs are plotted in figure 4.48c. The very first impression regarding this set

of PFs is it looks like C component that is plotted in a reference frameworks rotated around TD. Actually, when compared with the PFs for sub-region 7 which is under lower level of materials transportation and shear straining, the PFs in figure 4.48c is simply achieved by following the similar route of texture evolution just discussed due to combined effect of materials transportation and shear straining. For this sub-region, the shear reference frameworks are so rotated by the materials flow that the stronger (111) pole reach to the point that make the orientation distributions plotted in the PFs with ND-TD-RD coordinate system resemble a C component. Additional evidence supporting the rotated shear reference frame due to materials flow rather than the formation of real C component is if the C component is formed the two (111) pole near the center of (111) PF should be showing similar intensity, while in this case, one of them is showing much higher peak value. Meanwhile, it is noticed that the pixel of this are showing mainly green and red color, indicating the fact that grains located in this area are orientated with <100>//TD and <110>//TD. While this would give us a first impression that the <100> fiber/cube component or C component might be formed under further deformation with stable B/$\bar{B}$ texture as initial texture due to straining or dynamic recovery, the real fact is the distorted and rotated deformation geometries due to the complicated materials flow happen to rotate the <110> direction or <100> direction to the SD during the FSBE process.

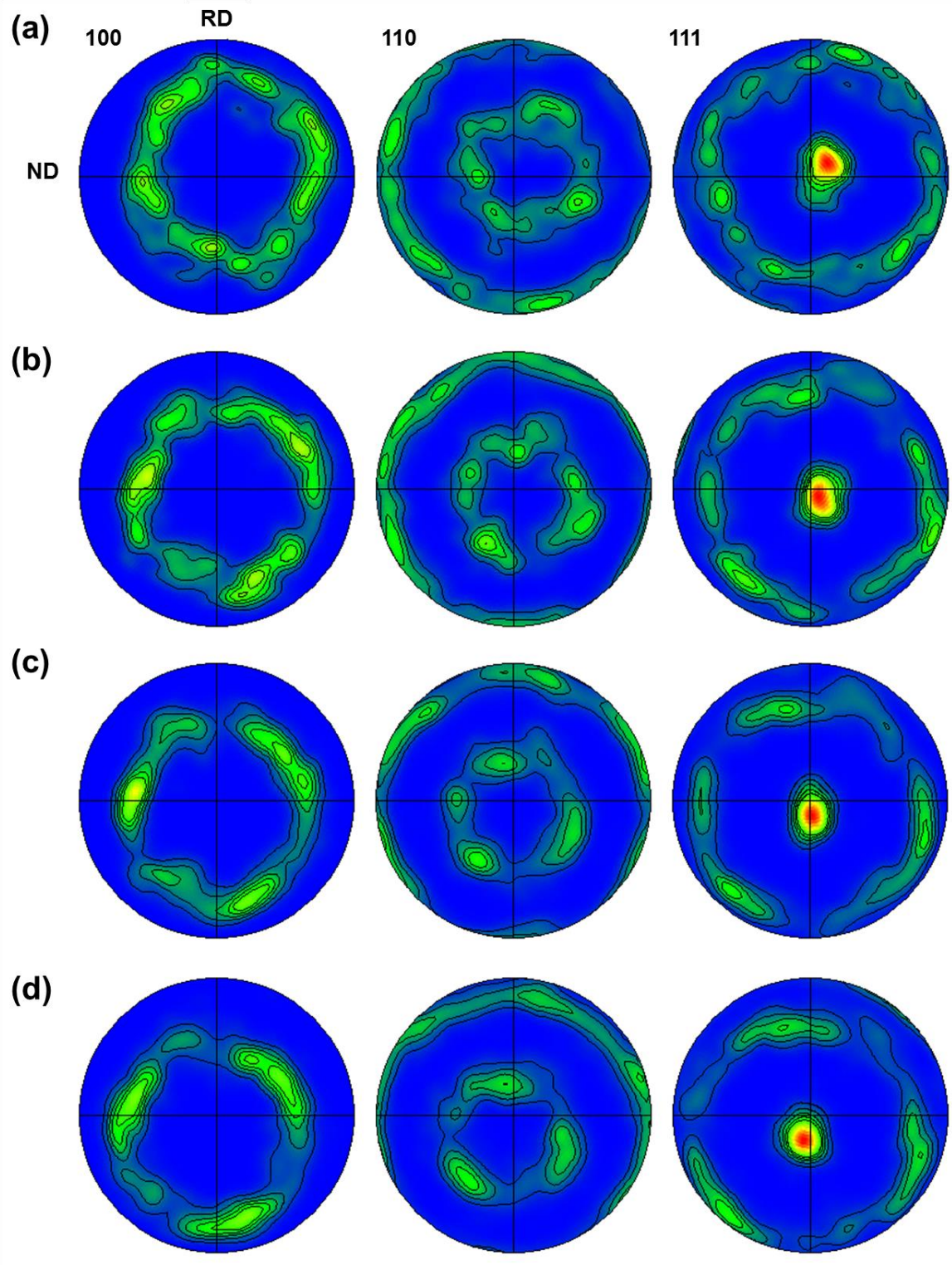

Figure 4.50 Pole figure showing texture variations within the PZ of 65mm sample

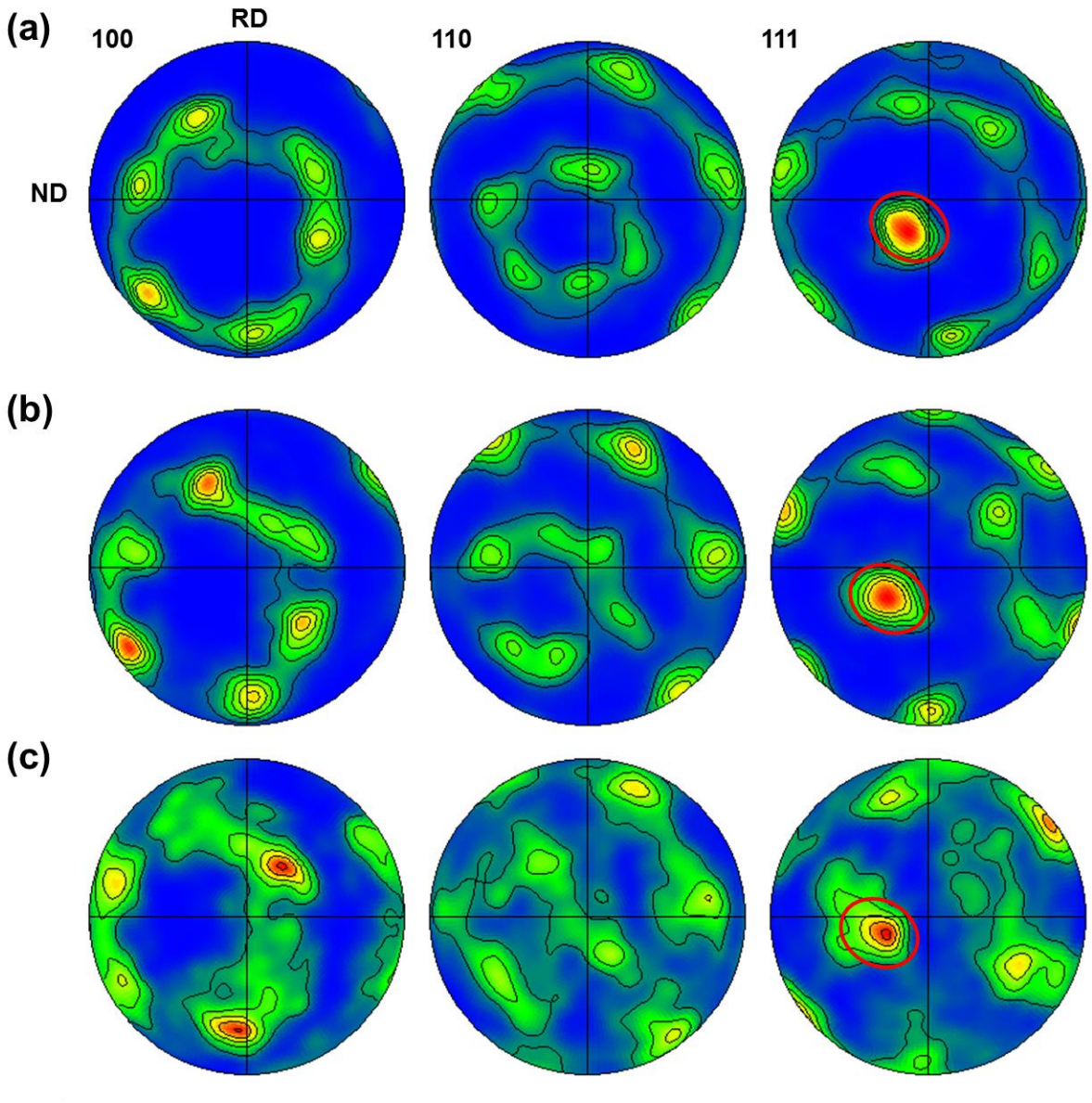

Figure 4.51 Pole figures showing texture variation near the transition region of the 65mm sample

It should be noted that the sub-region 8 is still located around 300um from the tool-materials interface even if it starting showing highly refined microstructure and low indexing rate of the EBSD analysis due to lattice straining. The last EBSD scan that is showing the grain structure located 100-300um from the tool-materials interface, where intense plastic deformation is expected, is performed as shown in fig4.48a with a small overlap with map2, in order to understand the microstructure and micro-texture evolution across the tube wall comprehensively. The IPF image and PFs of the third map are shown in figure 4.52.

It should be noted that there is a very small overlap between the second and third scan to guarantee that no information about texture or microstructure evolution is lost due to any gaps between these two scans. Also, the right end of this map is located within 100um from the tool-materials interface. At the very left side of the map shown in fig4.52a, grains are mainly showing <110>//TD and <100>//TD, as in the case of the sub-region8 of the second scan shown in 4.48a. The IPF image for this entire maps shows that grains exhibiting <110>//TD and <100>//TD are gradually transformed into <111>//TD with the grain structure refined to around 1um. The grains showing <100>//TD almost disappear at the later stage of transformation while limited amount of grains <110>//TD are still present. The scattered PFs of figure 4.52b are not showing any distinct feathers regarding the texture components while the contoured PFs in figure 4.52c demonstrates the formation of B/$\bar{B}$ components that is almost aligned to its ideal locations without any rigid body rotations. It can be seen that distribution of <110> direction has already been aligned to RD, which is the SD; at the same time the strongest 111 pole is only a couple

of degrees from TD, as represented in the (111) PF of figure 4.52c. However, the identified orientation distribution around the ideal B/$\bar{B}$ locations on the PFs is not showing strong, distinct and sharp characteristic, it is still stretched and scattered and looks like being transformed from other components. To unveil the formation of B/$\bar{B}$ components and analyze the micro-texture evolution step by step, the entire map will be divided into four sub-regions and will be named as sub-region 1-4, as illustrated by the four rectangles shown in figure 4.52a. The IPF image and corresponding PFs both in scattered and contoured format are shown in fig4.53. It can be seen the grains showing <100>//TD looks like a rotated cube component which can be easily interpreted as recovered grain structure based solely on the grain orientation. However, as discussed in the previous subsets, the formation of <100>//TD grains is mainly attributed to the materials transportation that can transform the shear-related texture in one shear reference frame to cube component projected in TD-RD-ND coordinate system. Additionally, these grains contain high density of LAGBs, which is typical for deformed grains. By comparing the contoured PFs shown in figure 4.53c with the ones in figure 4.51c, it can be easily concluded that the former pole figures are formed by rotating the later PFs around the TD for around 30 degrees, which corresponds to the circumferential materials flow, similar to the cases shown in figure 4.50 and figure 4.51. When the materials is getting close to the tool-materials interface and under further processed, as shown in figure 4.54 for sub-region 2. The IPF image is mainly consists of grain with <110>//TD and <111>//TD, while those with <100>//TD almost disappear. The contoured PFs indicate that the distribution of <110> directions is almost aligned to RD, which is

supposed to be its ideal shear direction. While the entire pole figures look like a C component transforming to B/$\bar{B}$ texture, it is still believed that the change of shear reference frame due to materials flow is the major reason. The fact that the distribution of <110> direction is close to the ideal location of SD indicates that the increased shear strain rate starts to overweight the effect of materials transportation that moves the entire PFs around ND. However, the materials transportation is still playing a significant role since the entire PFs are still moved by about 45-50 degrees around TD, and at the same time, the center pole of 111 is slightly moving back to the TD location, suggesting the fact the shear straining is taking over the effect of axial materials transportation too. As the amount of shear strain is further increased, no significant rotation of shear reference frame change is observed, as shown in figure 4.55 for sub-region3. It is noticed that the orientation distribution of <110> directions is almost aligned to the RD with a couple of degrees of in plane deviation. At the same time, the center pole of 111 is moved closer to the TD compared to sub-region2. Even if the texture formed at this stage is very close to the ideal B/$\bar{B}$ projected in TD-RD-ND frameworks, it is still showing scattering characteristic and seems like under transformation. However, it is certain that both axial and circumferential materials flow persist at this stage, the effect of shear deformation start playing a controlling factor, which contributes to the formation of B/$\bar{B}$ component. For the sub-region 4 that is even closer to the tool-materials interface where the shear strain level is even higher, the measured texture component is identified as ideal B/$\bar{B}$ component showing <111>//TD and <110>//RD with distinct and sharp poles, as shown in figure 4.57. It is believed that the effect of shear straining on the micro-texture

evolution is dominating compared to the materials transportation when the rate of shear strain is high enough.

To briefly summarize the texture evolution of map3:

1, shear reference frame is highly distorted by the strong materials flow

2, grains starting showing <100>//TD and <110>//TD, however, they should not be identified as cube/rotated cube and C component. The major reason is: the axial materials flow is relatively intense at some locations that rotated the shear reference frame in an out-of-plane fashion to a larger extent that the 100 and 110 poles happen to be moved to TD.

3, when the shear strain is getting higher at locations close to tool-material interface, the effect of shear straining overweight the contribution of materials flow, thus the ideal B/ B̄ component can be formed.

Regarding the texture evolution at 65mm location, a simplified model is proposed as illustrated if figure 4.57. The lines and arrows represent the effect of axial materials flow on the micro-texture evolution. The tube wall is classified into three regions labeled as region I, II and III. The region III encompasses the entire TMAZ, transition region and some part of the PZ. At these locations, the shear strain is relatively low since it is far away from the stirred zone or the tool-materials interface. At the same time, the axial materials flow is believed to come from the axial drag when the tool is plunged in or pulled out originating from the contact between the tool and the materials. However, at region III, this effect is also believed to be insignificant due to its distance from the tool-materials interface. Combining with the observations that the shear

reference frame at TMAZ and transition region is relatively fixed while at early stage of the PZ, minimal out-of-plane rotations of deformation frameworks is observed. Thus it can be concluded that in most part of region III the effect of axial materials flow is minimal and it might be slightly stronger in the earlier stage of PZ.

For region I that is highly deformed and located closely to the processing tool, strong materials transportation should also be expected, however, the shear deformation is so intense that the contribution of both the axial flow and circumferential flow on the shear reference frame change is almost negligible, as evidenced by the PFs in figure 4.56.

The most interesting part should be the region II where axial materials flow is playing a dominant role in changing the local deformation frameworks. A high gradient of both shear strain and axial materials flow is expected at this region. That is to say the effect of axial flow increases tremendously due to the axial drag of the tool once the distance between the analyzed region and the tool-materials interface reaches a certain value, while the shear strain rate is also increased, its absolute value is not high enough to change the effect of the materials transportation on the local shear reference frame. Additionally, the elongated grain structure shown in region II while refining to a finer level also suggests the impact of axial materials flow.

To summarize the texture evolution of 65mm specimen, several aspects can be noted:

1, the TMAZ is showing transformation from distorted cube/rotated cube component to either A or C components via two pathways depending on initial orientation and local deformation geometry, the local shear reference frame inside the

TMAZ is relatively constant. C component is mainly formed near the border between transition region and TMAZ, while the formation of A type texture is observed across the entire TMAZ

2, the transition region is mainly consists of C and A components, the corresponding local shear reference frame is identified to be the same as TMAZ

3, the shear reference frame for materials located inside the PZ is heavily affected by the materials transportation, both axially and circumferentially. The contribution of the axial component can change the shear reference frame in an out-of-plane fashion such that the orientation distribution can be visually resembles other components when project on TD-RD-ND coordinate system.

4, the texture components of the entire processing zone should be mainly $B/\bar{B}$, however, the strong materials flow could transported the texture components to another shear reference frame that makes it hard to identify. As in the case of PZ, PFs showing $B/\bar{B}$ component can be easily transport to another framework that result in the misidentification as C component or rotated cube.

5, Extra care must be taken to determine the shear reference frame should be determined carefully before analyzing the texture component

6, texture types measured near the tool material interface shows ideal $B/\bar{B}$ texture due to strong circumferential shear deformation

7, a simple model is proposed to specifically address the effect of axial materials flow on the shear reference frame thus the projected PFs in TD-RD-ND.

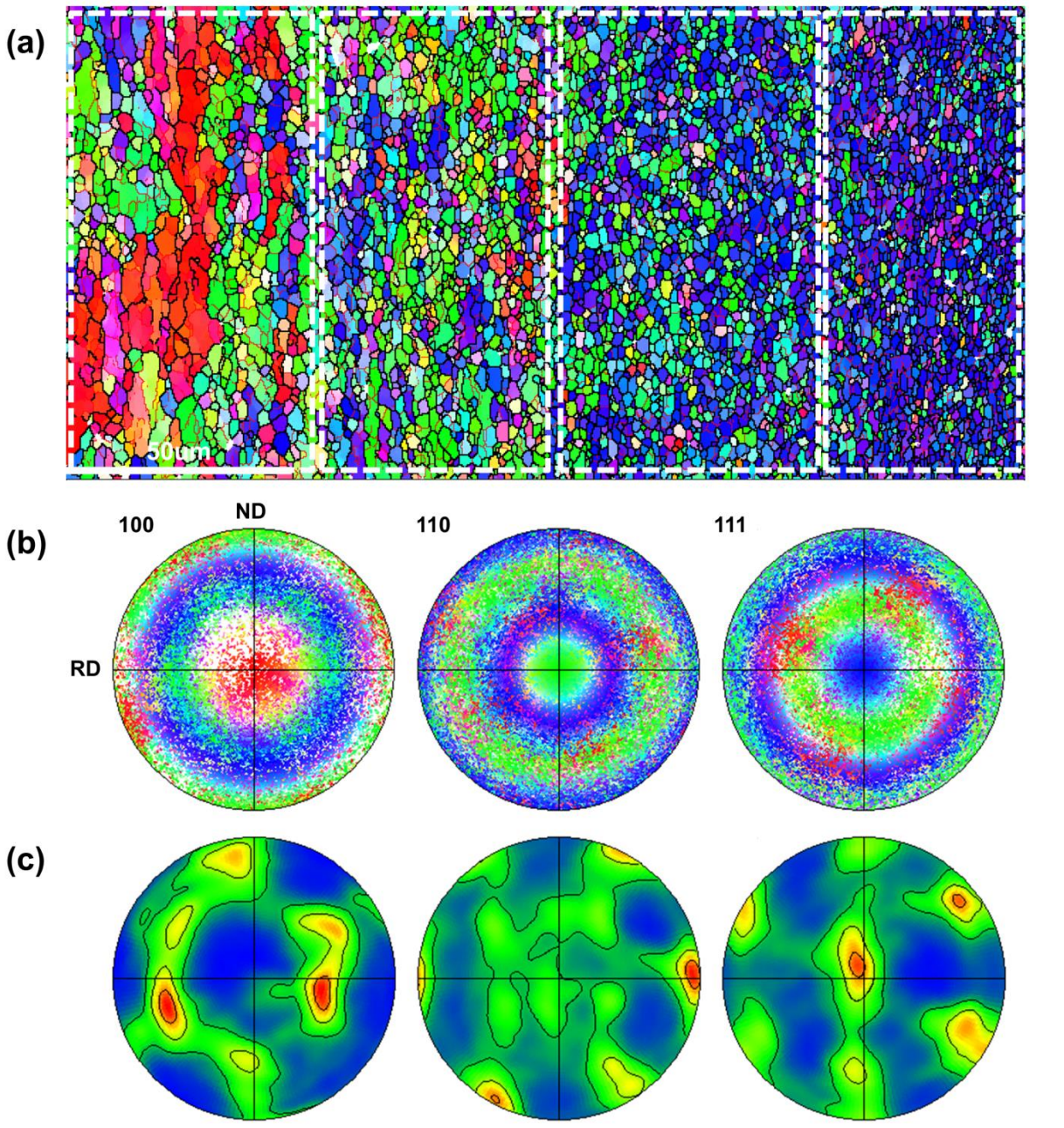

Figure 4.52 (a) IPF image (b) scattered pole figures and (c) contoured pole figure for region 3 at 65mm location

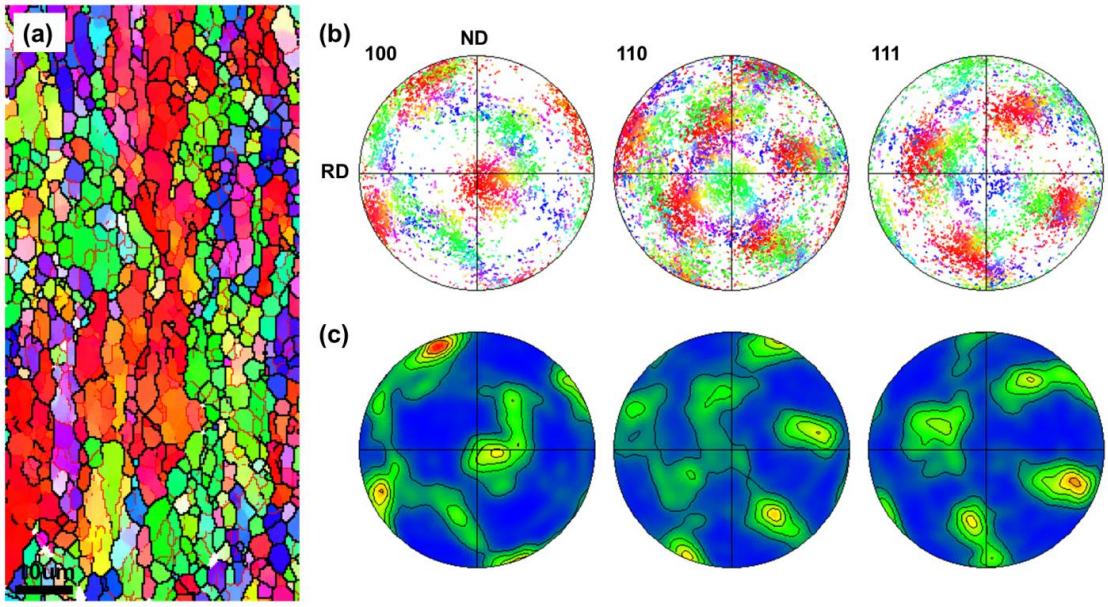

Figure 4.53 (a) IPF image (b) scattered pole figures and (c) contoured pole figures for sub-region 1 of figure 4.52a

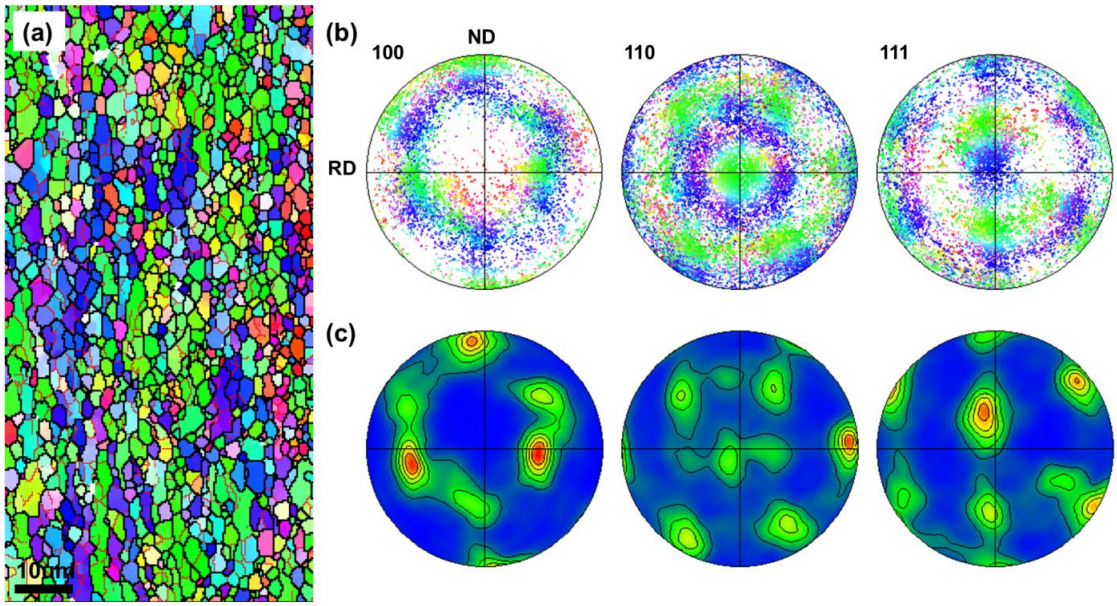

Figure 4.54 (a) IPF image (b) scattered pole figures and (c) contoured pole figures for sub-region 2 of figure 4.52a

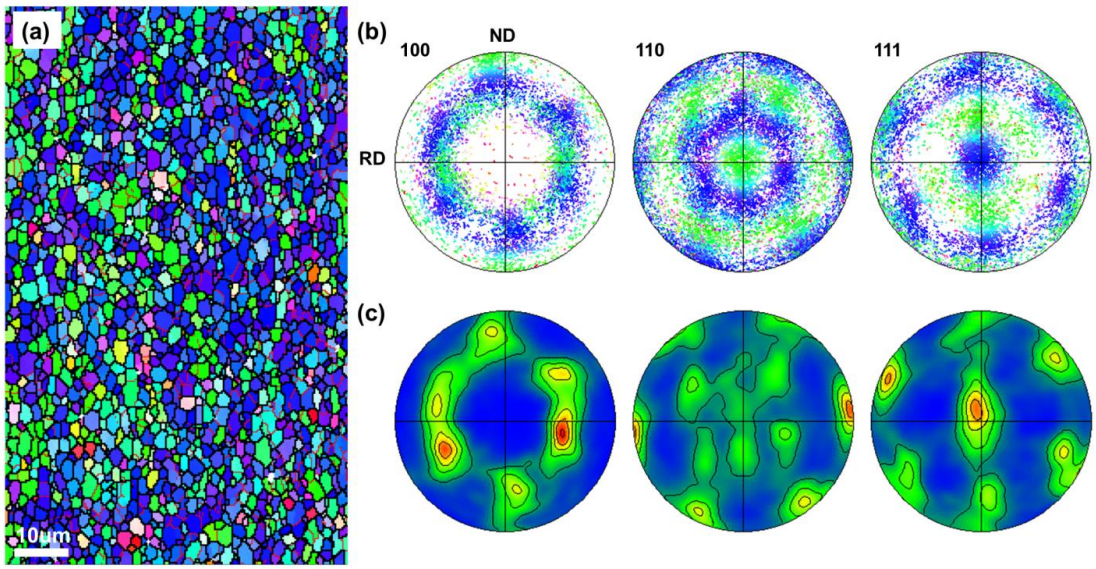

Figure 4.55 (a) IPF image (b) scattered pole figures and (c) contoured pole figures for sub-region 3 of figure 4.52a

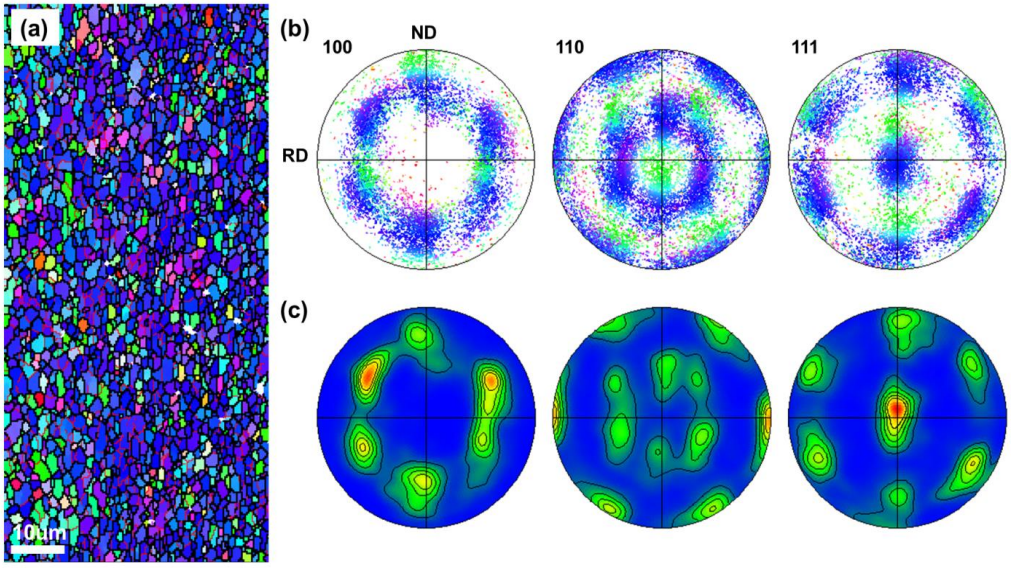

Figure 4.56 (a) IPF image (b) scattered pole figures and (c) contoured pole figures for sub-region 4 of figure 4.52a

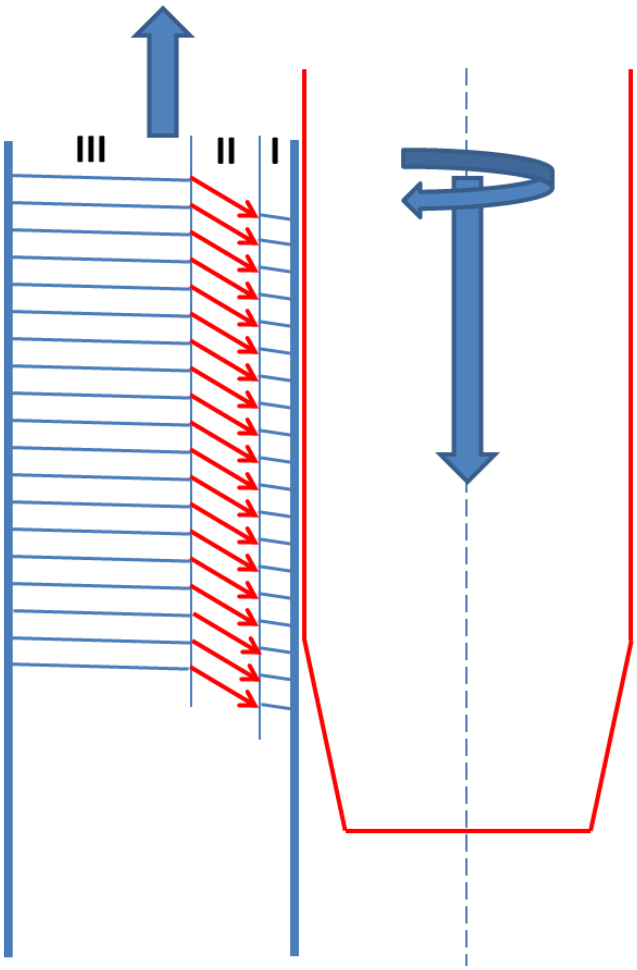

Figure 4.57 Simplified model explaining the micro-texture change at 65mm location

CHAPTER FIVE

FRICTION STIR BACK EXTRUSION OF AA7075-T6 ALLOY

In this chapter, microstructure, micro-texture, micro-hardness and mechanical properties of FSBE processed AA7075 Al alloy will be analyzed. The experimental results are presented followed by discussions on the underlying mechanisms that are responsible for corresponding materials behaviors. Discussions will be performed based on the analysis of present data and the information provided in literatures. It should be noted that when addressing multiple aspects of material behaviors of AA7075 Alloy under FSBE, comparisons with the case of AA6063 have always being made. Additionally, special attention is paid on the micro-texture evolution as well as recrystallization mechanisms. Finally, a critical evaluation is performed with respect to the difference in recrystallization mechanisms as well as microstructural evolution between AA6063 and AA7075 tubes.

Initial Microstructure and Micro-texture of As-received Materials

Initial microstructure and texture of the extruded and T6 treated AA7075 alloy are measured for the purpose of comparison. As shown in figure 5.1a, grain structure of as-received materials is characterized by grains with irregular shapes and high content of second phase particles with a broad size distribution in the cross section perpendicular to the extrusion direction. While IPF image taken on the cross section that is parallel to the extrusion suggest a highly elongated microstructure along the extrusion direction, as shown in figure 5.1b. This suggests that the initial grain structure is highly elongated

along the extrusion direction due to the previous extrusion process before the heat treating. However, the grain structure shown in figure 5.1b can be interpreted as a fully recrystallized grain structure since LAGBs and subgrains are barely noticed. Elongation of the recrystallized grains along extrusion direction is mainly attributed to the redistribution of dispersoids particles during the extrusion process which can inhibit grain boundary migration and grain growth along the directions that are perpendicular to extrusion direction. The PFs shown in figure 5.1c indicated that texture of the initial microstructure shown in figure 5.1b is nearly random and no fiber components that are typical for an extruded Al alloy have been noticed. Even if some relatively strong poles are noticed, they are largely because of some larger grains that showing certain orientations that can pop-out in the PFs.

Optical Microstructure of AA7075 Tube at Multiple Locations

Figure 5.2a is a stitched optical micrograph that is showing the microstructure near the bottom of processed AA7075 tube. The image is taken from tool/material interface where highest strain level is expected all the way to regions where grains structure is close to that of the BM. In order to evaluate microstructural change as a function of depth, the microstructure of several selected regions showing distinct characteristics are analyzed at higher magnifications, as represented by figure 5.2 b-e. It can be seen that the microstructure shown in figure 5.2b is featured by an equiaxed recrystallized grain structure with some slightly elongated grains, which is believed to be the PZ. At the location around 1mm from the tool/materials interface, the microstructure

is characterized by larger and high elongated grains that are stretch along the horizontal direction, as illustrated in figure 5.2c. It should be noted that considering the symmetrical nature of the process, these grains should be of a pancake shape rather than fiber-like. They are formed as a result of the geometric requirement of the applied shear strain as well as the compression effect of the processing tool while plunging. Surprisingly, the microstructure located around 2-2.5mm from the tool/materials interface consist mainly of equiaxed grains, as least from the view that is parallel to the extrusion direction, as shown in figure 5.2d. However, figure 5.2e suggests that the microstructure located around 3-3.5mm from tool/materials interface is mainly featured by grains elongated along the extrusion direction, which is similar to that of the BM. It seems that the initially high elongated grains along the extrusion direction starts to be affected by the strain field imposed by FSBE at the location corresponds to figure 5.2e. The grain aspect ratios tend to decrease due to plastic flow and compression effect of the tool tip. While at the location that is featured by the grain structure shown in figure 5.2d, additional shear strain is applied on these grains that are showing reduced aspect ratios in an earlier stage and result in a near equiaxed features. As the analyzed region get closer to the PZ, the intensity of shear strain and plastic flow increases sharply, grains showing equiaxed features are transformed to elongated grains again, while this time the stretching direction is along the materials flow and shear direction. It is also noted that the grains are refined with the grain width decreases significantly. The microstructure of this region is basically comprised of a mixture of elongated grains and some recrystallized small grains. Finally, at the location that is adjacent to the processing tool, the refined microstructure is formed

due to extensive dynamic recrystallization under high deformation temperature and strain rate.

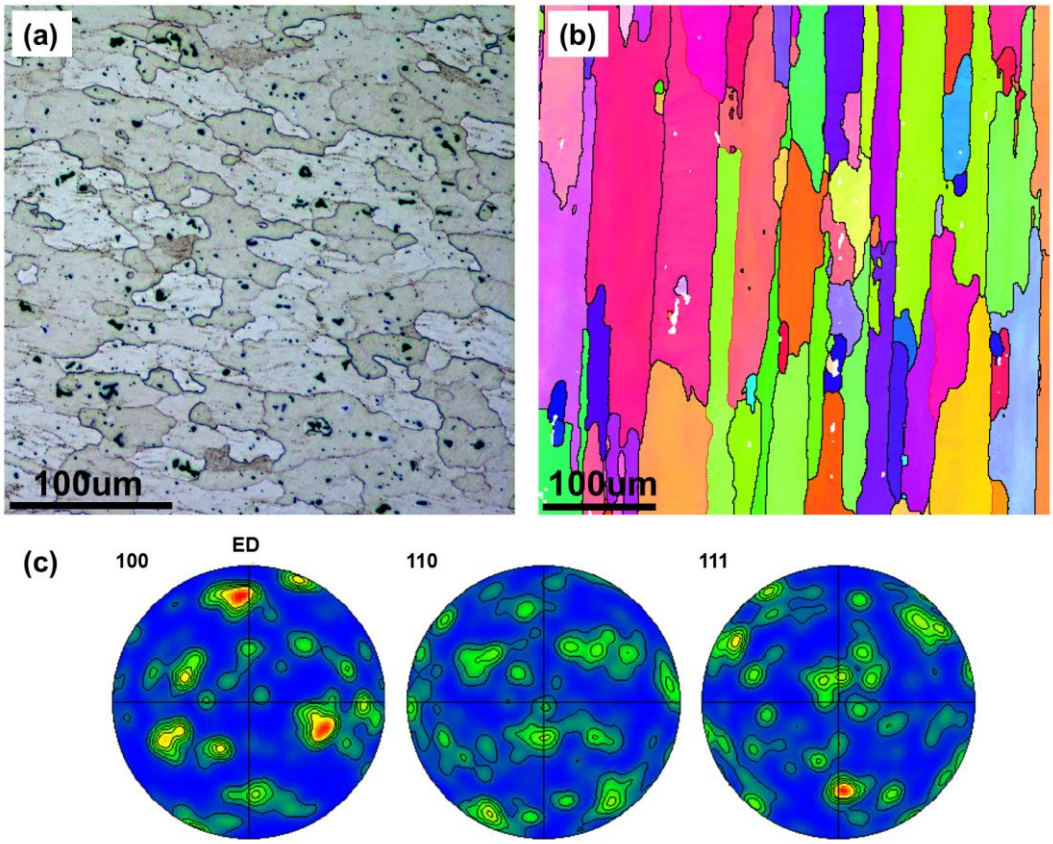

Figure 5.1(a) Microstructure perpendicular to ED (b) grain structure parallel to ED and (c) pole figures for as-received materials

When compared with the microstructural observations that have been made in the case of AA6063 alloy. Several major difference can be noticed: first, the grain size in the PZ is significantly finer in the processed AA7075 alloys, even if a higher processing temperature is expected due to more aggressive processing parameters being applied; second, the depth of dynamically recrystallized zone is only of 500-600um in size for

AA7075 alloy while it is measured to be 1.5um for AA6063 alloy; third, the elongated grain structure is extensively observed across the entire analyzed region shown in figure 5.2a, however, they are only observed in a narrow region that corresponds to the transition region of AA6063 alloys; finally, is seems that the penetration of the plastic flow that is introduced by the processing tool is similar in both alloys.

A basic conclusion that can be drawn based on the fact that the depth of processing affected zones is similar for both alloys is the effective strain as well as strain rate level should be similar for both alloys. Thus, the grain structure difference should be mainly related to materials properties. It is not true that AA7075 alloy is of higher strength than AA6063 alloys thus it is hard to be deformed and result in the elongated structures. Actually the flow stresses for these alloys at the processing temperature are incredibly close. It is believed that the grain structure formed in figure 5.2a is mainly a result of the solute dragging and pinning effects of dispersoids particles that are present in AA7075 alloy. Because of the presence of these particles, the grain boundaries or even dislocations can't move freely and form recrystallized grains. It is widely known that solute atoms can provide resistance to dislocation movement thus dynamic recovery and grain subdivision process can be retarded, which are crucial for generating newly recrystallized grains [55, 61]. In the case of the microstructure that is shown in figure 5.2a, it is highly possible that redistribution of dispersoid particles is achieved at the locations correspond to the microstructure shown in figure 5.2c, and that can also serve as one important reason for the formation of elongated grain structure. Thus the

microstructural difference can be essentially interpreted as different resistance to recrystallization for these alloys rather than the deformation conditions variations.

Regarding the grain size difference, it is believed that the dominant dynamic recrystallization mechanisms that contribute to the grain refinement are different for these two alloys, which will be detailed later. Also, it is possible that the final grain size is a result of both deformation and grain growth due to in situ annealing [62]. Under this circumstance, the AA7075 is showing smaller grain size simply because it is showing higher resistance to grain growth due to the pinning effect of dispersoid particles.

Optical microstructure across the tube wall at multiple locations of 10mm, 30mm and 55mm are shown in figure 5.3a-c, respectively. Similarly, the wall mainly consists of only PZ characterized by refined grain structure and TMAZ that is featured by highly distorted and elongated grains stretched along the extrusion direction due to strong plastic flow. Inhomogeneous microstructure is observed across the tube wall, while surprising it is relatively homogeneous along the tube wall. Additionally, it is very interesting that at 30mm location, a narrow strip of grains showing very large grains size compared to their neighbors are noticed near the tool/materials interface. These grains can be easily identified as a result of abnormal grain growth. Ideally, at locations adjacent to the tool/materials interface, additional shear strain is imposed to the materials by the rotating tool due to continued surface contact. However, as mentioned in the discussion about the microstructure evolution along the tube wall of AA6063 alloy, local contact conditions can vary according to local temperature change and material flow. Thus it is obvious that at 30mm location, minimal contact is expected between the processed materials and the

tool while the material is exposed to elevated temperature. This is very similar to the process of static annealing. However, typically static annealing take a much longer time than several seconds, which is our case, to trigger abnormal grain growth[79]. Since precise temperature measurements adjacent to the tool/materials interface are extremely difficult, it is assumed that local temperature can reach a higher level than that of a typical thermal treatment used to result in abnormal grain growth and expedite the growth kinetic exponentially. Abnormal grain growth has been reported in several investigations of FSW/FSP processed aluminum alloys [80], however, abnormal grain growth are typically observed during post annealing and associated with the alloys that contains a lot of pinning particles. As described in chapter 3, the microstructure captured at the 30mm region of a processed tube can be regarded as a later stage of the microstructure observed in 10mm location that is evolving during the process, the similar principle can be applied to the situation of 55mm, where abnormally grown grains disappears, as shown in figure 5.3c. It is believed that while the materials at 30mm location is flowing to 55mm region along the extrusion direction, extra shear deformation is applied to the flowing materials, resulting in breakdown and refinement of the large grains. As discussed earlier, material shrinkage as a result of temperature drop is expected near the top part of the tube, resulting in intense contact between rotating tool and the processed materials. As confirmed by the image quality near the PZ of figure 5.3c, the PZ is darkened due to excessive residual strain and localized shear deformation at relatively lower temperature; high residual strain level is also confirmed by image quality of EBSD mapping, represented by the band contrast. Thus, the temperature change and the evolution of

abnormally grown grains can be summarized as: when the materials is initially processed near the tip of the processing tool, refined recrystallized grain forms; while these grains are flowing through the tube corner and into the tube wall, they are subjected to extended thermal exposure; at locations near 30mm, abnormal grain growth is noticed due to excessive thermal exposure at elevated temperature while little additional deformation is applied to the materials due to poor contact; as the material flow from 30mm to 55mm location, additional shear is introduced to refine the abnormally grown grains because of temperature drop. However, a distinct feature of the microstructure at 55mm location is: even if additional shear strain and temperature drop is expected, the resulting penetration of the recrystallized region does not increase, unlike the AA6063 case. This might be explained from two perspectives: higher strain level is needed to trigger dynamic recrystallization in AA7075 alloys because of the pinning effect from solute atoms and dispersoid particles; absolute temperature drops thus strain increase is not as significant in the case of 7075 alloy.

When compared with AA6063 tubes, differences can be briefly summarized as: the microstructure is more homogeneous along the tube wall, abnormal grain growth is observed due to exposure to extremely high temperatures, penetration of the PZ is not increased by the additional shear deformation applied as a result of temperature drop.

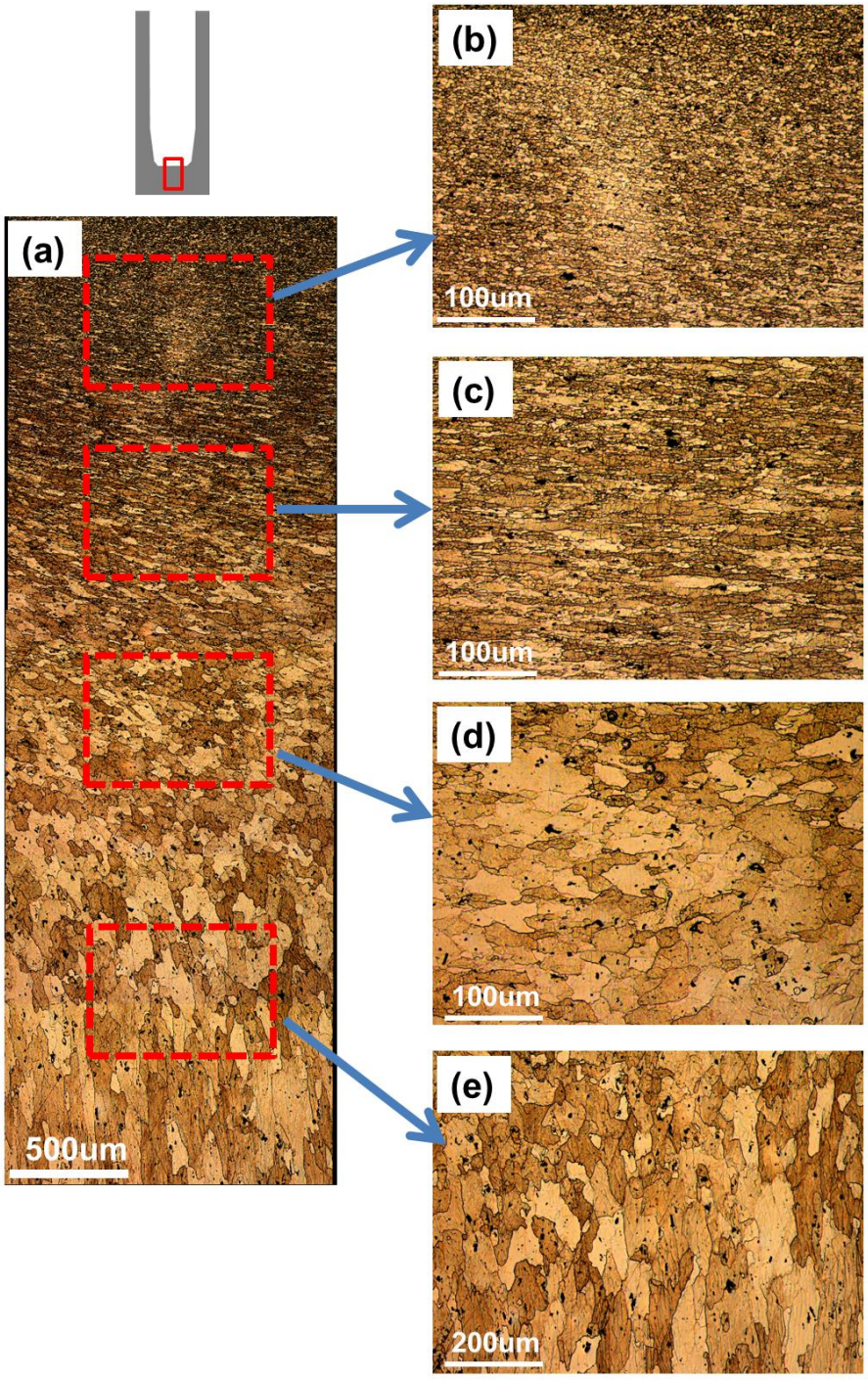

Figure 5.2 (a) Microstructure at tube bottom and (b)-(e) magnified images for selected regions

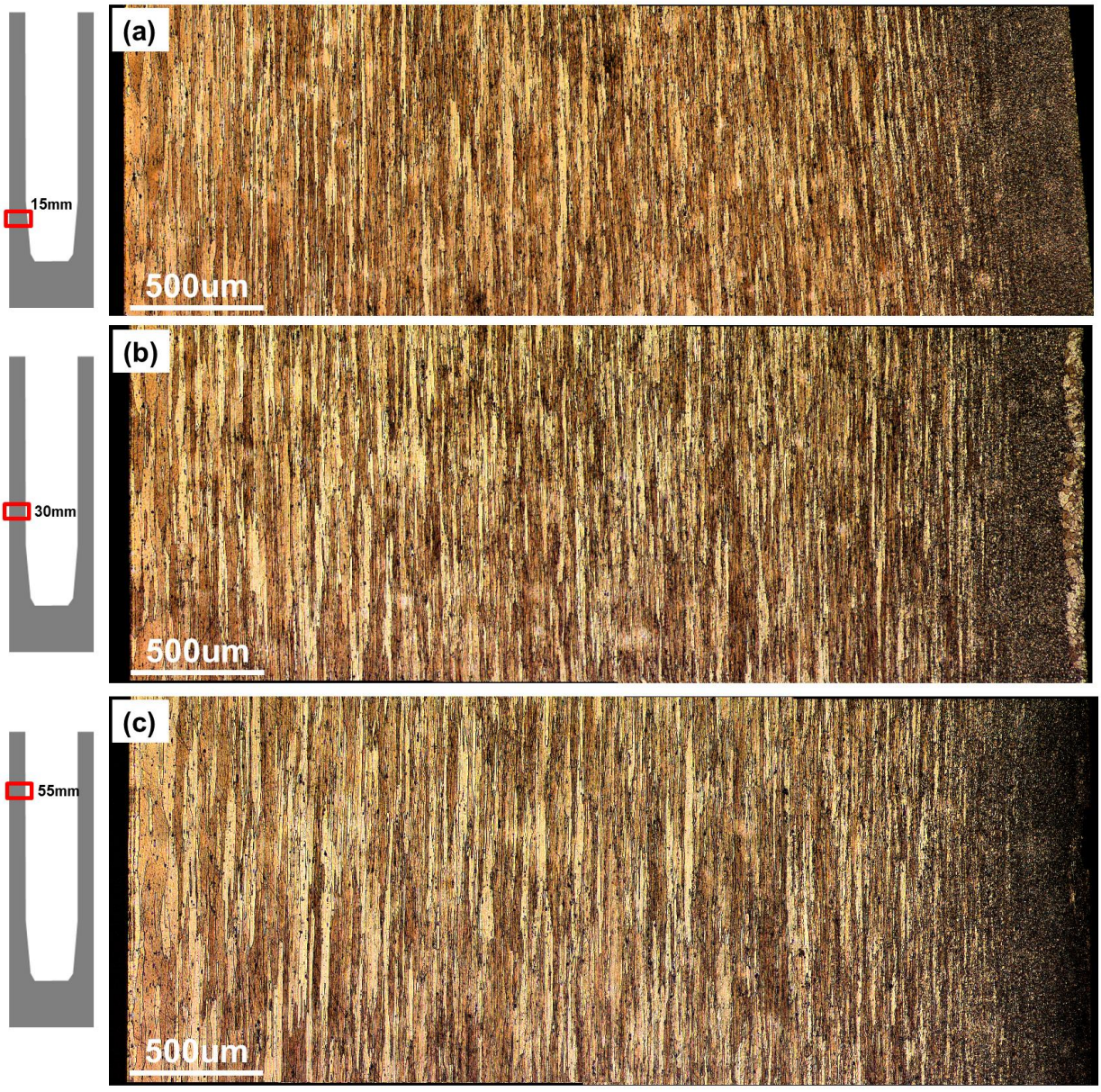

Figure 5.3 Optical microstructures across tube wall at (a) 10mm (b) 30mm and (c) 55mm locations

Micro-hardness Evaluation and Underlying Mechanisms

Vickers micro-hardness profiles were measured along the centerline of tube bottom as well as across the tube wall at 10mm, 30mm, 55mm and 65mm locations for

both as processed and post-process aged AA7075 tubes, the results are presented in figure 5.4. The analyzed locations are similar to the regions investigated by OM except 65mm location. Base on the OM analysis, no identifiable microstructural difference is found between 55mm and 65mm specimen. However, the corresponding micro-hardness variation is significant. In these figures illustrating micro-hardness profiles, the x-axis represents the distance from the region being tested to tool-materials interfaces. Vickers hardness value of as-received materials is determined to be around 180HV since it's T6 treated. As shown in figure 5.4 the general trend is Vickers hardness profiles of as-processed tubes are consistently lower than the value of as-received materials at all locations. Vickers hardness values are determined to be range from 125HV to 140HV for as processed tubes, depending on the exact analyzed locations. A post-process aging at 120℃ for 24 hours is able to restore the micro-hardness value up to 178HV, which is extremely close to the value of the base metal. However, in most cases, the HV value is restored to around 170-175HV, around 95% of the base metal; while some exceptions are observed in tube bottom as well as the 65mm specimen. As shown in figure 5.4e, both as-processed and post-aged hardness profiles are showing a relatively low level and the profiles decrease sharply along the testing traces, result in a Vickers hardness value as low as 125HV. On the contrary, its neighbor, 55mm specimen is showing significant post aging response.

It is generally believed that micro-hardness value of 7000 series aluminum alloy is mainly controlled by the behaviors of precipitates. The observations made from figure 5.4 suggest that dissolution of precipitates might occur during the FSBE process because

of imposed thermal cycle, resulting in the decreased micro-hardness value; while post process aging facilitates the reprecipitation of dissolved solute atoms in the form of hardening phases that contributes to the restoration of mechanical properties. Similar to the case of AA6063 alloy, dissolution of hardening precipitates of 7000 series alloy during the typical thermal cycle have been reported by Mahoney et al and Su et al. [17, 32]. It is also indicated that a post aging step can restore part of the mechanical properties by reprecipitating dispersed fine precipitates. Figure 5.5 shows TEM images obtained from as-received materials as well the PZ of both as-processed and post-aged tubes. The incident beam is controlled close to a <112> zone axis of the aluminum matrix in order to identify the precipitates clearly. As illustrated in figure 5.5a, the starting material that is T6 treated consist mainly of coarse Cr-bearing particles and finely dispersed precipitates that are less than 10nm in size, which are believed to be the strengthening precipitates [17]. On another hand, the TEM image taken from the PZ of as-processed tubes shows both coarse Cr-bearing particles and MgZn2 precipitates on the order of 50-100nm dispersed relatively uniformly throughout the matrix and no smaller strengthening precipitates have been observed, as illustrated by figure 5.5b. This basically confirmed the dissolution of strengthening precipitates during the FSBE process. However, the origin of these relatively coarse MgZn2 phase needs to be discussed. It is possible that these phases are formed during the initial heat treatment of the AA7075 rod and their contrast under TEM imaging conditions is weak compared to the finely dispersed hardening precipitates thus get blurred out. Also, it might be possible that these phases are formed during the cooling stage of FSBE, when the cooling rate is not fast enough,

some solutes atoms start to precipitate at elevated temperatures. However, this assumption might not be true for several reasons: first, the tube is water-quenched immediately after the processing, leaving minimal time for high temperature precipitation; second, even if slow cooling is expected, precipitation of coarse phases typically occurs near grain boundaries and around dispersoids particles forming PFZ, unless a very slow cooling cycle is performed; last but most important argument is if the coarse MgZn2 phases are formed mainly because of slow cooling rather than initially present, a depletion of solute atoms thus deterioration of mechanism properties after post aging should be expected since less solute atoms are available for the reprecipitation of strengthening phases with sizes of less than 10nm. Basically, it can be concluded that these MgZn2 phases are largely pre-exist in the starting materials. TEM microstructure for post-processed aged sample that is machined from the PZ is shown in figure 5.5c. It is noticed that the microstructure consists of mainly dispersed hardening phases, similar to the initially T6 treated alloys. However, it is very interesting to note that the strengthening precipitates are even small compared to that of the initial materials. A magnified view of the same sample is shown in figure 5.6. It can be seen from both bright field image and dark field image that the precipitates are less than 5nm in size. With this evidence, it can be confirmed that the restoration of mechanical properties should be mainly attributed to the reprecipitation of hardening precipitates during post aging. The TEM microstructure of post process aged specimen is similar to the initially T6 treated alloy, with even finer hardening precipitates. The reason for the formation of finer hardening precipitates during post aging is: our aging treatment is performed at 120℃,

while under industrial circumstance, a higher temperature is used to reduce heat treating cycles. At the tube bottom, Vickers hardness starts to decrease significantly in both as-processed and post-aged curves, beyond a depth of 2mm. This is related to the over-aging of the microstructure since at these location, temperature drops below the solutionzing temperature and fine precipitates start to be coarsened, as pointed out by Su et al. [17]. However, for 65mm specimen, the deterioration of mechanical properties is mainly related to slow cooling, which is generally believed to be detrimental to various mechanical properties of 7000 series alloys. The slow cooling is generated at later stages of the FSBE process when the materials flow toward the top of the tube and temperature drops. It should be noted that over-aging and slow cooling might generate similarly adverse effect, they are fundamentally different concepts and resulting microstructure is different. Unfortunately, we don't have any TEM results ready for these regions for the time being.

Generally speaking, thermal cycles of the FSBE process enable the dissolution of strengthening phases and result in lower hardness values; while a post aging step restores up to 95% hardness value of the starting materials by reprecipitating the dissolved solute atoms in the form of finely dispersed hardening precipitates. Over-aging and slow cooling effects are observed in tube bottom and very top end of the processed tubes.

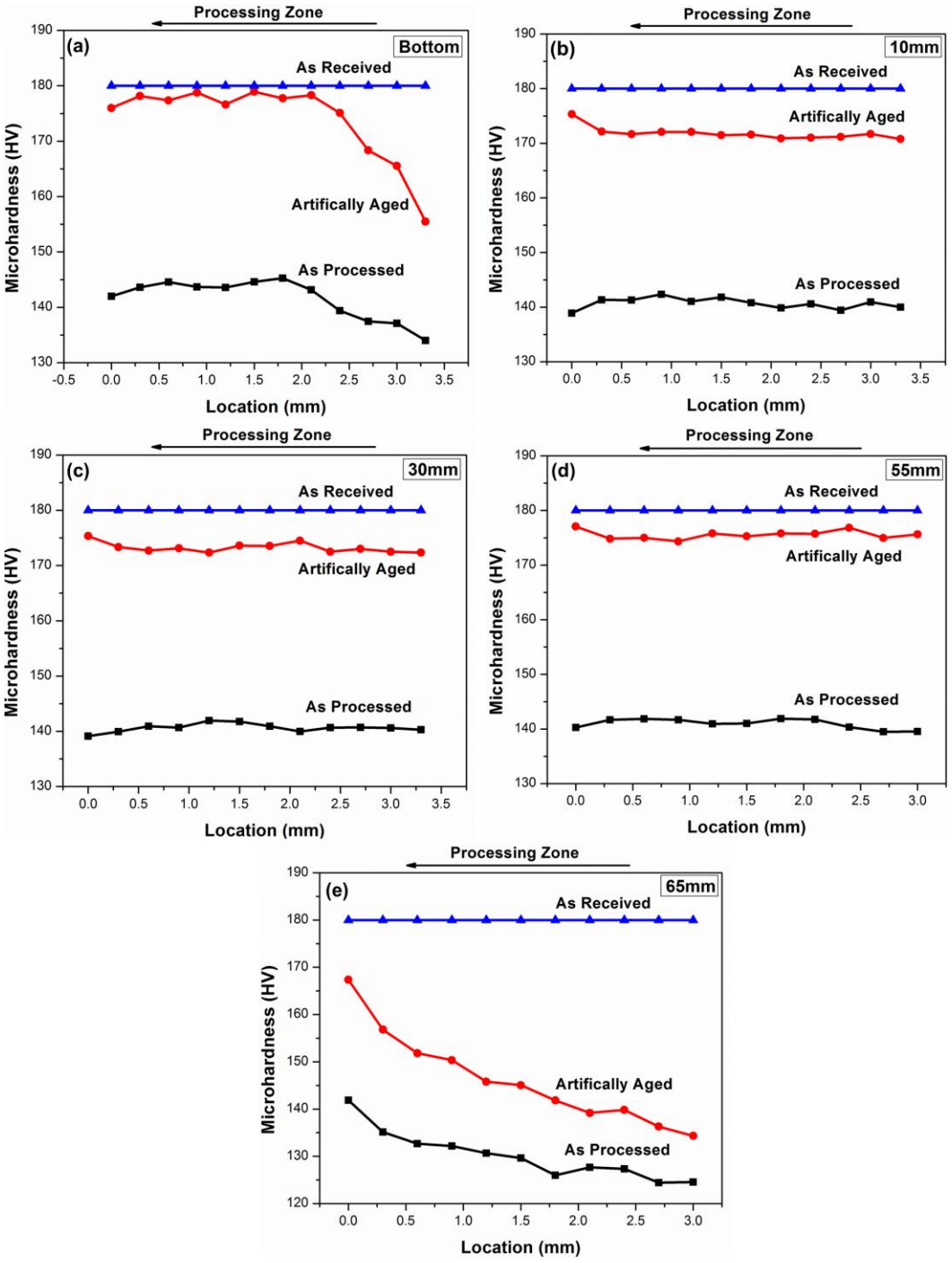

Figure 5.4 Micro-hardness profiles at (a) tube bottom (b) 10mm (b) 30mm (d) 55mm and (e) 65mm locations for both as processed and post aged samples

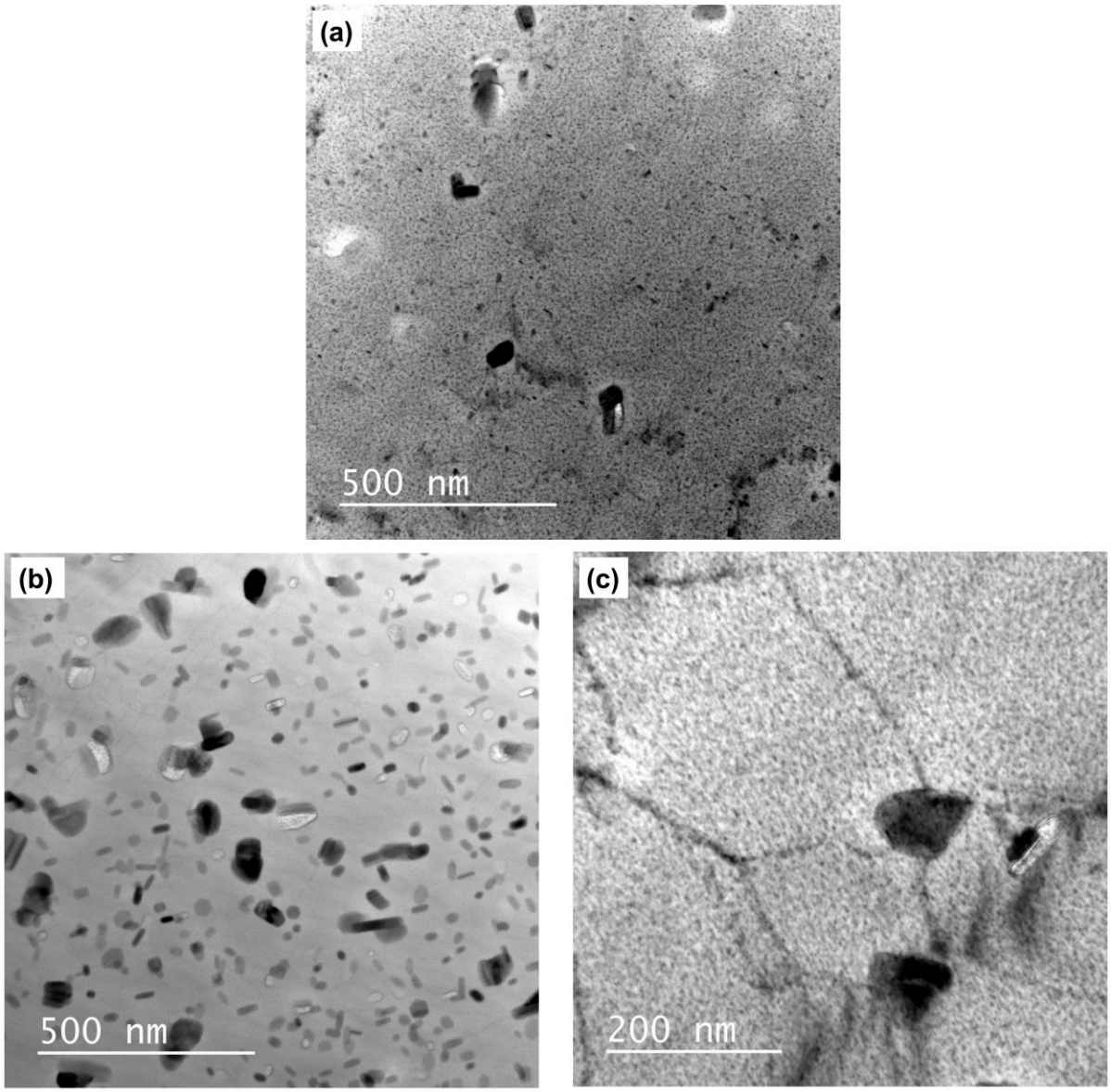

Figure 5.5 TEM micrographs illustrating the distribution and morphology of the precipitates in (a) as-received (b) as-processed and (c) post-aged 7075 alloy near the PZ

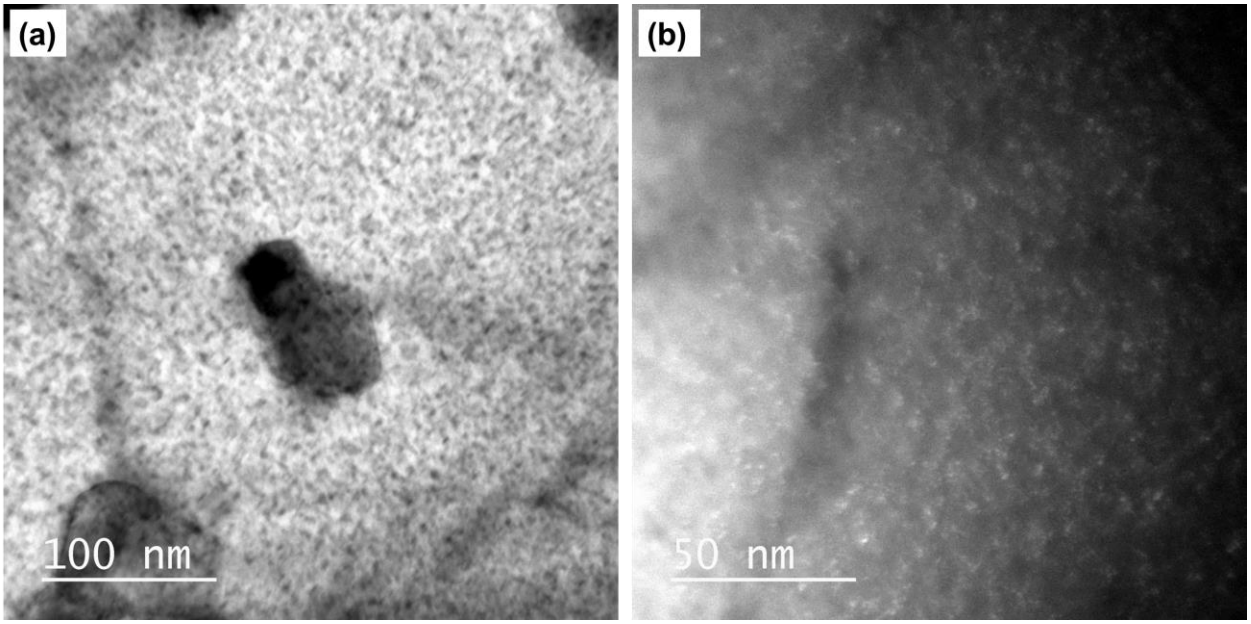

Figure 5.6 Magnified TEM micrographs showing the fine precipitates in post-aged specimen

Uniaxial Tension Tests

The tensile properties of as-received as well as processed specimens were evaluated and the engineering stress-strain curves are shown in figure 5.7. The major mechanical properties extracted from the curves are summarized in table 5.1. As received T6 treated AA7075 specimens shows yield strength, ultimate tensile strength and failure strain of 520Mpa, 590Mpa and 15.2%, respectively. After the FSBE process, the strength decreases significantly while failure strain is increased to 19.5%. This strength loss is because of the dissolution of strengthening precipitated during the thermal cycle imposed by FSBE. Post process artificial aging can significantly enhance the mechanical properties of the as-processed tubes, elevating the yield strength and tensile strength to 480Mpa and 559Mpa respectively. Compare with the as-received materials, the loss of

yield strength and tensile strength is only 7.7% and 5.25% respectively. It is obvious that the as-processed samples exhibit considerable hardening effect during post-aging, signifying the dominance of dissolution of precipitates during the thermal cycle of FSBE process and reprecipitation of finely dispersed hardening precipitates, which are confirmed by the TEM results.

By comparing with those investigation focused on the mechanical properties of 7000 series alloys [32], a very high percentage of mechanical properties is retained by the combined FSBE process and post processing aging. In other reports, the mechanical properties can't be significantly restored either because of the insufficient cooling rate after the process or other weak-links present in TMAZ or HAZ [32].

Table 5.1 Summary for the uniaxial tension tests of AA7075 tubes

Sample	YS(Mpa)	UTS(Mpa)	Failure Strain (%)
As-Received	**520**	**590**	**15.2**
As-Processed	**320**	**501**	**19.5**
Processed+Aged	**480**	**559**	**15.5**

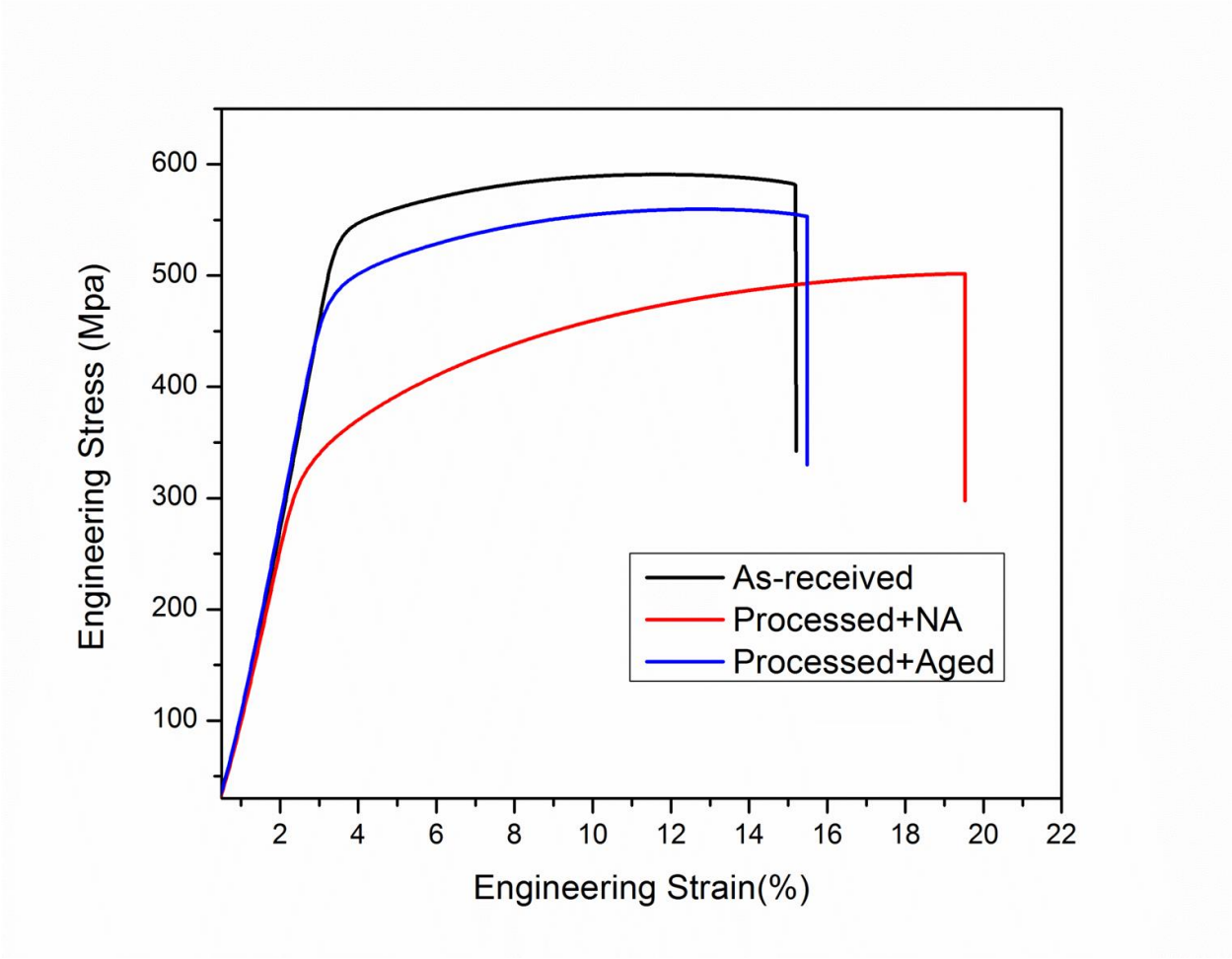

Figure 5.7 Tensile test curves for FSBE processed AA7075 tubes

Recrystallization Mechanisms for FSBE Processed AA7075 Tubes

In a previous chapter, dynamic recrystallization and grain refinement mechanisms that are identified during the FSBE process of AA6063 has been discussed systematically based on detailed grain structure analysis and its relationship to grain orientations, local misorientation and boundary distribution of both HAGBs and LAGBs. Using the findings and philosophies proposed in existing literatures as a baseline, several new observations have been made and some new thought and mechanisms are proposed in the case of FSBE processed AA6063 alloys. In this part of the dissertation, grain refinement

mechanisms of FSBE processed AA7075 alloy will be critically analyzed in comparison with the case of AA6063 alloy. It is well known that 7075 alloy is an ultra-high strength alloys with very high content of alloying elements and its deformation behavior as well recrystallization behavior is strongly affected by the precipitates and solute atoms. As shown by the optical micrographs captured along the cross sections of both AA6063 and AA7075 tubes, the corresponding microstructure evolution and grain refinement behaviors are different in the sense that the penetration of refined region is reduced in the case of AA7075 alloy while grains in the PZ are refined to a next level compared to AA6063 tubes, especially at the tube bottom. Similarly, to better understand the underlying mechanisms that are responsible for the grain refinement, investigations will be predominantly performed near the tube bottom where materials are subject to relatively simple plastic flow without being affect by deformation or thermal history, as in the cases of the tube wall.

Microstructure near the transition-PZ of the tube bottom is shown in figure 5.8a. It should be noted that the left part of the map is determined to be located within the PZ since the end of the map is only around 200um from the tool-materials interface, even if some elongated structure can still be recognized. The IPF image is colored with respect to the ‘Z’ axis that is perpendicular to SD-SPN plane since this strategy allow grains showing typical shear type textures being distinguished easily. On the transition side, elongated and distorted grains are observed with high density of LAGBs, as confirmed by grain boundary distribution mapping shown in figure 5.8b. One dominant characteristic of the grain structure near transition region is LAGBs are not well organized into ordered

subgrain boundaries as in the case of AA6063 alloys, rather they are relatively scattered and distributed mainly near the grain boundaries. This observation suggests that gradual lattice rotation of subgrains and absorption of dislocation into existing LAGB to transform into HAGB under continuous deformation might not be the major mechanism that is responsible for the grain refinement. It is proved to be the major mechanism that controls the grain refinement or even texture evolution of AA6063 alloy under FSBE, while the LAGBs distribution in the microstructure of aa6063 alloys is typically well-defined into subgrains and the progressive lattice rotation has been identified and discussed accordingly in a previous section. The scattered LAGB distribution near transition region of AA7075 alloy might further suggests the fundamental reason why the crystallographic texture observed in the FSW/FSP 7000 series alloys are always identified as close to random. The common belief that continuous grain subdivision and subgrain rotation across the initial grains will result in shear type texture can be excluded from the present discussion since no such LAGBs distribution is noticed. New mechanism that is controlling the microstructure evolution might inherently produce a grain structure with random texture. The texture is only briefly mentioned since it will be discussed separately once the refinement mechanism if fully understood.

Another observation that is of extreme importance is significant amount of small grains are formed near the grain typical recrystallization theory [55, 61, 81]. These grains are typically of small size that is less than 5um in diameter, which is much smaller than the subgrains that are formed in the interiors of elongated grains. A magnified view of the blue rectangle in the grain boundary mapping of figure 5.8 is illustrated in figure 5.9,

some regions showing high density of small recrystallized grains near original grain boundaries are highlighted. It is obvious that the formation of these grains is attributed to the activation of the first recrystallization mechanism that refers to the grain boundary bulging and progressive lattice rotation. It should be noted that this type of recrystallized grains has also been observed in the case of AA6063 tubes, where they are only occasionally noticed and their existence is believed to be of small impact to final grain structure. In contrast, grains formed following this mechanism are extensively observed both in the transition region and even in the PZ of AA7075 tubes. Grain boundary mapping for a subset that is taken within the PZ is presented in figure 5.10, it is obvious that grain structure of the PZ is actually featured by a bimodal distribution with small recrystallized grains decorating larger grains with a size of around 10-12um, which are actually close to the observed subgrain size near the PZ. It is very interesting to notice that these small grains are also formed within the PZ where no large grains are found. This signifies the fact that recrystallization at grain boundaries is still undergoing within the PZ and contribute to the formation of final refined grain structure. From a typical standpoint of CDRX near grain boundary via grain boundary serrations and progressive lattice rotation, this mechanism is primarily found in alloys exhibit strong solute dragging or lack of slip system [55]. In our case, since AA7075 alloy is highly alloyed to achieve high strength, high concentration of solute atoms, dispersoids as well as precipitates would interact strongly with the dislocations and inhibit their movements. In comparison, AA6063 alloys is a dilute alloys aimed at performing high corrosion resistance and low

quench sensitivity, the solute dragging effect is minimal, resulting in sporadic observation of CDRX at original grain boundaries.

Apart from scattered LAGBs distribution and the formation of small recrystallized grains, it should be mentioned that grains formed via the second mechanism that has been discussed in the case of AA6063 alloy has barely been noticed. As discussed in a previous chapter, this mechanism involves the formation of HAGBs at the junctions of subgrain boundaries. Since the distribution of LAGBs is very diffuse, not many such well-defined nucleation sites are generated to enable the formation of recrystallized grains via the second mechanism. In the case of PZ, grain structure is so refined that most of recrystallized grains don't even have subgrain network in their interiors, not even mention recrystallization at the junction of LAGBs. Thus it can be easily concluded that the effect of this mechanism on the microstructure evolution of FSBE processed AA7075 alloy is negligible. However, an example of this type of grains is shown in figure 5.11, it is noted that the corresponding mother grains contains decent amount of LAGBs in its interior and they happened to be distributed with order to some extent, while most of other elongated grain don't exhibit such characteristic. That might be the reason why such recrystallized grains are observed in this mother grain. The misorientation profile that goes across one of the newly formed grain indicates a misorientation angle of around 30 degrees.

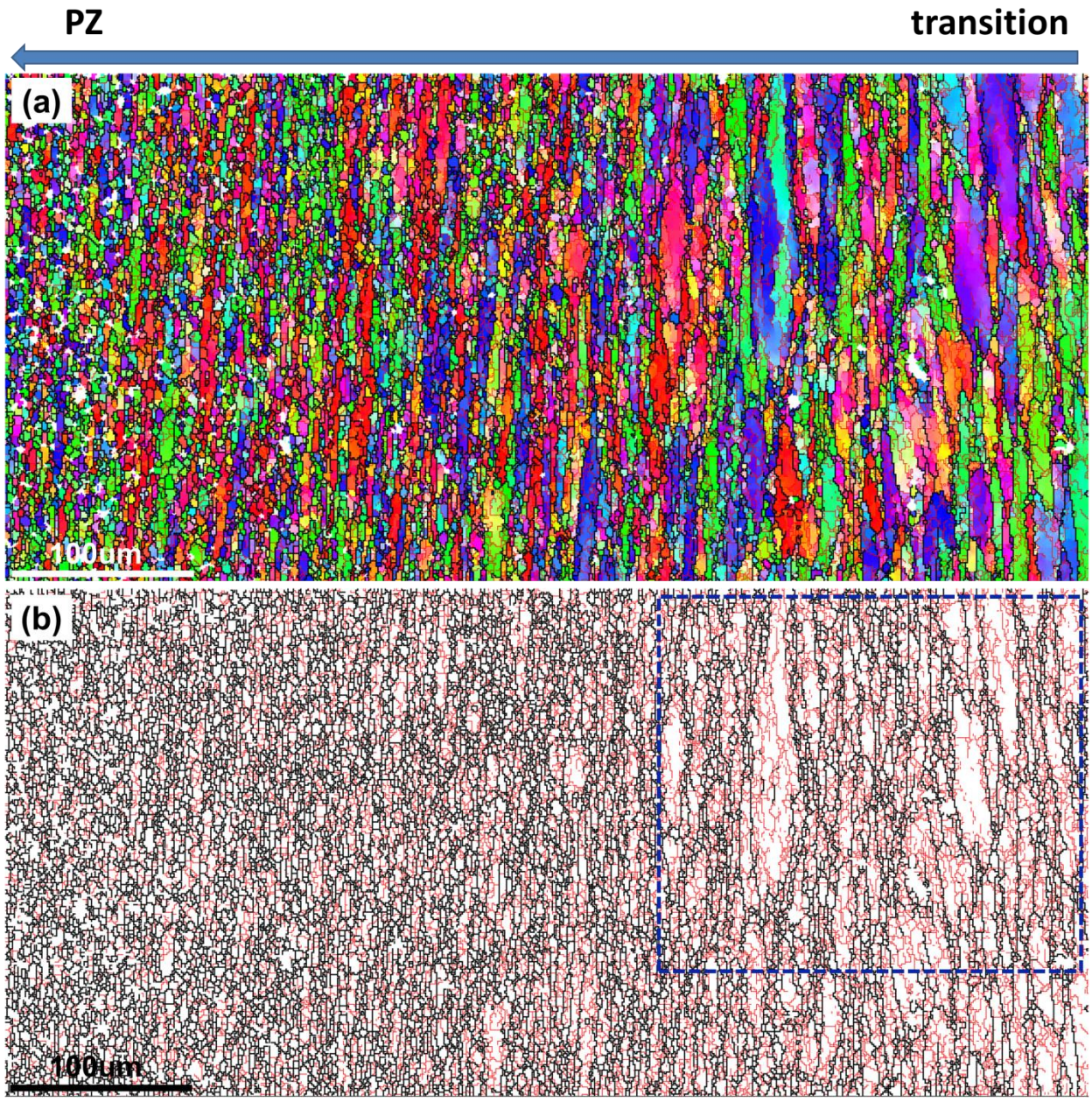

Figure 5.8 (a) IPF image and (b) grain boundary distribution near the transition-PZ region

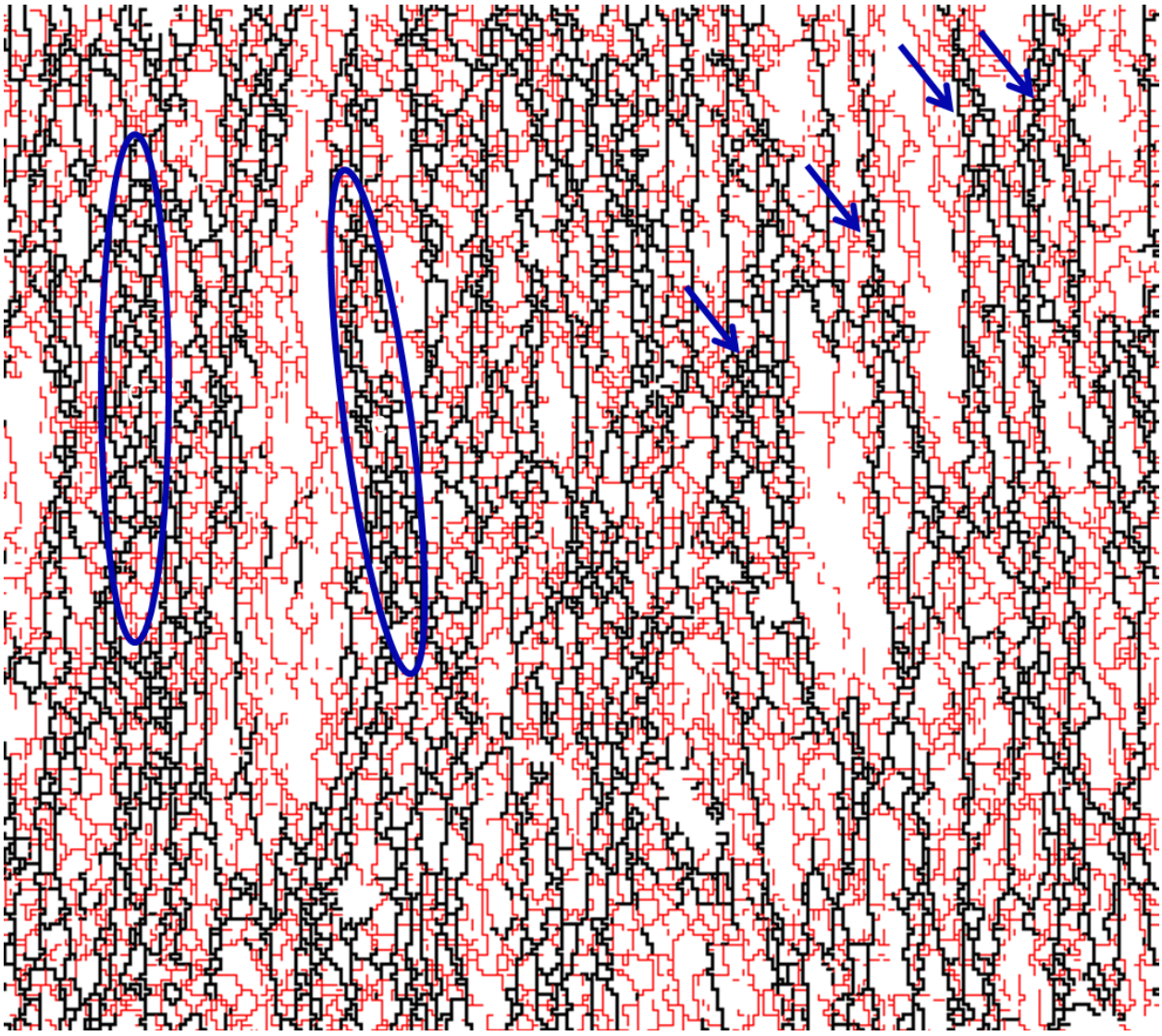

Figure 5.9 Magnified gain boundary distribution of the selected region in figure 5.8

Now another new question arose, since those smaller grains observed within the PZ shown in figure 5.10 are believed to be formed via CDRX that occurs near grain boundaries, then how these coarser grains are generated, what is their origin and by what refinement mechanism they are formed? It can be seen form figure 5.8 that grains near the PZ side of the map are highly stretch and elongated along the vertical direction, the

orientation based mapping suggested that near the end of transition region or even within the PZ, certain grains are so elongated that the width of the grain become so thin that it is almost equal to the subgrain size. Additional information involves that some well-defined grains surrounded by HAGBs within the PZ are still distributed vertically and showing similar orientations, even if they might be separated by grains showing other orientations. The most direction vision from figure 5.8 is a lot of elongated grains are showing a certain color, i.e. specific elongated grains tend to be split into pieces under deformation while isolated pieces are still distributed vertically and their orientations are represented by similar colors. These evidences strongly support the recrystallization mechanism of geometric dynamic recrystallization (GDX) that is normally triggered when the width of the grain is reduce to a similar size of stable subgrain size. More importantly, the size of these subgrains that are identified within the elongated grains near the PZ-transition interface is found to be similar to the coarser part of grains contained within the PZ, as represented in figure 5.10. A magnified view of a su B region extracted from the interface between PZ and transition region is shown in figure 5.12 to illustrated the LAGB distribution in the elongated grains that are tend to recrystallized via GDX. The white lines are used to distinguish the LAGBs that are showing 3-15 degrees misorientation clearly, while black arrows point out the typical grains that are subdivided horizontally by LAGBs and tend to undergo GDX. It should also be mentioned that a lot of shorter episodes or separated grains are also observed in figure 5.12. However, they might be at different evolutional stage of the GDX process.

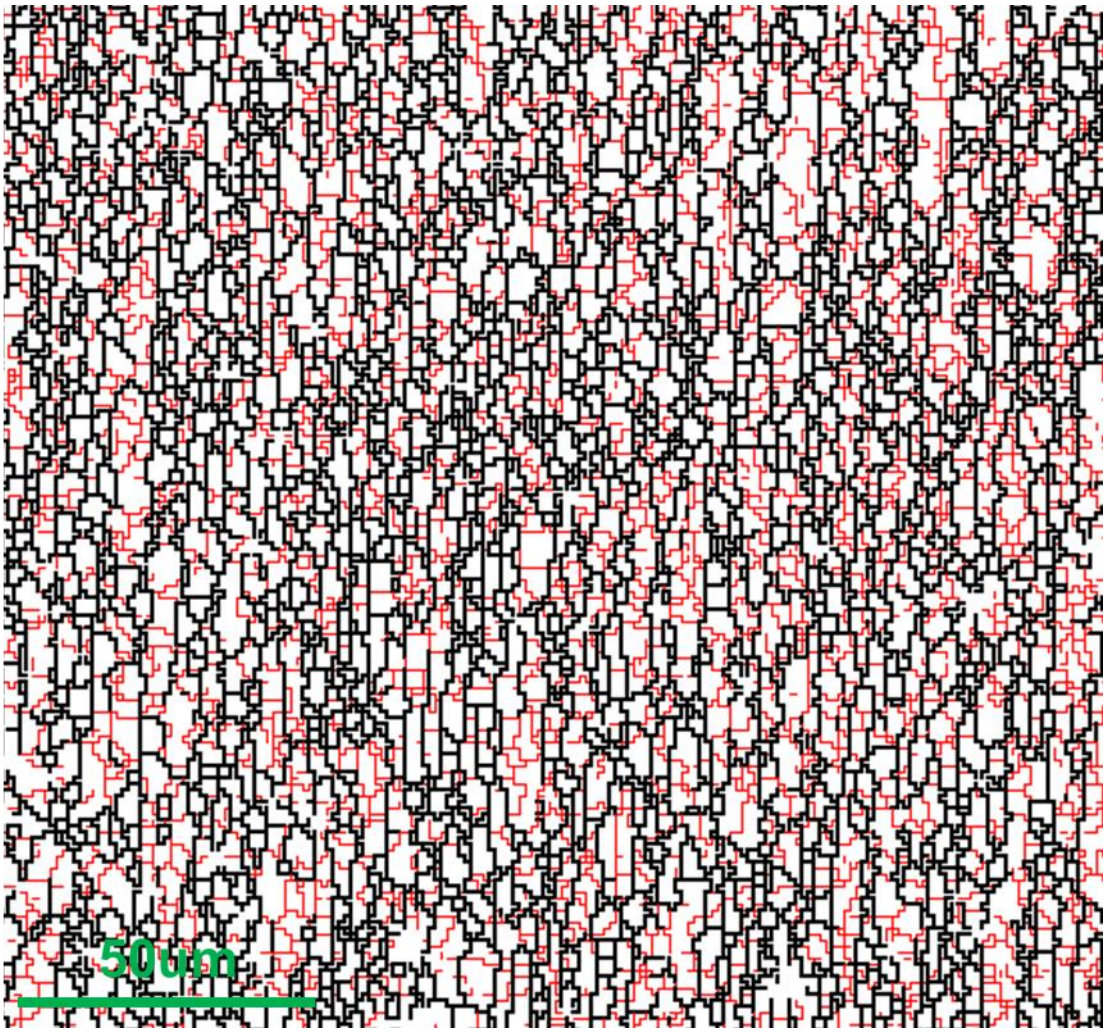

Figure 5.10 Magnified gain boundary distribution of the refined region

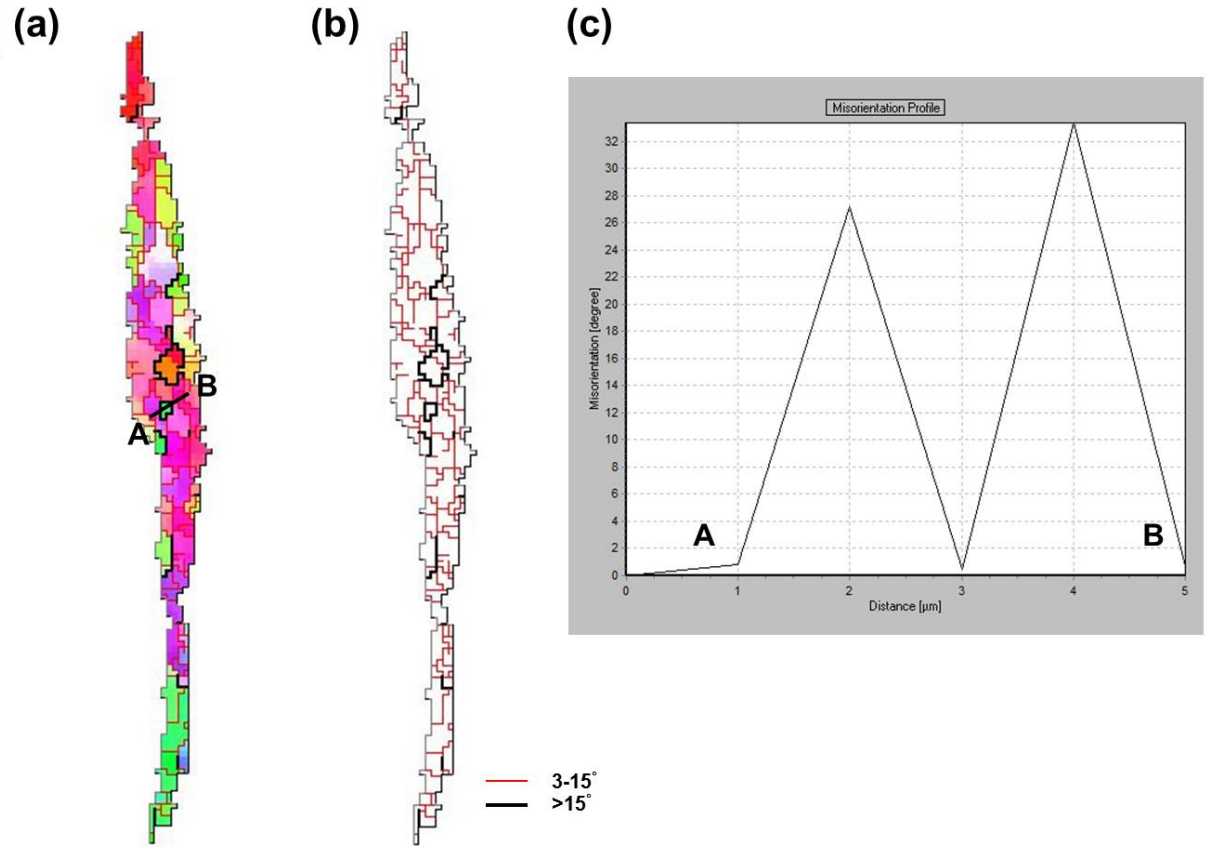

Figure 5.11 (a) IPF image (b) grain boundary distribution and (c) misorientation profile along A-B for an analyzed grain

In order to understand the next-step evolution of these horizontally subdivided grains whose width is similar to subgrain size under additional straining, further analysis is performed within the PZ, where grain structure development is believed to be more mature. A separated EBSD scan with finer step size is performed exclusively for the grain structure inside the PZ, as shown in figure 5.13. It should be noted the entire map is rotated by 90 degrees thus the stretching direction of the grains is horizontal, the map is color-coded with respect to the 'Z' axis for the same reason of being able to identifying

different texture component easily. It can be seen from the IPF figure shown in figure 5.13a that coarser grains with around 10um grain size are intermixed with fine grains that are less than 5um in size, actually the fine grain are typically in the range of 2-3um. The grain structure of the entire region is more mature with predominant HAGBs and no highly elongated grains separately by LAGBs are observed, as indicated by the grain map of figure 5.13b. It is obvious that a lot of grains exhibiting similar orientations (represented by similar colors) are aligned next to each other as 'strings' along the horizontal direction, which suggests the fact that they should be evolved from the same elongated grain at an earlier stage. More importantly, these grains are separated by well-developed HAGBs thus consolidate the refinement mechanism of GDX and the formation of relatively coarser grains in the PZ. An additional note regarding the grain structure observed in figure 5.13 is that most grains formed by GDX has been pinched off into smaller episodes or even isolated grains by their neighboring grains that are under development. Those small episode or individual grains start to intermix with other grains that are either generated by similar GDX mechanism but form different initial grains or grains formed via CDRX at grain boundaries. Finally, no clue can be found regarding its initial orientation and morphology.

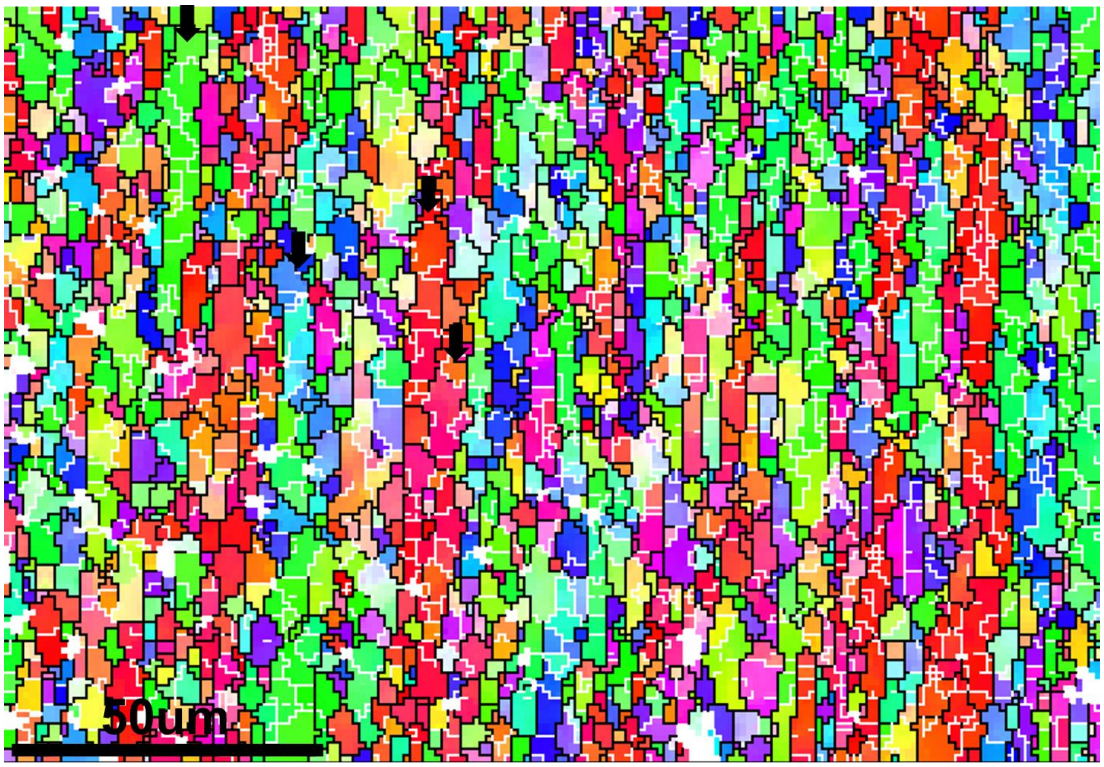

Figure 5.12 LAGB distributions near PZ-transition region of AA7075 tube

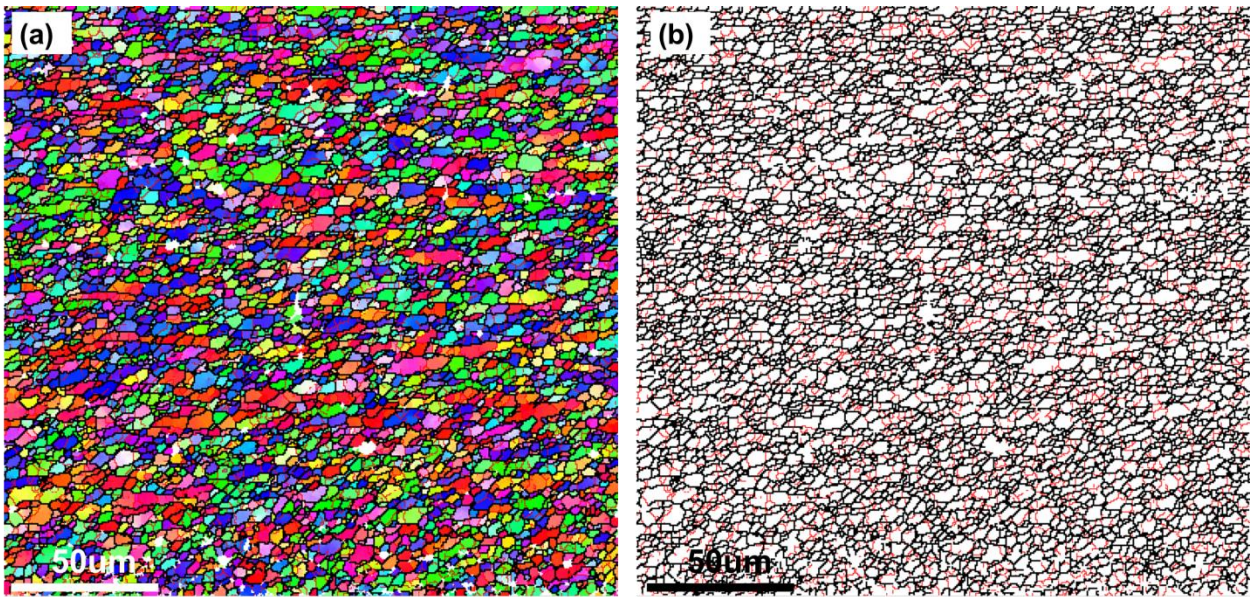

Figure 5.13 (a) IPF image and (b) grain boundary distribution of the PZ in AA7075 tubes

Several examples will be extracted from the map shown in figure 5.13 to enable detailed orientation and misorientation analysis. A typical array of grains is shown in figure 5.14, it is noticed that the string is basically consists of six individual grains that are separately by HAGB, while LAGBs aligned vertically are still observed. It seems that some of these LAGB are still under development and they just haven't accumulated enough misorientation to the level that can be defined as a separated grain. The misorientation profile along A-B suggests the formation of HAGBs with misorientation angles from 15 degrees all the way up to 55 degrees. It is also noted that all these grains are showing <111>//Z axis and it is inferred from the PF analysis shown in figure 5.14 that this set of grains change orientations by rotating around Z axis, result in the same colored coded grains. While some other groups of grains that are formed by GDX might be showing different trends, since the orientation spread and grain subdivision of the initial grain might not be strictly related to the 'Z' axis, which can result in a series of grains that are characterized by different colors in the IPF images and hard to be identified properly. However, in most cases, the split and rotations of subgrains undergoes GDX should not as ideal as the situation shown in figure 5.14. It can be easily concluded that these grains shown in figure 5.14 are formed via GDX when the thickness of the initial grain approach the subgrain size, the GDX mechanism can be confirmed both by their microscopic morphologies and crystallographic orientations, misorientation levels of HAGBs that are formed during GDX are not necessary being on the low end of HAGBs. Unfortunately, the underlying mechanism by which these LAGBs are transformed into HAGBs during GDX has not been figured out yet.

A more general case of GDX that is not showing any specific type of orientation splits is shown in figure 5.15. It can be seen from figure 5.15a that this group of grains is not characterized by similar colors, that means the grain orientation split does not occur based on the rotation along Z axis. However, it is still obvious that this set of grains is evolved from an initially deformed and elongated grain via GDX whose width is similar to subgrain size. Similarly, from the grain boundary mapping shown in figure 5.15b, it can be noticed that some LABGs are distributed vertically and haven't accumulate enough misorientation to become HAGBs. Corresponding PFs in figure 5.15d shows relatively scattered distribution of orientations for each pixel. It should be emphasized that this type of GDX that is not showing any specific evolutional tendency with respect to grain orientation is also a significant pathway that GDX follows, even if they are difficult to be identified compared to other cases in which a group of grains are colored similarly, such as the grains shown in figure 5.14. This will naturally lead to another question, what is final texture type if dynamic recrystallization is controlled by GDX? Based on our preliminary results, it is shown that newly formed grains from those elongated grains via GDX either shows a rotated orientation from their mother grains around a specific axis or more generally become somewhat randomly orientated. This might provide important indications for the formation of relatively random texture in the PZ of A7075 tubes, which will be investigated in detail in a later section.

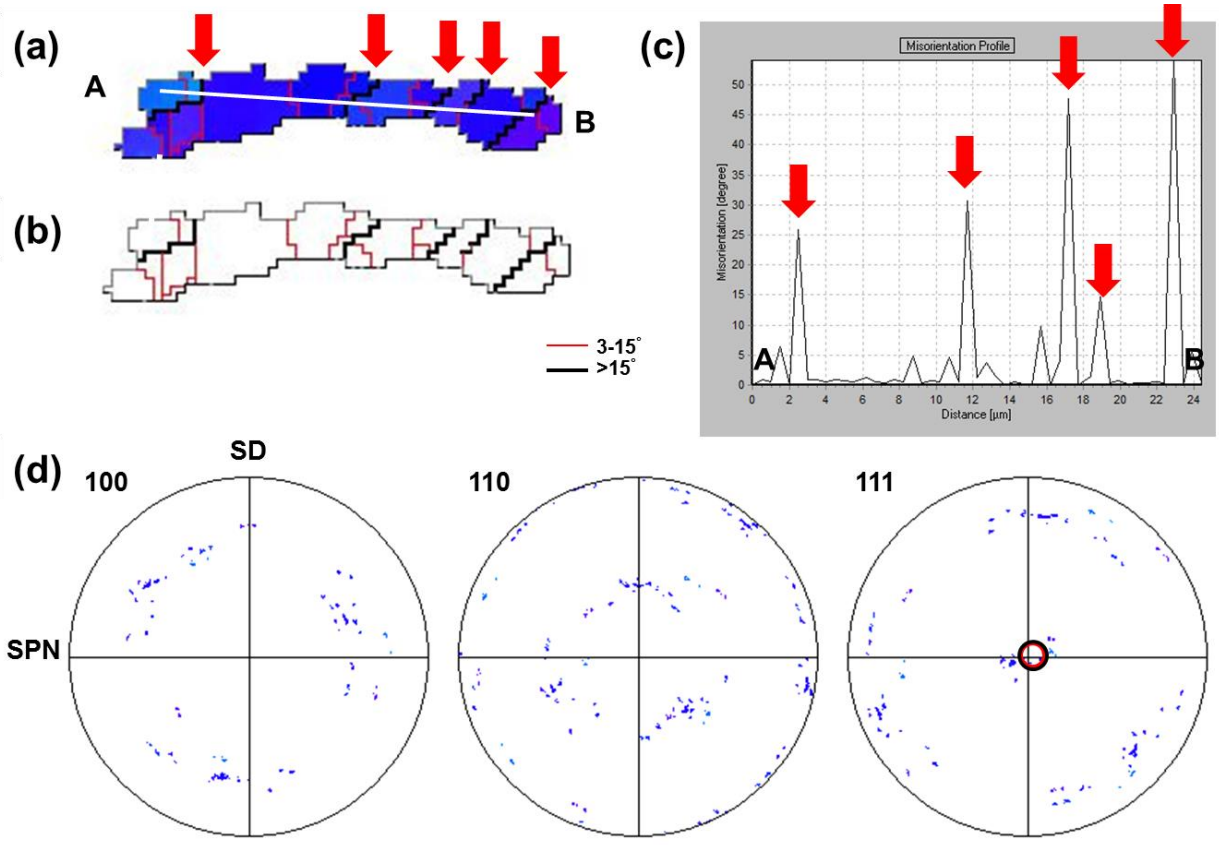

Figure 5.14 (a) IPF image (b) grain boundary distribution (c) misorientaion profile along A-B and (d) pole figures for a series of analyzed grains

It should also be noted that within the microstructure shown in figure 5.13, most of the larger recrystallized grains are not showing identifiable characteristics that can be directly proven to be a result of GDX, as in cases shown in figure 5.14 and figure 5.15. In a more general circumstance, those grains formed via GDX that are initially aligned horizontally will be pinched off into small episodes or even into separate grains, and finally these grains become isolated and intermixed with other grains under extended deformation and plastic flow. A set of grains showing this type of pinching off is

illustrated in figure 5.16. It can be seen that one block consist of three grains are separated from the original arrays of grains by its neighbors while the two episodes are still aligned horizontally. It is noticed that this behavior is similar to the pinching off of grain blocks as addressed in the discussion of grain structure evolution of FSBE processed AA6063 alloys. And it should mainly be attributed to the interaction between grains under intense straining; grain boundaries migration might also contribute to the pinching off procedure. However, its effect should be minimal in the case of AA7075 alloy due to strong solute drag.

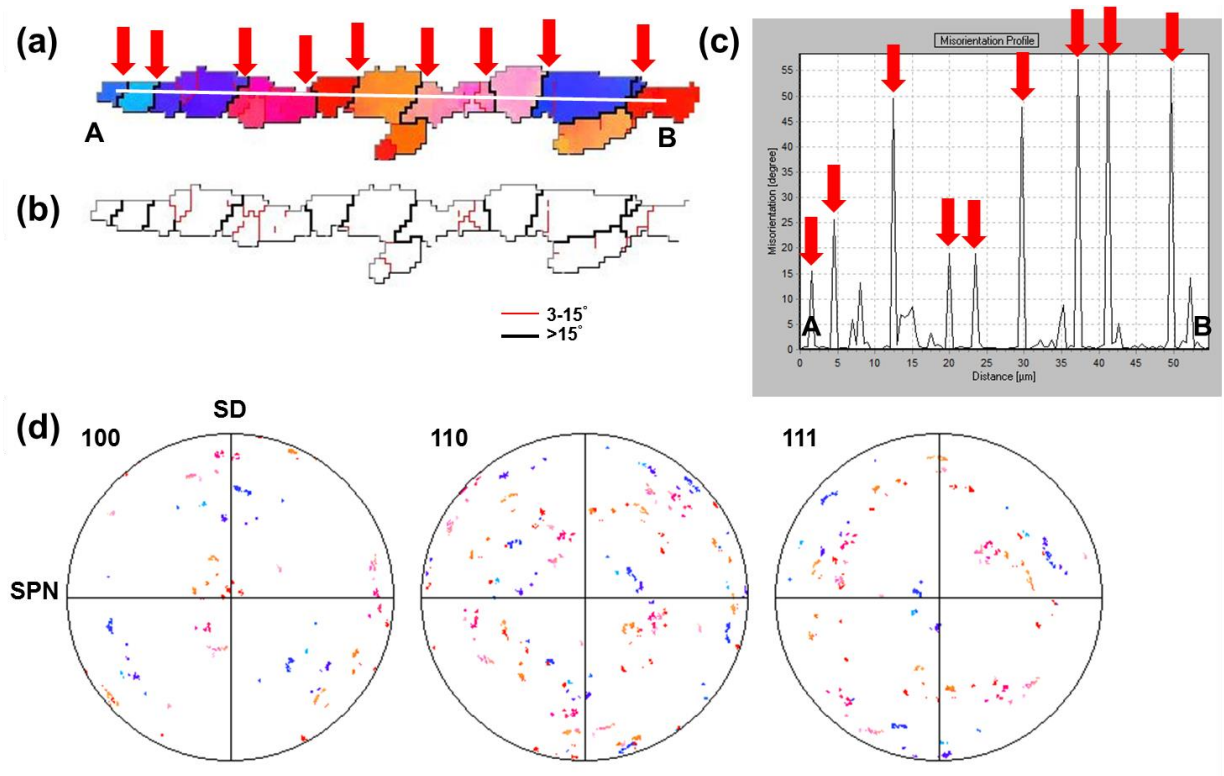

Figure 5.15 (a) IPF image (b) grain boundary distribution (c) misorientation profile along A-B and (d) pole figures for grains formed by GDX

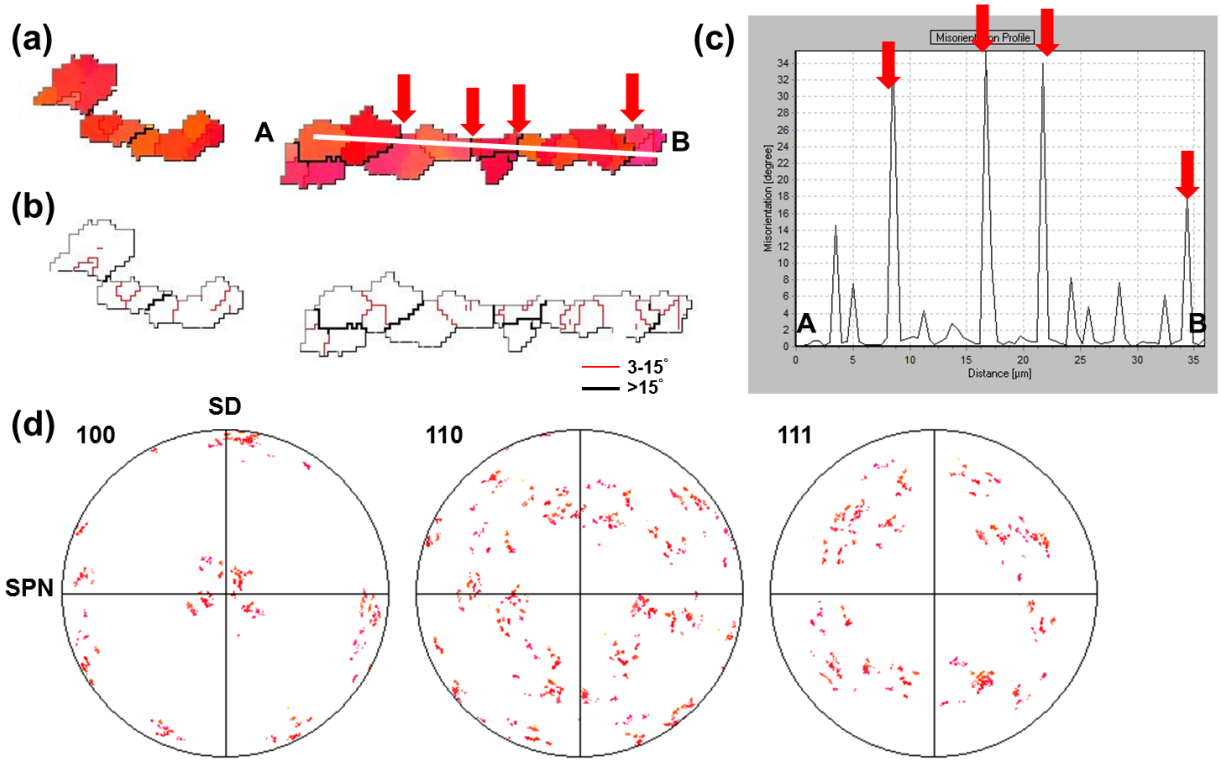

Figure 5.16 (a) IPF image (b) grain boundary distribution (c) misorientation profile along A-B and (d) pole figures for a series of analyzed grains

In general, the major recrystallization mechanisms that are responsible for the grain refinement of AA7075 alloy subjected to FSBE process are CDRX at grain boundaries and GDX. With CDRX, small grains with sizes of less than 5um are generated near the existing grain boundaries and forms necklace-like grain structure in the transition region; while within PZ, similarly, small grains are also formed and intermixed with larger grains that are formed via another mechanism. Regarding GDX, initial grains of the AA7075 alloy are highly elongated under shear straining and their width reach the subgrain size near the interface between transition region and PZ; then

these grains are mainly subdivided by LAGBs that are perpendicular to the direction of grain stretching; finally, these LAGBs are developed into HAGBs under further deformation and geometric recrystallized grains are formed within the PZ, the grains formed via GDX are relatively large compared to those resulted from the CDRX process at grain boundaries. It should be noted that the CDRX process occurs at grain boundaries is an operating mechanism across the entire map shown by figure 5.8 that contains both transition and PZ since small recrystallized grains are widely observed. However, the GDX mechanism only functionize near transition-PZ interface as well as within the PZ where strain level is high enough to reduce the width of deformed grain close to subgrain size and trigger GDX, resulting in recrystallized grains with a size of 5-10um. Since both CDRX at grain boundaries and GDX are the dominant refining mechanisms that contribute to the grain structure evolution of the PZ of AA7075 tubes, the final microstructure observed within the PZ is characterized by a bi-modal grain structure with coarser grains intermixed with finer grains that are formed by these two mechanisms, respectively.

As noted in the grain structure evolution of FSBE processed AA6063 alloys, the recrystallization mechanism mainly involves gradual lattice rotation and reorientation across the entire initial grains, either in the form of grain blocks or individual subgrains; while the effects of GDX and CDRX at grain boundaries are believed to be minimal despite the fact that some geometric effect is observed near the transition region and grains formed via CDRX at grain boundaries are also noticed within both transition region and PZ. Additionally, crystallographic texture observed in the case of FSBE

processed AA6063 alloy is characterized by a strong shear B/$\bar{B}$ component while the texture within the PZ of AA7075 tube is very weak and tends to be randomized. Then the question arises: why such a discrepancy develops for different alloys under similar processing conditions and what is the fundamental difference? It is widely known that the major difference between AA7075 and AA6063 alloys lies in the alloy contents. In the case of AA7075 alloy, a higher amount of alloy elements is added for the purpose of generating high strength compared to AA6063 alloy, also some auxiliary elements are added for other reasons. Basically high alloys contents mean more precipitates, dispersoid particles and also high solute content.

It might be true that high alloying content will fundamentally change the deformation mechanisms that control the slipping of dislocations and activate extra deformation modes under high temperature deformation, resulting in different refining mechanisms being operative. However, not sufficient data is provided for such assumptions. Meanwhile, it has been proved that alloying would only marginally modify the stacking fault energy (SFE) of the aluminum alloys [55, 57], which is related to the dislocation climb and cross-slip. Thus it is proposed that solute drag is playing a dominant effect on the grain structure formation of AA7075 alloy, it should be noted that the solute drag not only refers to the interaction between solutes and dislocations, rather it encompass the interactions between precipitates, dispersoids and solutes atoms with either dislocations or boundaries.

Fundamentally, the major effect of solute drag is inhibiting the movement of dislocations by strong interaction between pinning particles/solutes and mobile

dislocations. With solute dragging, several aspects should be noticed: first, dislocations are tend to be pinned and not being able to move freely to form well-defined subgrain boundaries, that is why the distribution LAGBs observed in the case of AA7075 tubes is very diffuse compared to the AA6063 alloy where ordered subgrain structure is formed; secondly, for those LAGBs that has already been formed, the solute/ particles would interact with the boundary and retard their movement, that why no ordered network of LAGBs are formed in AA7075 tubes; because of the pinning effect, dislocations can't migrate by long distance and that's the reason why some sporadic, individual LAGB are formed.

In the case of grain boundary CDRX, because of localized deformation near grain boundaries, dislocations are generated and concentrated around these regions, strong solute dragging can result in localized serration of the initial boundaries thus those ordered dislocations are able to aligned themselves into very small regions and forms small recrystallized grain by lattice rotation. This effect is prominent in AA7075 alloy since a large number of this type of grains are noticed across the PZ and transition region, the formation of this type of grains is directly related to the level of solute dragging, as point out by the classic theory of CDRX [55]. For AA6063 tubes, limited grains are generated as a result of CDRX at grain boundaries because of its dilute nature. The reason why GDX occurs in the case of AA7075 alloy under FSBE can be explained as: due to strong solute dragging, the dislocations formed in the grain interiors during plastic deformation can't migrate freely to a long distance to formed well defined subgrain structure, even if some subgrain structure are formed, it is still very hard for them to

develop HAGBs by absorbing mobile dislocation to build up enough misorientation level and being able to defined as HAGBs or separated grains because of the restricted movement of dislocations. Thus, grains of AA7075 alloys are subjected to such a high level of strain that they are so elongated to the extent when their width become similar to subgrain sizes and trigger GDX, before the LAGBs in the grain interiors are evolved into HAGBs via the retarded process of absorbing mobile dislocations and build up misorientations. While in the case of 6063 alloy, the migration of most mobile dislocations are not highly restricted that they can easily align themselves into ordered networks and form arrays of subgrains in the grain interiors during earlier stager of deformation, when the grains are not high elongated, as shown by the EBSD results near transition-TMAZ region. That is to say, before the AA6063 grains are elongated to the similar level of AA7075 alloys, which is obviously impossible based on our experimental results and understandings, the recrystallization has already been finished by the CDRX process across the entire grains and newly recrystallized grains are formed since HAGBs can be easily formed by absorbing mobile dislocations into existing arrays of LAGBs.

To summarize, the occurrence of both GDX and CDRX near grain boundaries are attributed to the solute drag and pinning of mobile dislocations. At the same time, the fundamental microstructural evolution and refinement mechanism is directly related to the level of solute dragging, originating from the addition of alloying elements. Our contributions of this part can be summarized into several points:

1, In-depth understanding of grain structure evolution and grain refinement mechanisms of AA7075 alloys during friction stir related process, substantiated by the

grain level investigations. It is widely reported that grain structure in FSW/FSP processed 7000 series alloys can be highly refined; however, the detailed mechanisms have not been addressed systematically. Some existing results pointed out DDRX as an important mechanism responsible for the grain refinement of 7000 series TEM analysis [10]. However, later discussions, even by the same authors [11, 70], agreed that its contribution to the microstructure is not significant, compared to other mechanisms.

Additionally, particle stimulated nucleation (PSN) is also proposed as a possible mechanism that is responsible for the formation of ultrafined grain structure as well as random crystallographic texture [11]. This mechanism seems to be attractive since it can perfectly explain the observation of ultrafined grains and random texture at the same time, while it turned out to be plausible since the contribution of second phase particles in stimulating nucleation can't be matched to the theoretical model for PSN base on the measured sizes. However, the investigation is performed on 5083 alloy which is also believed to show strong solute dragging. With our investigations, PSN is not discussed simply because no corresponding findings support the presence of PSN.

2, Comparative studies and discussions are performed for different alloys systems that are subjected to similar processing, with special attention paid to grain refinement mechanism and recrystallization behaviors, which has not been addressed in the existing literatures. Confirming the importance of solute dragging and provide a reasonable explanation for the scattered microstructural and textural results that have been reported in different alloy systems.

3, Highlight the contribution of different recrystallization mechanism to the microstructure evolution of different alloy systems

Micro-Texture Evaluation of FSBE Processed AA7075 Tubes

In this section, micro-texture results that are measured along the cross section of FSBE processed AA7075 tubes will be briefly demonstrated and analyzed. Similar to micro-hardness and optical microscopy analysis, textural measurements are performed across the tube wall at multiple locations as well as near the tube bottom. Even if significant difference between the measured texture results of AA7075 tubes and that of AA6063 tubes is noticed, the author is not intended to provide another exhaustive texture analysis for the AA7075 tubes across the entire cross section, simply because the general trend of the texture evolution for the case of AA7075 alloy is vague and scattered. Thus, in this section, the general plan is briefly reviewing the texture components that are observed across the tube wall at multiple locations, and discussing the relevant forming mechanism under different situations. Special attention will be paid to the texture formation as well as underlying mechanisms of recrystallized grain structure within the PZ near the tube bottom. Additionally, discussion will be made base on both the measured texture data and identified recrystallization mechanism in a previous part. Finally, a comprehensive comparison to the case of AA6063 tubes will be presented.

The IPF image of the microstructure and micro-texture observed near the tube bottom is shown in figure 5.17. EBSD scan is performed to a depth of around 2.2mm from tool-materials interface, which is similar to the case of AA6063 tube. The entire

map is color coded with respect to the extrusion direction, i.e. SPN in this shear reference frame. Five subsets are extracted from the map from the side close to BM to the processing region and PFs for each subset are plotted separately in figure 5.17 B f. The texture of sub1 can be interpreted as random texture and the PFs looks similar to as received materials, where some strong poles are observed due to the presence of certain larger grains. Grains within sub1 are showing reduced aspect ratios under applied strain field while still slightly elongated toward initial extrusion direction. Surprisingly, while those grains start to transform into elongated morphology along the SD under additional shear strain, as shown in the case of sub2, the micro-texture start to be characterized by a relatively strong <111>//SPN fiber texture, which is shown by figure 5.17c. In the case of sub3, where grains are further elongated along SD and featured by an increased aspect ratio as well as reduced grain width, the micro-texture is measured to be a stronger <111>//SPN fiber which is even closer to the ideal (111) pole, combined with a very weak (100)//SPN fiber. Sub4 is basically the microstructure near the transition region where significant amount of shear strain is applied and recrystallization start to take place within some grains, the microstructure is further elongated such that grain width is close to the subgrain size and being ready for the start of GDX. Corresponding micro-texture is measured to be a weak <100>//SPN fiber while <111>//SPN fiber is barely noticed, as illustrated in figure 5.17e. In the case of PZ, the micro-texture essentially becomes random with a very weak <100>//SPN component that might be inherited from some grains from transition region. The strongest pole on the PFs is only of two times of ideal random texture.

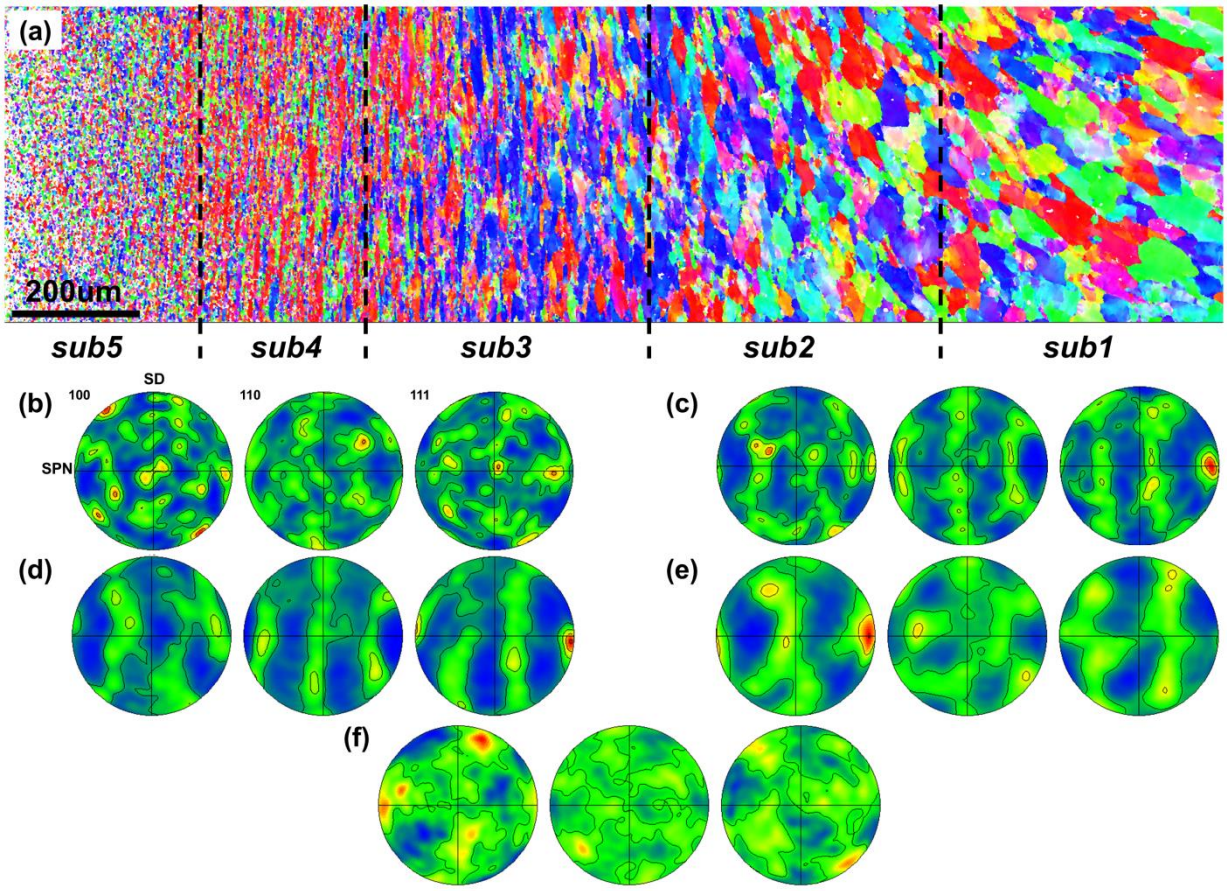

Figure 5.17 (a) IPF image of the tube bottom (b)-(f) Pole figures for sub1-sub5

It is obvious that the micro-texture in the tube bottom can be essentially defined or interpreted as fiber texture rather than simple shear components, despite the fact that shear strain is expected to be the dominant deformation mode. At the initial stage of deformation, highly elongated grains along ED are deformed and subjected to the effect of both compression and shearing, result in microstructure with reduced aspect ratios, as illustrated in the sub1 of figure 5.17. It is also noted that the texture is still randomized while the grains start showing near equiaxed morphologies. However, when the grains start to be stretched and elongated along SD, a <111> fiber start to form. It can be seen

from figure 5.17c that a (111) pole is developed close but not ideally located at <111> fiber positions. This can also be correlated to the IPF image of sub2, where the microstructure consists of equiaxed grains, similar to sub1, and some elongated grains that are just developed. With additional shear strain, the grain structure within the sub3 is characterized by fully developed elongated grains along SD, while the ideal <111>//SPN fiber is formed simultaneously with a stronger (111) pole. At the same time, a weak <100>//SPN type starts to form near the end of sub3 where higher strain or strain rate level is expected, as represented by those grains colored by red in the IPF image of sub3. Scrutinization of these grains indicates that they are typically of higher aspect ratios and subjected to higher strain levels. With the observations made in sub4, it can be concluded that the <111> fiber is transformed to <100> fiber under additional shear. It seems that <100> fiber is more stable under higher strain level while the <111> fiber is stable at moderate strain. Another possibility might be the grains tend to form <100>//SPN fiber while <111> fiber is only of a transitional type. An interesting phenomenon is this texture transformation corresponds to the geometry change of grains very well: when the elongated thick grains are developed into thinner and longer grains, the fiber texture changes from <111> fiber to <100> fiber, just like the transformation of initial random texture into <111>//SPN fiber corresponds to the grain morphology change from equiaxed to slightly elongated. Thus, to summarize, the texture development of FSBE processed AA7075 alloy outside the PZ can be basically related to strain level as well as morphologies of the grains. The micro-texture can be interpreted as fiber texture rather than shear texture. It might be possible that the alignment of SPN is more favored for this

alloy during the friction stir related process, contrary to the prevalent observation that the SD alignment is predominant. Despite the fact that the texture across the entire PZ-transition region-TMAZ can be defined as fiber type, the ideal shear component can still be observed. The distribution of grains showing ideal B/$\bar{B}$ texture components across the same map is shown in figure 5.18 with the PFs plotted in the SPN-SD framework confirmed the formation of ideal B/$\bar{B}$ texture with <110>//SD and <112>//SPN, as shown in figure 5.18b. It is obvious from figure 5.18a that these grains are distributed homogeneously across the entire map regardless of the level of shear deformation and grain morphologies. Additionally, basically no transitional texture components such as C type are noticed during our analysis, suggesting its instability and transient nature. It should be noted that based on the extensive observations of fiber texture rather than shear component, a plausible assumption might be proposed that either the strain or the effective shear strain is not sufficient to reorient the initial texture to a shear texture because AA7075 alloys is hard to deform and shows sluggish reaction to external strain due to solute pinning.

Now with the evidence shown in figure 5.18, this assumption can be easily excluded from our discussion since B/$\bar{B}$ texture are formed across the entire map, indicating the strain level is high enough for their formations even near TMAZ. This leads us to the new possible proposal that the stability of texture components might be the key answer. That means <100> fiber and <111> fiber can be formed and being stable during the shear deformation induced by the FSBE process, while only in the case of 7075 alloy. The <111> fiber tend to be form and being stable at lower strain level that

corresponds to grains showing lower aspect ratios while <100> fiber is noticed to be more stable at high strain level and the corresponding microstructure is composed of highly elongated grains. At the same time, typical stable shear components can also be formed while its strength is not as high as that of the fiber texture, thus not able to be identified clearly. Also, homogeneous distribution of grains exhibiting B/$\bar{B}$ components shown in figure 5.18 suggests that the stability of B/$\bar{B}$ type texture might be constant during the transformation. A side note need to be mentioned is: for AA7075 alloy since the dynamic recrystallization and dynamic recovery process is relatively sluggish compare to AA6063 alloy, a fully recrystallized grain structure is only formed in the region that is within 500um from tool-materials interface. However, that doesn't mean the effect shear strain is low in the case of AA7075 tubes. These highly elongated grains suggest the effect shear strain, while the only difference lies in AA6063 tend to be fully recrystallized at lower strain level (further away from the tool-materials interface), which happens for AA7075 alloy with a much higher strain level. Unfortunately, the fundamental mechanisms that contribute to the generation of fiber texture under shear dominant deformation mode have not been identified yet.

As presented in figure 5.17f, refined grains within the PZ exhibit a basically random texture, which is consistent with some existing reports [11, 54]. However, prevalent opinions attribute the formation of random texture to recrystallization via DDRX or PSN, which has not been fully substantiated yet. In our previous discussion regarding the microstructure evolution and recrystallization mechanism for FSBE-processed AA7075 alloy, it is clearly confirmed that the grain structure within the PZ is

formed via a synergic effect of GDX and CDRX near grain boundaries, which are strongly supported by experimental observations. In the case of CDRX, is has been proven that small grains formed near the grain boundaries are not necessarily showing similar orientations or following specific evolutional path of their mother grains since the local deformation near grain boundaries is always different from the externally imposed strain field. It has been confirmed in the recrystallization discussion of AA6063 alloy that the newly formed grains via CDRX at grain boundaries are showing random rotation and reorientation tendencies regardless of the corresponding orientations of their mother grains.

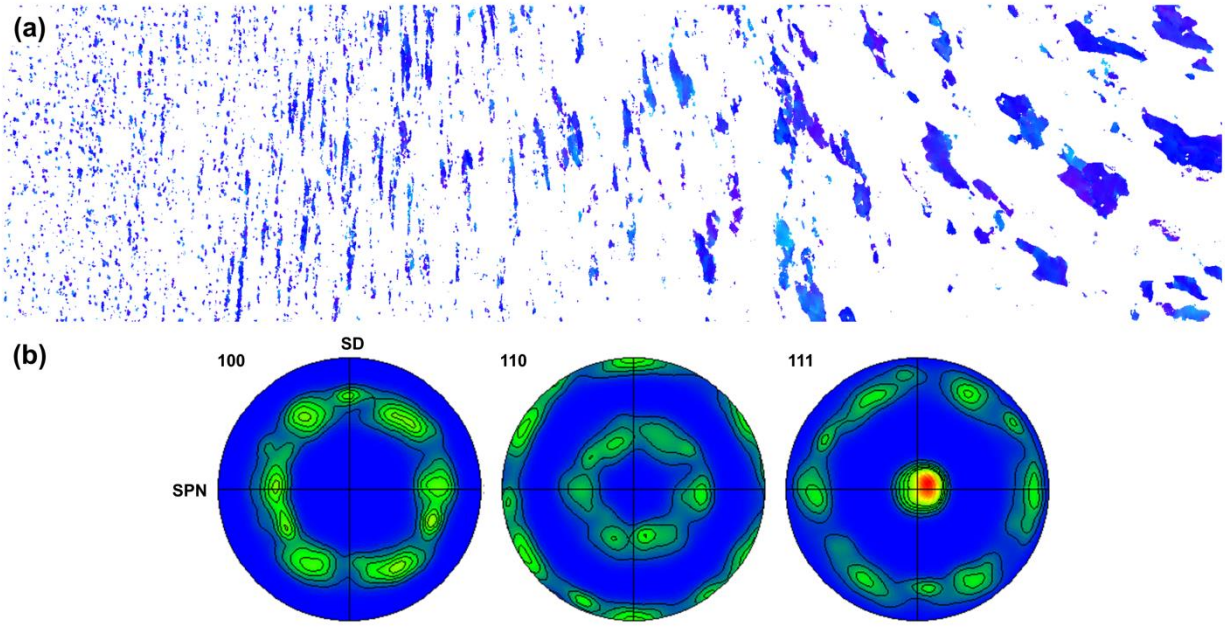

Figure 5.18 (a) Distribution of grains with B/ B̄ texture and (b) corresponding pole figures

On another hand, even if some discussions made regarding the crystallographic texture of grain structure that is formed via GDX pointed out that prior deformation texture might be retained during the transformation to a new grain structure due to lack of long-range migration of HAGBs [11] without providing any experimental evidence. However, in our case of AA7075 tubes, grain by grain analysis that is performed in the previous section intended to unveil the recrystallization mechanisms suggests that it is possible for the recrystallized grains formed via GDX to inherit the basic texture type that characterized their mother grains; however, a more general circumstance is a group of newly formed grains via GDX are randomly reoriented with respect to their elongated mother grains. Think about the GDX as a subdivision process for a deformed and elongated grain, it is almost impossible to have newly formed grains exhibit similar orientations to their mother grain while still separate by HAGBs. Thus the contribution of GDX to texture formation, in our case of AA7075 alloy, can be summarized as a major effect of texture randomization and minor retention of previous texture components. Actually that is why the texture measured within the PZ is showing a weak <100> fiber, which is inherited from the transition region of sub2, even if the entire PFs can be interpreted as being random. In a previous investigation performed by Prangnell et al. [71] that supports GDX process as major grain refinement mechanism involved in FSW/FSP, B/$\bar{B}$ shear texture components were observed while the author didn't correlate its formation to GDX process nor a detailed discussion regarding the texture formation is performed. However, from our perspective, logically, a direct connection between GDX and the formation of final shear texture components can't be built unless

sufficient experimental data is provided to support such philosophy. The formation of shear texture or other types such as fiber is inherent in materials and marginally affected by the grain refinement mechanisms, unless the mechanisms such as PSN and DDRX that fundamentally change the grain orientations occur extensively. However, up to now, no existing literature has confirmed the dominance of these mechanisms in FSW/FSP process Al even if they might contribute to the microstructure evolution to some extent. It is highly possible that the 2195 alloy analyzed by Prangnell et al. [71] inherently tend to form shear texture component, so they can either evolve into B/$\bar{B}$ after the split from GDX or B/$\bar{B}$ type can simply be partially formed during the subdivision process of GDX.

To briefly summarized the observation made in the case of 7075 texture:

1, Predominant fiber texture are noticed in the tube bottom of AA7075 alloy rather than shear components

2, B/$\bar{B}$ components are also observed and the corresponding grains are distributed homogeneous across the entire map being analyzed,

3, Fiber textures might be stable under such shear-controlled deformation modes in AA7075 alloys, <111>//SPN fiber is formed under lower strain level and it is transformed to <100>//SPN fiber with increased strain, accompanied by grain aspect ratio change.

4, Strong shear texture is not formed during the FSBE process of AA7075 alloys, it is not because the shear strain is insufficient; on the contrary, it is believed that the

AA7075 alloys is inherently hard to form shear type texture under current deformation modes. Unfortunately, the fundamental reasons have not been identified.

5, Random texture that has been observed in the PZ is explained based on the recrystallization mechanism of CDRX at grain boundaries and GDX that has been identified in previous sections. It is proposed that GDX and CDRX tend to randomize the texture component while the GDX might also partially retain the prior deformation texture, in this case a very weak <100>//SPN fiber is noticed in the PZ.

6, Contribution: little investigations have been performed to unveil the micro-texture formation of FSW/FSP processed ultra-high strength 7000 series aluminum alloys, especially its relationship to recrystallization mechanisms. Traditionally, either PSN or DDRX are just borrowed to explain the texture observed macroscopically. With our research new mechanism is proposed based on the identified grain refinement mechanisms and the texture measurement from TMAZ all the way to the PZ. GDX and CDRX at grain boundaries tend to randomize the texture. At the same time, no strong shear texture is formed during the entire texture evolution.

Texture across the tube wall at multiple locations will be presented but not be discussed in detail. It is going to be extremely complicated considering the complex materials flow that is involved during the FSBE process, and also the exhaustive textural analysis across the entire tube wall has been performed for AA6063 tubes. To make things worse, the texture formed in this AA7075 alloy is relatively weak and the ideal shear texture is barely observed, making it almost impossible to capture the deformation geometries at different locations across the tube wall as well as along the tube. However,

basic texture types that are observed across tube walls at multiple locations can be explained as fiber texture, even if they are distorted and rotated by the materials flow in an intricate fashion. The IPF images as well as texture results for 10mm, 30mm and 50mm locations are presented in figure 5.19-5.21 respectively. Some preliminary analysis shows that those stronger poles present on the pole figures are generally related to certain fiber components, they are rotated to different locations on the PFs due to localized materials flow and their deformation history. The texture components within the PZ are not showing similar types in all three cases. Nevertheless, it is almost certain that the texture component identified near the PZ is weakened and randomized, which is consistent with the conclusion drawn from the tube bottom.

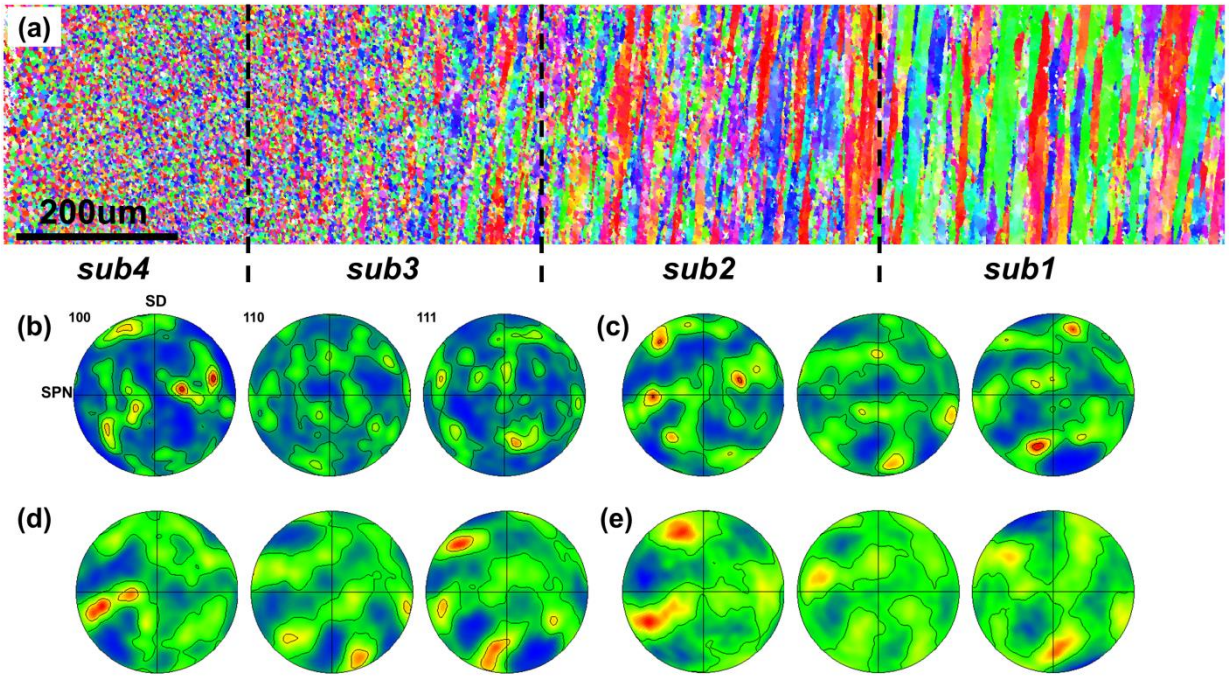

Figure 5.19 (a) IPF image of the tube wall at 10mm location (b)-(e) pole figures for sub1-sub4

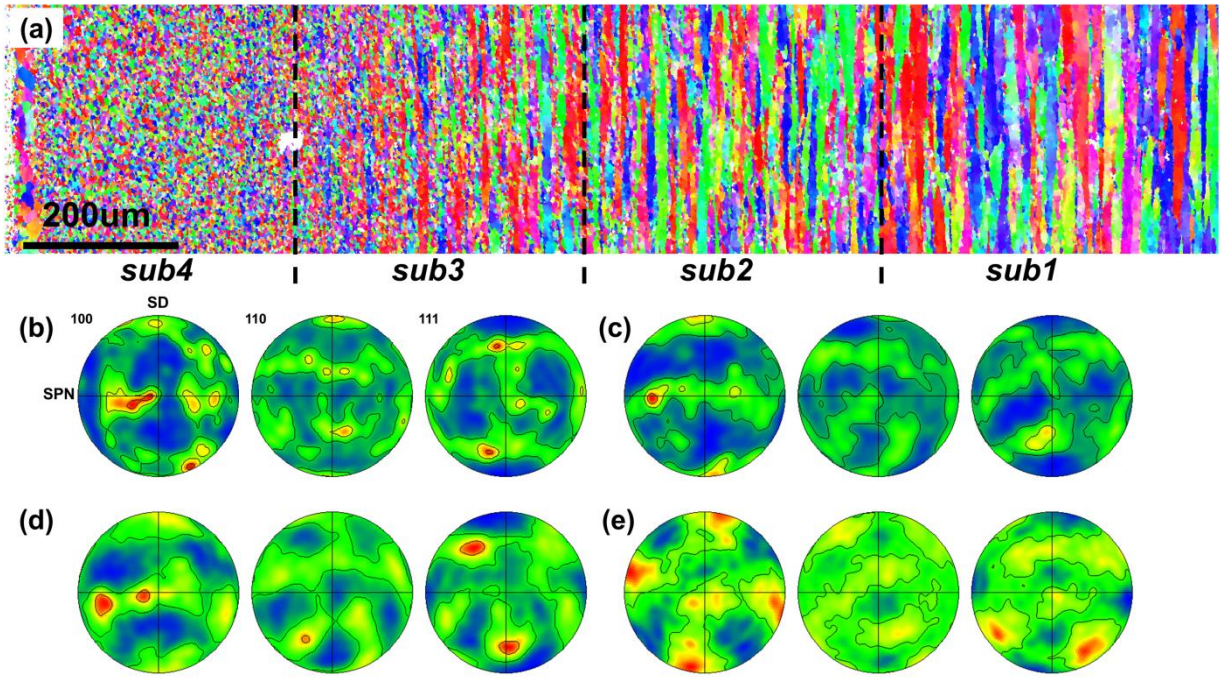

Figure 5.20 (a) IPF image of the tube wall at 30mm location (b)-(e) pole figures for sub1-sub4

Disparate types of texture are formed during the FSBE process of AA6063 and AA7075 alloys. In the case of AA6063 alloy, texture components can be understood and interpreted as simple shear texture, similar to the prevalent conclusion drew from FSW/FSP of aluminum alloys, despite the fact that some manipulation on the shear reference frameworks is needed. However, ideal shear type texture component has hardly been noticed in AA7075 tubes.

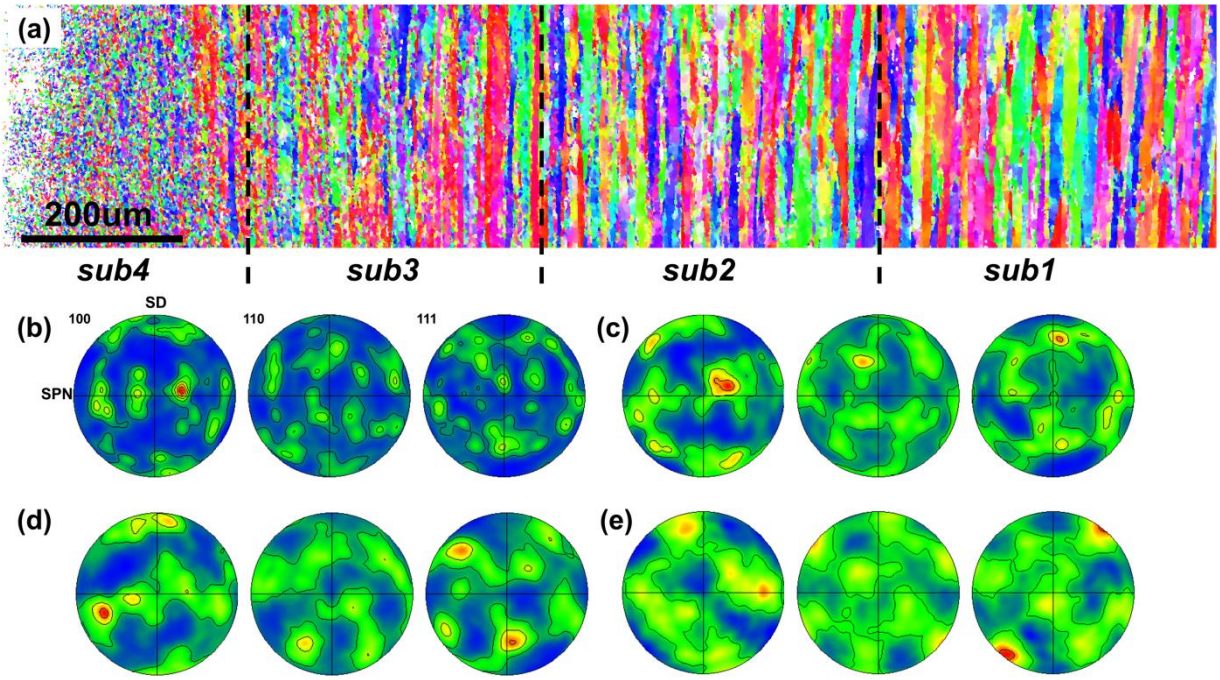

Figure 5.21 (a) IPF image of the tube wall at 55mm location (b)-(e) pole figures for sub1-sub4

It is plausible that static annealing might occur in the very short period of time while the tool was extracting. If that is the case, extensive cube-orientated grains with minimal LAGBs accompanied by grain growth should be expected, as observed by Suhuddin et al. [62]. However, in the case of AA7075 alloy, it seems that those grains showing <100>//ED, which might be related to cube/rotated cube components, are not formed by static annealing since they are neither showing a low density of LAGBs nor identifiable grain growth. Rather, it is most likely that these grains are directly evolved from the deformed microstructure under relevant recrystallization mechanisms. With the discussion performed in the texture analysis of AA7075 alloy, the <100> //ED is turned

out to be a fiber component that is formed during the deformation and being stable at relatively high strain level.

In order to discuss the texture difference noticed in these alloys when processed via FSBE, three major arguments are proposed as follows:

1, corresponding recrystallization mechanisms that are responsible for the formation of grain structure of each alloy are different, it should be pointed out that similar types of mechanisms might be operating during the dynamic recrystallization of all three alloys, their relative contribution to the final microstructure and texture can vary. In the case of 6063 alloys, grain structure evolution during dynamic recrystallization mainly involves the mechanisms of grain sub-division and subgrain rotations. As discussed in the DRX part of 6063 alloys, initially, LAGBs and subgrains tend to form near the original grain boundaries; with increasing amount of strain applied, the deformed grains are fully sub-divided into sub-regions (subgrains) by LAGBs, whose size is similar to those fully recrystallized grains within the PZ. Additionally, a strong shear type texture is identified in the PZ that matches the observation that grain structures are developed in a fashion of gradual sub-division and rotations according to the macroscopic deformation geometry. In a previous work performed by Fonda et.al [40], similar observations regarding grain structure as well as textural evolution were made in the FSW of a 2195 alloy.

On another side, in the case of 7075 alloy, this mechanism of grain subdivision and gradual subgrain rotation with strain is no longer the controlling mechanism that is related to dynamic recrystallization. As mentioned in the discussion of recrystallization

mechanism for these alloys, geometrical dynamic recrystallization tend to play a crucial role, thus the orientations of newly formed grains should be closely related to that of the grains where they evolve from, as proposed by Suhuddin and Humphreys et al [11, 61]. Based on our experimental data, it is found that grains formed via GDX will only partially inherit the previous texture, while to a larger extent, being randomized with respect to grain orientations. It should be noted that these pancake-shaped grains are not necessarily showing shear-texture related orientations, in reality most of them are not and the texture in the transition region of AA7075 tube is dominated by fiber component. Thus there is no chance for those new grains that are originated from them would be showing shear type textures. This might be the major reason why texture types observed near the PZ and transition region of FSBE processed tube are not related to the shear type components.

2, additionally, new grains 'nucleated' near previous grain boundaries by progressive lattice rotation and dynamic recovery are found to be able to modify and randomize texture, at the same time they contribute to the microstructural evolution and grain refinement. These grains are noticed in the transition region and TMAZ of AA6063 tube, and across the entire analyzed region of AA7075 tubes. This can be evidenced by the extensive observation of very small grain/subgrain formed near the grain boundaries of refined equiaxed grains showing low misorientations relative to their mother grains. However, it is assumed that these grains are not necessarily following the evolutional path of forming shear type texture because the local deformation near grain boundaries might differ from the macroscopically imposes shear strain. It is widely reported that the

deformation near grain boundary consist of inhomogeneous slipping, grain boundary plasticity and activation of extra slip systems. Since the newly formed grains are small in nature, their behavior can be rather affected by the grain boundaries, fundamentally because of the activation of different set of slip systems. Thus, it is most likely that these newly formed small grains are not evolving into a shear type texture or follow whatever reorientation pathways that the macroscopic straining dictates. Also, even if these newly formed grains would show similar orientations to the grains from which they are transformed, their mother grains should mainly be a result of GDX; as mentioned earlier, these grains are actually not showing shear type texture.

3, compare to AA6063 alloy, AA7075 alloy showing sluggish reaction to external shear deformation. It is noticed from previous results that arrays of ordered subgrain boundaries are readily formed inside AA6063 grains distorted by the strain field before being strained to a pancake-shaped morphology with very high aspect ratios. That means, due to fast DRV process and high mobility of subgrain boundaries, recrystallized grains are formed before the initial grains are strained to a pancake shape. Base on the geometric relationship that is used to determine the grain thickness in the normal direction under rolling discussion, the following formula can be applied to the shear deformation in our cases.

$$H = D_0 \exp(-\varepsilon)$$

On the contrary, grains within AA7075 alloy are highly elongated before fully transformed into equiaxed recrystallized grains. It is noticed from previous discussions that ordered array of subgrains are not formed until the grains are elongated to such a

high level that GDX can be triggered. Base on the geometric formula mentioned above, a much higher level of strain is imposed to achieve such an aspect ratio in the grain structure of AA7075 alloy, compared to AA6063 alloy.

With such a high strain level, the subgrain structure has not been fully developed and transform into stable grains with HAGBs, while in the cases of AA6063 tubes, ordered substructure is formed at a lower level of strain, indicated by lower aspect ratio of distorted initial grains. It can be concluded briefly that AA7075 alloys show a sluggish reaction to external strain with respect to the formation of subgrains and LAGBs. An ordered sub-structure can't be formed to enable extensive continuous dynamic recrystallization at strain level comparable to the case of AA6063 alloys. With this philosophy, assuming the grains, either recrystallized or unrecrystallized, are transforming into the orientations associated with shear type texture, the rate of transformation might be slow and still in transition thus not being identified clearly and properly. The underlying mechanism might be related to the solute drag of Al-Zn-Mg-Cu series due to high content of solutes, inhibiting the movement and rearrangement of mobile dislocations into LAGBs within the grains. However, strain and dislocations level accumulated near the GB, where high dislocation density and expedited dislocation movement is expected, can be high enough to overcome the dragging from solutes, and form the small grains via CDRX.

4, last but most important aspect is the stability of various texture components under the shear deformation induced by FSBE process. For 6063 alloy, shear textures are formed readily under deformation with a clear transition from initial fiber texture to

stable components through intermediate texture types. While AA7075 alloy tend to form a <111>//SPN fiber which is stable under low-medium strain levels and can be transformed to <100>//SPN fiber with addition strain applied. Stable shear texture B/$\bar{B}$ are also noticed but it is found to be weak compared to other fibers thus hard to be identified. It is believed that the <111> and <100> fibers are more stable and favored for 7075 alloy subjected to FSBE process and it is inherent from the materials itself. The fundamental reason is not clear by now. Under these circumstances, the micro-texture within the PZ would not be characterized by shear component regardless of the recrystallization mechanisms evolved since the material is fundamentally not favorable for the formation of shear textures or more favorable for other types of textures, in our case, fibers.

CONCLUSION

Systematic investigations regarding microstructure change, micro-texture evolution and mechanical properties of two commercial heat treatable aluminum alloy AA6063-T5 and AA7075-T6 under Friction Stir Back Extrusion processing have been performed. Recrystallization mechanisms responsible for grain refinement have been discussed for both alloys based on grain structure and grain orientation analysis. Mechanical properties are evaluated by both micro-hardness testing and uniaxial tension tests.

It is found that significant grain refinement has been achieved near the processing zone for both alloys. The refinement mechanism for AA6063-T5 alloys is determined to be progressive grain subdivision and dynamic recovery; while Geometric Dynamic Recrystallization and Continuous Dynamic Recrystallization at grain boundaries contribute to the grain refinement of AA7075 alloys when processed by Friction Stir Back Extrusion process. Micro-texture analysis suggests that the texture along AA6063 tube can be essentially interpreted by simple shear textures; however, rigid body rotations need to be applied to the measured pole figures to align them to local shear reference frame, in order to identify the texture components properly. For AA7075 alloy, texture near the processing zone is identified to be random while the corresponding thermomechanically affected zone is featured be a fiber texture. It is proposed that the random texture is a result of synergic effect of Geometric Dynamic Recrystallization and

Continuous Dynamic Recrystallization occurs near grain boundaries. Some new observations regarding recrystallization as well grain orientation change have been made and the underlying mechanisms are discussed.

Dissolution of hardening precipitates during the thermal cycles imposed by the process is observed for both alloys, resulting in a decreased strength and increased ductility. A post-process aging step restores the mechanical properties of the processed tubes by allowing the dissolved solute atoms to reprecipitate in the form of fine, dispersed phases, which can increase the strength and hardness. In the case of AA6063 alloy, mechanical properties of the tube are improved beyond the as-received materials; while 90% of the tensile strength and yield strength of AA7075-T6 alloy can be retained without losing any ductility. Also, mechanisms responsible for micro-hardness and mechanical properties variation are supported by TEM analysis.

FUTURE WORK

Accurate temperature measurements should be performed in the future work in the sense that it will help to understand the grain structure evolution such as grain growth and abnormal grain growth, it will also serve as an important indication for the precipitation sequence and materials flow. However, precise temperature measurements or the identification of thermal hysterias at different locations of the tube can be challenging since the process is a dynamic process, it is very hard to guarantee an excellent contact between the tips of thermocouple and materials being processed without being damaged by the deformation fields.

Additional TEM analysis should be done to reveal the precipitation behaviors at multiple locations along the tube. Grain boundary precipitation and the formation of PFZ should also be systematically investigated, since it has a profound impact on the materials behaviors especially for 7000 series alloys

Direct evidence for the proposed recrystallization mechanisms is desirable in future work, the mechanism of subgrain boundary nucleation should be analyzed with advanced techniques in order to reveal its origin, more discussion is needed to figure out whether it belongs to discontinuous or continuous dynamic recrystallization. The random texture formation in the PZ of AA7075 alloy should also be further analyzed to confirm the impact of PSN and verify the possibility of discontinuous dynamic recrystallization

Additionally, thermal conductivity change of the tube after the FSBE process should also be discussed.

A lot more potential works should be done for this topic and they will not be listed one by one for the time being.

REFERENCES

1. Mishra, R.S. and Z.Y. Ma, *Friction stir welding and processing.* Materials Science and Engineering: R: Reports, 2005. **50**(1–2): p. 1-78.
2. Ma, Z.Y., *Friction Stir Processing Technology: A Review.* Metallurgical and Materials Transactions A, 2008. **39**(3): p. 642-658.
3. Nandan, R., T. DebRoy, and H.K.D.H. Bhadeshia, *Recent advances in friction-stir welding – Process, weldment structure and properties.* Progress in Materials Science, 2008. **53**(6): p. 980-1023.
4. Threadgill, P.L., et al., *Friction stir welding of aluminium alloys.* International Materials Reviews, 2009. **54**(2): p. 49-93.
5. Yang, Q., et al., *Effect of tool geometry and process condition on static strength of a magnesium friction stir lap linear weld.* Materials Science and Engineering: A, 2011. **528**(6): p. 2463-2478.
6. Çam, G. and S. Mistikoglu, *Recent Developments in Friction Stir Welding of Al-alloys.* Journal of Materials Engineering and Performance, 2014. **23**(6): p. 1936-1953.
7. Seidel, T.U. and A.P. Reynolds, *Visualization of the material flow in AA2195 friction-stir welds using a marker insert technique.* Metallurgical and Materials Transactions A, 2001. **32**(11): p. 2879-2884.
8. Ouyang, J.H. and R. Kovacevic, *Material flow and microstructure in the friction stir butt welds of the same and dissimilar aluminum alloys.* Journal of Materials Engineering and Performance, 2002. **11**(1): p. 51-63.
9. Li, X., W. Tang, and A.P. Reynolds, *Visualization of Material Flow in Friction Extrusion*, in *ICAA13: 13th International Conference on Aluminum Alloys*. 2012, John Wiley & Sons, Inc. p. 1659-1664.
10. Rhodes, C.G., et al., *Fine-grain evolution in friction-stir processed 7050 aluminum.* Scripta Materialia, 2003. **48**(10): p. 1451-1455.
11. McNelley, T.R., S. Swaminathan, and J.Q. Su, *Recrystallization mechanisms during friction stir welding/processing of aluminum alloys.* Scripta Materialia, 2008. **58**(5): p. 349-354.
12. Liu, G., et al., *Microstructural aspects of the friction-stir welding of 6061-T6 aluminum.* Scripta Materialia, 1997. **37**(3): p. 355-361.
13. Murr, L.E., G. Liu, and J.C. McClure, *A TEM study of precipitation and related microstructures in friction-stir-welded 6061 aluminium.* Journal of Materials Science, 1998. **33**(5): p. 1243-1251.
14. Sato, Y., et al., *Microstructural evolution of 6063 aluminum during friction-stir welding.* Metallurgical and Materials Transactions A, 1999. **30**(9): p. 2429-2437.

15. Sato, Y., et al., *Precipitation sequence in friction stir weld of 6063 aluminum during aging.* Metallurgical and Materials Transactions A, 1999. **30**(12): p. 3125-3130.
16. Cabibbo, M., E. Meccia, and E. Evangelista, *TEM analysis of a friction stir-welded butt joint of Al–Si–Mg alloys.* Materials Chemistry and Physics, 2003. **81**(2–3): p. 289-292.
17. Su, J.Q., et al., *Microstructural investigation of friction stir welded 7050-T651 aluminium.* Acta Materialia, 2003. **51**(3): p. 713-729.
18. Sato, Y., S. Park, and H. Kokawa, *Microstructural factors governing hardness in friction-stir welds of solid-solution-hardened Al alloys.* Metallurgical and Materials Transactions A, 2001. **32**(12): p. 3033-3042.
19. Sato, Y., M. Urata, and H. Kokawa, *Parameters controlling microstructure and hardness during friction-stir welding of precipitation-hardenable aluminum alloy 6063.* Metallurgical and Materials Transactions A, 2002. **33**(3): p. 625-635.
20. Liu, H.J., et al., *Tensile properties and fracture locations of friction-stir-welded joints of 2017-T351 aluminum alloy.* Journal of Materials Processing Technology, 2003. **142**(3): p. 692-696.
21. Lim, S., et al., *Tensile behavior of friction-stri-welded Al 6061-T651.* Metallurgical and Materials Transactions A, 2004. **35**(9): p. 2829-2835.
22. Elangovan, K. and V. Balasubramanian, *Influences of post-weld heat treatment on tensile properties of friction stir-welded AA6061 aluminum alloy joints.* Materials Characterization, 2008. **59**(9): p. 1168-1177.
23. Gan, W., et al., *Properties of Friction-Stir Welded Aluminum Alloys 6111 and 5083.* Journal of Engineering Materials and Technology, 2008. **130**(3): p. 031007-031007.
24. Simar, A., et al., *Microstructure, local and global mechanical properties of friction stir welds in aluminium alloy 6005A-T6.* Materials Science and Engineering: A, 2008. **486**(1–2): p. 85-95.
25. Tang, W. and A.P. Reynolds, *Production of wire via friction extrusion of aluminum alloy machining chips.* Journal of Materials Processing Technology, 2010. **210**(15): p. 2231-2237.
26. Abu-Farha, F., *A preliminary study on the feasibility of friction stir back extrusion.* Scripta Materialia, 2012. **66**(9): p. 615-618.
27. Dinaharan, I., et al., *Microstructural Characterization of Pure Copper Tubes Produced by a Novel Method Friction Stir Back Extrusion.* Procedia Materials Science, 2014. **5**(0): p. 1502-1508.
28. Sarkari Khorrami, M. and M. Movahedi, *Microstructure evolutions and mechanical properties of tubular aluminum produced by friction stir back extrusion.* Materials & Design, 2015. **65**(0): p. 74-79.
29. Minler, J., *On the Manufacture of Lightweight Alloy Tubes via Friction Stir Back Extrusion: Process Evaluation and Material Performance.* MSEC, 2014.
30. Milner, J.L. and F. Abu-Farha, *Friction Stir Back Extrusion of Mg AZ31B-F: A Preliminary Investigation*, in *Magnesium Technology 2014*. 2014, John Wiley & Sons, Inc. p. 497-503.

31. Sato, Y. and H. Kokawa, *Distribution of tensile property and microstructure in friction stir weld of 6063 aluminum.* Metallurgical and Materials Transactions A, 2001. **32**(12): p. 3023-3031.
32. Mahoney, M.W., et al., *Properties of friction-stir-welded 7075 T651 aluminum.* Metallurgical and Materials Transactions A, 1998. **29**(7): p. 1955-1964.
33. Canova, G.R., U.F. Kocks, and J.J. Jonas, *Theory of torsion texture development.* Acta Metallurgica, 1984. **32**(2): p. 211-226.
34. Montheillet, F., M. Cohen, and J.J. Jonas, *Axial stresses and texture development during the torsion testing of Al, Cu and α-Fe.* Acta Metallurgica, 1984. **32**(11): p. 2077-2089.
35. Montheillet, F., P. Gilormini, and J.J. Jonas, *Relation between axial stresses and texture development during torsion testing: A simplified theory.* Acta Metallurgica, 1985. **33**(4): p. 705-717.
36. Toth, L.S., P. Gilormini, and J.J. Jonas, *Effect of rate sensitivity on the stability of torsion textures.* Acta Metallurgica, 1988. **36**(12): p. 3077-3091.
37. Tóth, L.S., K.W. Neale, and J.J. Jonas, *Stress response and persistence characteristics of the ideal orientations of shear textures.* Acta Metallurgica, 1989. **37**(8): p. 2197-2210.
38. Field, D., et al., *Heterogeneity of crystallographic texture in friction stir welds of aluminum.* Metallurgical and Materials Transactions A, 2001. **32**(11): p. 2869-2877.
39. Sato, Y., et al., *Microtexture in the friction-stir weld of an aluminum alloy.* Metallurgical and Materials Transactions A, 2001. **32**(4): p. 941-948.
40. Fonda, R.W., J.F. Bingert, and K.J. Colligan, *Development of grain structure during friction stir welding.* Scripta Materialia, 2004. **51**(3): p. 243-248.
41. Pouchou, J.-L., et al., *Large-Field EBSD Mapping: Application to the Microstructure of a Friction Stir Welding Nugget.* Microchimica Acta, 2004. **145**(1-4): p. 171-176.
42. Fonda, R.W. and K.E. Knipling, *Texture development in friction stir welds.* Science and Technology of Welding and Joining, 2011. **16**(4): p. 288-294.
43. Fonda, R.W. and J.F. Bingert, *Texture variations in an aluminum friction stir weld.* Scripta Materialia, 2007. **57**(11): p. 1052-1055.
44. *Friction stir welding of single crystal aluminium.* Science and Technology of Welding and Joining, 2007. **12**(4): p. 304-310.
45. Ahmed, M.M.Z., et al., *Quantifying crystallographic texture in the probe-dominated region of thick-section friction-stir-welded aluminium.* Scripta Materialia, 2008. **59**(5): p. 507-510.
46. Fonda, R.W., K.E. Knipling, and J.F. Bingert, *Microstructural evolution ahead of the tool in aluminum friction stir welds.* Scripta Materialia, 2008. **58**(5): p. 343-348.
47. Kang, S., et al., *Investigation of the material flow and texture evolution in friction-stir welded aluminum alloy.* Metals and Materials International, 2009. **15**(6): p. 1027-1031.

48. Shibayanagi, T., et al., *Textures in Single-Crystal Aluminum Friction Stir Spot Welds.* Metallurgical and Materials Transactions A, 2009. **40**(4): p. 920-931.
49. Ahmed, M.M.Z., et al., *Through-thickness crystallographic texture of stationary shoulder friction stir welded aluminium.* Scripta Materialia, 2011. **64**(1): p. 45-48.
50. Ahmed, M.M.Z., et al., *Microstructure, crystallographic texture and mechanical properties of friction stir welded AA2017A.* Materials Characterization, 2012. **64**(0): p. 107-117.
51. Fonda, R.W., K.E. Knipling, and D.J. Rowenhorst, *EBSD Analysis of Friction Stir Weld Textures.* JOM, 2014. **66**(1): p. 149-155.
52. Fonda, R., et al., *Material Flow in Friction Stir Welds.* Metallurgical and Materials Transactions A, 2013. **44**(1): p. 337-344.
53. Tayon, W., et al., *Texture Evolution within the Thermomechanically Affected Zone of an Al-Li Alloy 2195 Friction Stir Weld.* Metallurgical and Materials Transactions A, 2013. **44**(11): p. 4906-4913.
54. Su, J.Q., T.W. Nelson, and C.J. Sterling, *Grain refinement of aluminum alloys by friction stir processing.* Philosophical Magazine, 2006. **86**(1): p. 1-24.
55. Humphreys, F.J. and M. Hatherly, *Chapter 13 - Hot Deformation and Dynamic Restoration*, in *Recrystallization and Related Annealing Phenomena (Second Edition)*, F.J.H. Hatherly, Editor. 2004, Elsevier: Oxford. p. 415-V.
56. Humphreys, F.J. and M. Hatherly, *Chapter 5 - The Mobility and Migration of Boundaries*, in *Recrystallization and Related Annealing Phenomena (Second Edition)*, F.J.H. Hatherly, Editor. 2004, Elsevier: Oxford. p. 121-167.
57. Humphreys, F.J. and M. Hatherly, *Chapter 7 - Recrystallization of Single-Phase Alloys*, in *Recrystallization and Related Annealing Phenomena (Second Edition)*, F.J.H. Hatherly, Editor. 2004, Elsevier: Oxford. p. 215-IV.
58. Roberts, W. and B. Ahlblom, *A nucleation criterion for dynamic recrystallization during hot working.* Acta Metallurgica, 1978. **26**(5): p. 801-813.
59. Sandström, R. and R. Lagneborg, *A model for static recrystallisation after hot deformation.* Scripta Metallurgica, 1975. **9**(1): p. iii.
60. Wusatowska-Sarnek, A.M., H. Miura, and T. Sakai, *Nucleation and microtexture development under dynamic recrystallization of copper.* Materials Science and Engineering: A, 2002. **323**(1): p. 177-186.
61. Humphreys, F.J. and M. Hatherly, *Chapter 14 - Continuous Recrystallization During and after Large Strain Deformation*, in *Recrystallization and Related Annealing Phenomena (Second Edition)*, F.J.H. Hatherly, Editor. 2004, Elsevier: Oxford. p. 451-467.
62. Suhuddin, U.F.H.R., et al., *Grain structure and texture evolution during friction stir welding of thin 6016 aluminum alloy sheets.* Materials Science and Engineering: A, 2010. **527**(7–8): p. 1962-1969.
63. Baxter, G.J., et al., *The influence of transient strain-rate deformation conditions on the deformed microstructure of aluminium alloy Al–1% Mg.* Acta Materialia, 1999. **47**(8): p. 2367-2376.

64. Ion, S.E., F.J. Humphreys, and S.H. White, *Dynamic recrystallisation and the development of microstructure during the high temperature deformation of magnesium.* Acta Metallurgica, 1982. **30**(10): p. 1909-1919.
65. Doherty, R.D., et al., *Current issues in recrystallization: a review.* Materials Science and Engineering: A, 1997. **238**(2): p. 219-274.
66. Rosen, G.I., et al., *Microstructure and local crystallography of cold rolled aluminium.* Acta Metallurgica et Materialia, 1995. **43**(7): p. 2563-2579.
67. Gholinia, A., F.J. Humphreys, and P.B. Prangnell, *Production of ultra-fine grain microstructures in Al–Mg alloys by coventional rolling.* Acta Materialia, 2002. **50**(18): p. 4461-4476.
68. Jata, K.V. and S.L. Semiatin, *Continuous dynamic recrystallization during friction stir welding of high strength aluminum alloys.* Scripta Materialia, 2000. **43**(8): p. 743-749.
69. Hassan, K.A.A., et al., *Stability of nugget zone grain structures in high strength Al-alloy friction stir welds during solution treatment.* Acta Materialia, 2003. **51**(7): p. 1923-1936.
70. Su, J.-Q., T.W. Nelson, and C.J. Sterling, *Microstructure evolution during FSW/FSP of high strength aluminum alloys.* Materials Science and Engineering: A, 2005. **405**(1): p. 277-286.
71. Prangnell, P.B. and C.P. Heason, *Grain structure formation during friction stir welding observed by the 'stop action technique'.* Acta Materialia, 2005. **53**(11): p. 3179-3192.
72. Ren, S.R., Z.Y. Ma, and L.Q. Chen, *Effect of welding parameters on tensile properties and fracture behavior of friction stir welded Al–Mg–Si alloy.* Scripta Materialia, 2007. **56**(1): p. 69-72.
73. Woo, W., et al., *Influence of the Tool Pin and Shoulder on Microstructure and Natural Aging Kinetics in a Friction-Stir-Processed 6061–T6 Aluminum Alloy.* Metallurgical and Materials Transactions A, 2007. **38**(1): p. 69-76.
74. Ikeno, S., et al., *Transmission Electron Microscope Observation of Grain Boundary Precipitates in an Al-1 mass% Mg~ 2Si Alloy.* JOURNAL-SOCIETY OF MATERIALS SCIENCE JAPAN, 1993. **42**: p. 949-949.
75. Liu, F.C. and Z.Y. Ma, *Influence of Tool Dimension and Welding Parameters on Microstructure and Mechanical Properties of Friction-Stir-Welded 6061-T651 Aluminum Alloy.* Metallurgical and Materials Transactions A, 2008. **39**(10): p. 2378-2388.
76. Fonda, R.W. and J.F. Bingert, *Microstructural evolution in the heat-affected zone of a friction stir weld.* Metallurgical and Materials Transactions A, 2004. **35**(5): p. 1487-1499.
77. Woo, W., et al., *Texture analysis of a friction stir processed 6061-T6 aluminum alloy using neutron diffraction.* Acta Materialia, 2006. **54**(15): p. 3871-3882.
78. Xin, R., et al., *Changes in texture and microstructure of friction stir welded Mg alloy during post-rolling and their effects on mechanical properties.* Materials Science and Engineering: A, 2013. **582**(0): p. 178-187.

79. Humphreys, F.J. and M. Hatherly, *Chapter 10 - The Growth and Stability of Cellular Microstructures*, in *Recrystallization and Related Annealing Phenomena (Second Edition)*, F.J.H. Hatherly, Editor. 2004, Elsevier: Oxford. p. 321-331.
80. Charit, I. and R.S. Mishra, *Abnormal grain growth in friction stir processed alloys.* Scripta Materialia, 2008. **58**(5): p. 367-371.
81. Humphreys, F.J. and M. Hatherly, *Chapter 6 - Recovery After Deformation*, in *Recrystallization and Related Annealing Phenomena (Second Edition)*, F.J.H. Hatherly, Editor. 2004, Elsevier: Oxford. p. 169-213.